

**STABILITY, CONTROL, AND OPTIMIZATION OF NONLINEAR DYNAMICAL
SYSTEMS WITH APPLICATIONS IN ELECTRIC POWER NETWORKS**

A Dissertation
Presented to
The Academic Faculty

By

Amin Gholami

In Partial Fulfillment
of the Requirements for the Degree
Doctor of Philosophy in the
H. Milton Stewart School of Industrial and Systems Engineering (ISyE)

Georgia Institute of Technology

December 2021

© Amin Gholami 2021

**STABILITY, CONTROL, AND OPTIMIZATION OF NONLINEAR DYNAMICAL
SYSTEMS WITH APPLICATIONS IN ELECTRIC POWER NETWORKS**

Thesis committee:

Dr. Andy Sun, Advisor
School of Industrial and Systems Engineering
Georgia Institute of Technology

Dr. Daniel Molzahn
School of Electrical and Computer Engineering
Georgia Institute of Technology

Dr. Pascal Van Hentenryck
School of Industrial and Systems Engineering
Georgia Institute of Technology

Dr. Na (Lina) Li
School of Engineering and Applied Sciences
Harvard University

Dr. Santanu S. Dey
School of Industrial and Systems Engineering
Georgia Institute of Technology

Date approved: December 10, 2021

To my family, for their unconditional love and support

ACKNOWLEDGMENTS

I am very grateful to my advisor Professor Andy Sun for his intelligence, guidance, and endless help. I am greatly indebted to Andy for enthusiastically welcoming me into the field of Operations Research and showing me the beauty of mathematics. His approach to problem solving and thinking “outside the box” together with his high research and ethical standards have forever changed my philosophy of research.

I would like to thank the members of my thesis committee Professor Santanu Dey, Professor Pascal Van Hentenryck, Professor Daniel Molzahn, and Professor Na Li for their support, constructive feedback, and insightful discussions. I am also deeply indebted to Professor Maryam Saedifard for her unconditional support during my first year of Ph.D. at Georgia Tech.

I had the honor of being a member of GMI-GO team in the Department of Energy’s (DOE) ARPA-E Grid Optimization (GO) competition during the last two years of my Ph.D. I am deeply thankful to Professor Andy Sun for leading the team, and also to Kaizhao Sun and Shixuan Zhang for being a source of creativity, for their innovative ideas, and for their persistence and hard work. I must also thank Professor Santanu Dey and Professor Pascal Van Hentenryck for their constructive interactions. Thanks to Terrence W.K. Mak for his valuable suggestions. It has been very enjoyable and productive two years of working on extremely challenging and large-scale optimization problems.

The greatest about the Georgia Tech’s ISyE is the people and distinguished faculty. I am grateful to Professor Andy Sun, Professor Shabbir Ahmed, Professor Santanu Dey, and Professor Arkadi Nemirovski for their unique and inspiring courses on the fundamentals of Operations Research. I would like to thank Professor Edwin Romeijn and Professor Santanu Dey for serving as the chair and associate chair for graduate studies during my time in ISyE. I would like to also thank Amanda Ford, for serving as the graduate programs manager and for all her help.

I have been extremely lucky to have wonderful friends in my life. First and foremost, I would like to thank my dearest friend, Tohid Shekari. Tohid is very warm-hearted, generous, and caring. His integrity and diligence have always inspired me to tackle my problems in research and life in general. He unconditionally supported me during the most challenging and stressful days of my Ph.D. life, and I am forever indebted to him. I would also like to thank his wife, Shima, for her kindness, and I wish them all the best. A special thank goes to Mahsa for her kindness, sweet smile, and support. Thanks to Moussa Hodjat-Shamami, Sajad Khodadadian, Sara Kaboudvand and Yasaman Mohammadshahi for game nights, chats, and laughs that made up unforgettable memories. I shared wonderful memories with my lifetime friends including Mohammadreza Miranbeigi, Amir H. Hosseinnia, Morteza Rezaee, Nahid Aslani Amoli, Mahmoud Mehrabankhomartash, Sajjad Abdollahramezani, Saeed Ansari, Ali Taleb Zadeh Kasgari, Mahdi Jamei, Hadi Amini, and Hamid Gholami.

I want to thank my friends and cohorts in ISyE, especially Kaizhao Sun and Shixuan Zhang. Kaizhao and Shixuan are truly knowledgeable and hardworking, and I am grateful to them for all the great interactions, fun times, and for teaching me many lessons. Thanks to my officemate, Yu Yang, for introducing me to hot pot, and for our late night discussions about philosophy and mathematics. Finally, thanks to Bai Cui for great discussions and all the good times in our group meetings.

My thanks for my family will never be enough. This achievement lives on the support, sacrifice, and unconditional love of them. I am very blessed to have my dear Saeid, Farzan, Maryam, and Marjan in my life. I dedicate this thesis to my lovely parents. Thank you.

TABLE OF CONTENTS

Acknowledgments	iv
List of Tables	xiv
List of Figures	xvi
Summary	xix
Chapter 1: Introduction and Background	1
1.1 Background	3
1.1.1 Electric Power Systems and Swing Equations	3
1.1.2 Multi-Microgrids and Stability-Constrained Optimization	5
1.1.3 Second-Order Ordinary Differential Equations	6
1.2 Outline and Summary of Contributions	7
1.2.1 Chapter 2: Impact of Damping in Second-Order Dynamical Systems	7
1.2.2 Chapter 3: A Stability Certificate for Kron-Reduced Swing Equations	8
1.2.3 Chapter 4: A Stability Certificate for Structure-Preserving Swing Equations	9
1.2.4 Chapter 5: Stability and Control of Multi-Microgrids	9
1.2.5 Chapter 6: A Stability Certificate for Droop-Controlled Inverters . .	10
1.2.6 Chapter 7: Optimization-Based Load Shedding in Single Microgrids	11

1.2.7	Chapter 8: Stability-Constrained Optimization in Multi-Microgrids .	12
1.3	Related Publications	13
1.4	Notations	13
I	Stability and Control of Nonlinear Dynamical Systems	15
	Chapter 2: Impact of Damping in Second-Order Nonlinear Dynamical Systems	16
2.1	Introduction	16
2.1.1	Related Work	18
2.1.2	Main Results	19
2.1.3	Chapter Outline	21
2.2	Background	21
2.2.1	Problem Statement	21
2.3	Monotonic Effect of Damping	24
2.4	Impact of Damping on Hyperbolicity and Bifurcation	31
2.4.1	Necessary and Sufficient Conditions for Breaking Hyperbolicity . .	31
2.4.2	Bifurcation under Damping Variations	35
2.5	Power System Models and Impact of Damping	38
2.5.1	Power System Model	38
2.5.2	Jacobian of Swing Equations	40
2.5.3	Referenced Power System Model	41
2.5.4	Impact of Damping in Power Systems	43
2.6	Numerical Results	48
2.6.1	Case 1	49

2.6.2	Case 2	51
2.7	Final Remarks	53
Chapter 3: A Stability Certificate for Kron-Reduced Swing Equations		54
3.1	Introduction	54
3.1.1	Related Work	55
3.1.2	Main Results	56
3.1.3	Chapter Outline	56
3.2	Background	57
3.2.1	Autonomous Ordinary Differential Equations	57
3.2.2	Multi-Machine Swing Equations	59
3.3	Linearization and Spectrum of Jacobian	60
3.3.1	Linearization	60
3.3.2	Graph Induced by L and Its Spectral Properties	60
3.4	Sufficient Condition for the Stability of Swing Equations: A Fast Certificate	62
3.5	Numerical Results	63
3.6	Final Remarks	67
Chapter 4: A Stability Certificate for Structure-Preserving Swing Equations . .		68
4.1	Introduction	69
4.1.1	Related Work	69
4.1.2	Main Results	71
4.1.3	Chapter Outline	72
4.2	Structure-Preserving and Singular Perturbation Power System Models . . .	72

4.2.1	Structure-Preserving Model	73
4.2.2	Equilibrium Points	74
4.2.3	Singular Perturbation Model	75
4.3	Stability Certificate in Structure-Preserving and Singular Perturbation Models	76
4.3.1	Fast and Distributed Scheme for Stability Assessment	78
4.3.2	Remarks on Corollary 1	78
4.4	Numerical Results	80
4.4.1	Perturbed Model Approximation: Time-Domain Comparison	80
4.4.2	Perturbed Model Approximation: Modal Analysis	81
4.4.3	Fast and Distributed Stability Assessment	82
4.5	Final Remarks	84
Chapter 5: Stability and Control of Multi-Microgrids		86
5.1	Introduction	86
5.1.1	Related Work	87
5.1.2	Main Results	89
5.1.3	Chapter Outline	90
5.2	Background	91
5.2.1	Multi-Microgrid Model	91
5.3	Linearization and Spectrum of Jacobian	94
5.3.1	Linearization	94
5.3.2	Spectral Relationship Between Matrices J and L	95
5.3.3	A Directed Graph Induced by L	96

5.3.4	Spectral Properties of L	97
5.4	Stability of Multi-Microgrid Networks	97
5.4.1	The Main Stability Theorem	98
5.4.2	Intuition and Paradox Behind Condition (5.8)	99
5.4.3	Stability Condition in Structure-Preserving Networks	100
5.5	Numerical Results	103
5.5.1	Control Schemes and Braess's Paradox	103
5.5.2	Stability Measure and Location of Eigenvalues	106
5.5.3	Larger-Scale Systems	107
5.6	Final Remarks	109
Chapter 6: A Stability Certificate for Droop-Controlled Inverters		111
6.1	Introduction	111
6.1.1	Related Work	111
6.1.2	Main Results	112
6.1.3	Chapter Outline	113
6.2	Droop-Controlled Inverter Model	113
6.3	Linearization and Spectrum of Jacobian	115
6.3.1	Spectral Relationship Between Matrices J and L	116
6.4	Stability of Droop-Controlled Inverters	119
6.5	Perturbation Bounds for Eigenvalues: The Impact of Coupling Terms	124
6.6	Numerical Results	127
6.7	Final Remarks	130

II Optimization with Stability Constraints	131
Chapter 7: Optimization-Based Load Shedding in Single Microgrids	132
7.1 Introduction	132
7.1.1 Main Results	134
7.1.2 Chapter Outline	135
7.2 Overview of the Proposed Load Shedding Algorithm	135
7.3 Optimal Amount and Threshold for Activation of Load Shedding	136
7.3.1 Frequency Response of the μ G to an Islanding Event	137
7.3.2 Threshold for Activation of Load Shedding Scheme	138
7.3.3 Optimal Amount of Load Shedding	141
7.4 Optimization-Based Load Shedding Scheme	143
7.4.1 Basic Model	143
7.4.2 Linearization of the Basic Model	146
7.5 Numerical Results	148
7.6 Final Remarks	152
Chapter 8: Stability-Constrained Optimization in Multi-Microgrids	155
8.1 Introduction	155
8.1.1 Main Results	157
8.1.2 Chapter Outline	158
8.2 Resilient Operation of Multi-Microgrids	158
8.2.1 Structure of a Multi-Microgrid Network	158
8.2.2 Overview of the Proposed Resilient Operation Scheme	159

8.3	Frequency Response of Multi-Microgrids Subsequent to Islanding	161
8.3.1	Inertial Response	161
8.3.2	Droop Response	163
8.3.3	Steady State and Nadir Frequencies at COI	164
8.4	Resilient Operation Problem Formulation	166
8.4.1	Objective Function	166
8.4.2	Real-Time AC Power Flow Limitations in μ Gs	167
8.4.3	Real-Time AC Power Flow Limitations in the Linking Grid	168
8.4.4	DER Output Limitations and Binary Variable Declaration	170
8.4.5	Frequency Constraints and Reformulation	170
8.4.6	Overall MINLP Formulation	173
8.5	Solution Methodology	173
8.5.1	MISOCP Reformulation and Convexification	173
8.5.2	Cutting Plane Algorithm for Frequency Constraints	179
8.6	Numerical Results	181
8.6.1	Comparison with the MINLP-Based Scheme	182
8.6.2	Comparison with the Conventional UFLS Scheme	184
8.7	Final Remarks	186
Chapter 9: Conclusions and Future Work		187
9.1	Part I: Stability and Control of Nonlinear Dynamical Systems	187
9.2	Part II: Optimization with Stability Constraints	190
Appendices		192

Chapter A: Detailed Proofs of Chapter 2	193
A.1 Proof of Lemma 5	193
A.2 Stability of Symmetric Second-Order Systems with Nonsingular Damping .	193
A.3 Proof of Theorem 4	197
A.4 Proof of Proposition 2	197
A.5 Proof of Theorem 8	199
Chapter B: Detailed Proofs of Chapter 3	206
B.1 Proof of Theorem 10	206
Chapter C: Detailed Proofs of Chapter 4	209
C.1 Proofs of Corollary 1 and Theorem 11	209
C.1.1 Outline of the Proof of Corollary 1	210
C.1.2 Outline of the Proof of Theorem 11	211
Chapter D: Detailed Proofs of Chapter 5	213
D.1 Proof of Proposition 5	213
D.2 Proof of Theorem 12	213
D.3 Proof of Lemma 8	215
D.4 Proof of Theorem 13	217
References	219

LIST OF TABLES

3.1	Illustration of the proposed stability certificate in Theorem 10	64
3.2	Dynamic parameters and converged load flow data of the 3-bus test system.	65
5.1	Dynamic parameters and converged load flow data of the four-microgrid system.	105
5.2	Parameters to generate synthetic networks. $U([\ell_1, \ell_2])$ is uniform distribution on interval $[\ell_1, \ell_2]$	106
5.3	Parameters of the IEEE 33-bus system.	107
6.1	Dynamic parameters, domain of stability certificates, and angle range.	129
7.1	Constituent Terms in the Linearized Power Flow Equations [117]	146
7.2	Technical Data of DG Units	149
7.3	μ G Dynamic Data [107]	149
7.4	Simulated Contingencies	151
7.5	Comparison Between the Linear and Nonlinear Load Shedding Optimization Models	154
7.6	Computation Time of the Linear and Nonlinear Models	154
8.1	Technical Data of DERs	181
8.2	Dynamic Parameters of the VSC Controller in each μ G	181
8.3	Comparison Between the MISOCP and MINLP Models	183

- 8.4 Convergence of the Proposed Algorithm While Solving $MISOCP(\mathcal{R}, \mathcal{F})$. 184
- 8.5 Convergence of the Proposed Algorithm While Solving $MINLP(\mathcal{X}, \mathcal{F})$. 185

LIST OF FIGURES

2.1	Occurrence of supercritical Hopf bifurcation in Case 1. (a)-(c) Projection of limit cycles into different subspaces as the parameter γ changes. (d) Oscillations of the voltage angles ψ in radians and the angular frequency deviation ω in radians per seconds when $\gamma = 0$. Note that $\psi_3 \equiv 0$	50
2.2	Occurrence of subcritical Hopf bifurcation in Case 2. (a) Unstable limit cycles as the parameter γ changes. (b)-(c) Projection of limit cycles into different subspaces as the parameter γ changes. (d) The region of attraction of the equilibrium point when $\gamma = 0.25$. The unstable limit cycle is shown in red, while the orbits inside and outside of it are shown in green and blue, respectively. Note that $\psi_2 \equiv 0$	52
3.1	Histogram of the distribution of φ_{ij} for all (i, j) in different reduced IEEE standard test cases.	61
3.2	Spectrum of J in the IEEE 89-bus system.	65
3.3	Schematic diagram of the 3-bus test system.	66
3.4	Instability of the equilibrium point in the 3-bus test system. (a) There exist two eigenvalues with positive real part. (b) Starting from a neighborhood of the equilibrium point, the trajectories become unbounded.	66
3.5	Real part of the closest nonzero eigenvalue of J to the imaginary axis as a function of $\min_i \mathcal{S}_i$ in the IEEE 9-bus system.	67
4.1	Single line diagram of the WSCC system.	80
4.2	Simulation results of the WSCC system: exact model (solid) and singular perturbation model (dashed) with two different perturbation parameters. . .	82

4.3	Modal analysis of the WSCC system: eigenvalues of the exact model (red asterisks) and singular perturbation model (cyan circles) with two different perturbation parameters.	83
4.4	Verification of Assumption 1 in the WSCC system.	84
4.5	Variation of degree of stability due to variation of stability index (4.6).	84
5.1	Histogram of the distribution of φ_{ik} for all lines (i, k) in different IEEE and NESTA standard test cases.	97
5.2	Schematic diagram of four coupled microgrids.	105
5.3	Verifying the instability of the equilibrium point in Case (a2) of the four-microgrid system. (a) There exist two eigenvalues with positive real part. (b) Starting from a neighborhood of the equilibrium point, the orbits of the system diverge to infinity.	106
5.4	Illustration of stability certificate on the IEEE 33-bus system. (a) Spectrum of matrix J . (b) Value of stability index \mathcal{S}_i in different buses.	108
5.5	Trajectories of the frequency deviation ω_i for 6 DERs in the IEEE 33-bus system.	108
5.6	Synthetic multi- μ G networks satisfying condition (5.8). (a) Sparsity pattern of the 50-microgrid adjacency matrix, black points are ones. (b) 50-microgrid network. (c) Eigenvalues of the 50-microgrid network. (d) Sparsity pattern of the 100-microgrid adjacency matrix, black points are ones. (e) 100-microgrid network. (f) Eigenvalues of the 100-microgrid network.	109
6.1	Verifying the loose physical interaction between active power P and reactive power Q	128
6.2	Spectrum of J , and its diagonal blocks J^1 and J^4 . Verifying Lemma 9 and Theorem 15	130
7.1	The general framework of the proposed load shedding algorithm.	136
7.2	A typical frequency response of a μ G following an unintentional islanding event.	137
7.3	Block diagram of the adopted SFR model.	138

7.4	Single line diagram of the simulated μ G [119].	150
7.5	VOLL for different types of loads.	150
7.6	Comparison between the proposed and conventional UFLS methods in terms of load shedding.	151
7.7	Comparison between the proposed and conventional UFLS methods in terms of load shedding cost.	152
7.8	Comparison between the proposed and conventional UFLS methods in terms of minimum dynamic frequency.	152
7.9	Comparison between the proposed and conventional UFLS methods in terms of steady-state frequency.	153
8.1	Schematic diagram of a distribution system under islanding. (a) Multi- μ G network. (b) Linking grid.	160
8.2	The general framework of the proposed resilient operation approach.	161
8.3	Block diagram of the aggregated SFR model.	163
8.4	Comparison between the proposed MISOCP-based and conventional UFLS schemes for an islanding event with severity of 3200 kW. Permissible ranges of nadir and steady state frequencies are shown by horizontal bars.	186

SUMMARY

Electric power systems in recent years have witnessed an increasing adoption of renewable energy sources as well as restructuring of distribution systems into multiple microgrids. These trends, together with an ever-growing electricity demand, are making power networks operate closer to their stability margins, thereby raising numerous challenges for power system operators. In this thesis, we focus on two major challenges: How to efficiently assess and certify the stability of power systems; and how to optimize the operation of multiple microgrids while maintaining their stability.

In the first part of the thesis, we focus on the first question, and study one of the most fundamental models of power systems, namely the swing equation model. We develop sufficient conditions under which the equilibrium points of swing equations are asymptotically stable. We also discuss the connection between the stability of equilibrium points and the network structure. This for example reveals an analog of Braess's Paradox in power system stability, showing that adding power lines to the system may decrease the stability margin. Based on the developed theories, we also introduce several distributed control schemes for maintaining the stability of the system. Since swing equations belong to a more general class of second-order ordinary differential equations (ODEs) which are the cornerstone of studying many other physical and engineering systems, a considerable part of this thesis is devoted to the study of this general class of ODEs, where we investigate the impact of damping as a system parameter on the stability, hyperbolicity, and bifurcation in such systems.

In the second part of the thesis, we address the second question and provide a computationally efficient method for optimizing multi-microgrid operation while ensuring its stability. Our goal is to maintain the frequency stability of multi-microgrid networks under an islanding event and to achieve optimal load shedding and network topology control with AC power flow constraints. Attaining this goal requires solving a challenging op-

timization problem with stability constraints. To cope with this challenge, we develop a strong mixed-integer second-order cone programming (MISOCP)-based reformulation and a cutting plane algorithm for scalable computation of the problem. The optimization frameworks and stability certificates developed in this thesis can be used as powerful decision support tools for power system operators.

CHAPTER 1

INTRODUCTION AND BACKGROUND

Power system stability has been an important topic for many years. There has been continuing advancement in the understanding of stability in these systems. In the recent decade, however, the proliferation of renewable energy resources has added new dimensions to the problem. The uncertainty and volatility of these resources have brought about significant stochastic transitions from one operating point to another, thereby making the system more prone to instability. Another major consequence of moving towards more and more renewable resources is the loss of synchronous machines and their rotational inertia, which further results in serious stability challenges. These growing challenges, more than ever, warn us about the necessity of having a better understanding of power system stability. One of the most fundamental models used in studying power system stability (especially angle stability) is the *swing equation* model. This model describes the nonlinear relation between the power output and voltage angles at each generator node and can be used to analyze the short term dynamical behaviour of the system. Despite its simple-looking form, which will be presented shortly in this chapter, the dynamics of swing equations is extraordinarily rich and their application is ubiquitous in power system dynamical models and analysis. Unfortunately, the existing studies on these equations are either focused on the simplified lossless case or do not provide simple formulas to check if a given equilibrium point of such equations is stable. Indeed, an open problem is to find clear and easy-to-check conditions to certify the stability of lossy swing equations. Addressing this open problem is the main motivation of the present dissertation.

Swing equations belong to a more general class of second-order ordinary differential equations (ODEs) which are the cornerstone of studying many other physical and engineering systems such as an n -degree-of-freedom rigid body and a system of n coupled

oscillators, in particular Kuramoto oscillators with inertia. Part I of this dissertation begins with the study of such general class of second-order ODEs, where we investigate the impact of damping as a system parameter on the stability, hyperbolicity, and bifurcation in such systems.

We continue Part I of the dissertation by focusing on swing equations and the small-signal stability of power systems. We will answer some fundamental questions: Under what conditions an equilibrium point of swing equations is stable? What is the relation between the parameters of power systems and the stability of their equilibrium points? To address these questions, we make use of the unique structure of these equations and strive to develop sufficient conditions for the local stability of the equilibrium points.

Another important application of swing equations emerges in studying the stability of multi-microgrid networks. Here, each microgrid is an energy-independent unit which could be a block in the city such as a university or hospital. Based on the stability theories developed for swing equations in the previous parts, we study the stability of multi-microgrids. We also demonstrate an analog of Braess's Paradox in such networks, showing that adding power lines to the system may decrease the stability margin. Part I of the dissertation ends with the study of swing equations with variable voltage magnitudes. Such third-order models characterize the dynamics of droop-controlled inverters, which are important building blocks of smart distribution systems.

Part II of this dissertation is devoted to a more detailed study of multi-microgrid networks, from an optimization perspective. Our main goal in Part II is to provide a computationally efficient method for optimizing multi-microgrid operation while ensuring its stability. Achieving this goal requires solving a challenging optimization problem with stability constraints. To cope with this challenge, we first focus on single microgrids, and develop an optimization-based scheme for under frequency load shedding (UFLS) in a microgrid following an unintentional islanding (i.e., disconnection of the microgrid from the main grid). Next, we extend this scheme to multi-microgrids. We propose a comprehen-

sive optimization and real-time control framework for maintaining frequency stability of multi-microgrid networks under an islanding event and for achieving optimal load shedding and network topology control with AC power flow constraints. Part II ends with our discussion on a strong mixed-integer second-order cone programming (MISOCP)-based reformulation and a cutting plane algorithm for scalable computation of the problem.

In the following sections of this chapter, we provide a brief introduction to swing equations, multi-microgrids, and more general class of second-order differential equations. Next, we discuss the problems that are considered in each chapter of this dissertation and the challenges we face in solving them. We then provide a summary of our contributions. We conclude this chapter by presenting a list of related publications as well as the basic notations that are used throughout the dissertation.

1.1 Background

1.1.1 Electric Power Systems and Swing Equations

Consider an electric power system with the set of interconnected generators $\mathcal{N} = \{1, \dots, n\}$, $n \in \mathbb{N}$. Based on the classical small-signal stability assumptions [1], the mathematical model of this system is described by the following system of second-order nonlinear ODEs:

$$\frac{m_j}{\omega_s} \ddot{\delta}_j(t) + \frac{d_j}{\omega_s} \dot{\delta}_j(t) = P_{m_j} - \sum_{k=1}^n V_j V_k Y_{jk} \cos(\theta_{jk} - \delta_j + \delta_k) \quad \forall j \in \mathcal{N}. \quad (1.1)$$

Considering the state space $\mathcal{S} := \{(\delta, \omega) : \delta \in \mathbb{R}^n, \omega \in \mathbb{R}^n\}$, the dynamical system (1.1) can be represented as a system of first-order nonlinear ODEs, aka swing equations:

$$\dot{\delta}_j(t) = \omega_j(t) \quad \forall j \in \mathcal{N}, \quad (1.2a)$$

$$\frac{m_j}{\omega_s} \dot{\omega}_j(t) + \frac{d_j}{\omega_s} \omega_j(t) = P_{m_j} - \sum_{k=1}^n V_j V_k Y_{jk} \cos(\theta_{jk} - \delta_j + \delta_k) \quad \forall j \in \mathcal{N}, \quad (1.2b)$$

where for each generator $j \in \mathcal{N}$, $\delta_j(t)$ is the terminal voltage angle in radians, V_j is the terminal voltage magnitude in per unit, $\omega_j(t)$ is the deviation of the angular frequency from the nominal angular frequency in radians per seconds, ω_s is the nominal angular frequency in radians per seconds, m_j is the inertia constant in seconds, d_j is the unitless damping coefficient, P_{m_j} is the mechanical power in per unit, and t is the time in seconds. Moreover, $Y_{jk} \exp(i\theta_{jk})$ is the (j, k) entry of the reduced admittance matrix, with $Y_{jk} \in \mathbb{R}$ and $\theta_{jk} \in \mathbb{R}$. The reduced admittance matrix encodes the underlying graph structure of the power grid, which is assumed to be a connected graph in this dissertation.

The equilibrium points of swing equations (1.2) with zero transfer conductance (the so-called *lossless* model) have been studied in the 1980s (see e.g. Chiang *et al.* [2] and Zaborszky *et al.* [3].) They assume that there is a unique stable equilibrium point and a finite number of unstable equilibrium points in any 2π interval of generator angle coordinate. It is shown that the stability boundary of a stable equilibrium point consists of the stable manifolds of all the equilibrium points (and/or closed orbits) on the stability boundary. Moreover, various methods in the broad category of the so-called direct methods have been developed to estimate the region of attraction of equilibrium points [4, 5]. These methods not only avoid expensive time-domain integration of swing equations, but also provide a quantitative measure of the degree of stability. Unfortunately, the existing methods are mostly limited to lossless systems and require a significant computational effort. More recently, the authors in [6] have alleviated some of these drawbacks, by showing that there exists a convex set of Lyapunov functions certifying the transient stability of a given power system.

The characteristics of swing equations with nontrivial transfer conductance (the so-called *lossy* model) are more challenging to analyze. This is partly due to the fact that there is no global energy function for such systems [7], and therefore, some main approaches (e.g., the energy function method) to investigate these equations cannot be directly applied. Nonetheless, several approaches are devised over the years. For instance, reference [8]

computes numerical energy functions to deal with the effects of transfer conductances on the system behavior. Our work in this dissertation mainly focuses on lossy swing equations, but we also study lossless swing equations as a special case.

1.1.2 Multi-Microgrids and Stability-Constrained Optimization

Microgrids as building blocks of smart distribution grids, provide a unique infrastructure for integrating a wide range of distributed energy resources (DERs) with different static and dynamic characteristics. Microgrids are able to operate in island mode and energize a portion of the grid while the main grid is down. Restructuring of distribution systems into multiple microgrids, referred to as multi-microgrids, is one of the main ways of improving the resilience of the electricity grid. The structural modularity of such networks makes them remarkably resilient against extreme events, but inherently prone to instabilities nonetheless. A minor contingency in these networks may lead to cascading outages and a total blackout in all microgrids. There is, therefore, an urgent need for understanding the notion of stability in multi-microgrids. This urgent need motivated us to study multi-microgrids and devote three chapters of the dissertation to this topic.

Note that a key feature that distinguishes multi-microgrid networks from the conventional distribution systems is that each microgrid will be connected to the rest of the system via a point of common coupling (PCC). Moreover, each microgrid either has a voltage source inverter (VSI)-based interface at PCC or is composed of a network of DERs, e.g. VSIs, diesel generators (DGs), etc [9, 10]. On the other hand, it can be mathematically proved (see Lemma 7) that the frequency dynamics of a droop-controlled VSI is equivalent to the dynamics of a synchronous generator or DG, represented by swing equations [11], [12]. Therefore, from a modeling perspective, the dynamical model of multi-microgrids is closely related to that of interconnected generators [13], and analysis of multi-microgrids' behaviour is intertwined with an accurate understanding of swing equations. Accordingly, the swing equation studies in the first part of the dissertation help us get ready for the study

of multi-microgrids at the end of Part I as well as Part II.

As mentioned above, in a multi-microgrid network, each microgrid is able to operate in either island mode or grid-connected mode. An important challenge in these networks is to control the dangerous transients caused by the transition between the grid-connected and island modes. Several IEEE standards such as IEEE Std. 929-2000 [14] and IEEE Std. 1547.7-2013 [15] have highlighted this challenge and called for adaptive optimization and control schemes to be used in such circumstances. Addressing this challenge will be our main goal in Part II of this dissertation.

1.1.3 Second-Order Ordinary Differential Equations

As mentioned above, swing equations belong to a larger class of second-order ODEs of the form

$$M\ddot{x} + D\dot{x} + f(x) = 0, \quad (1.3)$$

and its corresponding first-order system

$$\begin{bmatrix} \dot{x} \\ \dot{y} \end{bmatrix} = \begin{bmatrix} 0 & I \\ 0 & -M^{-1}D \end{bmatrix} \begin{bmatrix} x \\ y \end{bmatrix} - M^{-1} \begin{bmatrix} 0 \\ f(x) \end{bmatrix}. \quad (1.4)$$

This general class will be discussed in Chapter 2. In (1.3) and (1.4), $f : \mathbb{R}^n \rightarrow \mathbb{R}^n$ is a continuously differentiable function, the dot denotes differentiation with respect to the independent variable $t \geq 0$, the dependent variable $x \in \mathbb{R}^n$ is a vector of state variables, and the coefficients $M \in \mathbb{S}^n$ and $D \in \mathbb{S}^n$ are constant $n \times n$ real symmetric matrices. We refer to M and D as the inertia and damping matrices, respectively. We restrict our attention to the case where M is nonsingular, thereby avoiding differential algebraic equations, and $D \in \mathbb{S}_+^n$ is positive semi-definite (PSD). We also investigate and discuss the case where M and D are not symmetric.

The dynamical model (2.1) has been of interest to many researchers who have studied necessary and sufficient conditions for its local stability [16, 17] or characterization of its stability regions [18]. When $f(x)$ is a linear function, this model coincides with the model of n -degree-of-freedom viscously damped vibration systems which are also extensively studied in the structural dynamics literature [19, 20, 21]. Equation (2.1) is also the cornerstone of studying many physical and engineering systems such as an n -generator electric power system [22], an n -degree-of-freedom rigid body [18], and a system of n coupled oscillators [23, 22, 24], in particular Kuramoto oscillators with inertia [25, 26].

1.2 Outline and Summary of Contributions

In this section, we present an outline and summarize the contributions of the dissertation.

Part I: Stability and Control of Nonlinear Dynamical Systems

1.2.1 Chapter 2: Impact of Damping in Second-Order Dynamical Systems

In Chapter 2, we aim to answer some natural questions about ODEs of the form (1.3): How does changing the damping matrix D affect the stability and hyperbolicity of equilibrium points? What are the conditions on D under which an equilibrium point is hyperbolic? When we lose hyperbolicity due to changing D , what kind of bifurcation happens?

- We show that in second-order systems increasing damping has a monotonic effect on the stability of equilibrium points. To establish this result, we prove that the rank of a complex symmetric matrix with PSD imaginary part does not decrease if its imaginary part is perturbed by a real symmetric PSD matrix, which may be of independent interest in the matrix perturbation theory. Moreover, we propose a necessary and sufficient condition for an equilibrium point of such systems to be hyperbolic. We also characterize a set of sufficient conditions for the occurrence of Hopf bifurcation, when the damping matrix varies as a smooth function of a one

dimensional bifurcation parameter.

- We show that the developed theoretical results have key applications in the stability of electric power systems (1.1). We prove that in a lossy power system with two or three generators, as long as only one generator is undamped, any equilibrium point is hyperbolic, and as soon as there are more than one undamped generator, a lossy system with any $n \geq 2$ generators may lose hyperbolicity at its equilibrium points. Finally, we perform bifurcation analysis to detect Hopf bifurcation and identify its type based on two interesting case studies.

1.2.2 Chapter 3: A Stability Certificate for Kron-Reduced Swing Equations

In Chapter 3, we study lossy swing equations (1.1). We first use Kron reduction [27] to eliminate all passive nodes and study the resulting reduced network. Our aim is to address two questions: Under what conditions an equilibrium point of lossy swing equations is asymptotically stable? What is the relation between the network structure of a power system and the stability of the equilibrium points of swing equations?

- We develop a sufficient condition under which the equilibrium points of lossy swing equations are locally asymptotically stable. In addition to providing new insights into the theory of stability, the derived conditions are easy to check, use only local information, and are suitable for real-time monitoring and fast stability assessment.
- The proposed stability certificate can be interpreted as enforcing an upper bound on the matrix norm of the Laplacian of the underlying graph of the system. We show that the aforementioned upper bound is proportional to the square of damping and inverse of inertia at each node of the power grid. These results provide new insights into the way the damping and inertia at each node of the system would affect the stability of equilibrium points. We also illustrate how the proposed condition provides a quantitative measure of the degree of stability in power systems.

1.2.3 Chapter 4: A Stability Certificate for Structure-Preserving Swing Equations

During the Kron reduction process, loads are considered constant impedances and reflected into the nodal admittance matrix which will be further reduced to a smaller matrix representing a reduced network of generator buses. The procedure of network reduction for eliminating the load buses will close our eyes on the relations between the structure of the underlying physical network and the stability properties of the system. In Chapter 4, we study structure-preserving swing equations introduced by Bergen and Hill [28]. The main assumption of this model is to use a frequency-dependent model for loads.

- We make use of singular perturbation techniques and Tikhonov's theorem [29] to establish the relationship between a structure-preserving model and its singular perturbation counterpart. Specifically, we show (under specific conditions) the stability properties of the structure-preserving model are the same as those of its singular perturbation counterpart. Therefore, the singular perturbation counterpart can be used for stability analysis instead of the the structure-preserving model, and this will facilitate our analysis.
- We strive to develop a sufficient condition that certifies the local asymptotic stability of equilibrium points of structure-preserving swing equations. The proposed certificate is a practical alternative to the eigenvalue computation-based methods, which can be quite computationally cumbersome for large-scale systems. We also introduce a control scheme for improving the small-signal stability of power systems.

1.2.4 Chapter 5: Stability and Control of Multi-Microgrids

In Chapter 5, we delve deeper into an important applications of swing equations in modeling multi-microgrid networks.

- We derive sufficient conditions to guarantee local stability equilibrium points of multi-microgrids in both lossless and lossy networks. The new certificates provide

significant insights about the interplay between system stability and reactive power absorption, voltage magnitude, network topology, and interface parameters of each microgrid. We also introduce a new weighted directed graph to study the spectral properties of the multi-microgrid Laplacian.

- Based on the developed theory, we introduce a fully distributed control scheme to adjust the dynamic parameters of each microgrid interface for maintaining the stability of the system. The stability conditions developed in this chapter surprisingly reveal an analog of Braess's Paradox in power system stability, showing that adding power lines to the system may decrease the stability margin [30]. We also revisit the stability of structure-preserving models from a graph-theoretic perspective (in Chapter 4, we studied structure-preserving models via singular perturbation techniques).

1.2.5 Chapter 6: A Stability Certificate for Droop-Controlled Inverters

In Chapter 6, we aim to extend our previous stability results to swing equations with variable voltage magnitudes. This leads to a third-order model which characterizes the dynamics of voltage angles, frequency deviations, and voltage magnitudes.

- We scrutinize the Jacobian of the third-order swing equations with variable voltage magnitude and strive to find its relation with the Jacobian of power flow equations. After investigating its spectral properties, we find an structural property of the Jacobian matrix which stems from the loose physical linkage between active and reactive powers. Taking advantage of this inherent property, we make a reasonable assumption (referred to as the decoupling assumption) and develop sufficient conditions under which an equilibrium point of the third-order model is asymptotically stable. Similar to the sufficient conditions developed in previous chapters, the derived conditions are easy to check, use only local information, and are suitable for real-time monitoring and fast stability assessment.

- We further investigate the aforementioned decoupling assumption and study the impact of coupling terms on the eigenvalues of the Jacobian matrix. Although the loose physical linkage between active and reactive powers is a well-known property in power systems and has been the basis for the fast decoupled load flow [31], we are not aware of any study on the impact of coupling terms and the robustness of the decoupled model under coupling perturbations. Here for the first time, we make use of the existing theorems in the literature such as Bauer–Fike theorem to provide residual bounds for the perturbation of Jacobian eigenvalues as the coupling terms change. Our findings shed light on the validity of the decoupling assumption for practical purposes.

Part II: Optimization with Stability Constraints

1.2.6 Chapter 7: Optimization-Based Load Shedding in Single Microgrids

In Part II of this dissertation, we aim to develop adaptive optimization and control schemes to handle the dangerous transients in microgrids caused by the transition between the grid-connected and island modes. Chapter 7 is devoted to design an efficient optimization and control scheme for single microgrids.

- We present an adaptive optimization-based load shedding scheme to curtail the minimum amount of loads to preserve the microgrid stability following an unintentional islanding event. The developed technique arranges a look-up table including the optimum amount and location of load curtailments. In particular, given a specific amount of power exchange between the microgrid and the upstream grid, the optimal total amount of load shedding is determined. This value depends on the response of both the generators and the loads to the islanding event. These responses are reflected in the system frequency response (SFR) model as well as the microgrid dynamic and static frequency limitations.

- We derive a mixed-integer linear programming (MILP) model for obtaining the amount of load drops at different buses. In the optimization model, an approximation of the microgrid AC operational limitations are considered to ensure the network security following the islanding event.

1.2.7 Chapter 8: Stability-Constrained Optimization in Multi-Microgrids

Finally, in Chapter 8, we explore the resilient operation of multi-microgrid networks after a scheduled or unscheduled islanding in a distribution system.

- We propose a framework that is strategically designed in two parts. In the first part, we develop a near real-time decision support tool which is used to determine the optimal reconfiguration of the multi-microgrid network, cooperation between microgrids (sharing their resources), new operating point of dispatchable DERs, and emergency load curtailments (if necessary). The second part of the framework pertains to the real-time monitoring and control of multi-microgrids based on the outcomes of the decision support tool. Specifically, we formulate the real-time resilient operation, including optimal power flow, optimal load shedding, and optimal topology reconfiguration, of a multi-microgrid network as a mixed-integer nonlinear programming (MINLP) problem. Then, we propose an MISOCP relaxation to this problem, which considerably improves the computational efficiency of our control framework and renders it scalable in practical systems.
- We derive necessary constraints for keeping the nadir and steady state frequency of the network within the permissible ranges, and introduce a new reformulation for frequency limitation constraints. This reformulation implicitly guarantees the frequency stability of the network after dangerous transients such as islanding. Next, we develop a set of valid inequalities and a separation scheme for incorporating the frequency constraints in the operation of a multi-microgrid network, and based on

that, we establish a cutting-plane approach to eliminate the frequency violations in a computationally effective way.

1.3 Related Publications

- **Chapter 2**
A. Gholami and X. A. Sun, “The impact of damping in second-order dynamical systems with applications to power grid stability,” Accepted for publication in *SIAM Journal on Applied Dynamical Systems*, 2021. arXiv:2010.06662 [math.DS].
- **Chapter 3**
A. Gholami and X. A. Sun, “A fast certificate for power system small-signal stability,” in *59th IEEE Conference on Decision and Control (CDC)*, pp. 3383–3388, 2020. arXiv:2008.02263 [math.OC].
- **Chapter 4**
A. Gholami and X. A. Sun, “A distributed scheme for stability assessment in large-scale structure preserving models via singular perturbation,” in *Proceedings of 54th Hawaii International Conference on Systems Sciences (HICSS)*, pp. 3169–3177, 2021. arXiv:2103.15333 [eess.SY].
- **Chapter 5**
A. Gholami and X. A. Sun, “Stability of multi-microgrids: New certificates, distributed control, and braess’s paradox,” Accepted for publication in *IEEE Transactions on Control of Network Systems*, 2021. arXiv:2103.15308 [eess.SY].
- **Chapter 6**
A. Gholami and X. A. Sun, “Stability of droop-controlled inverters with third-order model,” *Draft Paper*, 2021.
- **Chapter 7**
A. Gholami, T. Shekari, and X. A. Sun, “An adaptive optimization-based load shedding scheme in microgrids,” in *Proceedings of the 51st Hawaii International Conference on System Sciences (HICSS)*, pp. 2660–2669, 2018. **Best Paper Award.**
- **Chapter 8**
A. Gholami and X. A. Sun, “Towards resilient operation of multi-microgrids: An MISOCP-based frequency-constrained approach,” *IEEE Transactions on Control of Network Systems*, vol. 6, pp. 925–936, 2019.

1.4 Notations

Our notation is more or less standard. We use \mathbb{N} to denote the set of natural numbers, \mathbb{R} to denote the set of real numbers, \mathbb{R}_+ to denote the set of nonnegative real numbers, $\mathbb{C}_{-/ +}$ to

denote the set of complex numbers with negative/positive real part, and \mathbb{C}_0 to denote the set of complex numbers with zero real part. The set of real and complex n -vectors are denoted by \mathbb{R}^n and \mathbb{C}^n , respectively. Likewise, the set of real and complex $m \times n$ matrices are denoted by $\mathbb{R}^{m \times n}$ and $\mathbb{C}^{m \times n}$, respectively. We use parentheses to construct column vectors from comma separated lists. For instance, if $a \in \mathbb{R}^n$ and $b \in \mathbb{R}^m$, we have

$$(a, b) = \begin{bmatrix} a \\ b \end{bmatrix} \in \mathbb{R}^{n+m}.$$

$i = \sqrt{-1}$ is the imaginary unit. If $A \in \mathbb{C}^{m \times n}$, the transpose of A is denoted by A^\top , the real part of A is denoted by $\text{Re}(A)$, and the imaginary part of A is denoted by $\text{Im}(A)$. The conjugate transpose of A is denoted by A^* and defined by $A^* = \bar{A}^\top$, in which \bar{A} is the entrywise conjugate.

The matrix $A \in \mathbb{C}^{n \times n}$ is said to be symmetric if $A^\top = A$, Hermitian if $A^* = A$, and unitary if $A^*A = I$. The spectrum of a matrix $A \in \mathbb{R}^{n \times n}$ is denoted by $\sigma(A)$. We use \mathbb{S}^n to denote the set of real symmetric $n \times n$ matrices, \mathbb{S}_+^n to denote the set of real symmetric PSD $n \times n$ matrices, and \mathbb{S}_{++}^n to denote the set of real symmetric positive definite $n \times n$ matrices. For matrices A and B , the relation $B \succeq A$ means that A and B are real symmetric matrices of the same size such that $B - A$ is PSD; we write $A \succeq 0$ to express the fact that A is a real symmetric PSD matrix. Strict version $B \succ A$ of $B \succeq A$ means that $B - A$ is real symmetric positive definite, and $A \succ 0$ means that A is real symmetric positive definite.

For $A \in \mathbb{C}^{n \times n}$ and $\alpha, \beta \subseteq \{1, \dots, n\}$, the submatrix of entries in the rows indexed by α and columns indexed by β is denoted by $A[\alpha, \beta]$. Similarly, for a vector $x \in \mathbb{C}^n$, $x[\alpha]$ denotes the subvector consisting of entries indexed by α .

Part I

Stability and Control of Nonlinear Dynamical Systems

CHAPTER 2

IMPACT OF DAMPING IN SECOND-ORDER NONLINEAR DYNAMICAL SYSTEMS

In this chapter, we consider a broad class of second-order dynamical systems and study the impact of damping as a system parameter on the stability, hyperbolicity, and bifurcation in such systems. We prove a monotonic effect of damping on the hyperbolicity of the equilibrium points of the corresponding first-order system. This provides a rigorous formulation and theoretical justification for the intuitive notion that damping increases stability. To establish this result, we prove a matrix perturbation result for complex symmetric matrices with positive semidefinite perturbations to their imaginary parts, which may be of independent interest. Furthermore, we establish necessary and sufficient conditions for the breakdown of hyperbolicity of the first-order system under damping variations in terms of observability of a pair of matrices relating damping, inertia, and Jacobian matrices, and propose sufficient conditions for Hopf bifurcation resulting from such hyperbolicity breakdown. The developed theory has significant applications in the stability of electric power systems, which are one of the most complex and important engineering systems. In particular, we characterize the impact of damping on the hyperbolicity of the swing equation model which is the fundamental dynamical model of power systems, and demonstrate Hopf bifurcations resulting from damping variations.

2.1 Introduction

Newton's second law (stating that the rate of change of the linear momentum is equal to the force acting on the body) involves the second derivative of the position of the body with respect to time. Therefore, it comes as no surprise that the mathematical model of many physical systems is represented as second-order differential equations.

In this chapter, we study the class of second-order ordinary differential equations (ODEs) of the form

$$M\ddot{x} + D\dot{x} + f(x) = 0, \quad (2.1)$$

and its corresponding first-order system

$$\begin{bmatrix} \dot{x} \\ \dot{y} \end{bmatrix} = \begin{bmatrix} 0 & I \\ 0 & -M^{-1}D \end{bmatrix} \begin{bmatrix} x \\ y \end{bmatrix} - M^{-1} \begin{bmatrix} 0 \\ f(x) \end{bmatrix}, \quad (2.2)$$

where $f : \mathbb{R}^n \rightarrow \mathbb{R}^n$ is a continuously differentiable function, the dot denotes differentiation with respect to the independent variable $t \geq 0$, the dependent variable $x \in \mathbb{R}^n$ is a vector of state variables, and the coefficients $M \in \mathbb{S}^n$ and $D \in \mathbb{S}^n$ are constant $n \times n$ real symmetric matrices. We refer to M and D as the inertia and damping matrices, respectively. We restrict our attention to the case where M is nonsingular, thereby avoiding differential algebraic equations, and $D \in \mathbb{S}_+^n$ is positive semi-definite (PSD). We also investigate and discuss the case where M and D are not symmetric.

An important example of (2.1) is an electric power system with the set of interconnected generators $\mathcal{N} = \{1, \dots, n\}$, $n \in \mathbb{N}$ characterized by the second-order system

$$\frac{m_j}{\omega_s} \ddot{\delta}_j(t) + \frac{d_j}{\omega_s} \dot{\delta}_j(t) = P_{m_j} - \sum_{k=1}^n V_j V_k Y_{jk} \cos(\theta_{jk} - \delta_j + \delta_k) \quad \forall j \in \mathcal{N}, \quad (2.3)$$

where $\delta \in \mathbb{R}^n$ is the vector of state variables. The inertia and damping matrices in this case are $M = \frac{1}{\omega_s} \mathbf{diag}(m_1, \dots, m_n)$ and $D = \frac{1}{\omega_s} \mathbf{diag}(d_1, \dots, d_n)$. System (2.3), which is known as the *swing equations*, describes the nonlinear dynamical relation between the power output and voltage angle of generators [32, 17]. The first-order system associated with swing equations is also of the form (2.2), i.e.,

$$\dot{\delta}_j(t) = \omega_j(t) \quad \forall j \in \mathcal{N}, \quad (2.4a)$$

$$\frac{m_j}{\omega_s} \dot{\omega}_j(t) + \frac{d_j}{\omega_s} \omega_j(t) = P_{m_j} - \sum_{k=1}^n V_j V_k Y_{jk} \cos(\theta_{jk} - \delta_j + \delta_k) \quad \forall j \in \mathcal{N}, \quad (2.4b)$$

where $(\delta, \omega) \in \mathbb{R}^{n+n}$ is the vector of state variables. Note that each generator j is a second-order oscillator, which is coupled to other generators through the cosine term in (2.4b) and the admittance Y_{jk} encodes the graph structure of the power grid (see Section 2.5 for full details on swing equations).

Among the various aspects of model (2.1), the impact of damping matrix D on the stability properties of the model is one of the most intriguing topics [33, 21, 34]. Moreover, better understanding of the damping impact in swing equations (2.3) is of particular importance to the stability analysis of electric power systems [22]. Undamped modes and oscillations are the root causes of several blackouts, such as the WECC blackout on August 10, 1996 [35] as well as the more recent events such as the forced oscillation event on January 11, 2019 [36] in the Eastern Interconnection of the U.S. power grid. In order to maintain system stability in the wake of unexpected equipment failures, many control actions taken by power system operators are directly or indirectly targeted at changing the effective damping of system (2.3) [32, 37, 38]. In this context, an important question is *how the stability properties of power system equilibrium points change as the damping of the system changes*. Our main motivation is to rigorously address this question for the general model (2.1) and show its applications in power system model (2.3).

2.1.1 Related Work

Regarding damping effects in power systems, the results are sporadic and mostly based on empirical studies of small scale power systems. For example, it is known that the lossless swing equations (i.e., when the transfer conductances of power grid are zero, which corresponds to $\nabla f(x)$ in (2.1) being a real symmetric matrix for all x) have no periodic solutions, provided that all generators have a positive damping value [39]. It is also shown by numerical simulation that subcritical and supercritical Hopf bifurcations, and as a con-

sequence, the emergence of periodic solutions, could happen if the swing equations of a two-generator network are augmented to include any of the following four features: variable damping, frequency-dependent electrical torque, lossy transmission lines, and excitation control [40, 41]. Hopf bifurcation is also demonstrated in a three-generator undamped system as the load of the system changes [42], where several energy functions for such undamped lossy swing equations in the neighborhood of points of Hopf bifurcation are developed to help characterize Hopf bifurcation in terms of energy properties. Furthermore, a frequency domain analysis to identify the stability of the periodic orbits created by a Hopf bifurcation is presented in [43]. The existence and the properties of limit cycles in power systems with higher-order models are also numerically analyzed in [44, 45].

Another set of literature relevant to our work studies the role of power system parameters in the stability of its equilibrium points. For instance, the work presented in [37] examines the dependence of the transfer functions on the system parameters in the swing equation model. In [46], the role of inertia in the frequency response of the system is studied. Moreover, it is shown how different dynamical models can lead to different conclusions. Finally, the works on frequency stability, voltage stability, and transient stability in power systems [47, 48, 49, 50, 51, 52, 53, 54, 55] are conceptually related to our work.

2.1.2 Main Results

This chapter presents a thorough theoretical analysis of the role of damping in the stability of model (2.1)-(2.2). Our results provide rigorous formulation and theoretical justification for the intuitive notion that damping increases stability. The results also characterize the hyperbolicity and Hopf bifurcation of an equilibrium point of (2.2) through the inertia M , damping D , and Jacobian ∇f matrices. These general results are applied to swing equations (2.3) to provide new insights into the damping effects on the stability of power grids.

The contributions and main results of this chapter are summarized below.

1. We show that increasing damping has a monotonic effect on the stability of equilibrium points in a large class of ODEs of the form (2.1) and (2.2). In particular, we show that, when M is nonsingular symmetric, D is symmetric PSD, and $\nabla f(x_0)$ is symmetric at an equilibrium point $(x_0, 0)$ of the first-order system (2.2), if the damping matrix D is perturbed to D' which is more PSD than D , i.e. $D' - D \in \mathbb{S}_+^n$, then the set of eigenvalues of the Jacobian of (2.2) at $(x_0, 0)$ that have a zero real part will not enlarge as a set (Theorem 2). We also show that these conditions on $M, D, \nabla f(x_0)$ cannot be relaxed. To establish this result, we prove that the rank of a complex symmetric matrix with PSD imaginary part does not decrease if its imaginary part is perturbed by a real symmetric PSD matrix (Theorem 1), which may be of independent interest in the matrix perturbation theory.

2. We propose a necessary and sufficient condition for an equilibrium point $(x_0, 0)$ of the first-order system (2.2) to be hyperbolic. Specifically, when M and $\nabla f(x_0)$ are symmetric positive definite and D is symmetric PSD, then $(x_0, 0)$ is hyperbolic if and only if the pair $(M^{-1}\nabla f(x_0), M^{-1}D)$ is observable (Theorem 3). We extend the necessary condition to the general case where $M, D, \nabla f(x_0)$ are not symmetric (Theorem 4). Moreover, we characterize a set of sufficient conditions for the occurrence of Hopf bifurcation, when the damping matrix varies as a smooth function of a one dimensional bifurcation parameter (Theorem 5 and Theorem 6).

3. We show that the theoretical results have key applications in the stability of electric power systems. We propose a set of necessary and sufficient conditions for breaking the hyperbolicity in lossless power systems (Theorem 7). We prove that in a lossy system with two or three generators, as long as only one generator is undamped, any equilibrium point is hyperbolic (Theorem 8), and as soon as there are more than one undamped generator, a lossy system with any $n \geq 2$ generators may lose hyperbolicity at its equilibrium points (Proposition 3). Finally, we perform bifurcation analysis

to detect Hopf bifurcation and identify its type based on two interesting case studies.

2.1.3 Chapter Outline

The rest of this chapter is organized as follows. Section 2.2 introduces some notation and provides the problem statement. In Section 2.3, we rigorously prove that damping has a monotonic effect on the local stability of a large class of ODEs. Section 2.4 further investigates the impact of damping on hyperbolicity and bifurcation and presents a set of necessary and/or sufficient conditions for breaking the hyperbolicity and occurrence of bifurcations. Section 2.5 introduces the power system model (i.e., swing equations), provides a graph-theoretic interpretation of the system, and analyzes the practical applications of our theoretical results in power systems. Section 2.6 further illustrates the developed theoretical results through numerical examples, and finally, the chapter concludes with Section 2.7.

2.2 Background

2.2.1 Problem Statement

Consider the second-order dynamical system (2.1). The smoothness (continuous differentiability) of f is a sufficient condition for the existence and uniqueness of solution. We transform (2.1) into a system of $2n$ first-order ODEs of the form

$$\begin{bmatrix} \dot{x} \\ \dot{y} \end{bmatrix} = \begin{bmatrix} 0 & I \\ 0 & -M^{-1}D \end{bmatrix} \begin{bmatrix} x \\ y \end{bmatrix} - M^{-1} \begin{bmatrix} 0 \\ f(x) \end{bmatrix}. \quad (2.5)$$

If $f(x_0) = 0$ for some $x_0 \in \mathbb{R}^n$, then $(x_0, 0) \in \mathbb{R}^{n+n}$ is called an equilibrium point. The stability of such equilibrium points can be revealed by the spectrum of the Jacobian of the $2n$ -dimensional vector field in (2.5) evaluated at the equilibrium point. Note that $f : \mathbb{R}^n \rightarrow \mathbb{R}^n$ is a vector-valued function, and its derivative at any point $x \in \mathbb{R}^n$ is referred to as the Jacobian of f and denoted by $\nabla f(x) \in \mathbb{R}^{n \times n}$. This Jacobian of f should not be

confused with the Jacobian of the $2n$ -dimensional vector field in right-hand side of (2.5), which is

$$J(x) := \begin{bmatrix} 0 & I \\ -M^{-1}\nabla f(x) & -M^{-1}D \end{bmatrix} \in \mathbb{R}^{2n \times 2n}. \quad (2.6)$$

If the Jacobian J at an equilibrium point $(x_0, 0) \in \mathbb{R}^{n+n}$ has all its eigenvalues off the imaginary axis, then we say that $(x_0, 0)$ is a *hyperbolic* equilibrium point. An interesting feature of hyperbolic equilibrium points is that they are either unstable or asymptotically stable. Breaking the hyperbolicity (say due to changing a parameter of the system), leads to bifurcation. As mentioned before, we restrict our attention to the case where inertia matrix M is nonsingular. Instead, we scrutinize the case where damping matrix D is not full rank, i.e., the system is partially damped. This is a feasible scenario in real-world physical systems [34], and as will be shown, has important implications specially in power systems. Now, it is natural to ask the following questions:

- (i) How does changing the damping matrix D affect the stability and hyperbolicity of equilibrium points of system (2.5)?
- (ii) What are the conditions on D under which an equilibrium point is hyperbolic?
- (iii) When we lose hyperbolicity due to changing D , what kind of bifurcation happens?

Note that in these questions, the inertia matrix M is fixed, and the bifurcation parameter only affects the damping matrix D . Questions (i)-(iii) will be addressed in the following sections, but before that, we present Lemma 1 [17] which provides some intuition behind the role of different factors in the spectrum of the Jacobian matrix J . Let us define the concept of matrix pencil [56]. Consider $n \times n$ matrices Q_0, Q_1 , and Q_2 . A quadratic matrix pencil is a matrix-valued function $P : \mathbb{C} \rightarrow \mathbb{R}^{n \times n}$ given by $\lambda \mapsto P(\lambda)$ such that $P(\lambda) = \lambda^2 Q_2 + \lambda Q_1 + Q_0$.

Lemma 1. For any $x \in \mathbb{R}^n$, λ is an eigenvalue of $J(x)$ if and only if the quadratic matrix pencil $P(\lambda) := \lambda^2 M + \lambda D + \nabla f(x)$ is singular.

Proof. For any $x \in \mathbb{R}^n$, let λ be an eigenvalue of $J(x)$ and (v, u) be the corresponding eigenvector. Then

$$\begin{bmatrix} 0 & I \\ -M^{-1}\nabla f(x) & -M^{-1}D \end{bmatrix} \begin{bmatrix} v \\ u \end{bmatrix} = \lambda \begin{bmatrix} v \\ u \end{bmatrix}, \quad (2.7)$$

which implies that $u = \lambda v$ and $-M^{-1}\nabla f(x)v - M^{-1}Du = \lambda u$. Substituting the first equality into the second one, we get

$$(\nabla f(x) + \lambda D + \lambda^2 M)v = 0. \quad (2.8)$$

Since $v \neq 0$ (otherwise $u = \lambda \times 0 = 0$ which is a contradiction), equation (2.8) implies that the matrix pencil $P(\lambda) = \lambda^2 M + \lambda D + \nabla f(x)$ is singular.

Conversely, for any $x \in \mathbb{R}^n$, suppose there exists $\lambda \in \mathbb{C}$ such that $P(\lambda) = \lambda^2 M + \lambda D + \nabla f(x)$ is singular. Choose a nonzero $v \in \ker(P(\lambda))$ and let $u := \lambda v$. Accordingly, the characteristic equation (2.7) holds, and consequently, λ is an eigenvalue of $J(x)$. \square

To give some intuition, let us pre-multiply (2.8) by v^* to get the quadratic equation

$$v^* \nabla f(x) v + \lambda v^* D v + \lambda^2 v^* M v = 0, \quad (2.9)$$

which has roots

$$\lambda_{\pm} = \frac{-v^* D v \pm \sqrt{(v^* D v)^2 - 4(v^* M v)(v^* \nabla f(x) v)}}{2v^* M v}. \quad (2.10)$$

Equation (2.10) provides some insights into the impact of matrices D , M , and $\nabla f(x)$ on the eigenvalues of J . For instance, when $D \succeq 0$, it seems that increasing the damping matrix

D (i.e., replacing D with \hat{D} , where $\hat{D} \succeq D$) will lead to more over-damped eigenvalues. However, this argument is not quite compelling because by changing D , the eigenvector v would also change. Although several researchers have mentioned such arguments about the impact of damping [20], to the best of our knowledge, this impact has not been studied in the literature in a rigorous fashion. We will discuss this impact in the next section.

2.3 Monotonic Effect of Damping

In this section, we analytically examine the role of damping matrix D in the stability of system (2.1). Specifically, we answer the following question: let System-I and System-II be two second-order dynamical systems (2.1) with partial damping matrices $D_I \succeq 0$ and $D_{II} \succeq 0$, respectively. Suppose the two systems are identical in other parameters (i.e., everything except their dampings) and $(x_0, 0) \in \mathbb{R}^{2n}$ is an equilibrium point for both systems. Observe that changing the damping of system (2.1) does not change the equilibrium points. Here, we focus on the case where M and $L := \nabla f(x_0)$ are symmetric (these are reasonable assumptions in many dynamical systems such as power systems). Now, if System-I is asymptotically stable, what kind of relationship between D_I and D_{II} will ensure that System-II is also asymptotically stable? This question has important practical consequences. For instance, the answer to this question will illustrate how changing the damping coefficients of generators (or equivalently, the corresponding controller parameters of inverter-based resources) in power systems will affect the stability of equilibrium points. Moreover, this question is closely intertwined with a problem in matrix perturbation theory, namely given a complex symmetric matrix with PSD imaginary part, how does a PSD perturbation of its imaginary part affect the rank of the matrix? We answer the matrix perturbation question in Theorem 1, which requires Lemma 2 to Lemma 5 and Proposition 1. Finally, the main result about the monotonic effect of damping is proved in Theorem 2. The following lemma on Autonne-Takagi factorization is useful.

Lemma 2 (Autonne-Takagi factorization). *Let $S \in \mathbb{C}^{n \times n}$ be a complex matrix. Then $S^\top =$*

S if and only if there is a unitary $U \in \mathbb{C}^{n \times n}$ and a nonnegative diagonal matrix $\Sigma \in \mathbb{R}^{n \times n}$ such that $S = U\Sigma U^\top$. The diagonal entries of Σ are the singular values of S .

Proof. See e.g. [57, Chapter 4]. □

We also need the following lemmas to derive our main results. Lemma 3 generalizes a simple fact about complex numbers to complex symmetric matrices: a complex scalar $z \in \mathbb{C}, z \neq 0$ has a nonnegative imaginary part if and only if z^{-1} has a nonpositive imaginary part.

Lemma 3. *Let $S \in \mathbb{C}^{n \times n}$ be a nonsingular complex symmetric matrix. Then $\text{Im}(S) \succeq 0$ if and only if $\text{Im}(S^{-1}) \preceq 0$.*

Proof. Since S is nonsingular complex symmetric, by Autonne-Takagi factorization, there exists a unitary matrix U and a diagonal positive definite matrix Σ such that $S = U\Sigma U^\top$. The inverse S^{-1} is given by $S^{-1} = \bar{U}\Sigma^{-1}U^*$. The imaginary parts of S and S^{-1} are

$$\begin{aligned}\text{Im}(S) &= -\frac{1}{2}\mathbf{i}(U\Sigma U^\top - \bar{U}\Sigma U^*), \\ \text{Im}(S^{-1}) &= -\frac{1}{2}\mathbf{i}(\bar{U}\Sigma^{-1}U^* - U\Sigma^{-1}U^\top).\end{aligned}$$

The real symmetric matrix $2\text{Im}(S^{-1}) = \mathbf{i}(U\Sigma^{-1}U^\top - \bar{U}\Sigma^{-1}U^*)$ is unitarily similar to the Hermitian matrix $\mathbf{i}(\Sigma^{-1}U^\top U - U^*\bar{U}\Sigma^{-1})$ as

$$\begin{aligned}U^*(2\text{Im}(S^{-1}))U &= U^*(\mathbf{i}(U\Sigma^{-1}U^\top - \bar{U}\Sigma^{-1}U^*))U \\ &= \mathbf{i}(\Sigma^{-1}U^\top U - U^*\bar{U}\Sigma^{-1}),\end{aligned}$$

and is $*$ -congruent to $\mathbf{i}(U^\top U\Sigma - \Sigma U^*\bar{U})$ as

$$\begin{aligned}\Sigma U^*(2\text{Im}(S^{-1}))U\Sigma &= \mathbf{i}\Sigma(\Sigma^{-1}U^\top U - U^*\bar{U}\Sigma^{-1})\Sigma \\ &= \mathbf{i}(U^\top U\Sigma - \Sigma U^*\bar{U}).\end{aligned}$$

Note that the latter transformation is a *-congruence because $U\Sigma$ is nonsingular but not necessarily unitary. Hence, $2\text{Im}(S^{-1})$ has the same eigenvalues as $\mathbf{i}(\Sigma^{-1}U^\top U - U^*\bar{U}\Sigma^{-1})$ and has the same inertia as $\mathbf{i}(U^\top U\Sigma - \Sigma U^*\bar{U})$ by Sylvester's law of inertia. Furthermore, since $U^\top U$ is unitary and $\overline{U^\top U} = U^*\bar{U}$, then

$$\mathbf{i}(U^\top U\Sigma - \Sigma U^*\bar{U}) = (U^\top U)(\mathbf{i}(\Sigma U^\top U - U^*\bar{U}\Sigma))(U^*\bar{U}),$$

which implies that $\mathbf{i}(U^\top U\Sigma - \Sigma U^*\bar{U})$ has the same eigenvalues as $\mathbf{i}(\Sigma U^\top U - U^*\bar{U}\Sigma)$. Furthermore, since

$$U(\mathbf{i}(\Sigma U^\top U - U^*\bar{U}\Sigma))U^* = \mathbf{i}(U\Sigma U^\top - \bar{U}\Sigma U^*) = -2\text{Im}(S),$$

$\text{Im}(S^{-1})$ and $-\text{Im}(S)$ have the same inertia, i.e., they have the same number of positive eigenvalues and the same number of negative eigenvalues. Therefore, $\text{Im}(S) \succeq 0$ if and only if all eigenvalues of $\text{Im}(S^{-1})$ are nonpositive, that is, if and only if $\text{Im}(S^{-1}) \preceq 0$. \square

Lemma 4 shows how rank-one perturbation to the imaginary part of a nonsingular complex matrix preserves its nonsingularity.

Lemma 4. *Let $S \in \mathbb{C}^{n \times n}$ be a nonsingular complex symmetric matrix. If $\text{Im}(S) \succeq 0$, then $S + \mathbf{i}vv^\top$ is nonsingular for any real vector $v \in \mathbb{R}^n$.*

Proof. We use Cauchy's formula for the determinant of a rank-one perturbation [57]:

$$\begin{aligned} \det(S + \mathbf{i}vv^\top) &= \det(S) + \mathbf{i}v^\top \text{adj}(S)v \\ &= \det(S) + \mathbf{i}v^\top S^{-1}v \det(S) \\ &= \det(S)(1 + \mathbf{i}v^\top S^{-1}v) \\ &= \det(S)(1 - v^\top \text{Im}(S^{-1})v + \mathbf{i}v^\top \text{Re}(S^{-1})v), \end{aligned}$$

where $\text{adj}(S)$ is the adjugate of S , which satisfies $\text{adj}(S) = (\det(S))S^{-1}$. Since $\det(S) \neq$

0, we only need to prove that the complex scalar $z := (1 - v^\top \text{Im}(S^{-1})v + iv^\top \text{Re}(S^{-1})v)$ is nonzero for any $v \in \mathbb{R}^n$. By Lemma 3, $\text{Im}(S^{-1}) \preceq 0$, thus $\text{Re}(z) = 1 - v^\top \text{Im}(S^{-1})v \geq 1$. This proves that any rank-one update on the imaginary part of S is nonsingular. \square

Now, we extend Lemma 4 to the case where the perturbation is a general real PSD matrix.

Proposition 1. *Let $S \in \mathbb{C}^{n \times n}$ be a nonsingular complex symmetric matrix with $\text{Im}(S) \succeq 0$. Then, for any real PSD matrix $E \in \mathbb{S}_+^n$, $S + iE$ is nonsingular.*

Proof. Since E is a real PSD matrix, its eigendecomposition gives $E = \sum_{\ell=1}^n v_\ell v_\ell^\top$, where v_ℓ is an eigenvector scaled by the ℓ -th eigenvalue of E . Now, we need to show that $S + \sum_{\ell=1}^n iv_\ell v_\ell^\top$ is nonsingular. According to Lemma 4, $\tilde{S}_\ell := S + iv_\ell v_\ell^\top$ is nonsingular for each $\ell \in \{1, \dots, n\}$. Moreover, \tilde{S}_ℓ is a complex symmetric matrix with $\text{Im}(\tilde{S}_\ell) \succeq 0$. Therefore, Lemma 4 can be consecutively applied to conclude that $S + iE$ is nonsingular. \square

Remark 1. *The assumption of S being complex symmetric cannot be relaxed. For example, consider unsymmetric matrix*

$$S = \begin{bmatrix} 1 + i & \sqrt{2} \\ -\sqrt{2} & -1 \end{bmatrix}, E = \begin{bmatrix} 0 & 0 \\ 0 & 1 \end{bmatrix}, S + iE = \begin{bmatrix} 1 + i & \sqrt{2} \\ -\sqrt{2} & -1 + i \end{bmatrix}.$$

Then, $\text{Im}(S) \succeq 0$, $\det(S) = 1 - i$, but $\det(S + iE) = 0$. Likewise, the assumption of E being real PSD cannot be relaxed.

Before proceeding further with the analysis, let us recall the concept of principal submatrix. For $A \in \mathbb{C}^{n \times n}$ and $\alpha \subseteq \{1, \dots, n\}$, the (sub)matrix of entries that lie in the rows and columns of A indexed by α is called a principal submatrix of A and is denoted by $A[\alpha]$. We also need Lemma 5 about rank principal matrices. In what follows, the direct sum of two matrices A and B is denoted by $A \oplus B$.

Lemma 5 (rank principal matrices). *Let $S \in \mathbb{C}^{n \times n}$ and suppose that $n > \mathbf{rank}(S) = r \geq 1$. If S is similar to $B \oplus 0_{n-r}$ (so $B \in \mathbb{C}^{r \times r}$ is nonsingular), then S has a nonsingular r -by- r principal submatrix, that is, S is rank principal.*

Proof. See Section A.1. □

Now we are ready to state our main matrix perturbation result.

Theorem 1. *Suppose $A \in \mathbb{S}^n$ is a real symmetric matrix, and $D \in \mathbb{S}_+^n$ and $E \in \mathbb{S}_+^n$ are real symmetric PSD matrices. Then $\mathbf{rank}(A + \mathbf{i}D) \leq \mathbf{rank}(A + \mathbf{i}D + \mathbf{i}E)$.*

Proof. Define $r := \mathbf{rank}(A + \mathbf{i}D)$ and note that if $r = 0$, i.e., $A + \mathbf{i}D$ is the zero matrix, then the rank inequality holds trivially. If $r \geq 1$, the following two cases are possible.

For $r = n$: in this case $S := A + \mathbf{i}D$ is a nonsingular complex symmetric matrix with $\text{Im}(S) \succeq 0$, and according to Proposition 1, $A + \mathbf{i}D + \mathbf{i}E$ is also nonsingular, i.e., $\mathbf{rank}(A + \mathbf{i}D + \mathbf{i}E) = n$. Thus, in this case, the rank inequality $\mathbf{rank}(A + \mathbf{i}D) \leq \mathbf{rank}(A + \mathbf{i}D + \mathbf{i}E)$ holds with equality.

For $1 \leq r < n$: since $A + \mathbf{i}D$ is complex symmetric, using Autonne-Takagi factorization in Lemma 2, $A + \mathbf{i}D = U\Sigma U^\top$ for some unitary matrix U and a diagonal real PSD matrix Σ . Moreover, $r = \mathbf{rank}(A + \mathbf{i}D)$ will be equal to the number of positive diagonal entries of Σ . In this case, $A + \mathbf{i}D$ is unitarily similar to $\Sigma = B \oplus 0_{n-r}$, for some nonsingular diagonal $B \in \mathbb{R}^{r \times r}$. According to Lemma 5, there exists a principal submatrix of $A + \mathbf{i}D$ with size r that is nonsingular, that is, there exists an index set $\alpha \subseteq \{1, \dots, n\}$ with $\text{card}(\alpha) = r$ such that $A[\alpha] + \mathbf{i}D[\alpha]$ is nonsingular. Note that $A[\alpha] + \mathbf{i}D[\alpha]$ is also complex symmetric. Now, using the same index set α of rows and columns, we select the principal submatrix $E[\alpha]$ of E . Recall that if a matrix is PSD then all its principal submatrices are also PSD. Therefore, $D[\alpha] \succeq 0$ and $E[\alpha] \succeq 0$. Using the same argument as in the previous case of this proof, we have $\mathbf{rank}(A[\alpha] + \mathbf{i}D[\alpha]) = \mathbf{rank}(A[\alpha] + \mathbf{i}D[\alpha] + \mathbf{i}E[\alpha]) = r$. On the one hand, according to our assumption, we have $\mathbf{rank}(A + \mathbf{i}D) = \mathbf{rank}(A[\alpha] + \mathbf{i}D[\alpha]) = r$.

On the other hand, we have

$$\mathbf{rank}(A + iD + iE) \geq \mathbf{rank}(A[\alpha] + iD[\alpha] + iE[\alpha]) = r = \mathbf{rank}(A + iD). \quad (2.11)$$

Note that the inequality in (2.11) holds because the rank of a principal submatrix is always less than or equal to the rank of the matrix itself. In other words, by adding more columns and rows to a (sub)matrix, the existing linearly independent rows and columns will remain linearly independent. Therefore, the rank inequality $\mathbf{rank}(A + iD) \leq \mathbf{rank}(A + iD + iE)$ also holds in this case. \square

We now use Theorem 1 to answer the question of how damping affects stability. In particular, Theorem 2 shows a monotonic effect of damping on system stability. Namely, when $\nabla f(x_0)$ is symmetric at an equilibrium point $(x_0, 0)$, the set of eigenvalues of the Jacobian $J(x_0)$ that lie on the imaginary axis does not enlarge, as the damping matrix D becomes more positive semidefinite.

Theorem 2 (Monotonicity of imaginary eigenvalues in response to damping). *Consider the following two systems,*

$$M\ddot{x} + D_I\dot{x} + f(x) = 0, \quad (\text{System-I})$$

$$M\ddot{x} + D_{II}\dot{x} + f(x) = 0, \quad (\text{System-II})$$

where $M \in \mathbb{S}^n$ is nonsingular and $D_I, D_{II} \in \mathbb{S}_+^n$. Suppose $(x_0, 0)$ is an equilibrium point of the corresponding first-order systems defined in (2.5). Assume $L := \nabla f(x_0) \in \mathbb{S}^n$. Denote J_I, J_{II} as the associated Jacobian matrices at x_0 as defined in (2.6). Furthermore, let $C_I \subseteq \mathbb{C}_0$ (resp. $C_{II} \subseteq \mathbb{C}_0$) be the set of eigenvalues of J_I (resp. J_{II}) with a zero real part, which may be an empty set. Then the sets C_I, C_{II} of eigenvalues on the imaginary

axis satisfy the following monotonicity property,

$$D_{II} \succeq D_I \implies \mathcal{C}_{II} \subseteq \mathcal{C}_I. \quad (2.12)$$

Proof. Recall the Jacobian matrices are defined as

$$J_I = \begin{bmatrix} 0 & I \\ -M^{-1}L & -M^{-1}D_I \end{bmatrix}, J_{II} = \begin{bmatrix} 0 & I \\ -M^{-1}L & -M^{-1}D_{II} \end{bmatrix},$$

at an equilibrium point $(x_0, 0)$. According to Lemma 1, $i\beta \in \mathcal{C}_I$ if and only if the quadratic matrix pencil $P_I(i\beta) := (L - \beta^2 M) + i\beta D_I$ is singular. The same argument holds for \mathcal{C}_{II} . Since J_I and J_{II} are real matrices, their complex eigenvalues will always occur in complex conjugate pairs. Therefore, without loss of generality, we assume $\beta \geq 0$. Note that for any $\beta \geq 0$ such that $i\beta \notin \mathcal{C}_I$ the pencil $P_I(i\beta) = (L - \beta^2 M) + i\beta D_I$ is nonsingular. Moreover, $(L - \beta^2 M) \in \mathbb{S}^n$ is a real symmetric matrix and $\beta D_I \in \mathbb{S}_+^n$ is a real PSD matrix. According to Theorem 1,

$$\begin{aligned} r &= \mathbf{rank}(L - \beta^2 M + i\beta D_I) \\ &\leq \mathbf{rank}(L - \beta^2 M + i\beta D_I + i\beta(D_{II} - D_I)) \\ &= \mathbf{rank}(L - \beta^2 M + i\beta D_{II}), \end{aligned}$$

consequently, $P_{II}(i\beta) = L - \beta^2 M + i\beta D_{II}$ is also nonsingular and $i\beta \notin \mathcal{C}_{II}$. This implies that $\mathcal{C}_{II} \subseteq \mathcal{C}_I$ and completes the proof. \square

Remark 2. In the above theorem, the assumption of $L = \nabla f(x_0)$ being symmetric cannot be relaxed. For example, consider

$$f(x_1, x_2) = \begin{bmatrix} 2x_1 + \sqrt{2}x_2 \\ -\sqrt{2}x_1 \end{bmatrix}, D_I = \begin{bmatrix} 1 & 0 \\ 0 & 0 \end{bmatrix}, D_{II} = \begin{bmatrix} 1 & 0 \\ 0 & 1 \end{bmatrix}, M = \begin{bmatrix} 1 & 0 \\ 0 & 1 \end{bmatrix}.$$

Here, the origin is the equilibrium point of the corresponding first-order systems, and $L = \nabla f(0, 0)$ is not symmetric. The set of eigenvalues with zero real part in (System-I) and (System-II) are $\mathcal{C}_I = \emptyset$ and $\mathcal{C}_{II} = \{\pm i\}$. Accordingly, we have $D_{II} \succeq D_I$, but $\mathcal{C}_{II} \not\subseteq \mathcal{C}_I$.

2.4 Impact of Damping on Hyperbolicity and Bifurcation

2.4.1 Necessary and Sufficient Conditions for Breaking Hyperbolicity

We use the notion of observability from control theory to provide a necessary and sufficient condition for breaking the hyperbolicity of equilibrium points in system (2.5) when the inertia, damping, and Jacobian of f satisfy $M \in \mathbb{S}_{++}^n, D \in \mathbb{S}_+^n, \nabla f(x_0) \in \mathbb{S}_{++}^n$ at an equilibrium point $(x_0, 0)$ (Theorem 3). We further provide a sufficient condition for the existence of purely imaginary eigenvalues in system (2.5) when $M, D, \nabla f(x_0)$ are not symmetric (Theorem 4). Such conditions will pave the way for understanding Hopf bifurcations in these systems. Observability was first related to stability of second-order system (2.1) by Skar [58].

Definition 1 (observability). *Consider the matrices $A \in \mathbb{R}^{m \times m}$ and $B \in \mathbb{R}^{n \times m}$. The pair (A, B) is observable if $Bx \neq 0$ for every right eigenvector x of A , i.e.,*

$$\forall \lambda \in \mathbb{C}, x \in \mathbb{C}^m, x \neq 0 \text{ s.t. } Ax = \lambda x \implies Bx \neq 0.$$

We will show that the hyperbolicity of an equilibrium point $(x_0, 0)$ of system (2.5) is intertwined with the observability of the pair $(M^{-1}\nabla f(x_0), M^{-1}D)$. Our focus will remain on the role of the damping matrix $D \in \mathbb{S}_+^n$ in this matter. Note that if the damping matrix D is nonsingular, the pair $(M^{-1}\nabla f(x_0), M^{-1}D)$ is always observable because the nullspace of $M^{-1}D$ is trivial. Furthermore, if the damping matrix D is zero, the following lemma holds.

Lemma 6. *In an undamped system (i.e., when $D = 0$), for any $x \in \mathbb{R}^n$ the pair $(M^{-1}\nabla f(x), M^{-1}D)$*

can never be observable. Moreover, for any $x \in \mathbb{R}^n$

$$\lambda \in \sigma(J(x)) \iff \lambda^2 \in \sigma(-M^{-1}\nabla f(x)).$$

Proof. The first statement is an immediate consequence of Definition 1 and the second one follows from Lemma 1. \square

The next theorem yields a necessary and sufficient condition on the damping matrix D for breaking the hyperbolicity of an equilibrium point.

Theorem 3 (hyperbolicity in second-order systems: symmetric case). *Consider the second-order ODE system (2.1) with inertia matrix $M \in \mathbb{S}_{++}^n$ and damping matrix $D \in \mathbb{S}_+^n$. Suppose $(x_0, 0) \in \mathbb{R}^{n+n}$ is an equilibrium point of the corresponding first-order system (2.5) with the Jacobian matrix $J \in \mathbb{R}^{2n \times 2n}$ defined in (2.6) such that $L = \nabla f(x_0) \in \mathbb{S}_{++}^n$. Then, the equilibrium point $(x_0, 0)$ is hyperbolic if and only if the pair $(M^{-1}L, M^{-1}D)$ is observable.*

Proof. According to Lemma 6, if $D = 0$, the pair $(M^{-1}L, M^{-1}D)$ can never be observable. Moreover, $M^{-1}L = M^{-\frac{1}{2}}\hat{L}M^{\frac{1}{2}}$, where $\hat{L} := M^{-\frac{1}{2}}LM^{-\frac{1}{2}}$. This implies that $M^{-1}L$ is similar to (and consequently has the same eigenvalues as) \hat{L} . Note that \hat{L} is *-congruent to L . According to Sylvester's law of inertia, \hat{L} and L have the same inertia. Since $L \in \mathbb{S}_{++}^n$, we conclude that $\hat{L} \in \mathbb{S}_{++}^n$. Therefore, the eigenvalues of $M^{-1}L$ are real and positive, i.e., $\sigma(M^{-1}L) \subseteq \mathbb{R}_{++} = \{\lambda \in \mathbb{R} : \lambda > 0\}$. Meanwhile, when $D = 0$, we have $\mu \in \sigma(J) \iff \mu^2 \in \sigma(-M^{-1}L)$, hence all eigenvalues of J would have zero real parts, i.e., $\sigma(J) \subseteq \mathbb{C}_0$, and consequently, the theorem holds trivially. In the sequel, we assume that $D \neq 0$.

Necessity: Suppose the pair $(M^{-1}L, M^{-1}D)$ is observable, but assume the equilibrium point is not hyperbolic, and let us lead this assumption to a contradiction. Since $L = \nabla f(x_0)$ is nonsingular, Lemma 1 asserts that $0 \notin \sigma(J)$. Therefore, there must exist $\beta > 0$ such that $i\beta \in \sigma(J)$. By Lemma 1, $i\beta \in \sigma(J)$ if and only if the matrix pencil $(M^{-1}L +$

$i\beta M^{-1}D - \beta^2 I$ is singular:

$$\det \left(M^{-\frac{1}{2}} (M^{-\frac{1}{2}} L M^{-\frac{1}{2}} + i\beta M^{-\frac{1}{2}} D M^{-\frac{1}{2}} - \beta^2 I) M^{\frac{1}{2}} \right) = 0,$$

or equivalently, $\exists(x + iy) \neq 0$ such that $x, y \in \mathbb{R}^n$ and

$$\begin{aligned} & (M^{-\frac{1}{2}} L M^{-\frac{1}{2}} + i\beta M^{-\frac{1}{2}} D M^{-\frac{1}{2}} - \beta^2 I)(x + iy) = 0 \\ \iff & \begin{cases} (M^{-\frac{1}{2}} L M^{-\frac{1}{2}} - \beta^2 I)x - \beta M^{-\frac{1}{2}} D M^{-\frac{1}{2}} y = 0, \\ (M^{-\frac{1}{2}} L M^{-\frac{1}{2}} - \beta^2 I)y + \beta M^{-\frac{1}{2}} D M^{-\frac{1}{2}} x = 0. \end{cases} \end{aligned} \quad (2.13)$$

Let $\hat{L} := M^{-\frac{1}{2}} L M^{-\frac{1}{2}}$, $\hat{D} := M^{-\frac{1}{2}} D M^{-\frac{1}{2}}$, and observe that

$$\begin{cases} y^\top (\hat{L} - \beta^2 I)x = y^\top (\beta \hat{D} y) = \beta y^\top \hat{D} y \geq 0, \\ x^\top (\hat{L} - \beta^2 I)y = x^\top (-\beta \hat{D} x) = -\beta x^\top \hat{D} x \leq 0, \end{cases}$$

where we have used the fact that \hat{D} is *-congruent to D . According to Sylvester's law of inertia, \hat{D} and D have the same inertia. Since $D \succeq 0$, we conclude that $\hat{D} \succeq 0$. As $(\hat{L} - \beta^2 I)$ is symmetric, we have $x^\top (\hat{L} - \beta^2 I)y = y^\top (\hat{L} - \beta^2 I)x$. Therefore, we must have $x^\top \hat{D} x = y^\top \hat{D} y = 0$. Since $\hat{D} \succeq 0$, we can infer that $x \in \ker(\hat{D})$ and $y \in \ker(\hat{D})$. Now considering $\hat{D}y = 0$ and using the first equation in (2.13) we get

$$(\hat{L} - \beta^2 I)x = 0 \iff M^{-\frac{1}{2}} L M^{-\frac{1}{2}} x = \beta^2 x, \quad (2.14)$$

multiplying both sides from left by $M^{-\frac{1}{2}}$ we get $M^{-1} L (M^{-\frac{1}{2}} x) = \beta^2 (M^{-\frac{1}{2}} x)$. Thus, $\hat{x} := M^{-\frac{1}{2}} x$ is an eigenvector of $M^{-1} L$. Moreover, we have

$$M^{-1} D \hat{x} = M^{-1} D M^{-\frac{1}{2}} x = M^{-\frac{1}{2}} (\hat{D} x) = 0,$$

which means that the pair $(M^{-1}L, M^{-1}D)$ is not observable; we have arrived at the desired contradiction.

Sufficiency: Suppose the equilibrium point is hyperbolic, but assume that the pair $(M^{-1}L, M^{-1}D)$ is not observable; we will show that this assumption leads to a contradiction. According to Definition 1, $\exists \lambda \in \mathbb{C}, x \in \mathbb{C}^n, x \neq 0$ such that

$$M^{-1}Lx = \lambda x \text{ and } M^{-1}Dx = 0. \quad (2.15)$$

We make the following two observations. Firstly, as it is shown above, we have $\sigma(M^{-1}L) \subseteq \mathbb{R}_{++}$. Secondly, since L is nonsingular, the eigenvalue λ in (2.15) cannot be zero. Based on the foregoing two observations, when the pair $(M^{-1}L, M^{-1}D)$ is not observable, there must exist $\lambda \in \mathbb{R}_+, \lambda \neq 0$ and $x \in \mathbb{C}^n, x \neq 0$ such that (2.15) holds. Define $\xi = \sqrt{-\lambda}$, which is a purely imaginary number. The quadratic pencil $M^{-1}P(\xi) = \xi^2 I + \xi M^{-1}D + M^{-1}L$ is singular because $M^{-1}P(\xi)x = \xi^2 x + \xi M^{-1}Dx + M^{-1}Lx = -\lambda x + 0 + \lambda x = 0$. By Lemma 1, ξ is an eigenvalue of J . Similarly, we can show $-\xi$ is an eigenvalue of J . Therefore, the equilibrium point is not hyperbolic, which is a desired contradiction. \square

As mentioned above, if matrix D is nonsingular, the pair $(M^{-1}\nabla f(x_0), M^{-1}D)$ is always observable. Indeed, if we replace the assumption $D \in \mathbb{S}_+^n$ with $D \in \mathbb{S}_{++}^n$ in Theorem 3, then the equilibrium point $(x_0, 0)$ is not only hyperbolic but also asymptotically stable. This is proved in Theorem 17 in Section A.2.

Another interesting observation is that when an equilibrium point is hyperbolic, Theorem 3 confirms the monotonic behaviour of damping in Theorem 2. Specifically, suppose an equilibrium point $(x_0, 0)$ is hyperbolic for a value of damping matrix $D_I \in \mathbb{S}_+^n$. Theorem 3 implies that the pair $(M^{-1}\nabla f(x_0), M^{-1}D_I)$ is observable. Note that if we change the damping to $D_{II} \in \mathbb{S}_+^n$ such that $D_{II} \succeq D_I$, then the pair $(M^{-1}\nabla f(x_0), M^{-1}D_{II})$ is also observable. Hence, the equilibrium point $(x_0, 0)$ of the new system with damping D_{II} is also hyperbolic. This is consistent with the monotonic behaviour of damping which is

proved in Theorem 2.

Under additional assumptions, Theorem 3 can be partially generalized to a sufficient condition for the breakdown of hyperbolicity when L , M , and D are not symmetric as in the following

Theorem 4 (hyperbolicity in second-order systems: unsymmetric case). *Consider the second-order ODE system (2.1) with nonsingular inertia matrix $M \in \mathbb{R}^{n \times n}$ and damping matrix $D \in \mathbb{R}^{n \times n}$. Suppose $(x_0, 0) \in \mathbb{R}^{n+n}$ is an equilibrium point of the corresponding first-order system (2.5) with the Jacobian matrix $J \in \mathbb{R}^{2n \times 2n}$ defined in (2.6) such that $L = \nabla f(x_0) \in \mathbb{R}^{n \times n}$. If $M^{-1}L$ has a positive eigenvalue λ with eigenvector x such that x is in the nullspace of $M^{-1}D$, then the spectrum of the Jacobian matrix $\sigma(J)$ contains a pair of purely imaginary eigenvalues.*

Proof. The proof is similar to that of Theorem 3 and is given in Section A.3. □

2.4.2 Bifurcation under Damping Variations

In Section 2.4.1, we developed necessary and/or sufficient conditions for breaking the hyperbolicity through purely imaginary eigenvalues. Naturally, the next question is: what are the consequences of breaking the hyperbolicity? To answer this question, consider the parametric ODE

$$M\ddot{x} + D(\gamma)\dot{x} + f(x) = 0, \quad (2.16)$$

which satisfies the same assumptions as (2.1). Suppose $D(\gamma)$ is a smooth function of $\gamma \in \mathbb{R}$, and $(x_0, 0) \in \mathbb{R}^{n+n}$ is a hyperbolic equilibrium point of the corresponding first-order system at $\gamma = \gamma_1$ with the Jacobian matrix $J(x, \gamma)$ defined as

$$J(x, \gamma) = \begin{bmatrix} 0 & I \\ -M^{-1}\nabla f(x) & -M^{-1}D(\gamma) \end{bmatrix} \in \mathbb{R}^{2n \times 2n}. \quad (2.17)$$

Let us vary γ from γ_1 to γ_2 and monitor the equilibrium point. There are two ways in which the hyperbolicity can be broken. Either a simple real eigenvalue approaches zero and we have $0 \in \sigma(J(x_0, \gamma_2))$, or a pair of simple complex eigenvalues approaches the imaginary axis and we have $\pm i\omega_0 \in \sigma(J(x_0, \gamma_2))$ for some $\omega_0 > 0$. The former corresponds to a fold bifurcation, while the latter is associated with a Hopf (more accurately, Poincare-Andronov-Hopf) bifurcation¹. The next theorem states the precise conditions for a Hopf bifurcation to occur in system (2.16).

Theorem 5. *Consider the parametric ODE (2.16), with inertia matrix $M \in \mathbb{S}_{++}^n$ and damping matrix $D(\gamma) \in \mathbb{S}_+^n$. Suppose $D(\gamma)$ is a smooth function of γ , $(x_0, 0) \in \mathbb{R}^{n+n}$ is an isolated equilibrium point of the corresponding first-order system, and $L := \nabla f(x_0) \in \mathbb{S}_{++}^n$. Assume the following conditions are satisfied:*

- (i) *There exists $\gamma_0 \in \mathbb{R}$ such that the pair $(M^{-1}L, M^{-1}D(\gamma_0))$ is not observable, that is,*
 $\exists \lambda \in \mathbb{C}, v \in \mathbb{C}^n, v \neq 0$ *such that*

$$M^{-1}Lv = \lambda v \text{ and } M^{-1}D(\gamma_0)v = 0. \quad (2.18)$$

- (ii) *$i\omega_0$ is a simple eigenvalue of $J(x_0, \gamma_0)$, where $\omega_0 = \sqrt{\lambda}$.*

- (iii) *$\text{Im}(q^*M^{-1}D'(\gamma_0)v) \neq 0$, where $D'(\gamma_0)$ is the derivative of $D(\gamma)$ at $\gamma = \gamma_0$, $\ell_0 = (p, q) \in \mathbb{C}^{n+n}$ is a left eigenvector of $J(x_0, \gamma_0)$ corresponding to eigenvalue $i\omega_0$, and ℓ_0 is normalized so that $\ell_0^*r_0 = 1$ where $r_0 = (v, i\omega_0v)$.*

- (iv) *$\det(P(\kappa)) \neq 0$ for all $\kappa \in \mathbb{Z} \setminus \{-1, 1\}$, where $P(\kappa)$ is the quadratic matrix pencil given by $P(\kappa) := \nabla f(x_0) - \kappa^2\omega_0^2M + i\kappa\omega_0D(\gamma_0)$.*

Then, there exists smooth functions $\gamma = \gamma(\varepsilon)$ and $T = T(\varepsilon)$ depending on a parameter ε with $\gamma(0) = \gamma_0$ and $T(0) = 2\pi|\omega_0|^{-1}$ such that there are nonconstant periodic solutions of

¹It can be proved that we need more parameters to create extra eigenvalues on the imaginary axis unless the system has special properties such as symmetry [59].

(2.16) with period $T(\varepsilon)$ which collapses into the equilibrium point $(x_0, 0)$ as $\varepsilon \rightarrow 0$.

Proof. By Theorem 3, condition (i) implies that the Jacobian matrix (2.17) at $(x, \gamma) = (x_0, \gamma_0)$ possesses a pair of purely imaginary eigenvalues $\pm i\omega_0$, where $\omega_0 = \sqrt{\lambda}$. Moreover, a right eigenvector of $i\omega_0$ is $(v, i\omega_0 v)$, where v is from (2.18). According to condition (ii), the eigenvalue $i\omega_0$ is simple. Therefore, according to the eigenvalue perturbation theorem [60, Theorem 1], for γ in a neighborhood of γ_0 , the matrix $J(x_0, \gamma)$ has an eigenvalue $\xi(\gamma)$ and corresponding right and left eigenvectors $r(\gamma)$ and $\ell(\gamma)$ with $\ell(\gamma)^* r(\gamma) = 1$ such that $\xi(\gamma)$, $r(\gamma)$, and $\ell(\gamma)$ are all analytic functions of γ , satisfying $\xi(\gamma_0) = i\omega_0$, $r(\gamma_0) = r_0$, and $\ell(\gamma_0) = \ell_0$. Let us differentiate the equation $J(x_0, \gamma)r(\gamma) = \xi(\gamma)r(\gamma)$ and set $\gamma = \gamma_0$, to get

$$J'(x_0, \gamma_0)r(\gamma_0) + J(x_0, \gamma_0)r'(\gamma_0) = \xi'(\gamma_0)r(\gamma_0) + \xi(\gamma_0)r'(\gamma_0). \quad (2.19)$$

After left multiplication by ℓ_0^* , and using $\ell_0^* r_0 = 1$, we obtain the derivative of $\xi(\gamma)$ at $\gamma = \gamma_0$:

$$\xi'(\gamma_0) = \begin{bmatrix} p^* & q^* \end{bmatrix} \begin{bmatrix} 0 & 0 \\ 0 & -M^{-1}D'(\gamma_0) \end{bmatrix} \begin{bmatrix} v \\ i\omega_0 v \end{bmatrix} = -i\omega_0 q^* M^{-1}D'(\gamma_0)v.$$

Now, $\text{Im}(q^* M^{-1}D'(\gamma_0)v) \neq 0$ in condition (iii) implies that $\text{Re}(\xi'(\gamma_0)) \neq 0$ which is a necessary condition for Hopf bifurcation. Therefore, the results follow from the Hopf bifurcation theorem [61, Section 2]. Note that $J(x_0, \gamma)$ is singular if and only if $\nabla f(x_0)$ is singular. Thus, nonsingularity of $\nabla f(x_0)$ is necessary for Hopf bifurcation. \square

If one or more of the listed conditions in Theorem 5 are not satisfied, we may still have the birth of a periodic orbit but some of the conclusions of the theorem may not hold true. The bifurcation is then called a degenerate Hopf bifurcation. For instance, if the transversality condition (iii) is not satisfied, the stability of the equilibrium point may not change, or multiple periodic orbits may bifurcate [61]. The next theorem describes a safe

region for damping variations such that fold and Hopf bifurcations will be avoided.

Theorem 6. *Consider the parametric ODE (2.16), with a nonsingular inertia matrix $M \in \mathbb{R}^{n \times n}$. Suppose the damping matrix $D(\gamma) \in \mathbb{R}^{n \times n}$ is a smooth function of γ , $(x_0, 0) \in \mathbb{R}^{n+n}$ is a hyperbolic equilibrium point of the corresponding first-order system at $\gamma = \gamma_0$, and $L := \nabla f(x_0) \in \mathbb{R}^{n \times n}$. Then, the following statements hold:*

(i) *Variation of γ in \mathbb{R} will not lead to any fold bifurcation.*

(ii) *Under the symmetric setting, i.e., when $M \in \mathbb{S}_{++}^n$, $D(\gamma) \in \mathbb{S}_+^n$, and $L \in \mathbb{S}_{++}^n$, variation of γ in \mathbb{R} will not lead to any Hopf bifurcation, as long as $D(\gamma) \succeq D(\gamma_0)$. If in addition the equilibrium point is stable, variation of γ in \mathbb{R} will not make it unstable, as long as $D(\gamma) \succeq D(\gamma_0)$.*

Proof. According to Lemma 1, zero is an eigenvalue of J if and only if the matrix $L = \nabla f(x_0)$ is singular. Therefore, the damping matrix D has no role in the zero eigenvalue of J . The second statement follows from Theorem 2. \square

The above theorem can be straightforwardly generalized to bifurcations having higher codimension.

2.5 Power System Models and Impact of Damping

The Questions (i)-(iii) asked in Section 2.2.1 and the theorems and results discussed in the previous parts of this chapter arise naturally from the foundations of electric power systems. These results are useful tools for analyzing the behaviour and maintaining the stability of power systems. In the rest of this chapter, we focus on power systems to further explore the role of damping in these systems.

2.5.1 Power System Model

Consider a power system with the set of interconnected generators $\mathcal{N} = \{1, \dots, n\}$, $n \in \mathbb{N}$. Based on the classical small-signal stability assumptions [1], the mathematical model

for a power system is described by the following second-order system:

$$\frac{m_j}{\omega_s} \ddot{\delta}_j(t) + \frac{d_j}{\omega_s} \dot{\delta}_j(t) = P_{m_j} - P_{e_j}(\delta(t)) \quad \forall j \in \mathcal{N}. \quad (2.20)$$

Considering the state space $\mathcal{S} := \{(\delta, \omega) : \delta \in \mathbb{R}^n, \omega \in \mathbb{R}^n\}$, the dynamical system (2.20) can be represented as a system of first-order nonlinear autonomous ODEs, aka swing equations:

$$\dot{\delta}_j(t) = \omega_j(t) \quad \forall j \in \mathcal{N}, \quad (2.21a)$$

$$\frac{m_j}{\omega_s} \dot{\omega}_j(t) + \frac{d_j}{\omega_s} \omega_j(t) = P_{m_j} - P_{e_j}(\delta(t)) \quad \forall j \in \mathcal{N}, \quad (2.21b)$$

where for each generator $j \in \mathcal{N}$, P_{m_j} and P_{e_j} are mechanical and electrical powers in per unit, m_j is the inertia constant in seconds, d_j is the unitless damping coefficient, ω_s is the synchronous angular velocity in electrical radians per seconds, t is the time in seconds, $\delta_j(t)$ is the rotor electrical angle in radians, and finally $\omega_j(t)$ is the deviation of the rotor angular velocity from the synchronous velocity in electrical radians per seconds. For the sake of simplicity, henceforth we do not explicitly write the dependence of the state variables δ and ω on time t . The electrical power P_{e_j} in (2.21b) can be further spelled out:

$$P_{e_j}(\delta) = \sum_{k=1}^n V_j V_k Y_{jk} \cos(\theta_{jk} - \delta_j + \delta_k) \quad (2.22)$$

where V_j is the terminal voltage magnitude of generator j , and $Y_{jk} \exp(i\theta_{jk})$ is the (j, k) entry of the reduced admittance matrix, with $Y_{jk} \in \mathbb{R}$ and $\theta_{jk} \in \mathbb{R}$. The reduced admittance matrix encodes the underlying graph structure of the power grid, which is assumed to be a connected graph in this chapter. Note that for each generator $j \in \mathcal{N}$, the electrical power P_{e_j} in general is a function of angle variables δ_k for all $k \in \mathcal{N}$. Therefore, the dynamics of generators are interconnected through the function $P_{e_j}(\delta)$ in (2.20) and (2.21).

Definition 2 (flow function). *The smooth function $P_e : \mathbb{R}^n \rightarrow \mathbb{R}^n$ given by $\delta \mapsto P_e(\delta)$ in*

(2.22) is called the flow function.

The smoothness of the flow function (it is \mathcal{C}^∞ indeed) is a sufficient condition for the existence and uniqueness of the solution to the ODE (2.21). The flow function is translationally invariant with respect to the operator $\delta \mapsto \delta + \alpha \mathbf{1}$, where $\alpha \in \mathbb{R}$ and $\mathbf{1} \in \mathbb{R}^n$ is the vector of all ones. In other words, $P_e(\delta + \alpha \mathbf{1}) = P_e(\delta)$. A common way to deal with this situation is to define a reference bus and refer all other bus angles to it. This is equivalent to projecting the original state space \mathcal{S} onto a lower dimensional space. We will delve into this issue in Section 2.5.3.

2.5.2 Jacobian of Swing Equations

Let us take the state variable vector $(\delta, \omega) \in \mathbb{R}^{2n}$ into account and note that the Jacobian of the vector field in (2.21) has the form (2.6) where $M = \frac{1}{\omega_s} \mathbf{diag}(m_1, \dots, m_n)$ and $D = \frac{1}{\omega_s} \mathbf{diag}(d_1, \dots, d_n)$. Moreover, $f = P_e - P_m$ and $\nabla f = \nabla P_e(\delta) \in \mathbb{R}^{n \times n}$ is the Jacobian of the flow function with the entries:

$$\begin{aligned} \frac{\partial P_{e_j}}{\partial \delta_j} &= \sum_{k \neq j} V_j V_k Y_{jk} \sin(\theta_{jk} - \delta_j + \delta_k), \forall j \in \mathcal{N} \\ \frac{\partial P_{e_j}}{\partial \delta_k} &= -V_j V_k Y_{jk} \sin(\theta_{jk} - \delta_j + \delta_k), \forall j, k \in \mathcal{N}, k \neq j. \end{aligned}$$

Let \mathcal{L} be the set of transmission lines of the reduced power system. We can rewrite

$\partial P_{e_j} / \partial \delta_j = \sum_{k=1, k \neq j}^n w_{jk}$ and $\partial P_{e_j} / \partial \delta_k = -w_{jk}$, where

$$w_{jk} = \begin{cases} V_j V_k Y_{jk} \sin(\varphi_{jk}) & \forall \{j, k\} \in \mathcal{L} \\ 0 & \text{otherwise,} \end{cases} \quad (2.23)$$

and $\varphi_{jk} = \theta_{jk} - \delta_j + \delta_k$. Typically, we have $\varphi_{jk} \in (0, \pi)$ for all $\{j, k\} \in \mathcal{L}$ [17]. Thus, it is reasonable to assume that the equilibrium points (δ^0, ω^0) of the dynamical system (2.21)

are located in the set Ω defined as

$$\Omega = \{(\delta, \omega) \in \mathbb{R}^{2n} : 0 < \theta_{jk} - \delta_j + \delta_k < \pi, \forall \{j, k\} \in \mathcal{L}, \omega = 0\}.$$

Under this assumption, the terms $w_{jk} > 0$ for all transmission lines $\{j, k\} \in \mathcal{L}$. Consequently, $\partial P_{e_j} / \partial \delta_j \geq 0, \forall j \in \mathcal{N}$ and $\partial P_{e_j} / \partial \delta_k \leq 0, \forall j, k \in \mathcal{N}, k \neq j$. Moreover, $\nabla P_e(\delta)$ has a zero row sum, i.e., $\nabla P_e(\delta) \mathbf{1} = 0 \implies 0 \in \sigma(\nabla P_e(\delta))$. Given these properties, $\nabla P_e(\delta^0)$ turns out to be a singular M-matrix for all $(\delta^0, \omega^0) \in \Omega$ [17]. Recall that a matrix A is an *M-matrix* if the off-diagonal elements of A are nonpositive and the nonzero eigenvalues of A have positive real parts [62]. Finally, if the power system under study has a connected underlying undirected graph, the zero eigenvalue of $\nabla P_e(\delta^0)$ will be simple [17].

In general, the Jacobian $\nabla P_e(\delta)$ is not symmetric. When the power system is *lossless*, i.e., when the transfer conductances of the grid are zero, then $\theta_{jj} = -\frac{\pi}{2}, \forall j \in \mathcal{N}$ and $\theta_{jk} = \frac{\pi}{2}, \forall \{j, k\} \in \mathcal{L}$. In a lossless system, $\nabla P_e(\delta)$ is symmetric. If in addition an equilibrium point (δ^0, ω^0) belongs to the set Ω , then $\nabla P_e(\delta^0) \in \mathbb{S}_+^n$, because $\nabla P_e(\delta^0)$ is real symmetric and diagonally dominant [63].

2.5.3 Referenced Power System Model

The translational invariance of the flow function P_e gives rise to a zero eigenvalue in the spectrum of $\nabla P_e(\delta)$, and as a consequence, in the spectrum of $J(\delta)$. This zero eigenvalue and the corresponding nullspace pose some difficulties in monitoring the hyperbolicity of the equilibrium points, specially during Hopf bifurcation analysis. As mentioned in Section 2.5.1, this situation can be dealt with by defining a reference bus and referring all other bus angles to it. Although this is a common practice in power system context [1], the spectral and dynamical relationships between the original system and the referenced system are not rigorously analyzed in the literature. In this section, we fill this gap to facilitate our

analysis in the later parts.

Referenced Model

Define $\psi_j := \delta_j - \delta_n, \forall j \in \{1, 2, \dots, n-1\}$ and reformulate the swing equation model (2.21) into the *referenced model*

$$\dot{\psi}_j = \omega_j - \omega_n \quad \forall j \in \{1, \dots, n-1\}, \quad (2.24a)$$

$$\dot{\omega}_j = -\frac{d_j}{m_j}\omega_j + \frac{\omega_s}{m_j}(P_{m_j} - P_{e_j}^r(\psi)) \quad \forall j \in \{1, \dots, n\}, \quad (2.24b)$$

where for all j in $\{1, \dots, n\}$ we have

$$P_{e_j}^r(\psi) = \sum_{k=1}^n V_j V_k Y_{jk} \cos(\theta_{jk} - \psi_j + \psi_k), \quad (2.25)$$

and $\psi_n \equiv 0$. The function $P_e^r : \mathbb{R}^{n-1} \rightarrow \mathbb{R}^n$ given by (2.25) is called the referenced flow function.

The Relationship

We would like to compare the behaviour of the two dynamical systems (2.21) and (2.24).

Let us define the linear mapping $\Psi : \mathbb{R}^n \times \mathbb{R}^n \rightarrow \mathbb{R}^{n-1} \times \mathbb{R}^n$ given by $(\delta, \omega) \mapsto (\psi, \omega)$ such that

$$\Psi(\delta, \omega) = \{(\psi, \omega) : \psi_j := \delta_j - \delta_n, \forall j \in \{1, 2, \dots, n-1\}\}.$$

This map is obviously smooth but not injective. It can also be written in matrix form

$$\Psi(\delta, \omega) = \begin{bmatrix} T_1 & 0 \\ 0 & I_n \end{bmatrix} \begin{bmatrix} \delta \\ \omega \end{bmatrix}$$

where $I_n \in \mathbb{R}^{n \times n}$ is the identity matrix, $\mathbf{1} \in \mathbb{R}^{n-1}$ is the vector of all ones, and

$$T_1 := \begin{bmatrix} I_{n-1} & -\mathbf{1} \end{bmatrix} \in \mathbb{R}^{(n-1) \times n}. \quad (2.26)$$

The next proposition, which is proved in Section A.4, establishes the relationship between the original model (2.21) and the referenced model (2.24).

Proposition 2. *Let (δ^0, ω^0) be an equilibrium point of the swing equation (2.21) and (n_-, n_0, n_+) be the inertia² of its Jacobian at this equilibrium point. The following two statements hold:*

- (i) $\Psi(\delta^0, \omega^0)$ is an equilibrium point of the referenced model (2.24).
- (ii) $(n_-, n_0 - 1, n_+)$ is the inertia of the Jacobian of (2.24) at $\Psi(\delta^0, \omega^0)$.

Remark 3. *Note that the equilibrium points of the referenced model (2.24) are in the set*

$$\tilde{\mathcal{E}} = \left\{ (\psi, \omega) \in \mathbb{R}^{n-1} \times \mathbb{R}^n : \omega_j = \omega_n, \forall j \in \{1, \dots, n-1\}, \right. \\ \left. P_{m_j} = P_{e_j}^r(\psi) + d_j \omega_n / \omega_s, \forall j \in \{1, \dots, n\} \right\}$$

where ω_n is not necessarily zero. Therefore, the referenced model (2.24) may have extra equilibrium points which do not correspond to any equilibrium point of the original model (2.21).

2.5.4 Impact of Damping in Power Systems

The theoretical results in Section 2.3 and Section 2.4 have important applications in electric power systems. For example, Theorem 2 is directly applicable to lossless power systems, and provides new insights to improve the situational awareness of power system operators. Recall that many control actions taken by power system operators are directly or indirectly

²Inertia of a matrix (see e.g. [57] for a definition) should not be confused with the inertia matrix M .

targeted at changing the effective damping of the system [32, 37, 38]. In this context, Theorem 2 determines how the system operator should change the damping of the system in order to avoid breaking the hyperbolicity and escaping dangerous bifurcations.

Now, consider the case where a subset of power system generators have zero damping coefficients. Such partial damping is possible in practice specially in inverter-based resources (as damping coefficient corresponds to a controller parameter which can take zero value). The next theorem and remark follow from Theorem 3, and show how partial damping could break the hyperbolicity in lossless power systems.

Theorem 7 (purely imaginary eigenvalues in lossless power systems). *Consider a lossless network (2.21) with an equilibrium point $(\delta^0, \omega^0) \in \Omega$. Suppose all generators have positive inertia and nonnegative damping coefficients. Then, $\sigma(J(\delta^0))$ contains a pair of purely imaginary eigenvalues if and only if the pair $(M^{-1}\nabla P_e(\delta^0), M^{-1}D)$ is not observable.*

Proof. As mentioned above, we always assume the physical network connecting the power generators is a connected (undirected) graph. Under this assumption, as mentioned in Section 2.5.2, matrix $L := \nabla P_e(\delta^0)$ has a simple zero eigenvalue with a right eigenvector $\mathbf{1} \in \mathbb{R}^n$, which is the vector of all ones [17]. Moreover, since the power system is lossless and $(\delta^0, \omega^0) \in \Omega$, we have $L \in \mathbb{S}_+^n$. If $D = 0$, the pair $(M^{-1}L, M^{-1}D)$ can never be observable. Using a similar argument as in the first part in the proof of Theorem 3, it can be shown that $M^{-1}L$ has a simple zero eigenvalue and the rest of its eigenvalues are positive, i.e., $\sigma(M^{-1}L) \subseteq \mathbb{R}_+ = \{\lambda \in \mathbb{R} : \lambda \geq 0\}$. Meanwhile, when $D = 0$, we have $\mu \in \sigma(J) \iff \mu^2 \in \sigma(-M^{-1}L)$. Notice that a power grid has at least two nodes, i.e. $n \geq 2$, and hence, $M^{-1}L$ has at least one positive eigenvalue, i.e., $\exists \lambda \in \mathbb{R}_+, \lambda > 0$ such that $\lambda \in \sigma(M^{-1}L)$. Hence, $\mu = \sqrt{-\lambda}$ is a purely imaginary number and is an eigenvalue of J . Similarly, we can show that $-\mu$ is an eigenvalue of J . Consequently, the theorem holds in the case of $D = 0$. In the sequel, we assume that $D \neq 0$.

Necessity: Assume there exists $\beta > 0$ such that $i\beta \in \sigma(J)$. We will show that the pair $(M^{-1}L, M^{-1}D)$ is not observable. By Lemma 1, $i\beta \in \sigma(J)$ if and only if the matrix pencil

$(M^{-1}L + \mathbf{i}\beta M^{-1}D - \beta^2 I)$ is singular:

$$\det \left(M^{-\frac{1}{2}} (M^{-\frac{1}{2}} L M^{-\frac{1}{2}} + \mathbf{i}\beta M^{-\frac{1}{2}} D M^{-\frac{1}{2}} - \beta^2 I) M^{\frac{1}{2}} \right) = 0,$$

or equivalently, $\exists(x + \mathbf{i}y) \neq 0$ such that $x, y \in \mathbb{R}^n$ and

$$\begin{aligned} & (M^{-\frac{1}{2}} L M^{-\frac{1}{2}} + \mathbf{i}\beta M^{-\frac{1}{2}} D M^{-\frac{1}{2}} - \beta^2 I)(x + \mathbf{i}y) = 0 \\ \iff & \begin{cases} (M^{-\frac{1}{2}} L M^{-\frac{1}{2}} - \beta^2 I)x - \beta M^{-\frac{1}{2}} D M^{-\frac{1}{2}} y = 0, \\ (M^{-\frac{1}{2}} L M^{-\frac{1}{2}} - \beta^2 I)y + \beta M^{-\frac{1}{2}} D M^{-\frac{1}{2}} x = 0. \end{cases} \end{aligned} \quad (2.27)$$

Let $\hat{L} := M^{-\frac{1}{2}} L M^{-\frac{1}{2}}$, $\hat{D} := M^{-\frac{1}{2}} D M^{-\frac{1}{2}}$, and observe that

$$\begin{cases} y^\top (\hat{L} - \beta^2 I)x = y^\top (\beta \hat{D} y) = \beta y^\top \hat{D} y \geq 0, \\ x^\top (\hat{L} - \beta^2 I)y = x^\top (-\beta \hat{D} x) = -\beta x^\top \hat{D} x \leq 0, \end{cases}$$

where we have used the fact that \hat{D} is *-congruent to D . According to Sylvester's law of inertia, \hat{D} and D have the same inertia. Since $D \succeq 0$, we conclude that $\hat{D} \succeq 0$. As $(\hat{L} - \beta^2 I)$ is symmetric, we have $x^\top (\hat{L} - \beta^2 I)y = y^\top (\hat{L} - \beta^2 I)x$. Therefore, we must have $x^\top \hat{D} x = y^\top \hat{D} y = 0$. Since $\hat{D} \succeq 0$, we can infer that $x \in \ker(\hat{D})$ and $y \in \ker(\hat{D})$. Now considering $\hat{D}y = 0$ and using the first equation in (2.27) we get

$$(\hat{L} - \beta^2 I)x = 0 \iff M^{-\frac{1}{2}} L M^{-\frac{1}{2}} x = \beta^2 x, \quad (2.28)$$

multiplying both sides from left by $M^{-\frac{1}{2}}$ we get $M^{-1}L(M^{-\frac{1}{2}}x) = \beta^2(M^{-\frac{1}{2}}x)$. Thus, $\hat{x} := M^{-\frac{1}{2}}x$ is an eigenvector of $M^{-1}L$. Moreover, we have

$$M^{-1}D\hat{x} = M^{-1}DM^{-\frac{1}{2}}x = M^{-\frac{1}{2}}(\hat{D}x) = 0,$$

which means that the pair $(M^{-1}L, M^{-1}D)$ is not observable.

Sufficiency: Suppose the pair $(M^{-1}L, M^{-1}D)$ is not observable. We will show that $\sigma(J)$ contains a pair of purely imaginary eigenvalues. According to Definition 1, $\exists \lambda \in \mathbb{C}, x \in \mathbb{C}^n, x \neq 0$ such that

$$M^{-1}Lx = \lambda x \text{ and } M^{-1}Dx = 0. \quad (2.29)$$

We make the following two observations. Firstly, as it is shown above, we have $\sigma(M^{-1}L) \subseteq \mathbb{R}_+$. Secondly, L has a simple zero eigenvalue and a one-dimensional nullspace spanned by $\mathbf{1} \in \mathbb{R}^n$. We want to emphasize that this zero eigenvalue of L cannot break the observability of the pair $(M^{-1}L, M^{-1}D)$. Note that $\ker(L) = \ker(M^{-1}L)$ and $M^{-1}L\mathbf{1} = 0$ implies that $M^{-1}D\mathbf{1} \neq 0$ because $D \neq 0$. Based on the foregoing two observations, when the pair $(M^{-1}L, M^{-1}D)$ is not observable, there must exist $\lambda \in \mathbb{R}_+, \lambda \neq 0$ and $x \in \mathbb{C}^n, x \neq 0$ such that (2.29) holds. Define $\xi = \sqrt{-\lambda}$, which is a purely imaginary number. The quadratic pencil $M^{-1}P(\xi) = \xi^2 I + \xi M^{-1}D + M^{-1}L$ is singular because $M^{-1}P(\xi)x = \xi^2 x + \xi M^{-1}Dx + M^{-1}Lx = -\lambda x + 0 + \lambda x = 0$. By Lemma 1, ξ is an eigenvalue of J . Similarly, we can show $-\xi$ is an eigenvalue of J . Therefore, $\sigma(J)$ contains the pair of purely imaginary eigenvalues $\pm \xi$. \square

The following remark illustrates how Theorem 7 can be used in practice to detect and damp oscillations in power systems.

Remark 4. Consider the assumptions of Theorem 7 and suppose there exists a pair of purely imaginary eigenvalues $\pm i\beta \in \sigma(J(\delta^0))$ which give rise to Hopf bifurcation and oscillatory behaviour of the system. This issue can be detected by observing the oscillations in power system state variables (through phasor measurement units (PMUs) [38]). According to Theorem 7, we conclude that $\beta^2 \in \sigma(M^{-1}\nabla P_e(\delta^0))$. Let $\mathcal{X} := \{x^1, \dots, x^k\}$ be a set of independent eigenvectors associated with the eigenvalue $\beta^2 \in \sigma(M^{-1}\nabla P_e(\delta^0))$, i.e., we assume that the corresponding eigenspace is k -dimensional. According to Theorem 7,

we have $M^{-1}Dx^\ell = 0, \forall x^\ell \in \mathcal{X}$, or equivalently, $Dx^\ell = 0, \forall x^\ell \in \mathcal{X}$. Since D is diagonal, we have $d_j x_j^\ell = 0, \forall j \in \{1, \dots, n\}, \forall x^\ell \in \mathcal{X}$. In order to remove the purely imaginary eigenvalues, we need to make sure that $\forall x^\ell \in \mathcal{X}, \exists j \in \{1, \dots, n\}$ such that $d_j x_j^\ell \neq 0$. This can be done for each $x^\ell \in \mathcal{X}$ by choosing a $j \in \{1, \dots, n\}$ such that $x_j^\ell \neq 0$ and then increase the corresponding damping d_j from zero to some positive number, thereby rendering the pair $(M^{-1}\nabla P_e(\delta^0), M^{-1}D)$ observable.

Theorem 7 gives a necessary and sufficient condition for the existence of purely imaginary eigenvalues in a lossless power system with *nonnegative* damping and positive inertia. It is instructive to compare it with an earlier result in [63], which shows that when all the generators in a lossless power system have *positive* damping d_j and positive inertia m_j , then any equilibrium point in the set Ω is asymptotically stable. This is also proved in Theorem 17 of Section A.2 for the general second-order model (2.1).

Recall that the simple zero eigenvalue of the Jacobian matrix $J(\delta^0)$ in model (2.21) stems from the translational invariance of the flow function defined in Definition 2. As mentioned earlier, we can eliminate this eigenvalue by choosing a reference bus and refer all other bus angles to it. According to Proposition 2, aside from the simple zero eigenvalue, the Jacobians of the original model (2.21) and the referenced model (2.24) have the same number of eigenvalues with zero real part. Hence, Theorem 7 provides a necessary and sufficient condition for breaking the hyperbolicity in the referenced lossless power system model (2.24).

In lossy power systems, matrix $\nabla P_e(\delta)$ may not be symmetric. In this case, Theorem 4 can be used for detecting purely imaginary eigenvalues. Meanwhile, let us discuss some noteworthy cases in more detail. Theorem 8 asserts that in small lossy power networks with only one undamped generator, the equilibrium points are always hyperbolic. The proof is provided in Section A.5.

Theorem 8. *Let $n \in \{2, 3\}$ and consider an n -generator system with only one undamped generator. Suppose $(\delta^0, \omega^0) \in \Omega$ holds, the underlying undirected power network graph is*

connected, and $\nabla P_e(\delta)$. Then the Jacobian matrix $J(\delta^0)$ has no purely imaginary eigenvalues. We allow the network to be lossy, but we assume $\partial P_{e_j}/\partial \delta_k = 0$ if and only if $\partial P_{e_k}/\partial \delta_j = 0$. The lossless case is a special case of this.

The following counterexample shows that as long as there are two undamped generators, the Jacobian $J(\delta)$ at an equilibrium point may have purely imaginary eigenvalues.

Proposition 3. For any $n \geq 2$, consider an $(n + 1)$ -generator system with 2 undamped generators and the following $(n + 1)$ -by- $(n + 1)$ matrices $L = \nabla P_e(\delta^0)$, D , and M :

$$L = \begin{bmatrix} 1 & -\frac{1}{n} & -\frac{1}{n} & \dots & -\frac{1}{n} \\ -\frac{1}{n} & 1 & -\frac{1}{n} & \dots & -\frac{1}{n} \\ \vdots & \vdots & \vdots & \ddots & \vdots \\ -\frac{1}{n} & -\frac{1}{n} & -\frac{1}{n} & \dots & 1 \end{bmatrix},$$

$$D = \mathbf{diag}([0, 0, d_3, d_4, \dots, d_{n+1}]), \quad M = I_{n+1}.$$

Then $\pm i\beta \in \sigma(J(\delta^0))$, where $\beta^2 = 1 + \frac{1}{n}$.

Proof. Let $\beta^2 = 1 + \frac{1}{n}$ and observe that $\mathbf{rank}(L - \beta^2 M) = 1$ and $\mathbf{rank}(\beta D) = (n + 1) - 2 = n - 1$. The rank-sum inequality [57] implies that

$$\mathbf{rank}(L - \beta^2 M - i\beta D) \leq \mathbf{rank}(L - \beta^2 M) + \mathbf{rank}(-i\beta D) = 1 + (n - 1) = n,$$

that is $\det(L + i\beta D - \beta^2 M) = 0$. Now according to Lemma 1, the latter is equivalent to $i\beta \in \sigma(J(\delta^0))$. This completes the proof. Also note that the constructed L is not totally unrealistic for a power system. \square

2.6 Numerical Results

Two case studies will be presented to illustrate breaking the hyperbolicity and the occurrence of Hopf bifurcation under damping variations. Additionally, we adopt the center

manifold theorem to determine the stability of bifurcated orbits. Note that using the center manifold theorem, a Hopf bifurcation in an n -generator network essentially reduces to a planar system provided that aside from the two purely imaginary eigenvalues no other eigenvalues have zero real part at the bifurcation point. Therefore, for the sake of better illustration we focus on small-scale networks.

2.6.1 Case 1

Consider a 3-generator system with $D = \text{diag}([\gamma, \gamma, 1.5])$, $M = I_3$, $Y_{12} = Y_{13} = 2Y_{23} = i$ p.u., $P_{m_1} = -\sqrt{3}$ p.u., and $P_{m_2} = P_{m_3} = \sqrt{3}/2$ p.u. The load flow problem for this system has the solution $V_j = 1$ p.u. $\forall j$ and $\delta_1 = 0$, $\delta_2 = \delta_3 = \pi/3$. Observe that when $\gamma = 0$, the pair $(M^{-1}\nabla P_e(\delta^0), M^{-1}D)$ is not observable, and Theorem 7 implies that the spectrum of the Jacobian matrix $\sigma(J)$ contains a pair of purely imaginary eigenvalues. Moreover, this system satisfies the assumptions of Proposition 3, and consequently, we have $\pm i\sqrt{1.5} \in \sigma(J)$. In order to eliminate the zero eigenvalue (to be able to use the Hopf bifurcation theorem), we adopt the associated referenced model using the procedure described in Section 2.5.3. The conditions (i)-(iv) of Theorem 5 are satisfied (specifically, the transversality condition (iii) holds because $\text{Im}(q^* M^{-1}D'(\gamma_0)v) = -0.5$), and accordingly, a periodic orbit bifurcates at this point. To determine the stability of bifurcated orbit, we compute the *first Lyapunov coefficient* $l_1(0)$ as described in [59]. If the first Lyapunov coefficient is negative, the bifurcating limit cycle is stable, and the bifurcation is supercritical. Otherwise it is unstable and the bifurcation is subcritical. In this example, we get $l_1(0) = -1.7 \times 10^{-3}$ confirming that the type of Hopf bifurcation is supercritical and a stable limit cycle is born. Figs. (2.1a)-(2.1c) depict these limit cycles when the parameter γ changes. Moreover, Fig. (2.1d) shows the oscillations observed in the voltage angles and frequencies when $\gamma = 0$.

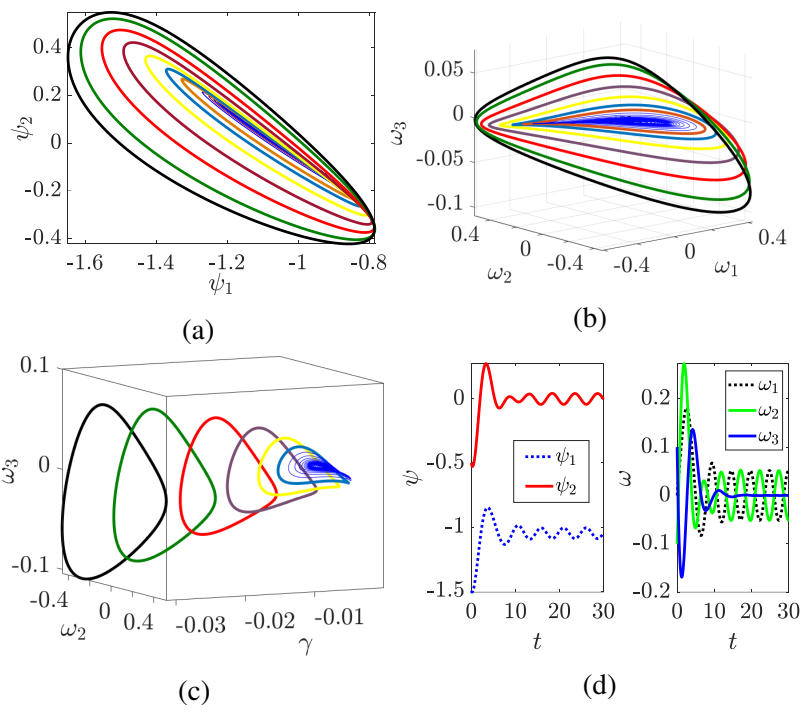


Figure 2.1: Occurrence of supercritical Hopf bifurcation in Case 1. (a)-(c) Projection of limit cycles into different subspaces as the parameter γ changes. (d) Oscillations of the voltage angles ψ in radians and the angular frequency deviation ω in radians per seconds when $\gamma = 0$. Note that $\psi_3 \equiv 0$.

2.6.2 Case 2

Next, we explore how damping variations could lead to a Hopf bifurcation in lossy systems. It is proved in Theorem 8 that a 2-generator system with only one undamped generator cannot experience a Hopf bifurcation. To complete the discussion, let us consider a fully-damped (i.e., all generators have nonzero damping) lossy 2-generator system here. Note also that the discussion about a fully-undamped case is irrelevant (see Lemma 6). Suppose $M = I_2$, $D = \text{diag}([\gamma, 1])$, $Y_{12} = -1 + i5.7978$ p.u., $P_{m_1} = 6.6991$ p.u., and $P_{m_2} = -4.8593$ p.u. The load flow problem for this system has the solution $V_j = 1$ p.u. $\forall j$ and $\delta_1 = 1.4905$, $\delta_2 = 0$. We observe that $\gamma = 0.2$ will break the hyperbolicity and lead to a Hopf bifurcation with the first Lyapunov coefficient $l_1(0.2) = 1.15$. This positive value for $l_1(0.2)$ confirms that the type of Hopf bifurcation is subcritical and an unstable limit cycle bifurcates for $\gamma \geq 0.2$. Therefore, the situation can be summarized as follows:

- If $\gamma < 0.2$, there exists one unstable equilibrium point.
- If $\gamma = 0.2$, a subcritical Hopf bifurcation takes place and a unique small unstable limit cycle is born.
- If $\gamma > 0.2$, there exists a stable equilibrium point surrounded by an unstable limit cycle.

Figs. (2.2a)-(2.2c) depict the bifurcating unstable limit cycles when the parameter γ changes in the interval $[0.2, 0.35]$. This case study sheds lights on an important fact: bifurcation can happen even in fully damped systems, provided that the damping matrix D reaches a critical point (say D_c). When $D \preceq D_c$, the equilibrium point is unstable. On the other hand, when $D \succ D_c$, the equilibrium point becomes stable but it is still surrounded by an unstable limit cycle. As we increase the damping parameter, the radius of the limit cycle increases, and this will enlarge the region of attraction of the equilibrium point. Note that the region of attraction of the equilibrium point is surrounded by the unstable limit

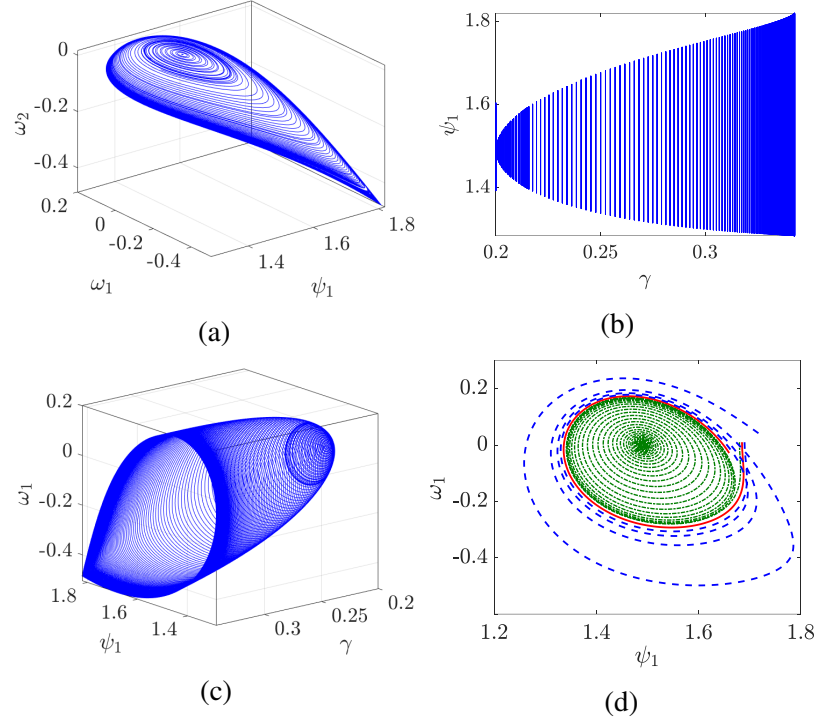


Figure 2.2: Occurrence of subcritical Hopf bifurcation in Case 2. (a) Unstable limit cycles as the parameter γ changes. (b)-(c) Projection of limit cycles into different subspaces as the parameter γ changes. (d) The region of attraction of the equilibrium point when $\gamma = 0.25$. The unstable limit cycle is shown in red, while the orbits inside and outside of it are shown in green and blue, respectively. Note that $\psi_2 \equiv 0$.

cycle. This also confirms the monotonic behaviour of damping proved in Theorem 2. Fig. (2.2d) shows the region of attraction surrounded by the unstable limit cycle (in red) when $\gamma = 0.25$. In this figure, the green orbits located inside the cycle are spiraling in towards the equilibrium point while the blue orbits located outside the limit cycle are spiraling out.

Although both supercritical and subcritical Hopf bifurcations lead to the birth of limit cycles, they have quite different practical consequences. The supercritical Hopf bifurcation which occurred Section 2.6.1 corresponds to a soft or noncatastrophic stability loss because a stable equilibrium point is replaced with a stable periodic orbit, and the system remains in a neighborhood of the equilibrium. In this case, the system operator can take appropriate measures to bring the system back to the stable equilibrium point. Conversely, the subcritical Hopf bifurcation in Section 2.6.2 comes with a sharp or catastrophic loss of stability.

This is because the region of attraction of the equilibrium point (which is bounded by the unstable limit cycle) shrinks as we decrease the parameter γ and disappears once we hit $\gamma = 0.2$. In this case, the system operator may not be able to bring the system back to the stable equilibrium point as the operating point may have left the region of attraction.

2.7 Final Remarks

In this chapter, we have presented a comprehensive study on the role of damping in a large class of dynamical systems, including electric power networks. Paying special attention to partially-damped systems, it is shown that damping plays a monotonic role in the hyperbolicity of the equilibrium points. We have proved that the hyperbolicity of the equilibrium points is intertwined with the observability of a pair of matrices, where the damping matrix is involved. We have also studied the aftermath of hyperbolicity collapse, and have shown both subcritical and supercritical Hopf bifurcations can occur as damping changes. It is shown that Hopf bifurcation cannot happen in small power systems with only one undamped generator. In the process, we have developed auxiliary results by proving some important spectral properties of the power system Jacobian matrix, establishing the relationship between a power system model and its referenced counterpart, and finally addressing a fundamental question from matrix perturbation theory. Among others, the numerical experiments have illustrated how damping can change the region of attraction of the equilibrium points. We believe our results are of general interest to the community of applied dynamical systems, and provide new insights into the interplay of damping and oscillation in one of the most important engineering system, the electric power systems.

CHAPTER 3

A STABILITY CERTIFICATE FOR KRON-REDUCED SWING EQUATIONS

In Chapter 2, we studied a large class of second-order differential equations. In this chapter, we study an important example of such second-order differential equations, namely swing equations. Swing equations are an integral part of a large class of power system dynamical models used in rotor angle stability assessment. Despite intensive studies, some fundamental properties of lossy swing equations are still not fully understood.

In this chapter, we develop a sufficient condition for certifying the stability of equilibrium points of these equations, and illustrate the effects of damping, inertia, and network topology on the stability properties of such equilibrium points. The proposed certificate is suitable for real-time monitoring and fast stability assessment, as it is purely algebraic and can be evaluated in a parallel manner. Moreover, we provide a novel approach to quantitatively measure the degree of stability in power grids using the proposed certificate. Extensive computational experiments are conducted, demonstrating the practicality and effectiveness of the proposal.

3.1 Introduction

Power system stability has been an important topic in power engineering for many years. There has been continuing advancement in the understanding of the stability issues of the system. In the recent decade, the proliferation of renewable energy resources has added new dimensions to the problem. The uncertainty and volatility of these resources have brought about significant stochastic transitions from one operating point to another [64], thereby making the system more prone to instability.

Owing to the complexity and high dimensionality of power systems, several CIGRE and IEEE Task Forces have classified power system stability into appropriate categories

with the aim of facilitating the assessment of the problem [65]. In each category, a set of simplifying assumptions are made and an appropriate system model with a reasonable level of details is adopted. One of the most fundamental models used in several categories of stability (especially rotor angle stability) is the swing equation model. This model describes the nonlinear relation between the power output and voltage angles of synchronous generators and can be used to analyze the short term dynamical behaviour of the system.

The application of swing equations is not restricted to the characterization of interconnected synchronous machines. They can also be used to model the behavior of inverter-based resources, which can be controlled to emulate the behavior of synchronous machines [9]. Despite such a wide range of applications, some basic questions on the equilibrium points of swing equations are not fully understood. In particular,

- (i) Under what conditions an equilibrium point of swing equations with nontrivial transfer conductance is asymptotically stable?
- (ii) What is the relation between the network structure of a power system and the stability of the equilibrium points of swing equations?

Such challenging questions have perplexed many researchers over the years. In the next section, we review the parts of the puzzle which have been solved.

3.1.1 Related Work

In [54], the authors extend the lossy swing equation model by considering the dynamics of the excitation system, and ensure the asymptotic stability of the operating points by designing a nonlinear feedback control for the generator excitation field. In [58], the local stability of swing equations with nontrivial transfer conductance is examined by linearization and conditions for stability of equilibrium points are established. It is found that undamped swing equations can be stable only under very special circumstances. Another set of literature that address similar questions are the recent studies of the synchronization

of Kuramoto oscillators that are applicable to the stability analysis of lossy swing equations with strongly overdamped generators [66]. Furthermore, exploring question (ii), the recent work [67] statistically studies the impact of topology of the network on transient stability.

3.1.2 Main Results

In this chapter, we aim to address questions (i) and (ii), and provide a rigorous analysis of the stability of equilibrium points in lossy swing equation models. There are two main contributions in the present chapter.

- We characterize the relationship between the Jacobian of swing equations and the underlying graph of power grids. Specifically, we associate a weighted graph with the swing equation model and then mathematically describe the relationship between the spectrum of the graph Laplacian and the spectrum of the swing equation Jacobian.
- We develop a sufficient condition under which the equilibrium points of lossy swing equations are stable. In addition to providing new insights into the theory of stability, the derived conditions are easy to check, use only local information, and are suitable for real-time monitoring and fast stability assessment. The proposed stability certificate can be interpreted as enforcing an upper bound on the matrix norm of the Laplacian of the underlying graph of the system. We show that the aforementioned upper bound is proportional to the square of damping and inverse of inertia at each node of the power grid. These results provide new insights into the way the damping and inertia at each node of the system would affect the stability of equilibrium points. We also illustrate how the proposed condition provides a quantitative measure of the degree of stability in power systems.

3.1.3 Chapter Outline

The rest of this chapter is organized as follows. Section 3.2 provides a brief background on autonomous ordinary differential equations as well as swing equations. In Section 3.3,

the swing equation model is linearized and the linkage between the Jacobian of swing equations and the underlying graph of the power grid is established. Section 3.4 is devoted to the main results on the stability of the swing equation equilibrium points. Section 3.5 further illustrates the developed analytical results through numerical examples, and finally, the chapter concludes with Section 3.6.

3.2 Background

3.2.1 Autonomous Ordinary Differential Equations

Suppose $f : \mathbb{R}^n \rightarrow \mathbb{R}^n$ is a smooth vector field, where the term smooth here means continuously differentiable. An autonomous ODE is an equation of the form

$$\dot{x} = f(x), \tag{3.1}$$

where the dot denotes differentiation with respect to the independent variable t (here a measure of time), and the dependent variable x is a vector of state variables.

Definition 3 (equilibrium point). *Consider ODE (3.1). If $f(x_0) = 0$ for some $x_0 \in \mathbb{R}^n$, then x_0 is called an equilibrium point.*

Let us define the function $\phi : \mathbb{R} \times \mathbb{R}^n \rightarrow \mathbb{R}^n$ as follows: for any $x \in \mathbb{R}^n$, let $t \mapsto \phi(t, x)$ be the solution of the ODE (3.1), that is, $\frac{d\phi}{dt}(t, x) = f(\phi(t, x))$, $\forall t \in \mathbb{R}$. Moreover, $\phi(0, x) = x$. The smoothness of the vector field f is a sufficient condition for existence and uniqueness of solution.

Definition 4 (stability). *An equilibrium point x_0 of the ODE (3.1) is*

- *stable (in the sense of Lyapunov) if for each $\epsilon > 0$, there exists a number $\xi > 0$ such that $\|\phi(t, x) - x_0\| < \epsilon$, $\forall t \geq 0$ whenever $\|x - x_0\| < \xi$;*
- *unstable if it not stable;*

- asymptotically stable if it is stable and ξ can be chosen such that $\lim_{t \rightarrow \infty} \|\phi(t, x) - x_0\| = 0$ whenever $\|x - x_0\| < \xi$.

Note that the above definitions of stability are not restricted to equilibrium points. They can also refer to arbitrary solutions of the ODE. See [68, p. 22] for details on different types of stability and their definitions.

Definition 5 (hyperbolicity). *If x_0 is an equilibrium point of ODE (3.1) and if the Jacobian $\nabla f(x_0)$ has all its eigenvalues not on the imaginary axis, then we say that x_0 is a hyperbolic equilibrium point.*

Hyperbolicity plays a central role in dynamical system analysis, as it enables us to understand the nonlinear dynamics of (3.1) through its linearized counterpart

$$\dot{x} = \nabla f(x_0)(x - x_0). \quad (3.2)$$

In particular, the local dynamics at a hyperbolic equilibrium point of (3.1) is topologically conjugate to the dynamics of the linear system (3.2) by the Hartman–Grobman theorem [68].

Theorem 9 (Hartman–Grobman). *If x_0 is a hyperbolic equilibrium point for the ODE (3.1), then there is an open set \mathcal{U} containing x_0 and a homeomorphism \mathcal{H} with domain \mathcal{U} such that the orbits of the differential equation (3.1) are mapped by \mathcal{H} to orbits of the linearized system (3.2) in the set \mathcal{U} .*

An interesting feature of hyperbolic equilibrium points is that they are either unstable or asymptotically stable. Moreover, if x_0 is an equilibrium point for the ODE (3.1) and if all eigenvalues of the linear transformation $\nabla f(x_0)$ have negative real parts, then x_0 is asymptotically stable. An interested reader is referred to [68] for a more comprehensive study of ODE and dynamical systems.

3.2.2 Multi-Machine Swing Equations

Consider a power system with the set of generators $\mathcal{N} = \{1, \dots, n\}$, $n \in \mathbb{N}$. As mentioned in Section 2.5.1, the mathematical model for a power system is described by the following system of nonlinear autonomous ODEs, aka swing equations:

$$\dot{\delta}_i(t) = \omega_i(t), \quad \forall i \in \mathcal{N}, \quad (3.3a)$$

$$\frac{m_i}{\omega_s} \dot{\omega}_i(t) + \frac{d_i}{\omega_s} \omega_i(t) = P_{m_i} - P_{e_i}(\delta(t)), \quad \forall i \in \mathcal{N}, \quad (3.3b)$$

where for each generator $i \in \mathcal{N}$, P_{m_i} and P_{e_i} are respectively the mechanical and electrical power in per unit, m_i is the inertia constant in seconds, d_i is the unitless damping coefficient, ω_s is the synchronous angular velocity in electrical radians per seconds, t is the time in seconds, $\delta_i(t)$ is the rotor electrical angle in radians, and finally $\omega_i(t)$ is the deviation of the rotor angular velocity from the synchronous velocity in electrical radians per seconds. Henceforth we do not explicitly write the dependence of the state variables δ and ω on time t . The electrical power P_{e_i} in (3.3b) is given by:

$$P_{e_i}(\delta) = \sum_{j=1}^n V_i V_j Y_{ij} \cos(\theta_{ij} - \delta_i + \delta_j), \quad (3.4)$$

where V_i is the terminal voltage magnitude of generator i , and $Y_{ij} \angle \theta_{ij}$ is the (i, j) entry of the reduced admittance matrix.

Recall from Definition 2 in Section 2.5.1 that the function $P_e : \mathbb{R}^n \rightarrow \mathbb{R}^n$ given by $\delta \mapsto P_e(\delta)$ in (3.4) is called the flow function. Recall also that we addressed the translational invariance of the flow function in Section 2.5.3.

3.3 Linearization and Spectrum of Jacobian

3.3.1 Linearization

The Jacobian of the vector field in (3.3) is given by

$$J := \begin{bmatrix} 0 & I \\ -M^{-1}L & -M^{-1}D \end{bmatrix} \in \mathbb{R}^{2n \times 2n}, \quad (3.5)$$

where $I \in \mathbb{R}^{n \times n}$ is the identity matrix, $M = \frac{1}{\omega_s} \mathbf{diag}(m_1, \dots, m_n)$, and $D = \frac{1}{\omega_s} \mathbf{diag}(d_1, \dots, d_n)$.

Moreover, $L \in \mathbb{R}^{n \times n}$ is the Jacobian of the flow function with the diagonal entries:

$$L_{ii} = \frac{\partial P_{e_i}}{\partial \delta_i} = \sum_{j \neq i} V_i V_j Y_{ij} \sin(\theta_{ij} - \delta_i + \delta_j), \forall i \in \mathcal{N},$$

and off-diagonal entries

$$L_{ij} = \frac{\partial P_{e_i}}{\partial \delta_j} = -V_i V_j Y_{ij} \sin(\theta_{ij} - \delta_i + \delta_j), \forall i, j \in \mathcal{N}, j \neq i.$$

Recall that Lemma 1 illustrated the spectral relationship between J and L via a singularity constraint. Hence, matrix L plays an important role in the stability of equilibrium points. Next, we look more closely at the spectrum of L .

3.3.2 Graph Induced by L and Its Spectral Properties

The Jacobian L of the flow function encodes the graph structure of the power network. To see this, we can define a weighted directed graph $\mathcal{G} = (\mathcal{N}, \mathcal{A}, \mathcal{W})$ where each node $i \in \mathcal{N}$ corresponds to a generator and each directed arc $(i, j) \in \mathcal{A}$ corresponds to the entry (i, j) , $i \neq j$ of the Jacobian matrix L . We further define a weight for each arc $(i, j) \in \mathcal{A}$:

$$w_{ij} = V_i V_j Y_{ij} \sin(\varphi_{ij}), \quad \forall (i, j) \in \mathcal{A}, \quad (3.6)$$

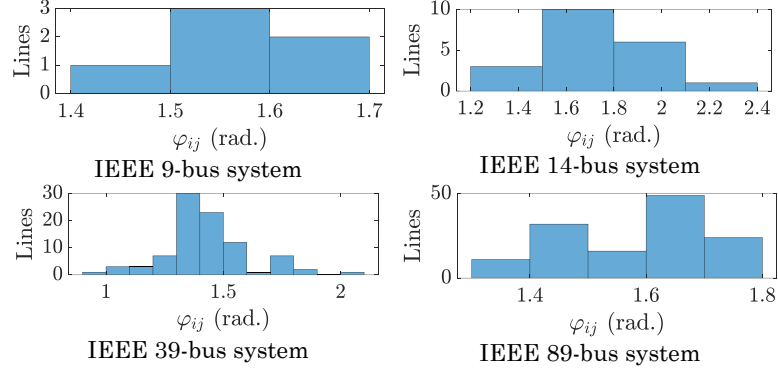


Figure 3.1: Histogram of the distribution of φ_{ij} for all (i, j) in different reduced IEEE standard test cases.

where $\varphi_{ij} := \theta_{ij} - \delta_i + \delta_j$. With the above definitions, we can see that the Jacobian matrix L of the flow function in (3.5) is indeed the Laplacian of the directed graph \mathcal{G} defined as $L = D^+(\mathcal{G}) - A(\mathcal{G})$, where $D^+(\mathcal{G})$ is a diagonal matrix with the i -th diagonal entry being the sum of all the weights of the out-going arcs incident to node i , and $A(\mathcal{G})$ is the adjacency matrix of \mathcal{G} . Later, in Section 5.3.3, we will discuss the digraph induced by L in more details.

In general, the arc weights w_{ij} can be positive or negative, and matrix L is not necessarily symmetric. In practice, however, w_{ij} varies in a small positive range. Fig. 3.1 illustrates the histogram of the angle φ_{ij} for all (i, j) in different reduced IEEE standard test cases, where the load flow solution is provided by MATPOWER [69]. Accordingly, $\varphi_{ij} \in (0, \pi)$ in all of these cases. We make the following reasonable assumption that the equilibrium points of swing equations (3.3) are located in the set Ω defined as

$$\Omega = \{(\delta, \omega) \in \mathbb{R}^{2n} : 0 < \varphi_{ij} < \pi, \forall (i, j) \in \mathcal{A}, \omega = 0\}.$$

Proposition 4. *Let $(\delta^*, \omega^*) \in \Omega$ be an equilibrium point of swing equations (3.3). The Jacobian matrix L at this point is a singular M-matrix. In particular, L has the following properties:*

- (i) $L = \lambda_0 I - B$ for some nonnegative matrix B (i.e., $b_{ij} \geq 0, \forall i, j$) and some $\lambda_0 \geq \rho$,

where ρ is a maximal (non-negative) eigenvalue of B .

(ii) All principal minors of L are non-negative.

(iii) L has at least one zero eigenvalue, $\mathbf{1}$ is an eigenvector, and the real part of each non-zero eigenvalue of L is positive.

Proof. When $(\delta^*, \omega^*) \in \Omega$, we have $\frac{\partial P_{e_i}}{\partial \delta_i} \geq 0, \forall i \in \mathcal{N}$ and $\frac{\partial P_{e_i}}{\partial \delta_j} \leq 0, \forall (i, j) \in \mathcal{A}, i \neq j$. Since L has zero row sum, we have $L\mathbf{1} = 0 \implies 0 \in \sigma(L)$. Furthermore, the sum of the absolute values of the nondiagonal entries in the i -th row of L is equal to L_{ii} , that is

$$L_{ii} = \sum_{j \neq i} |L_{ij}| \quad \forall i \in \mathcal{N}. \quad (3.7)$$

Let $\mathbb{D}(L_{ii})$ be a closed disc centered at L_{ii} with radius L_{ii} . According to the Gershgorin circle theorem, every eigenvalue of L lies within at least one of the Gershgorin discs $\mathbb{D}(L_{ii})$, which are located on the right half plane. This shows (iii). The equivalence of (iii) with (i) and (ii) is a fundamental property of M-matrices [62]. \square

We will use property (iii) of matrix L shown in the above proposition later to prove our main result in the next section.

3.4 Sufficient Condition for the Stability of Swing Equations: A Fast Certificate

In this section, we present our main result on the stability of the swing equation equilibrium points.

Theorem 10. *Let $(\delta^*, \omega^*) \in \Omega$ be an equilibrium point of swing equations (3.3). Suppose all generators have positive damping coefficient and inertia, and the underlying undirected graph of the power grid is connected. If condition*

$$\sum_{j \neq i} V_i V_j Y_{ij} \sin(\theta_{ij} - \delta_i^* + \delta_j^*) \leq \frac{d_i^2}{2m_i}, \forall i \in \mathcal{N} \quad (3.8)$$

holds, then the equilibrium point is asymptotically stable.

The proof of Theorem 10 is given in Appendix B.1.

Remark 5. Condition (3.8) provides a practical and efficient way to certify the small-signal stability of the equilibrium points. The left-hand side of condition (3.8) is closely related to the reactive power output of a generator. Note that at an equilibrium point the reactive power injected from bus i into the network is $Q_i = -\sum_{j=1}^n V_i V_j Y_{ij} \sin(\theta_{ij} - \delta_i^* + \delta_j^*)$. Intuitively, when a generator is supplying more reactive power, the left-hand side of condition (3.8) decreases, and this helps make condition (3.8) satisfied. This interpretation will be further discussed in Chapter 5.

It is worth mentioning that in [70], small-signal stability of lossless swing equations is studied. It is shown that if $(\delta^*, \omega^*) \in \Omega$ is an equilibrium point, then the equilibrium point is locally asymptotically stable. Theorem 10 is a generalization of such results to lossy swing equations. Contrary to the lossless case, we will show in the next section that an equilibrium point in lossy networks could be unstable even if it belongs to the set Ω .

3.5 Numerical Results

In this section, we test the practicality of the assumptions on which Theorem 10 is based. We also show how conservative condition (3.8) is, and how it can be used not only as a fast stability certificate, but also as a quantitative measure of the degree of stability.

Table 3.1 provides the details of testing Theorem 10 and condition (3.8) on different IEEE standard test systems [69]. All these systems have a connected underlying graph and nonzero transfer conductances. The second column of Table 3.1 shows the domain of φ_{ij} in these test cases. Recall that $\varphi_{ij} = \theta_{ij} - \delta_i + \delta_j$ is the argument of the sin function, and having $\varphi_{ij} \in (0, \pi)$ ensures that an equilibrium point (δ^*, ω^*) belongs to the set Ω . As can be seen, this property holds in all test cases of Table 3.1, and therefore, the assumptions of Theorem 10 hold in a wide variety of practical power systems.

Table 3.1: Illustration of the proposed stability certificate in Theorem 10

Test case	$\text{Dom}(\varphi_{ij}/\pi)$	$\text{Dom}(\mathcal{S}_i)$	$ \Re(\lambda_2) $
IEEE 9-bus	[0.48, 0.52]	[- 0.79, -0.22]	3.18
IEEE 14-bus	[0.43, 0.66]	[- 5.08, -0.03]	2.17
IEEE 30-bus	[0.36, 0.66]	[- 12.26, -0.51]	0.75
IEEE 39-bus	[0.37, 0.62]	[- 7.73, -0.12]	4.95
IEEE 89-bus	[0.45, 0.59]	[- 143.75, 1166.9]	4.15
IEEE 89-bus mod.	[0.25, 0.97]	[- 280.19, -0.49]	4.14
IEEE 118-bus	[0.42, 0.63]	[- 241.73, -0.21]	0.11
IEEE 300-bus	[0.30, 0.72]	[- 266.99, -3.04]	0.15

Next, let us define

$$\mathcal{S}_i := \sum_{j \neq i} V_i V_j Y_{ij} \sin(\theta_{ij} - \delta_i^* + \delta_j^*) - \frac{d_i^2}{2m_i},$$

and recall that according to condition (3.8) in Theorem 10, if $\mathcal{S}_i \leq 0, \forall i \in \mathcal{N}$, then the equilibrium point of swing equations is asymptotically stable. The third column of Table 3.1 provides the domain of \mathcal{S}_i , i.e., $[\min_i \mathcal{S}_i, \max_i \mathcal{S}_i]$. Accordingly, $\mathcal{S}_i \leq 0$ holds for all test cases, except the IEEE 89-bus system. Note that the corresponding equilibrium points in these systems are all stable. While the evaluation of condition (3.8) confirms the stability of equilibrium points in all other cases, it gives an inconclusive answer in the IEEE 89-bus case. However, here we show how condition (3.8) can be used as a quantitative measure of the degree of stability. The positive values of \mathcal{S}_i in the IEEE 89-bus system pertain to the bus numbers 6233, 6798, 7960, and 9239, indicating that the stability of the system can be improved by making \mathcal{S}_i negative in these buses via appropriate corrective actions. Exploring the structure of the system reveals that each of these buses is connected to the rest of the grid through a line with a relatively small resistance. As a corrective action, we change these resistances as follows: $r(659, 9239) = 6 \times 10^{-5} \rightarrow 0.5 \times 10^{-3}$, $r(659, 7960) = 6 \times 10^{-5} \rightarrow 1 \times 10^{-3}$, $r(659, 6233) = 6 \times 10^{-5} \rightarrow 2 \times 10^{-3}$, and $r(659, 6798) = 7 \times 10^{-5} \rightarrow 1.5 \times 10^{-3}$, where all the values are in p.u. With this corrective action (which can be implemented through flexible AC transmission system (FACTS) devices), we will

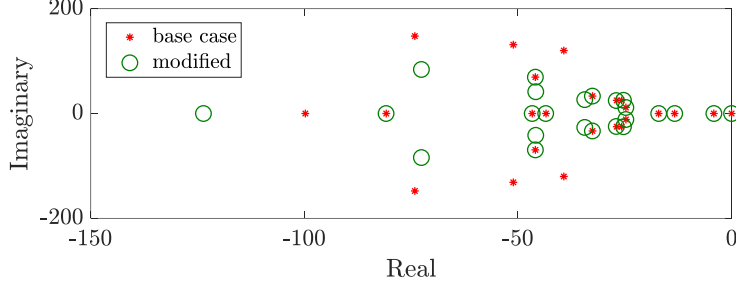


Figure 3.2: Spectrum of J in the IEEE 89-bus system.

Table 3.2: Dynamic parameters and converged load flow data of the 3-bus test system.

i	m_i [sec.]	d_i	P_{m_i} [p.u.]	V_i [p.u.]	δ_i^* [rad]	\mathcal{S}_i
1	6.1	1.5	0.89	0.9	-0.30	6.98
2	10	1	15.06	0.9	0.36	12.73
3	4.5	1.8	2.53	0.913	-0.12	8.91

have $\mathcal{S}_i \leq 0, \forall i \in \mathcal{N}$ and condition (3.8) will hold true, certifying the stability of the system (see the test case IEEE 89-bus mod. in Table 3.1). Fig. 3.2 depicts the spectrum of J in the IEEE 89-bus system before and after implementing the corrective actions. As can be seen, the magnitude of the imaginary parts of the eigenvalues in $\sigma(J)$ is reduced, and their real parts are mainly moved towards $-\infty$, thereby making the modified system less oscillatory. Evidently, condition (3.8) increased the stability margins of the system. Finally, $\lambda_2 \in \sigma(J)$ denotes the closest nonzero eigenvalue of J to the imaginary axis, and the fourth column of Table 3.1 depicts this value in different cases. Note that the proposed stability certificate can be fully parallelized, thereby making it even more reliable and resilient for real-time applications.

Next, we provide an example of an unstable equilibrium point and show how enforcing condition (3.8) will make the equilibrium point stable. Consider the 3-bus system in Fig. 3.3 whose dynamic parameters and converged load flow data are provided in Table 3.2. As can be observed from the last column of Table 3.2, we have $\mathcal{S}_i \geq 0, \forall i \in \mathcal{N}$, i.e., condition (3.8) is violated in all buses of this system, indicating that the system does not have sufficient stability margins. The instability of this equilibrium point can be verified through eigenvalue analysis and time domain simulation, as depicted in Fig. 3.4. In order to achieve

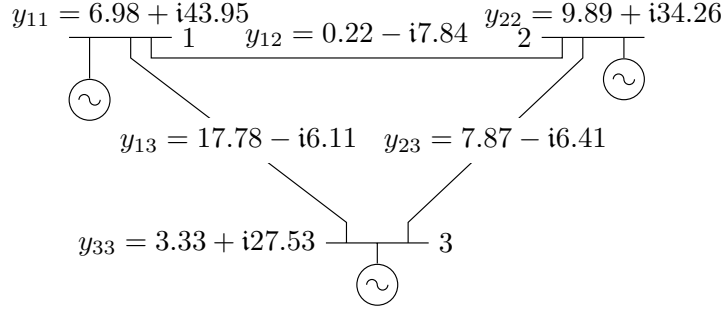


Figure 3.3: Schematic diagram of the 3-bus test system.

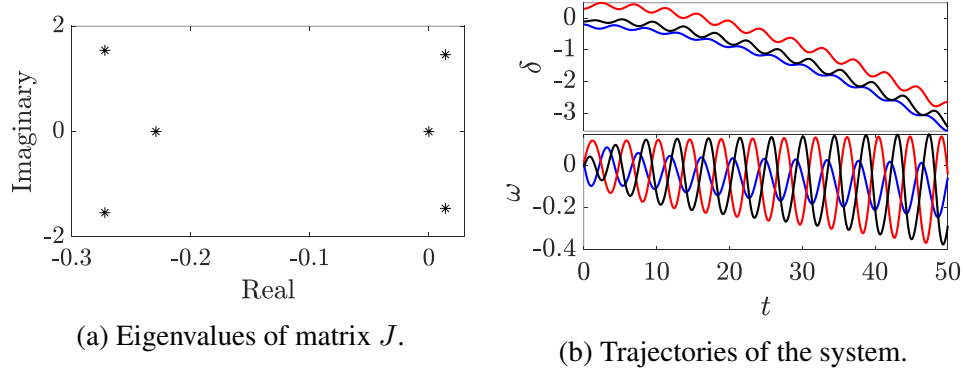


Figure 3.4: Instability of the equilibrium point in the 3-bus test system. (a) There exist two eigenvalues with positive real part. (b) Starting from a neighborhood of the equilibrium point, the trajectories become unbounded.

stability, the power system operator can enforce condition (3.8) either by moving the current equilibrium point to a new point (e.g., through adding constraint (3.8) to the optimal power flow problem) or by making the current equilibrium point stable through adjusting the right-hand side of condition (3.8). Particularly, the latter is possible if we have inverter-based resources where the inertia m_i and damping d_i are adjustable parameters of their controllers. In this case, by setting $M = \mathbf{diag}(0.9, 0.9, 0.9)$ and $D = \mathbf{diag}(4.5, 4.9, 4.8)$, we would have $\mathcal{S}_1 = -4.08$, $\mathcal{S}_2 = -0.55$, and $\mathcal{S}_3 = -3.52$, thereby certifying the stability of the system.

We conclude our numerical experiments by further illustrating the effect of condition (3.8) on the spectrum of matrix J . We have varied the operating point and parameters (inertia and damping) of the IEEE 9-bus system, and for each operating point or parameter value we have recorded λ_2 as well as $\min_i \mathcal{S}_i$. Fig. 3.5 shows the relationship between λ_2

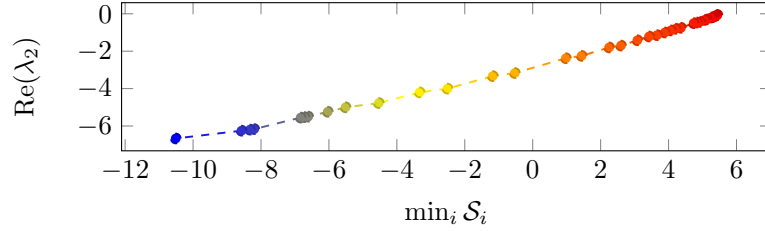


Figure 3.5: Real part of the closest nonzero eigenvalue of J to the imaginary axis as a function of $\min_i \mathcal{S}_i$ in the IEEE 9-bus system.

and $\min_i \mathcal{S}_i$ as the system operating point and parameters change. Accordingly, a smaller $\min_i \mathcal{S}_i$ yields a farther λ_2 from the imaginary axis.

3.6 Final Remarks

This chapter is aimed at finding a computationally efficient way to certify the stability of power system equilibrium points. We have shown if the matrix norm of the Laplacian of the underlying graph is upper bounded by a specific value, then the equilibrium point is stable. The aforementioned upper bound is proportional to the square of damping and inverse of inertia at each node of the power grid. This fact also sheds light on the interplay of inertia, damping, and graph of the system, and provides profound insights into how power system should be designed and operated to be stable. A worthwhile direction for future research would be extending condition (3.8) as a function of network connectivity measure.

CHAPTER 4

A STABILITY CERTIFICATE FOR STRUCTURE-PRESERVING SWING EQUATIONS

In Chapter 3, we studied the stability of equilibrium points of swing equations in Kron-reduced networks. During the Kron reduction process, loads are considered constant impedances and reflected into the nodal admittance matrix which will be further reduced to a smaller matrix representing a reduced network of generator buses. The procedure of network reduction for eliminating the load buses will close our eyes on the relations between the structure of the underlying physical network and the stability properties of the system.

In 1981, Bergen and Hill introduced their well-known structure-preserving model [28] for the swing equation. The main assumption of this model is to use a frequency-dependent model for loads. In this chapter, we base our stability analyses upon this structure-preserving model. This model leads to more realistic analyses, and since its introduction, many researchers have based their investigations upon it. Specifically, we develop a stability certificate for structure-preserving swing equations. To develop the certificate, we use singular perturbation techniques and Tikhonov's theorem [29], and in the process, we establish the relationship between the structure-preserving model and its singular perturbation counterpart.

Moreover, we propose a fully distributed control scheme which uses only local measurements and its computational cost does not increase with the size of the system. The validity of our findings and the effectiveness of the control scheme are numerically illustrated on the WSCC system. Later, in Section 5.4.3, we will revisit the stability of structure-preserving models from a graph-theoretic perspective.

4.1 Introduction

The rapid growth of renewable energy sources, open access transmission, intensifying competition in electricity markets, and aging transmission infrastructure are reshaping the operation of power systems in new ways that raise unprecedented challenges to the stability of the power grid. Mitigating power system instability would be a real challenge for power system operators. The advent of wide area measurement system could pave the way for improving the situational awareness of system operators and set the stage for new ways of stability assessment in power systems. Nonetheless, there is an urgent need for developing novel methods that combine the classical model-based approaches with the new measurement-based ones in order to achieve faster stability monitoring and assessment. This chapter is motivated by this urgent need and aims to develop a fully distributed control scheme for the small-signal stability of the structure-preserving swing equation model of power systems.

4.1.1 Related Work

Broadly speaking, the vast literature on power system stability can be classified based on two modeling assumptions. The first and the more classical one assumes the stability model under study is fully known, whereas the second stream of research is model-free and adopts synchronized wide-area measurements in order to monitor and address the stability problem [71], [72]. In this measurement-based approach, the underlying model of the system is not necessarily known. Our work in the present chapter is an attempt to combine the measurement-based and model-based approaches with the aim of achieving faster stability assessment.

Considering the model-based approach, the classical model for rotor angle stability analysis is the swing equation [17]. This model is based on representing loads as constant impedances, and then incorporating load impedances into the nodal admittance matrix for

a reduced network with only generator buses. Much effort has been devoted to understanding the stability properties of this network-reduced model, e.g. studying its small-signal stability [17], hyperbolicity and bifurcation [73], phase portrait [3], constructing energy functions and Lyapunov functions [74], and using direct methods [4].

Among the various simplifying assumptions applied to the swing equation [1], ignoring the transfer conductance of the transmission lines and load dynamics are the most unrealistic ones. In 1981, Bergen and Hill introduced their well-known structure-preserving model [28] for the swing equation. The main assumption of this model is to use a frequency-dependent model for loads. In the present chapter, we base our stability analyses upon this structure-preserving model. The structure-preserving model leads to more realistic analyses, and since its introduction, many researchers have based their investigations upon it. For instance, in [75], Dorfler *et al.* show that locally near the synchronization manifold, the phase and frequency dynamics of the Bergen and Hill network-preserving model are topologically conjugate to the phase dynamics of a nonuniform Kuramoto model together with decoupled and stable frequency dynamics. In [76], the transient stability problem in a structure-preserving model is addressed using the quadratic Lyapunov functions approach.

The use of a network-preserving model enables us to study the impact of network topology and system parameters on the system stability. In this regard, a related study is [37], where the classical network-reduced swing equation model is used to examine how the network topology (i.e., the reduced fictitious network) will affect the system transfer function.

In this chapter, we tackle the small-signal stability problem in network-preserving models. Recall that *small-signal stability* concerns with the ability of a power system to maintain generator phase synchronism under small disturbances [65]. There is a large body of work on the model-based small-signal stability assessment [77, 78, 79, 80, 58]. For instance, [77] proposes a method to damp inter-area oscillations using system loads, and [78] examines the role of wind turbine integration in these inter-area oscillations. In [80], small-signal stability of power systems is investigated based on matrix pencils and the

generalized eigenvalue problem. The paper compares different formulations and the state-of-the-art solvers. Finally, in [58] it is shown that unstable equilibrium solutions for swing equations may exist even though the rotor angles are less than $\pi/2$ out of phase.

4.1.2 Main Results

In this chapter, we combine the measurement-based and model-based approaches to develop a condition that certifies the small-signal stability of a structure-preserving swing equation model. The proposed certificate is a practical alternative to the eigenvalue computation-based methods, which can be quite computationally cumbersome for large-scale systems. We also introduce a control scheme for improving the system small-signal stability.

The proposed control and assessment schemes can be implemented in a completely distributed fashion and do not require any information exchange between the neighboring generators and areas. This property makes them particularly suitable for fast assessment in large-scale power systems and when proprietary information from neighboring areas or power plants cannot be shared.

In the process, we investigate the impact of network topology and system parameters (generator's inertia and damping) on the stability of the system. We introduce a stability index which provides a quantitative measure of the degree of stability.

We make use of singular perturbation techniques to establish the relationship between a structure-preserving model and its singular perturbation counterpart. Specifically, we show (under specific conditions) the stability properties of the structure-preserving model are the same as those of its singular perturbation counterpart. Therefore, the singular perturbation counterpart can be used for small-signal analysis instead of the the structure-preserving model, and this will facilitate our analysis.

4.1.3 Chapter Outline

The rest of this chapter is organized as follows. Section 4.2 introduces the structure-preserving model as well as its singular perturbation counterpart. The main results of this chapter are presented in Section 4.3. Section 4.4 further exhibits the validity and conservativeness of the proposed stability certificate. Finally, the chapter concludes with Section 4.5.

4.2 Structure-Preserving and Singular Perturbation Power System Models

The classical swing equation model discussed in Section 2.5.1 is based on a set of simplifying assumptions (see [1] for the details of the assumptions) out of which ignoring the transfer conductances is the most unrealistic one. This issue stems from the fact that the loads are considered constant impedances and reflected into the nodal admittance matrix which will be further reduced to a smaller matrix representing a reduced network of generator buses. Ignoring the real part of this reduced admittance matrix seems, therefore, unreasonable since this real part is not only representing the resistive part of the transmission lines, but also the active power consumption of the system. Aside from this, the procedure of network reduction for eliminating the load buses will close our eyes on the relations between the structure of the underlying network and the stability properties of the system. With these in mind, the small-signal stability analysis in this chapter is based on the standard structure-preserving model [28]. This model incorporates the nonlinear swing equation dynamics of generators as well as the frequency-dependent dynamics of loads. The model also preserves the original network topology (rather than undergoing the usual Kron reduction). We will exploit this preservation of topology later to analyze the effect of network topology on the stability of the system.

4.2.1 Structure-Preserving Model

Since generators are connected to the network through transient reactances, it is convenient to introduce fictitious buses representing the internal generator voltages, and further consider the transient reactances to be a transmission line. In the sequel, we assume that this transformation has been done, and therefore, the buses of the network can be categorized into generator buses (internal generator buses) and load buses. Moreover, with this transformation, no load is connected to generator buses and vice versa.

Consider an n -bus power system for some $n \in \mathbb{N}$ with the set of transmission lines \mathcal{E} . Let $\mathcal{G} = \{1, \dots, n_0\}$ be the set of generator buses, and $\mathcal{L} = \{n_0 + 1, \dots, n\}$ be the set of load buses. Based on the classical small-signal stability assumptions [28], the structure-preserving model of this power system is

$$m_i \ddot{\delta}_i + d_i \dot{\delta}_i = P_{m_i} - P_{e_i} \quad \forall i \in \mathcal{G}, \quad (4.1a)$$

$$d_i \dot{\delta}_i = -P_{d_i} - P_{e_i} \quad \forall i \in \mathcal{L}, \quad (4.1b)$$

where (4.1a) and (4.1b) characterize the the dynamics of generator buses and load buses, respectively. In these equations, δ_i is the bus voltage angle in radians. For each generator bus $i \in \mathcal{G}$, P_{m_i} is the mechanical power in per unit. Moreover, $m_i = \frac{M_i}{\omega_s}$ and $d_i = \frac{D_i}{\omega_s}$, where $M_i > 0$ is the inertia constant in seconds, $D_i > 0$ is the unitless damping coefficient, and ω_s is the synchronous angular velocity in electrical radians per seconds.

For each load bus $i \in \mathcal{L}$, $d_i > 0$ is the frequency-dependence coefficient and P_{d_i} is the load value in per unit at the current operating point.

In general, the real power drawn by load $i \in \mathcal{L}$ is a nonlinear function of voltage and frequency. Under small-signal stability assumptions, voltages are constant, and for small frequency variations around an operating point P_{d_i} , it is reasonable to consider the

frequency-dependent load model

$$-P_{e_i} = P_{d_i} + d_i \dot{\delta}_i \quad \forall i \in \mathcal{L}. \quad (4.2)$$

This load model describes the dynamics at load buses in (4.1b). Note that as $d_i \rightarrow 0$ in (4.2), we approach a constant-power load model. In (4.1) and (4.2), P_{e_i} is the active electrical power injected from bus i into the network, and is given by

$$P_{e_i} = \sum_{j=1}^n V_i V_j Y_{ij} \cos(\theta_{ij} - \delta_i + \delta_j), \quad (4.3)$$

where V_i represents the voltage magnitude of the i th bus which is assumed to be constant, and $Y_{ij} \angle \theta_{ij}$ is the (i, j) th entry of the nodal admittance matrix.

4.2.2 Equilibrium Points

The *state* of system (4.1) is characterized by the vector $x = (\delta_1, \dots, \delta_n, \dot{\delta}_1, \dots, \dot{\delta}_{n_0})^\top$. An *equilibrium point* of system (4.1) is a state x^* such that if the system reaches x^* , it will stay there permanently. Particularly, in (4.1), an equilibrium point x^* is of the form $x^* = (\delta_1^*, \dots, \delta_n^*, 0, \dots, 0)^\top$. Indeed, the generator frequency deviations are zero, i.e., $\dot{\delta}_i^* = 0, \forall i \in \mathcal{G}$, and the set of bus angles $\delta_i^*, \forall i \in \mathcal{G} \cup \mathcal{L}$ is a solution to the following system of active power flow equations

$$\begin{aligned} P_{m_i} &= \sum_{j=1}^n V_i V_j Y_{ij} \cos(\theta_{ij} - \delta_i^* + \delta_j^*) & \forall i \in \mathcal{G}, \\ -P_{d_i} &= \sum_{j=1}^n V_i V_j Y_{ij} \cos(\theta_{ij} - \delta_i^* + \delta_j^*) & \forall i \in \mathcal{L}. \end{aligned}$$

Recall from Section 2.5.3, that solution of the above active power flow equations is not unique since any shift c in the bus angles, i.e., $\delta_i^* + c, \forall i \in \mathcal{G} \cup \mathcal{L}$ is also a solution. However, this translational invariance can be dealt with by defining a reference bus and

referring all other bus angles to it.

Assumption 1. *An equilibrium point of system (4.1) satisfies the condition $0 < (\theta_{ij} - \delta_i^* + \delta_j^*) < \pi$ for all transmission lines $(i, j) \in \mathcal{E}$.*

Recall that this is a reasonable assumption since the entries of the admittance matrix, i.e., $Y_{ij} \angle \theta_{ij}$ satisfy $\frac{\pi}{2} \leq \theta_{ij} < \pi, \forall (i, j) \in \mathcal{E}$. In lossless networks, we have $\theta_{ij} = \frac{\pi}{2}$, and thus Assumption 1 translates to $|\delta_i^* - \delta_j^*| < \frac{\pi}{2}$. More generally, the X/R ratio, i.e., the ratio of the line reactance to the line resistance is significantly above unity in lossy transmission networks. Therefore, θ_{ij} is close to $\frac{\pi}{2}$, and Assumption 1 translates to $|\delta_i^* - \delta_j^*| < \gamma < \frac{\pi}{2}$, for some number γ close to $\frac{\pi}{2}$.

4.2.3 Singular Perturbation Model

To facilitate the analysis, we study the *singular perturbation model* of dynamical system (4.1):

$$m_i \ddot{\delta}_i + d_i \dot{\delta}_i = P_{m_i} - P_{e_i} \quad \forall i \in \mathcal{G}, \quad (4.4a)$$

$$\varepsilon \ddot{\delta}_i + d_i \dot{\delta}_i = -P_{d_i} - P_{e_i} \quad \forall i \in \mathcal{L}, \quad (4.4b)$$

where the variables $\delta_i, \forall i \in \mathcal{L}$ are multiplied by a *small positive parameter* ε . Note that by setting $\varepsilon = 0$ we will return to the original unperturbed model (4.1). The main motivation for working with the singular perturbation model (4.4) in this chapter is that it will pave the way for developing a stability certificate for the equilibrium points. Naturally, it is important to find the relationship between this auxiliary model (4.4) and the original structure-preserving model (4.1). If the two models have the same stability properties, then it is reasonable to work with the model that is easier to analyze. We will see if this is the case in the next section.

Note that, the form of the equilibrium points of the singular perturbation system (4.4) is similar to those of system (4.1), discussed in Section 4.2.2. Likewise, Assumption 1 can

be applied to system (4.4).

4.3 Stability Certificate in Structure-Preserving and Singular Perturbation Models

Three questions naturally arise regarding the equilibrium points of systems (4.1) and (4.4):

Q1 Which equilibrium points are stable?

Q2 What is the relationship between the stability of an equilibrium point and the parameters (e.g., damping, inertia, network topology, etc.) of the system?

Q3 What is the relationship between the stability of system (4.1) and its singular perturbation counterpart (4.4)?

In Chapter 3, we answered Q1 and Q2 for Kron-reduced swing equations. Now, our goal is to address these questions for structure-preserving swing equations. Obviously, Q1 can be addressed by finding the eigenvalues of the Jacobian matrix associated with the first-order representation of the system (see (C.1) and (C.2) in Appendix C.1 for more details). Another possibility is to numerically construct a Lyapunov function for this system using semidefinite programming techniques. Clearly, both of these ways are computationally expensive and not applicable to realistic large-scale systems. Corollary 1 provides a computationally tractable condition to certify the stability of an equilibrium point, therefore, provides an answer to Q1 and Q2.

Corollary 1. *Consider the singular perturbation model (4.4) with an equilibrium point x^* that satisfies Assumption 1. Moreover, suppose the underlying undirected graph of the power grid is connected. If the condition*

$$-Q_i - V_i^2 B_{ii} \leq \frac{d_i^2}{2m_i} \quad \forall i \in \mathcal{G}, \quad (4.5)$$

is satisfied, then the equilibrium point is locally asymptotically stable. In (4.5), Q_i denotes

the reactive power injected from bus i into the network, given by

$$Q_i = - \sum_{j=1}^n V_i V_j Y_{ij} \sin(\theta_{ij} - \delta_i^* + \delta_j^*).$$

Furthermore, B_{ii} is the imaginary part of the i th diagonal element of the bus admittance matrix.

Proof. The proof follows from Theorem 10, and is outlined in Appendix C.1. □

Next, Theorem 11 answers Q3. This theorem justifies the use of singular perturbation for stability analysis. Recall that an equilibrium point is hyperbolic, if the Jacobian of the corresponding first-order system has no eigenvalues on the imaginary axis.

Theorem 11. *Consider the structure-preserving model (4.1) and its singular perturbation counterpart (4.4). The following statements hold:*

- (i) *If x^* is an exponentially stable equilibrium point of the unperturbed model (4.1), then the corresponding equilibrium point of the singular perturbation model (4.4) is also exponentially stable, for sufficiently small ε .*
- (ii) *Suppose for every sufficiently small ε , y^* is an asymptotically stable equilibrium point of the singular perturbation model (4.4). If x^* is a corresponding hyperbolic equilibrium point of the unperturbed model (4.1), then x^* is also asymptotically stable.*

We outline the proof of the above theorem in Appendix C.1. For detailed definitions of the terms used above, see [68]. Roughly speaking, Theorem 11 states that under certain conditions (i.e., if the equilibrium points of systems (4.1) and (4.4) are hyperbolic for any small ε), then the stability properties of an equilibrium point of system (4.1) is the same as those of system (4.4). Therefore, we can confidently use the results of Corollary 1, as the stability certificate in this theorem will also guarantee the stability of the original structure-preserving system (4.1).

4.3.1 Fast and Distributed Scheme for Stability Assessment

The proposed control scheme is based on Corollary 1. Specifically, condition (4.5) offers a distributed control rule instructing how to change the operating point and parameters of the system in order to move towards stability. For our purposes, it is convenient to reorder the terms in (4.5) and define the stability index

$$\mathcal{S}_i := -Q_i - V_i^2 B_{ii} - \frac{d_i^2}{2m_i} \quad \forall i \in \mathcal{G}. \quad (4.6)$$

The proposed scheme works as follows: Using local measurements of reactive power Q_i and voltage V_i , each generator computes the value of \mathcal{S}_i for itself. If each generator makes sure its \mathcal{S}_i is nonpositive, then the small-signal stability of the entire system is guaranteed.

Note that the proposed scheme is totally distributed and does not need any information from the neighboring generators. This property makes it suitable for fast small-signal stability assessment in large-scale power systems. We will show in Section 4.4.3 that \mathcal{S}_i can be used as an stability index, that is, as \mathcal{S}_i moves towards $-\infty$, the system roughly speaking becomes more stable (the real part of eigenvalues of the system moves towards $-\infty$).

A more conservative stability certificate will also be presented in the next section in Corollary 2. According to this corollary, the small-signal stability can be certified based only on the local network topology information. This criterion is useful for topology design and planning problems, where system operators only have limited information about the operating point of the system.

4.3.2 Remarks on Corollary 1

First and foremost, condition (4.5) in Corollary 1 revolves only around the generator buses, confirming that small-signal stability is concerned with the rotor angle stability of the generators.

The variable Q_i in (4.5) is the net reactive power injected from bus i into the network,

that is, if the generator at bus i is supplying reactive power, then $Q_i > 0$. Otherwise, if it is consuming reactive power, then $Q_i < 0$. Intuitively, when the generator at bus i is a supplier of reactive power, the first term on the left-hand side of (4.5) is negative, and this situation will help condition (4.5) hold, thereby improving the stability of the system.

Recall that $Y_{ii}\angle\theta_{ii} = G_{ii} + iB_{ii} = \sum_{j=1}^n y_{ij}$, where $y_{ij} = g_{ij} + ib_{ij}$ is the admittance of line (i, j) , with $g_{ij} \geq 0$ and $b_{ij} \leq 0$. Therefore, $B_{ii} \leq 0$, and the second term on the left-hand side of (4.5) is always positive. Here, it is assumed that y_{ii} , i.e., the admittance-to-ground at bus i is negligible. Otherwise, we may have $B_{ii} > 0$, and the second term on the left-hand side of (4.5) could be negative.

Condition (4.5) enforces an upper bound which is proportional to the square of damping and inverse of inertia. This is consistent with the intuition that if we increase the damping, the stability margin of the system will increase. However, it is not intuitive (could be a paradox) that decreasing the inertia of a generator will increase the stability margin.

By adding more transmission lines to the system, $|B_{ii}|$ will increase, and this in turn could increase the left-hand side of (4.5) and lead to instability. This can be called the Braess's Paradox [30] in power system stability. The next corollary will further illustrate this stability paradox.

Corollary 2. *Consider the singular perturbation model (4.4) with an equilibrium point x^* that satisfies Assumption 1. Moreover, suppose the underlying undirected graph of the power grid is connected. If the condition*

$$\sum_{j=1, j \neq i}^n V_i V_j Y_{ij} \leq \frac{d_i^2}{2m_i}, \quad \forall i \in \mathcal{G} \quad (4.7)$$

is satisfied, then the equilibrium point is locally asymptotically stable.

This corollary directly follows from the proof of Corollary 1 provided in Appendix C.1. Counterintuitively, according to (4.7), adding more power lines can lead to violating the sufficient condition for stability and making the system unstable. This Braess's Paradox in

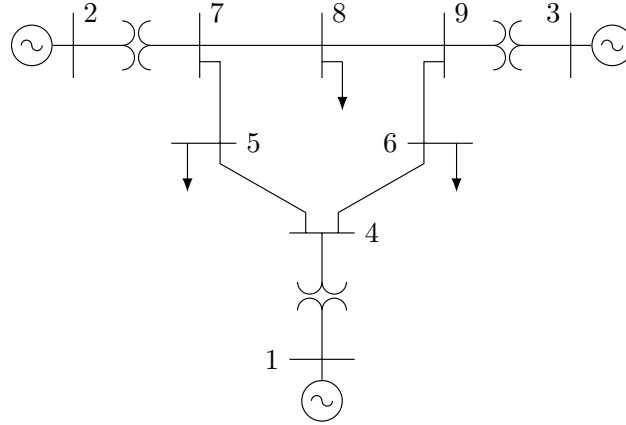


Figure 4.1: Single line diagram of the WSCC system.

power systems has been also acknowledged for example in [81, 82, 83] in different context and using different approaches.

4.4 Numerical Results

Consider the popular western system coordinating council (WSCC) 9-bus 3-generator system [69], depicted in Fig. 4.1. The base MVA is 100, the system frequency is 60 Hz, the network has nonzero transfer conductances, and the line complex powers are around hundreds of MVA each.

In Sections 4.4.1 and 4.4.2, we verify Theorem 11 by showing that the singular perturbation model (4.4) can be used instead of the network-preserving model (4.1) for stability analysis. Then, in Section 4.4.3, we show the application of Corollary 1 in fast and distributed stability assessment.

4.4.1 Perturbed Model Approximation: Time-Domain Comparison

The singular perturbation model (4.4) can be viewed as an approximation of the network-preserving model (4.1). In Fig. 4.2, the upper figure in each subfigure (a) and (b) compares the voltage angle δ_i at generator buses of the exact (solid) structure-preserving model with those of the approximate (dashed) singular perturbation model. The trajectories of the

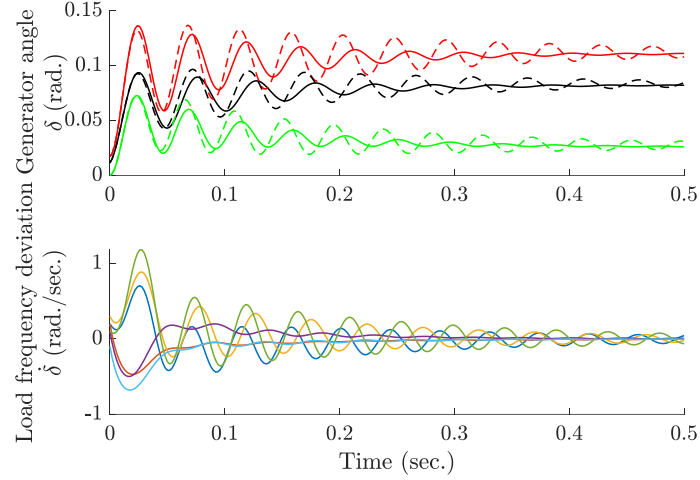
two models clearly converge to the same stable equilibrium point, confirming Theorem 11. Moreover, as we decrease the perturbation parameter ε from 10^{-2} in subfigure (a) to 2×10^{-3} in subfigure (b), the approximation error also decreases. Indeed, it can be rigorously proved that the aforementioned estimation is $\mathcal{O}(\varepsilon)$.

Fig. 4.2 also shows the frequency deviation $\dot{\delta}_i$ at load buses of the singular perturbation model. Recall that these $\dot{\delta}_i, \forall i \in \mathcal{L}$ were the state variables whose time derivative was multiplied by ε in (4.4b). From (4.4b), the time derivative of $\dot{\delta}_i$ at load buses is $\ddot{\delta}_i = (-d_i \dot{\delta}_i - P_{d_i} - P_{e_i})/\varepsilon$, which can be large when ε is small. Accordingly, in Fig. 4.2 (b) with a smaller ε compared to Fig. 4.2 (a), the dynamics of $\dot{\delta}_i$ at load buses converges more rapidly to zero.

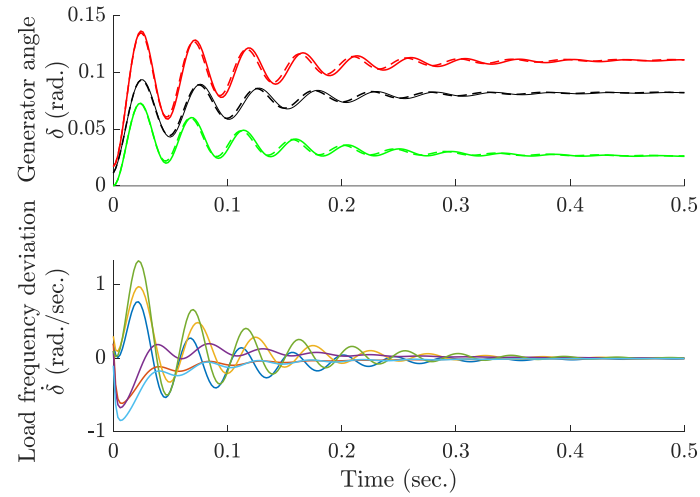
4.4.2 Perturbed Model Approximation: Modal Analysis

Fig. 4.3 provides a comparison between the eigenvalues associated with the Jacobian matrix of models (4.1) and (4.4). The two models have a set of eigenvalues which are close to each other. Additionally, note that the state space of the singular perturbation model has more dimensions (in this WSCC example, it has 6 additional dimensions which is equal to the number of load buses). These additional eigenvalues are also shown separately in each subfigure.

Comparing Figs. 4.3(a) and 4.3(b), as the perturbation parameter gets smaller, the set of eigenvalues of model (4.1) approaches those of model (4.4). Moreover, using a smaller perturbation parameter, the additional eigenvalues of the singular perturbation model move towards $-\infty$. Indeed, as $\varepsilon \rightarrow 0$, the two systems will have a set of common eigenvalues, while the additional eigenvalues of the singular perturbation model will approach $-\infty$. Finally, observe that as $\varepsilon \rightarrow 0$, the eigenvalues of the singular perturbation model do not approach the imaginary axis. According to Theorem 11, the equilibrium points of the two models (4.1) and (4.4) have the same stability properties. This justifies the use of model (4.4) instead of model (4.1) for stability assessment.



(a) Using perturbation parameter $\varepsilon = 10^{-2}$.

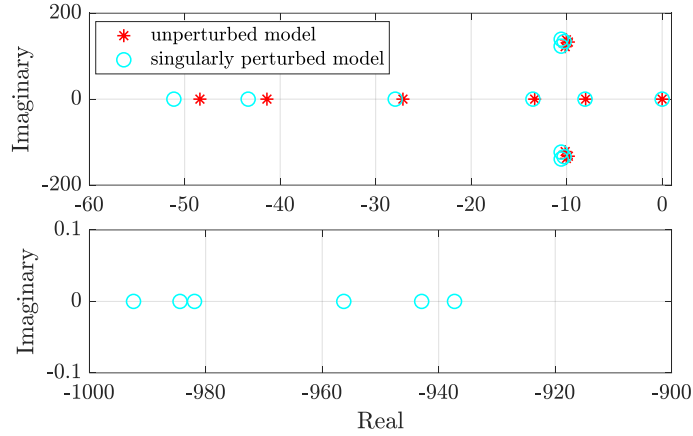


(b) Using perturbation parameter $\varepsilon = 2 \times 10^{-3}$.

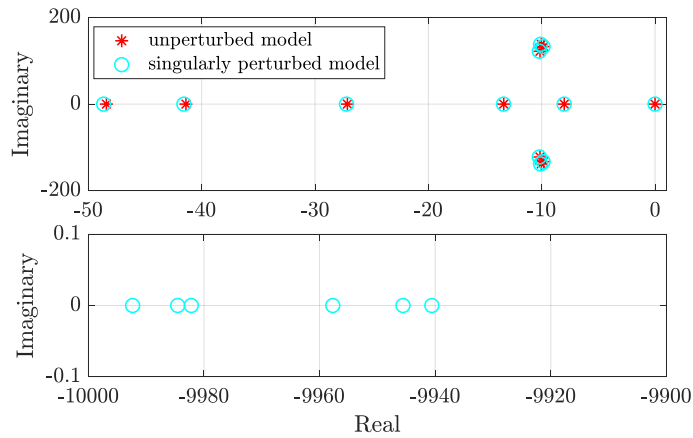
Figure 4.2: Simulation results of the WSCC system: exact model (solid) and singular perturbation model (dashed) with two different perturbation parameters.

4.4.3 Fast and Distributed Stability Assessment

As mentioned previously, Assumption 1 is reasonable and holds in practice. Fig. 4.4 confirms this issue for the WSCC system. As can be seen, the angles $(\theta_{ij} - \delta_i^* + \delta_j^*)$ for all transmission lines are perfectly located within the interval 0 to π rad. Moreover, Theorem 11 has been verified in Sections 4.4.1 and 4.4.2, thereby justifying the use of Corollary 1 and the singular perturbation model for stability assessment. In this section, we test the efficacy of the scheme proposed in Section 4.3.1.



(a) Using perturbation parameter $\varepsilon = 10^{-3}$.



(b) Using perturbation parameter $\varepsilon = 10^{-4}$.

Figure 4.3: Modal analysis of the WSCC system: eigenvalues of the exact model (red asterisks) and singular perturbation model (cyan circles) with two different perturbation parameters.

Recall when the stability index \mathcal{S}_i defined in (4.6) is negative for all generators, then by Corollary 1, the equilibrium point of the system is asymptotically stable. Note that the converse may not be true, i.e., \mathcal{S}_i could be positive while the system is stable. However, even in such cases, \mathcal{S}_i can be viewed as an index, showing the degree of stability.

Consider the WSCC system under different operating points as well as different system parameters (generators' inertia and damping). As the operating points or system parameters vary, the eigenvalues of the system may also move to either right half-plane (less stable) or left half-plane (more stable). Now, the stability index (4.6) helps us understand how

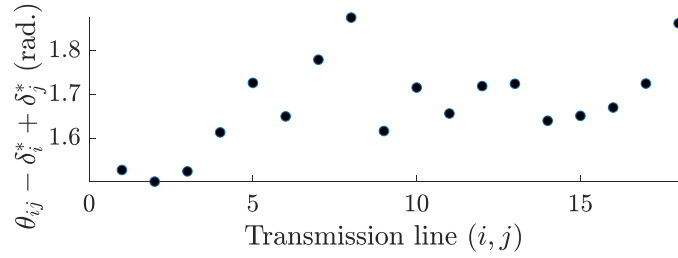


Figure 4.4: Verification of Assumption 1 in the WSCC system.

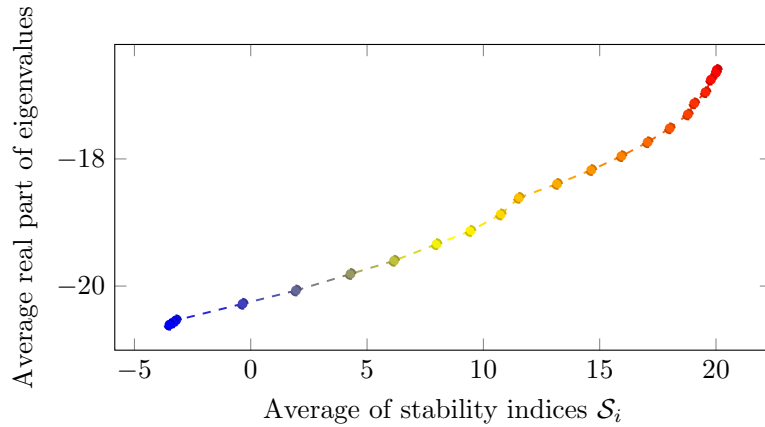


Figure 4.5: Variation of degree of stability due to variation of stability index (4.6).

the eigenvalues move if we vary operating points or system parameters. Fig. 4.5 shows the variation in the real parts of eigenvalues of model (4.4) as a function of changes in the stability index (4.6). In this figure, under all operating conditions and system parameters, the equilibrium point is asymptotically stable. However, as the average of stability indices moves towards negative value (i.e., the violation of condition (4.5) decreases and at some point the condition holds), the average real part of eigenvalues move towards $-\infty$, making the operating point more stable.

4.5 Final Remarks

We showed under reasonable assumptions, the small-signal stability of the classical structure-preserving model is equivalent to its singular perturbation counterpart. Based on this equivalence, we developed a novel stability certificate for the structure-preserving model. The

certificate can be computed in a fully distributed fashion, using only local information, and can be used for real-time monitoring. The certificate suggests that the eigenvalues of the system will move towards the left half-plane by increasing generators' damping and decreasing generators' inertia. It also reveals a paradox that adding more transmission lines can lead to the violation of the stability certificate and making the system unstable. The stability certificate could be incorporated as a constraint into various problems such as the optimal power flow problem in order to guarantee and improve the stability of solutions. Our results could also be extended towards tighter and nonlocal stability certificates.

CHAPTER 5

STABILITY AND CONTROL OF MULTI-MICROGRIDS

In the previous chapters, we studied the stability of swing equations. Now, we delve deeper into an important applications of swing equations in modeling multi-microgrid (multi- μ G) networks. Specifically, we derive sufficient conditions to guarantee small-signal stability of multi- μ Gs in both lossless and lossy networks. The new stability certificate for lossy networks only requires local information, thus leads to a fully distributed control scheme. Moreover, we study the impact of network topology, interface parameters (virtual inertia and damping), and local measurements (voltage magnitude and reactive power) on the stability of the system. The proposed stability certificate suggests the existence of Braess's Paradox in the stability of multi- μ Gs, i.e. adding more connections between microgrids could worsen the multi- μ G system stability as a whole.

We also extend the presented analysis to structure-preserving network models, and provide a stability certificate as a function of original network parameters, instead of the Kron reduced network parameters. Stability of structure-preserving models was also addressed in Chapter 4, but here we revisit the problem from a graph-theoretic perspective. We provide a detailed numerical study of the proposed certificate, the distributed control scheme, and a coordinated control approach with line switching. The simulation shows the effectiveness of the proposed stability conditions and control schemes in a four- μ G network, IEEE 33-bus system, and several large-scale synthetic grids.

5.1 Introduction

Restructuring of distribution systems into multi- μ Gs is one of the main ways of improving the resilience of the electricity grid. The structural modularity of such networks makes them remarkably resilient against extreme events, but inherently prone to instabilities nonethe-

less. A minor contingency in these networks may lead to cascading outages and a total blackout in all microgrids. There is, therefore, an urgent need for understanding the notion of stability in multi- μ Gs. The present chapter is motivated by this urgent need and is aimed at characterizing the conditions under which a multi- μ G is locally stable. We also attempt to understand how the topology and parameters of the network would affect the stability of a multi- μ G, and how we can monitor and guarantee its stability using a distributed control scheme.

5.1.1 Related Work

A key feature that distinguishes future multi- μ G networks from the conventional distribution systems is that each microgrid will be connected to the rest of the system via a point of common coupling (PCC). Moreover, each microgrid either has a voltage source inverter (VSI)-based interface at PCC or is composed of a network of distributed energy resources (DERs), e.g. VSIs, diesel generators (DGs), etc [9, 10]. On the other hand, it can be mathematically proved (see Lemma 7) that the frequency dynamics of a droop-controlled VSI is equivalent to the dynamics of a synchronous generator or DG, represented by swing equations [11], [12]. Therefore, from a modeling perspective, the dynamical model of multi- μ Gs is closely related to that of interconnected generators [13], and analysis of multi- μ Gs' behaviour is intertwined with an accurate understanding of swing equations.

Swing equations can be studied from a graph-theoretic perspective, where the main focus is on investigating the relationship between the underlying graph structure of the power system and the system stability [84, 85, 86, 70, 87]. Our work in this chapter falls into this research category. We refer to [70] and [87] for a comprehensive survey on this topic. In particular, the existing results on the small-signal stability of lossless swing equations are reviewed and studied in [70]. It is shown that if bus angle differences at an equilibrium point are less than $\pi/2$, then the equilibrium point is locally asymptotically stable. The present chapter provides a generalization of such results to lossy swing equations. Con-

trary to the lossless case, we will show that an equilibrium point in lossy networks could be unstable even if bus angle differences are less than $\pi/2$.

Swing equations also play an important role in studying droop-controlled inverters in microgrids. In the literature, various models with different complexities have been adopted for droop-controlled inverters, including first-order models [88], second-order models [9, 11, 13], third-order models [89], and higher-order models [90, 91, 92]. Each model is useful for studying a particular aspect of droop-controlled inverters such as their frequency stability, voltage stability, or electromagnetic transients. The application of swing equations is more common in second-order models and frequency stability [11, 13]. Swing equations with variable voltage magnitudes also appear in third-order models. For instance, in [89], each inverter is modeled by a third-order differential equation including swing equations with variable voltage magnitudes. Using this model, sufficient conditions are derived for boundedness of trajectories in lossy microgrids as well as asymptotic stability of equilibrium points in lossless microgrids. In the present chapter, we focus on frequency stability and adopt a second-order model with constant voltage magnitudes for each inverter. In comparison with [89], in the lossless case, our results match the results of [89, See Remark 5.11]. In the lossy case, our sufficient condition in this chapter certifies the asymptotic stability of equilibrium points instead of boundedness of trajectories as in [89]. Nonetheless, our model for inverters here is different, and a direct comparison seems unfair.

The framework in [90] (and the follow-up articles [91, 92]) utilizes a more detailed dynamical model for inverter-based microgrids, modeling the droop-based frequency and voltage controls as well as the electromagnetic transients of power lines. After performing a model order reduction and constructing a Lyapunov function for the reduced model, a set of decentralized sufficient conditions are developed for guaranteeing the small-signal stability of the equilibrium points. In the present chapter, we pursue the same goal as in [90, 91, 92], i.e., finding decentralized sufficient conditions for small-signal stability. However, our focus is more on frequency stability, and deriving more explicit stability conditions that

reveal the role of network topology and parameters in small-signal stability.

The small-signal stability of multi- μ Gs is studied in [9], where various control frameworks are proposed for the microgrids' interface. Moreover, a plug-and-play rule is proposed in [13], guaranteeing the stability of multi- μ Gs without requiring the global knowledge of network topology or operating conditions. The multi- μ G model in the present chapter is similar to the one in [13], except we do not incorporate a local integral control. Corollary 2 in the present chapter matches the plug-and-play rule in [13]. Moreover, the main result in Theorem 12 generalizes the main result of [13] because our stability certificate considers the real-time operating condition of the system and is less conservative. Our result is also a generalization of the result in [11] as we do not require uniform damping of inverters.

Another set of literature that are conceptually related to our work in this chapter are the recent studies on power grid synchronization [93], frequency control [52, 55], voltage stability [94], and also the study of Kuramoto oscillators which has been linked to the stability analysis of lossy power systems with strongly overdamped generators [66].

5.1.2 Main Results

The main contributions of this chapter can be summarized below.

- **Stability Certificates:** We derive explicit sufficient conditions that certify small-signal stability of multi- μ Gs for both lossless and lossy networks. The new certificates provide significant insights about the interplay between system stability and reactive power absorption, voltage magnitude at PCC, network topology, and interface parameters of each microgrid. We also introduce a new weighted directed graph to study the spectral properties of the multi- μ G Laplacian.
- **Distributed Control:** In addition to providing new insights into the theory of stability, the derived stability certificates use only local information and are suitable for real-time monitoring and fast stability assessment. Based on the developed theory,

we introduce a fully distributed control scheme to adjust the dynamic parameters of each microgrid interface for maintaining the stability of the system.

- **Analog of Braess’s Paradox:** The stability conditions developed in this chapter surprisingly reveal an analog of Braess’s Paradox in power system stability, showing that adding power lines to the system may decrease the stability margin [30]. The current chapter rigorously establishes the impact of switching-off lines, increasing damping, and decreasing virtual inertia on improving system stability.
- **Generalization to Structure-Preserving Models:** We extend the presented analysis to structure-preserving power network models. Specifically, we prove a monotonic relationship between entries of a nodal admittance matrix and its Kron reduced counterpart. This monotonic relationship enables us to derive a stability condition as a function of original network parameters, instead of the Kron reduced network parameters. This is beneficial to real-time distributed control as the network parameters constantly change and Kron reduction may not be available to individual controllers.

We believe the findings in this chapter are also applicable to other problems whose models display similar structural properties, such as small-signal stability assessment in the transmission level and synchronization of coupled second-order nonlinear oscillators.

5.1.3 Chapter Outline

The rest of this chapter is organized as follows. Section 5.2 provides a brief background on multi- μ Gs. In Section 5.3, the multi- μ G model is linearized and several properties of the Jacobian matrix are proved. Section 5.4 is devoted to the main results on sufficient conditions for the stability of multi- μ Gs. Section 5.5 further illustrates the developed analytical results through numerical examples, and finally, the chapter concludes with Section 5.6.

5.2 Background

5.2.1 Multi-Microgrid Model

Consider a distribution network represented as an undirected graph $\mathcal{G} = (\mathcal{N}, \mathcal{E})$, where \mathcal{N} is the set of nodes and \mathcal{E} is the set of edges. Each node in \mathcal{N} represents a microgrid and each edge in \mathcal{E} represents an electrical branch connecting the two microgrids across the branch. We will refer to \mathcal{G} as the linking grid [10]. The linking grid \mathcal{G} is *connected* if for any two nodes $i, k \in \mathcal{N}, i \neq k$ there exists a path between i and k consisting of power lines with nonzero admittance. To begin the study, let us assume that each microgrid is modeled by a grid-forming VSI connected to a node of the linking grid.

Given the time window of small-signal stability assessment, characterization of each microgrid by a VSI can be understood in two ways:

1. The first possibility is that a microgrid contains an ensemble of devices (e.g., grid-forming inverters, diesel generators, and loads) whose aggregate behavior can be modeled by a VSI. The derivation of the aggregated VSI model is out of the scope of this thesis. We refer to [95, 96] for details. Moreover, we restrict the type of microgrid DERs to grid-forming VSIs, DGs, and more generally to those whose dynamics can be captured by swing equations.
2. The second possibility is that a microgrid is connected to the linking grid through a grid-forming VSI at PCC [9, 10, 13]. VSI-based interfaces decouple the intra-microgrid dynamics from the grid side, and consequently, the interactions among different microgrids will be primarily determined by the VSI control law [9, 10].

When the model order reduction in way 1 introduces major errors, or VSI interfaces in 2 do not exist, it is inevitable that the internal structure, DERs, and loads of the microgrid be explicitly modeled. Later in Section 5.4.3, we will introduce a way to consider a structure-preserving model for each microgrid and extend our stability analysis to such cases. Let us

for now focus on the case where each microgrid is represented as a node in the linking grid $\mathcal{G} = (\mathcal{N}, \mathcal{E})$ and modeled by a VSI.

Accordingly, the dynamics of a multi- μ G network is characterized by the following system of nonlinear autonomous ordinary differential equations (ODEs):

$$\dot{\delta}_i(t) = \omega_i(t) \quad \forall i \in \mathcal{N}, \quad (5.1a)$$

$$m_i \dot{\omega}_i(t) + d_i \omega_i(t) = P_{s_i} - P_{e_i}(\delta(t)) \quad \forall i \in \mathcal{N}, \quad (5.1b)$$

where for each microgrid $i \in \mathcal{N}$, P_{s_i} is the active power setpoint in per unit, P_{e_i} is the outgoing active power flow in per unit, m_i is the virtual inertia in seconds induced by the delay in droop control, d_i is the unitless damping coefficient, t is the time in seconds, $\delta_i(t)$ is the terminal voltage angle in radian, and finally $\omega_i(t)$ is the deviation of the angular frequency from the nominal angular frequency in radian per seconds. For the sake of simplicity, henceforth we do not explicitly write the dependence of the state variables δ and ω on time t .

The PCC of two microgrids i and k are connected via a power line with the admittance $y_{ik} = g_{ik} + ib_{ik}$, where $g_{ik} \geq 0$ and $b_{ik} \leq 0$. In transmission-level small-signal stability studies, the conductance g_{ik} of transmission lines is commonly assumed to be zero (aka lossless model). While this is a reasonable assumption in the transmission level, it may not hold in the distribution level and multi- μ G networks. Therefore, our analysis will be based on the general lossy case, and we discuss the lossless model as a special case. Let y_{ii} denote the admittance-to-ground at PCC i and define the symmetric admittance matrix given by the diagonal elements $Y_{ii} \angle \theta_{ii} = \sum_{k=1}^n y_{ik}$ and off-diagonal elements $Y_{ik} \angle \theta_{ik} = -y_{ik}$. Based on this definition, the function P_{e_i} in (5.1b) can be further spelled out:

$$P_{e_i}(\delta) = \sum_{k=1}^n V_i V_k Y_{ik} \cos(\theta_{ik} - \delta_i + \delta_k), \quad (5.2)$$

where V_i is the PCC terminal voltage magnitude of microgrid i .

Recall from Definition 2 in Section 2.5.1 that the function $P_e : \mathbb{R}^n \rightarrow \mathbb{R}^n$ given by $\delta \mapsto P_e(\delta)$ in (5.2) is called the flow function. Recall also that we addressed the translational invariance of the flow function in Section 2.5.3.

Observe that equilibrium points of the multi- μ G dynamical system (5.1) are of the form $(\delta^*, \omega^*) \in \mathbb{R}^{2n}$ where δ^* is a solution to the active power flow problem $P_{e_i}(\delta^*) = P_{s_i}, \forall i \in \mathcal{N}$ and $\omega^* = 0$. We seek an answer to the following question: under what conditions is an equilibrium point (δ^*, ω^*) locally asymptotically stable? A perfect answer to this question should give us a purely algebraic condition, shedding light on the relation between the stability of the equilibrium point and the parameters of system (5.1) (i.e., the interface parameters m_i and d_i , the setpoints P_{s_i} , and the underlying graph of the multi- μ G network). The rest of this chapter is devoted to finding such an answer.

As mentioned before, model (5.1) is identical to the well-known swing equation model describing the dynamics of interconnected synchronous generators [1], and this is because VSI control schemes are widely devised to emulate the behavior of synchronous machines [9, 10, 12]. Indeed, the equivalence of the dynamics of synchronous generators and droop-controlled VSIs can be rigorously formalized. Specifically, a droop-controlled VSI at node $i \in \mathcal{N}$ can be modeled as [11]:

$$\dot{\delta}_i(t) = -k_i (P_{m_i}(t) - P_{d_i}), \quad (5.3a)$$

$$\tau_i \dot{P}_{m_i}(t) = -P_{m_i}(t) + P_{e_i}, \quad (5.3b)$$

where $k_i \geq 0$ is the droop gain, $P_{m_i} \in \mathbb{R}$ is the measured active power, $P_{d_i} \in \mathbb{R}$ is the desired active power setpoint, and $\tau_i \geq 0$ is the time constant of the low-pass filter of the power measurement. Now, the next lemma shows the droop-controlled VSI model (5.3) can be reparametrized as the swing equation model (5.1).

Lemma 7 (VSI model reparametrization). *The dynamics of the droop-controlled VSI model (5.3) is equivalent to the dynamics of the swing equation model (5.1).*

Proof. Consider the VSI model (5.3) and define the new variable $\omega_i(t)$ as

$$\omega_i(t) := \dot{\delta}_i(t) = -k_i (P_{m_i}(t) - P_{d_i}). \quad (5.4)$$

Thus, using the new variable $\omega_i(t)$, equation (5.3a) can be written as (5.1a). By substituting $P_{m_i}(t) = -\omega_i(t)/k_i + P_{d_i}$ into (5.3b), we get

$$-\tau_i \dot{\omega}_i(t)/k_i = \omega_i(t)/k_i - P_{d_i} + P_{e_i}.$$

Now, for each node $i \in \mathcal{N}$, define the virtual inertia coefficient $m_i := \tau_i/k_i$, virtual damping $d_i := 1/k_i$, and active power setpoint $P_{s_i} := P_{d_i}$. Therefore, (5.3b) is equivalent to (5.1b). \square

Similar derivations can be found for example in [11, 97]. Accordingly, the application of model (5.1) is not restricted to the characterization of interconnected microgrids. The model (and consequently, the results developed in this chapter) can be applied to a system of interconnected synchronous machines, coupled oscillators, etc.

5.3 Linearization and Spectrum of Jacobian

5.3.1 Linearization

Let us take the state variable vector $(\delta, \omega) \in \mathbb{R}^{2n}$ into account and note that the first step in studying the stability of multi- μ G equilibrium points is to analyze the Jacobian of the vector field in (5.1):

$$J := \begin{bmatrix} 0 & I \\ -M^{-1}L & -M^{-1}D \end{bmatrix} \in \mathbb{R}^{2n \times 2n} \quad (5.5)$$

where $I \in \mathbb{R}^{n \times n}$ is the identity matrix, $M = \mathbf{diag}(m_1, \dots, m_n)$, and $D = \mathbf{diag}(d_1, \dots, d_n)$. Throughout the chapter, we assume M and D are nonsingular. Moreover, $L \in \mathbb{R}^{n \times n}$ is the

Jacobian of the flow function with the entries:

$$L_{ii} = \sum_{k=1, k \neq i}^n V_i V_k Y_{ik} \sin(\theta_{ik} - \delta_i + \delta_k), \forall i \in \mathcal{N} \quad (5.6a)$$

$$L_{ik} = -V_i V_k Y_{ik} \sin(\theta_{ik} - \delta_i + \delta_k), \forall i \neq k \in \mathcal{N}. \quad (5.6b)$$

The matrix L plays a prominent role in the spectrum of the Jacobian matrix J (and as a consequence, in the stability properties of the equilibrium points of multi- μ Gs). We illustrate this role in the following subsection.

5.3.2 Spectral Relationship Between Matrices J and L

Recall from Lemma 1 that the eigenvalues of J and L are linked through a singularity constraint. Now, Proposition 5 illustrates the relationship between the kernels and the multiplicity of the zero eigenvalue of the two matrices J and L .

Proposition 5. *Consider the Jacobian matrix J in (5.5). The following statements hold:*

- (i) *The kernel of L is the orthogonal projection of the kernel of J onto the linear subspace $\mathbb{R}^n \times \{0\}$. That is, $\ker(L) = \mathbf{proj}(\ker(J))$.*
- (ii) *The geometric multiplicity of the zero eigenvalue in $\sigma(J)$ and $\sigma(L)$ are equal.*
- (iii) *J is nonsingular if and only if L is nonsingular.*

Proof. See Appendix D.1. □

As the role of L in the spectrum of J became more clear, we scrutinize the spectrum of L in the next subsection. Our final goal is to use the spectral properties of L together with the relationships established in Lemma 1 and Proposition 5 to derive a stability certificate for multi- μ Gs.

5.3.3 A Directed Graph Induced by L

The linking grid of a multi- μ G is represented by the undirected graph \mathcal{G} defined in Section 5.2.1. However, to fully represent the Jacobian L of the flow function (5.2), we need to introduce a new *weighted directed* graph (digraph). Let $\vec{\mathcal{G}} = (\mathcal{N}, \mathcal{A}, \mathcal{W})$, where each node $i \in \mathcal{N}$ corresponds to a microgrid and each directed arc $(i, k) \in \mathcal{A}$ corresponds to the entry (i, k) , $i \neq k$ of the admittance matrix. We further define a weight for each arc $(i, k) \in \mathcal{A}$:

$$w_{ik} = V_i V_k Y_{ik} \sin(\varphi_{ik}), \quad (5.7)$$

where $\varphi_{ik} := \theta_{ik} - \delta_i + \delta_k$. With the above definitions, we can see that the Jacobian matrix L of the flow function, which appeared in (5.6), is indeed the *Laplacian* of the weighted digraph $\vec{\mathcal{G}}$. In general, the arc weights w_{ik} can take any values in \mathbb{R} , and the matrix L is not necessarily symmetric. In practice, however, w_{ik} varies in a small nonnegative range. Figure 5.1 illustrates the histogram of the angle φ_{ik} for all lines (i, k) in different IEEE and NESTA standard distribution test cases, where the converged load flow data are obtained from MATPOWER [69]. Accordingly, $\varphi_{ik} \in (0, \pi)$ in all of these cases. Thus, it is reasonable to assume that the equilibrium points (δ^*, ω^*) of the multi- μ G dynamical system (5.1) are located in the set Ω defined as

$$\Omega = \{(\delta, \omega) \in \mathbb{R}^{2n} : 0 < \theta_{ik} - \delta_i + \delta_k < \pi, \forall (i, k) \in \mathcal{A}, \omega = 0\}.$$

Under this assumption, the arc weights $w_{ik} > 0$ for all arcs (i, k) . So, there are two arcs (i, k) and (k, i) between microgrids i and k if and only if the two microgrids are physically connected. We always assume the physical network connecting all the microgrids is a connected (undirected) graph. The weighted digraph $\vec{\mathcal{G}}$ will be used to study the spectral properties of L .

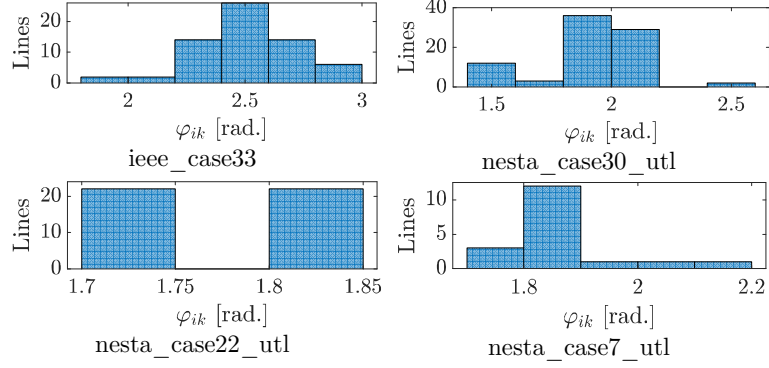


Figure 5.1: Histogram of the distribution of φ_{ik} for all lines (i, k) in different IEEE and NESTA standard test cases.

5.3.4 Spectral Properties of L

When φ_{ij} 's satisfy the above angle assumption, the following proposition shows that L is a singular M-matrix. Moreover, the zero eigenvalue of L is simple, i.e. the algebraic and geometric multiplicities are one, which is important for preventing bifurcation from happening in the multi- μ grid network.

Proposition 6. *Let $(\delta^*, \omega^*) \in \Omega$ be an equilibrium point of the multi- μ G system (5.1). Assume the linking grid \mathcal{G} is connected. The Jacobian matrix L defined by (5.6) at this equilibrium point has the following properties:*

- (i) L has a zero eigenvalue with an eigenvector $\mathbf{1}$, and the real part of each nonzero eigenvalue of L is positive, i.e. L is a singular M-matrix.
- (ii) The zero eigenvalue of L is simple.

Properties (i) and (ii) of L shown in the above proposition will be used in the next section to prove the stability of J in the main result of the chapter.

5.4 Stability of Multi-Microgrid Networks

Now we are ready to answer the fundamental question posed in Section 5.2.1: under what conditions is an equilibrium point (δ^*, ω^*) locally asymptotically stable?

5.4.1 The Main Stability Theorem

Theorem 12. *Let $(\delta^*, \omega^*) \in \Omega$ be an equilibrium point of the multi- μ G system (5.1). Let $B \in \mathbb{R}^{n \times n}$ denote the imaginary part of the admittance matrix. Suppose all microgrid interfaces have positive damping coefficients and inertia, and the linking grid \mathcal{G} is connected. Then, the following statements hold:*

- (a) *The Jacobian J at this equilibrium point has a zero eigenvalue with geometric multiplicity of one.*
- (b) *All the nonzero real eigenvalues of J are negative.*
- (c) *Let Q_i be the net outgoing reactive power flow from microgrid PCC i . If*

$$-Q_i - V_i^2 B_{ii} \leq \frac{d_i^2}{2m_i}, \quad \forall i \in \mathcal{N} \quad (5.8)$$

then all the nonzero eigenvalues of J , both real and complex, are located in the left half plane, i.e., $\sigma(J) \subset \mathbb{C}_- \cup \{0\}$, and the equilibrium point is locally asymptotically stable.

- (d) *If the transfer conductance of the lines is zero, then all the nonzero eigenvalues of J are located in the left half plane, and the equilibrium point is locally asymptotically stable.*

Proof. See Appendix D.2. □

Remark 6. *Properties (a) and (b) hold independently of the sufficient conditions in (c) and (d). Property (d) says if the network is lossless, then regardless of (c), any equilibrium point is stable. If instead the network is lossy, then not every equilibrium point is stable and condition (5.8) provides a new certificate to guarantee the small-signal stability of an equilibrium point.*

Remark 7. Notice that a salient feature of condition (5.8) is that it only requires local information at each microgrid interface, hence, leads to a fully distributed control scheme to stabilize the multi- μ G system. Detailed numerical simulation will be shown in Section 5.5.

5.4.2 Intuition and Paradox Behind Condition (5.8)

Condition (5.8) in Theorem 12 provides a practical and efficient way to certify the stability of the equilibrium points in general lossy multi- μ G networks. It also introduces a distributed control rule for tuning the interface parameters of each microgrid without compromising the network stability. In this section, we will explore the intuition behind this theory as well as two interesting paradoxes that come with it.

- **Note 1:** The variable Q_i in (5.8) is the net reactive power that microgrid i injects into the rest of the multi- μ G network, that is, if microgrid i is supplying reactive power, then $Q_i > 0$. Otherwise, if it is consuming reactive power, then $Q_i < 0$. Intuitively, when microgrid i is a supplier of reactive power, the first term on the left-hand side of (5.8) is negative, and this situation will help condition (5.8) hold.
- **Note 2:** Recall that $Y_{ii}\angle\theta_{ii} = G_{ii} + \mathbf{i}B_{ii} = \sum_{k=1}^n y_{ik}$, where $y_{ik} = g_{ik} + \mathbf{i}b_{ik}$ is the admittance of line (i, k) , with $g_{ik} \geq 0$ and $b_{ik} \leq 0$. Therefore, $B_{ii} \leq 0$, and the second term on the left-hand side of (5.8) is always positive. Here, it is assumed that y_{ii} , i.e., the admittance-to-ground at PCC i is negligible. Otherwise, we may have $B_{ii} > 0$, and the second term on the left-hand side of (5.8) could be negative.
- **Note 3:** The first two notes clarify that the left-hand side of (5.8) can be negative if microgrid i is supplying reactive power; otherwise it is positive. Consequently, condition (5.8) is not trivial.
- **Note 4:** Condition (5.8) enforces an upper bound which is proportional to the square of damping and inverse of inertia. This is consistent with the intuition that if we

increase the damping, the stability margin of the system will increase. However, it is not intuitive (could be a paradox) that decreasing the virtual inertia of a microgrid interface will increase the stability margin.

- **Note 5:** By adding more transmission lines to the system, $|B_{ii}|$ will increase, and this in turn could increase the left-hand side of (5.8) and lead to the violation of this condition. This can be called the Braess's Paradox in power system stability.

Corollary 2 further illustrates the aforementioned Braess's Paradox. Counterintuitively, according to Corollary 2, adding more power lines can lead to violating the sufficient condition for stability. This Braess's Paradox in power systems has been also acknowledged in [81] and [13] in different contexts and using different approaches. Note that removing lines from a network could make the system more vulnerable to contingencies and eliminate the reliability benefits of having more transmission line capacity. This trade-off should be taken into account during the design and operation of power grids.

5.4.3 Stability Condition in Structure-Preserving Networks

Motivation

The stability certificate (5.8) in Section 5.4.1 is derived for the linking grid $\mathcal{G} = (\mathcal{N}, \mathcal{E})$, where each microgrid is reduced to one node modeled as a grid-forming inverter using the swing equation. In this section, we consider the more general situation, where the internal active and passive elements of a microgrid are explicitly modeled. In particular, let $\mathcal{G}^d = (\mathcal{N}^d, \mathcal{E}^d)$ be the distribution network composed of all microgrids $\mathcal{G}_i = (\mathcal{N}_i, \mathcal{E}_i)$ for $i \in \mathcal{N}$ as subnetworks. The buses \mathcal{N}_i of microgrid i may include both active nodes (i.e., those connected to DGs and/or VSIs) and passive nodes (i.e., those connected to a constant admittance load).

In order to study the stability property of \mathcal{G}^d , we first use Kron reduction to eliminate all passive nodes from each microgrid and study the resulting reduced network \mathcal{G}^r . The

stability condition (5.8) can be applied to \mathcal{G}^r . However, such a certificate is expressed in the system states and parameters of \mathcal{G}^r , not of the original network \mathcal{G}^d . This is not desirable, as it obscures the relations between the topology of the original network and the stability properties of the equilibrium points. Moreover, the parameters of the Kron-reduced network \mathcal{G}^r may not be available to the individual microgrid controllers in real time. We want to find a stability certificate for the Kron-reduced network \mathcal{G}^r , expressed in the system states and network topology of the original network \mathcal{G}^d .

To tackle this challenge, we first identify in Section 5.4.3 a sufficient condition on the admittances of the original network \mathcal{G}^d , under which certain monotonic relationship between the admittances of \mathcal{G}^d and \mathcal{G}^r can be obtained. Then in Section 5.4.3, we use this monotonicity property to derive a stability certificate expressed directly in states and parameters of \mathcal{G}^d .

The Kron-Reduced and Original Networks

Definition 6. *Let Y be the nodal admittance matrix of a microgrid $\mathcal{G}_i = (\mathcal{N}_i, \mathcal{E}_i)$, where the set of active and passive nodes are denoted by $\alpha, \beta \subseteq \mathcal{N}_i$, respectively. The Kron reduction of \mathcal{G}_i that eliminates all nodes in β has an admittance matrix given by $Y^r := Y[\alpha, \alpha] - Y[\alpha, \beta]Y[\beta, \beta]^{-1}Y[\beta, \alpha]$. This Kron-reduced network is denoted by \mathcal{G}_i^r .*

Assumption 2 below is widely satisfied in distribution grids.

Assumption 2. *The nodal admittance matrix $Y = G + \mathbf{i}B$ of a distribution grid satisfies $G_{ik} \leq 0, B_{ik} \geq 0$, for all $i \neq k$, and $G_{ii} \geq 0, B_{ii} \leq 0$ for self-admittances.*

Assumption 3 below is the sufficient condition used in Lemma 8 to derive a monotonicity relation between the admittances of the original and Kron-reduced networks.

Assumption 3. *Let $Y = G + \mathbf{i}B$ be the nodal admittance matrix of a distribution grid. There exist two fixed real numbers ν_{\min} and ν_{\max} that satisfy*

$$0 \leq \nu_{\min} \leq \nu_{\max} \leq \sqrt{1 + 2\nu_{\min}^2} \quad (5.9)$$

such that, for every line (i, k) , the conductance G_{ik} and susceptance B_{ik} are bounded as

$$\nu_{\min}|G_{ik}| \leq |B_{ik}| \leq \nu_{\max}|G_{ik}|. \quad (5.10)$$

Remark 8. By (5.10), if $G_{ik} = 0$, then $B_{ik} = 0$; otherwise, $\nu_{\min} \leq |B_{ik}|/|G_{ik}| \leq \nu_{\max}$, where the upper and lower bounds satisfy (5.9). As an example, if $\nu_{\min} = 5$, then we can set $\nu_{\max} = \sqrt{1 + 2 \cdot 5^2} = 7.14$. Then, according to (5.10), all lines have $|B_{ik}|/|G_{ik}|$ ratio between 5 and 7.14, which is typical in distribution grids, especially in microgrids.

Lemma 8. Suppose the nodal admittance matrix $Y = G + iB$ of a distribution grid satisfies Assumptions 2 and 3 and the Kron-reduced matrix $Y^r = G^r + iB^r$ from eliminating a passive node $k_0 \in \mathcal{N}_i$ satisfies Assumption 3. Then, Y^r also satisfies Assumption 2. Furthermore, the monotonicity condition, $B_{kk}^r \geq B_{kk}$, holds for all nodes $k \neq k_0$.

See Appendix D.3 for the proof of this lemma.

Stability Condition as a Function of Original Network

Recall that the Kron-reduced network \mathcal{G}^r is obtained by Kron-reducing all passive nodes in all the microgrids. So \mathcal{G}^r only contains active nodes and its dynamical system is defined by model (5.1), where each active node has a swing equation. The next theorem is the key result of this section that states a stability certificate for \mathcal{G}^r but expressed in the states, network topology, and parameters of the original multi- μ G, where microgrids are allowed to have an arbitrary internal structure with DGs, grid-forming inverters, and passive loads.

Theorem 13. Suppose Assumption 2 holds for all the microgrids $\mathcal{G}_i = (\mathcal{N}_i, \mathcal{E}_i)$ for $i \in \mathcal{N}$ in the distribution grid \mathcal{G}^d and Assumption 3 holds for the reduced admittance matrix of \mathcal{G}^d resulting from removing any passive node k_0 in \mathcal{G}_i for any $i \in \mathcal{N}$. Then an equilibrium point of the Kron-reduced grid \mathcal{G}^r is locally asymptotically stable, if the following condition

holds

$$-Q_k - V_k^2 B_{kk} \leq \frac{d_k^2}{2m_k}, \quad \forall k \in \alpha_i, i \in \mathcal{N}, \quad (5.11)$$

where $\alpha_i \subseteq \mathcal{N}_i$ is the set of active nodes in microgrid \mathcal{G}_i and all quantities $Q_k, V_k, B_{kk}, d_k, m_k$ correspond to the original network \mathcal{G}^d .

The proof of this theorem is given in Appendix D.4.

5.5 Numerical Results

In this section, we test various aspects of Theorems 12 and 13, and show how they can be used not only as a fast stability certificate, but also as a quantitative measure of the degree of stability. Furthermore, we demonstrate that condition (5.8) offers a distributed control rule to retain and ensure the stability of interconnected microgrids in an emergency situation.

Let us define

$$\mathcal{S}_i := -Q_i - V_i^2 B_{ii} - \frac{d_i^2}{2m_i},$$

and recall that according to condition (5.8) in Theorem 12, if $\mathcal{S}_i \leq 0, \forall i \in \mathcal{N}$, then the equilibrium point of the multi- μ G system is guaranteed to be asymptotically stable.

5.5.1 Control Schemes and Braess's Paradox

Consider the four-microgrid system shown in Fig. 5.2a and its load-flow and dynamical data tabulated in Case (a1) of Table 5.1. The system is normally operating in this case, but $\mathcal{S}_i > 0, \forall i \in \mathcal{N}$ and Theorem 12 does not certify the stability of the system. Such a positive \mathcal{S}_i for all microgrids indicates that the multi- μ G system, albeit operating normally, is close to its stability margins. We will show how a credible contingency could push such an uncertified system into instability.

Internal Outage Leads to Instability: Subsequent to a generation outage inside microgrid μG_4 , the active power P_{s_4} changes from -4.06 to -7.06 , i.e., this microgrid starts to get 3 p.u. more active power from the linking grid to compensate for its internal outage. In response, microgrid μG_3 aids μG_4 by using its internal generation capacity and changing its active power P_{s_3} from -2.25 to 0.25 . See Case (a2) in Table 5.1. Such a smart, resilient, and self-healing multi- μG system seems very appealing and is indeed one of the main purposes of building these interconnected systems. However, as it was hinted by positive values of \mathcal{S}_i (i.e., violation of condition (5.8)), this new equilibrium point of the multi- μG system is unstable. The instability of this equilibrium point can be verified through eigenvalue analysis and time domain simulation, as depicted in Fig. 5.3. Now, Theorem 12 offers two remedial approaches to ensure system stability.

A Distributed Control Scheme: The first approach is based on a distributed control rule instructing how to change the interface controller parameters d_i or m_i in order to improve the multi- μG stability (recall the characterization of m_i and d_i for microgrids described in Section 5.2.1). Based on local measurements of reactive power Q_i and voltage V_i , each microgrid can increase its damping d_i and/or decrease its virtual inertia to ensure that condition (5.8) is satisfied. The key features of the distributed control scheme include 1) by increasing d_i^2/m_i the system can always be stabilized according to condition (5.8); 2) the operating point of the system is not changed; 3) no information exchange from the neighboring microgrids is required. Implementing this approach, we reach to Case (a3) in Table 5.1. The stability of the same equilibrium point as in Case (a2) is certified.

A Coordinated Control Scheme: The second approach offers coordination of a more general set of corrective actions including change of interface controller parameters d_i or m_i , change of reactive power Q_i or voltage magnitude V_i , and change of network topology. Condition (5.8) instructs which actions will improve the stability of the equilibrium point. The equilibrium point of the system may be moved in the coordinated control scheme to achieve corrective actions with smaller magnitude. To illustrate, we choose a combination

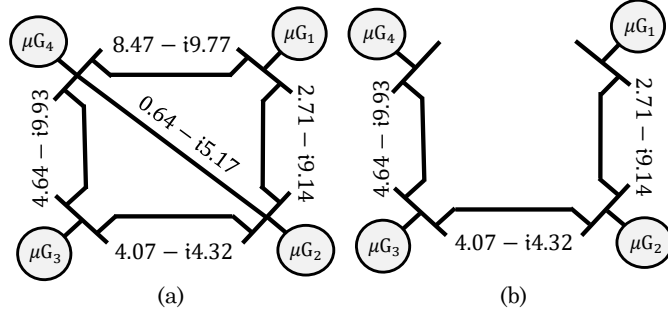


Figure 5.2: Schematic diagram of four coupled microgrids.

Table 5.1: Dynamic parameters and converged load flow data of the four-microgrid system.

	i	m_i	d_i	P_{s_i} [p.u.]	V_i [p.u.]	δ_i^* [rad]	\mathcal{S}_i
Case (a1)	1	5.76	1.03	13.13	0.95	0.75	21.18
	2	9.20	1.61	0.39	0.95	0.28	16.85
	3	9.32	1.86	-2.25	1.05	-0.18	12.12
	4	4.92	1.50	-4.06	1.05	-0.07	16.12
Case (a2)	1	5.76	1.03	13.13	0.96	0.47	21.17
	2	9.20	1.61	0.39	0.95	0.07	16.50
	3	9.32	1.86	0.25	0.99	-0.25	13.08
	4	4.92	1.50	-7.06	1.02	-0.37	13.53
Case (a3)	1	0.50	4.62	13.13	0.96	0.47	-0.074
	2	0.56	4.32	0.39	0.95	0.07	-0.035
	3	0.66	4.19	0.25	0.99	-0.25	-0.037
	4	0.56	3.92	-7.06	1.02	-0.37	-0.001
Case (b)	1	0.80	4.03	5.72	1.05	0.8	-0.0036
	2	0.56	3.90	0.40	1.05	0.24	-0.0668
	3	0.70	3.78	0.25	1.05	-0.62	-0.0057
	4	0.68	3.49	-2.11	0.95	-0.8	-0.0205

of all available options to find a stable equilibrium point. Let us reconfigure the network by switching two lines off (see Fig. 5.2(b)) and also modify the dynamic parameters to reach Case (b) in Table 5.1. The new equilibrium point satisfies condition (5.8) and therefore is stable. Note that by removing distribution lines from case (a), the value of $|B_{ii}|, \forall i \in \{1, 2, 4\}$ will decrease. Moreover, increasing damping and decreasing inertia will increase the right-hand side of (5.8). Consistent with Braess's Paradox, switching off two lines indeed improves system stability.

Table 5.2: Parameters to generate synthetic networks. $U([\ell_1, \ell_2])$ is uniform distribution on interval $[\ell_1, \ell_2]$.

Admittances	$b = U([-1, 0])$ [p.u.], $g = b \times U([0, 0.5])$ [p.u.]
Voltages	$V = U([0.95, 1.05])$ [p.u.], $\delta = U([-0.5, 0.5])$ [rad]
Interface settings	$d = U([1.5, 3])$, $m = U([0.4, 2])$ [sec.]

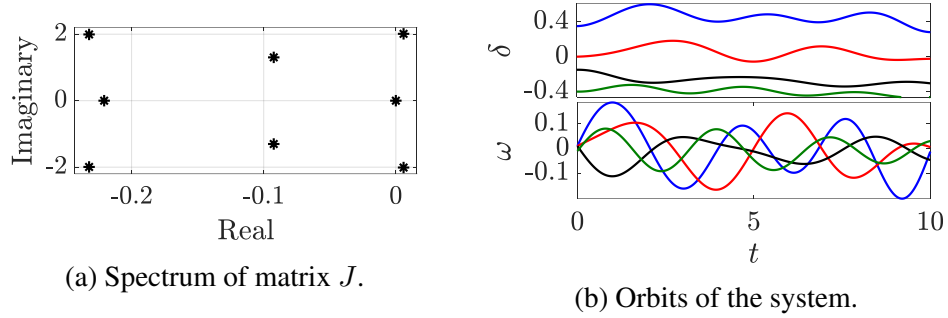


Figure 5.3: Verifying the instability of the equilibrium point in Case (a2) of the four-microgrid system. (a) There exist two eigenvalues with positive real part. (b) Starting from a neighborhood of the equilibrium point, the orbits of the system diverge to infinity.

5.5.2 Stability Measure and Location of Eigenvalues

As mentioned above, condition (5.8) can be used not only as a fast stability certificate, but also as a quantitative measure of the degree of stability. To further illustrate this, consider the IEEE 33-bus network during islanded operation, consisting of 4 DGs and 2 storage units interfaced via VSIs [98]. The load, line, and DG data can be found in [69, 99, 98], and Table 5.3. Here, we first compute the Kron-reduced system to obtain a network of interconnected DGs. Note that Theorem 13 is applicable to this reduced network because by Lemma 7 the dynamical model of interconnected droop-controlled VSIs can be reparametrized as the swing equation model (5.1). Observe that according to Fig. 5.1, the assumption $\varphi_{ik} \in (0, \pi)$ holds in this system. We assume the network is operating at 80% of the nominal load, and the interface parameters k_i , τ_i , m_i , d_i , and setpoints are designed following Theorem 13 (see Table 5.3). The simulations are carried out in MATLAB.

Fig. 5.4 shows the spectrum of matrix J along with the value of $\mathcal{S}_i, \forall i \in \{1, \dots, 6\}$ under three different operating points referred to as Cases 1 to 3. In Case 1, $\mathcal{S}_i > 0$ for $i = 4$ and $i = 6$. Moreover, in Case 2, $\mathcal{S}_i > 0$ for $i = 6$. Case 3 is the only case where

Table 5.3: Parameters of the IEEE 33-bus system.

i	1	2	3	4	5	6
Bus index	8	13	16	19	25	26
DER type	DG	DG	DG	VSI	DG	VSI
d_i	1.7	1.7	2	1	2	1.2
m_i	0.5	0.5	0.6	0.7	0.6	0.7
Base values	$P_{\text{base}} = 100 \text{ MW}, V_{\text{base}} = 12.66 \text{ kV}$					

$\mathcal{S}_i \leq 0, \forall i \in \{1, \dots, 6\}$, and condition (5.11) guarantees that the system is asymptotically stable in this case. According to this figure, in all three cases the non-zero eigenvalues of J are located in the left half plane and the system is asymptotically stable. However, from Case 1 to Case 3, as we move towards satisfying $\mathcal{S}_i \leq 0, \forall i \in \{1, \dots, 6\}$, the magnitude of the imaginary parts of the eigenvalues in $\sigma(J)$ is reduced, and their real parts are mainly moved towards $-\infty$, thereby making the system less oscillatory. Indeed, a smaller value of \mathcal{S}_i (say when $\mathcal{S}_i > 0$) means the violation of constraint $\mathcal{S}_i \leq 0$ is smaller, and it is easier to enforce condition (5.11), and therefore to make sure we have reached stability. Evidently, the value of \mathcal{S}_i can be seen as a stability measure, i.e., it roughly indicates how stable the system is. This application of condition (5.11) was also shown in the four-microgrid test case in the previous section.

Finally, Fig. 5.5 depicts the frequency trajectories of the system in Case 3, where condition (5.11) holds. As can be seen, after a transient, all frequency deviations converge to zero, and the equilibrium point, which was certified by Theorem 13, is asymptotically stable. The initial condition in this simulation is chosen arbitrary within a reasonable range.

5.5.3 Larger-Scale Systems

Next, we test the proposed stability certificate on a set of large-scale synthetic networks. Figs. 5.6b and 5.6e show two examples of such multi- μG networks consisting of 50 and 100 microgrids, respectively. The network graphs are randomly generated, the sparsity patterns of their adjacency matrix are depicted in Figs. 5.6a and 5.6d, and the corresponding static and dynamic parameters are given Table 5.2. Note also that the diameter (i.e., the

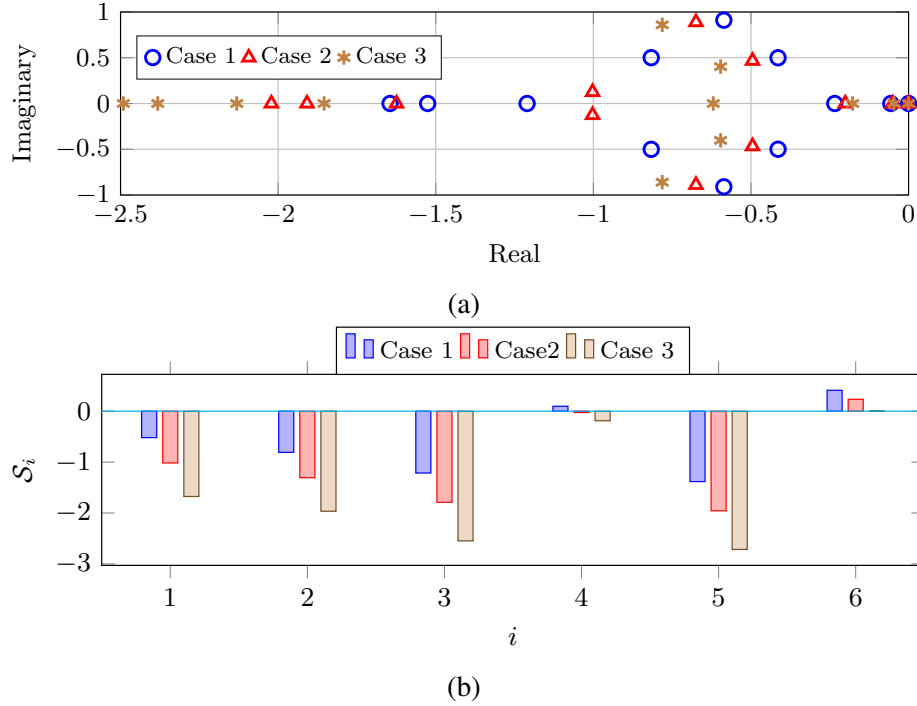


Figure 5.4: Illustration of stability certificate on the IEEE 33-bus system. (a) Spectrum of matrix J . (b) Value of stability index S_i in different buses.

longest graph geodesic) of the graphs 5.6b and 5.6e are 6 and 8, respectively. Adopting the aforementioned distributed control rule, each microgrid adjusts its controller parameters d_i and m_i (within the permissible range) to meet condition (5.8). Obeying this rule at an equilibrium point guarantees that all nonzero eigenvalues of the Jacobian matrix J have negative real part, and consequently, the equilibrium point is locally asymptotically stable (see Figs. 5.6c and 5.6f).

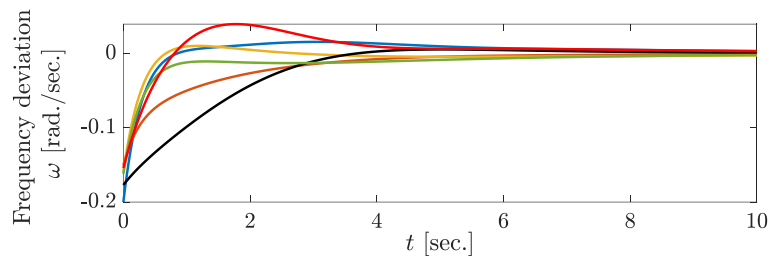


Figure 5.5: Trajectories of the frequency deviation ω_i for 6 DERs in the IEEE 33-bus system.

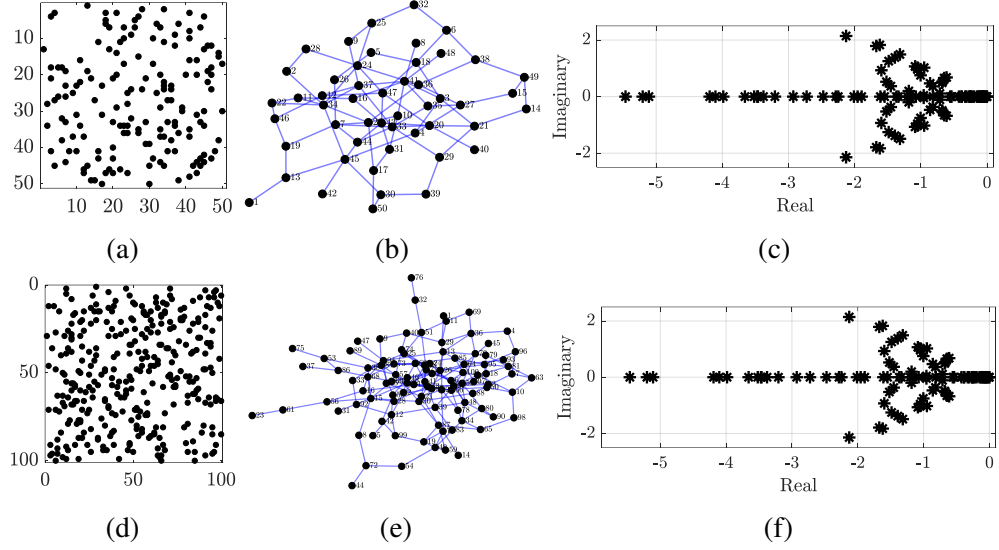


Figure 5.6: Synthetic multi- μ G networks satisfying condition (5.8). (a) Sparsity pattern of the 50-microgrid adjacency matrix, black points are ones. (b) 50-microgrid network. (c) Eigenvalues of the 50-microgrid network. (d) Sparsity pattern of the 100-microgrid adjacency matrix, black points are ones. (e) 100-microgrid network. (f) Eigenvalues of the 100-microgrid network.

5.6 Final Remarks

This chapter proposes new stability certificates for the small-signal stability of multi- μ Gs. In particular, we prove in Theorem 12 that an equilibrium point of a multi- μ G system is locally asymptotically stable if either i) the network is lossless; or ii) in a lossy network, a local condition (i.e., condition (5.8)) is satisfied at each microgrid PCC/DER, which roughly speaking requires:

$$\left(\begin{array}{c} \text{Reactive power} \\ \text{absorption} \end{array} \right) + \frac{\text{Voltage magnitude}}{\text{Line reactance}} \leq \frac{\text{Damping}^2}{2 \cdot \text{Inertia}}.$$

This condition sheds new light on the interplay of system stability, network topology, and dynamic parameters. It also provides a fully distributed control scheme that is guaranteed to stabilize the multi- μ G system. The new certificate also reveals an analog of Braess's Paradox in multi- μ G control that adding more lines in the linking grid may worsen system

stability, and switching off lines may improve stability margin. The proposed condition in Theorems 12 and 13 can improve the situational awareness of system operators by providing a fast stability certificate as well as showing how different corrective actions would make the equilibrium point stable. In the literature, several stability criteria are developed based on various dynamical models, focusing on different aspects of stability. Finding a proper way to compare and merge these criteria and deriving a unified stability criterion will be an interesting direction for future work, and the framework proposed in [90, 91, 92] is a promising step towards this direction.

CHAPTER 6

A STABILITY CERTIFICATE FOR DROOP-CONTROLLED INVERTERS

In the previous chapters, we studied second-order swing equations, where voltage magnitudes were assumed to be constant. In this chapter, we aim to relax this assumption and study swing equations where voltage magnitudes are also considered state variables. Such a third-order model characterizes the dynamics of droop-controlled inverters. Accordingly, this chapter is also motivated by the growing interest in the smart grid technology and the prominent role of droop-controlled inverters in this new technology. We attempt to answer the same fundamental question: Under what conditions an equilibrium point of third-order inverter model is asymptotically stable? After making a number of reasonable and practical assumptions, we strive to derive a set of sufficient conditions for the local stability of the equilibrium points of these models.

6.1 Introduction

6.1.1 Related Work

In the literature, various models with different complexities have been adopted for droop-controlled inverters, including first-order models [88], second-order models [9, 11, 13], third-order models [89], and higher-order models [90, 91, 92]. Each model is useful for studying a particular aspect of droop-controlled inverters such as their frequency stability, voltage stability, or electromagnetic transients. Swing equations with variable voltage magnitudes appear in third-order models. For instance, in [89], each inverter is modeled by a third-order differential equation including swing equations with variable voltage magnitudes. Using this model, sufficient conditions are derived for boundedness of trajectories in lossy microgrids as well as asymptotic stability of equilibrium points in lossless microgrids.

In the present chapter, we adopt a similar third-order model for each inverter. In comparison with [89], in the lossy case, we derive a sufficient condition in this chapter that certifies the asymptotic stability of equilibrium points instead of boundedness of trajectories as in [89].

In a similar vein, a distributed safety certification for droop-controlled inverters is proposed in [100]. Moreover, a sum-of-squares based algorithm is used to present a computational approach to obtain these safety certificates in a distributed manner. One major drawback in such methods is their scalability. In this chapter, we strive to cope with this challenge and develop a stability certificate for large-scale systems.

6.1.2 Main Results

In this chapter, we aim to extend our previous stability results to swing equations with variable voltage magnitudes. This leads to a third-order model which characterizes the dynamics of voltage angles, frequency deviations, and voltage magnitudes. There are two main contributions in the present chapter.

- We scrutinize the Jacobian of the third-order swing equations with variable voltage magnitude and strive to find its relation with the Jacobian of power flow equations. After investigating its spectral properties, we find an structural property of the Jacobian matrix which stems from the loose physical linkage between active and reactive powers. Taking advantage of this inherent property, we make a reasonable assumption (referred to as the decoupling assumption) and develop sufficient conditions under which an equilibrium point of the third-order model is asymptotically stable. Similar to the sufficient conditions developed in previous chapters, the derived conditions are easy to check, use only local information, and are suitable for real-time monitoring and fast stability assessment.
- We further investigate the aforementioned decoupling assumption and study the impact of coupling terms on the eigenvalues of the Jacobian matrix. Although the loose

physical linkage between active and reactive powers is a well-known property in power systems and has been the basis for the fast decoupled load flow [31], we are not aware of any study on the impact of coupling terms and the robustness of the decoupled model under coupling perturbations. Here for the first time, we make use of the existing theorems in the literature such as Bauer–Fike theorem to provide residual bounds for the perturbation of Jacobian eigenvalues as the coupling terms change. Our findings shed light on the validity of the decoupling assumption for practical purposes.

6.1.3 Chapter Outline

The rest of this chapter is organized as follows. Section 6.2 introduces a third-order model for droop-controlled inverters. In Section 6.3, the third-order model is linearized and the linkage between its Jacobian and the Jacobian of the power flow function is established. Section 6.4 is devoted to our main results on the stability of equilibrium points of the third-order model. In Section 6.5, we analyze the spectrum of the third-order model Jacobian under perturbations. Section 6.6 further illustrates the developed theoretical results through numerical examples, and finally, the chapter concludes with Section 6.7.

6.2 Droop-Controlled Inverter Model

The mathematical model for a set of droop-controlled inverters $\mathcal{N} = \{1, \dots, n\}$, $n \in \mathbb{N}$ is described by the following system of ODEs [89, 100]:

$$\dot{\delta}_i = \omega_i, \quad \forall i \in \mathcal{N} \quad (6.1a)$$

$$\tau_i \dot{\omega}_i = -\omega_i + \lambda_i^p (P_i^{set} - P_i), \quad \forall i \in \mathcal{N} \quad (6.1b)$$

$$\tau_i \dot{v}_i = v_i^0 - v_i + \lambda_i^q (Q_i^{set} - Q_i), \quad \forall i \in \mathcal{N} \quad (6.1c)$$

where for each $i \in \mathcal{N}$, $\lambda_i^p > 0$ and $\lambda_i^q > 0$ are the droop coefficients associated with the active power vs. frequency and the reactive power vs. voltage droop curves, respectively. τ_i is the time constant of a low-pass filter used for the active and reactive power measurements. δ_i, ω_i and v_i are the voltage angle, frequency deviation, and voltage magnitude. v_i^0 is the nominal voltage magnitude. P_i^{set} and Q_i^{set} are the active power and reactive power set points. More importantly, P_i and Q_i are the active and reactive power injected into the network:

$$P_i = \sum_{j=1}^n v_i v_j Y_{ij} \cos(\theta_{ij} - \delta_i + \delta_j), \quad \forall i \in \mathcal{N} \quad (6.2a)$$

$$Q_i = - \sum_{j=1}^n v_i v_j Y_{ij} \sin(\theta_{ij} - \delta_i + \delta_j), \quad \forall i \in \mathcal{N} \quad (6.2b)$$

where $Y_{ij} \angle \theta_{ij}$ is the (i, j) entry of the reduced admittance matrix. The admittance matrix encodes the underlying graph structure of the power grid, which is assumed to be a connected graph in this chapter.

Remark 9. *The equilibrium points of model (6.1) are of the form $(\delta^*, 0, v^*) \in \mathbb{R}^{3n}$, where δ^* and v^* are solutions to equations*

$$P_i = P_i^{\text{set}}, \quad v_i^0 - v_i + \lambda_i^q (Q_i^{\text{set}} - Q_i) = 0, \quad \forall i \in \mathcal{N}.$$

Note that if $v^ = v^0$, then equilibrium points are of the form $(\delta^*, 0, v^0) \in \mathbb{R}^{3n}$, where δ^* is a solution to power flow equations*

$$P_i = P_i^{\text{set}}, \quad Q_i = Q_i^{\text{set}}, \quad v_i = v_i^0, \quad \forall i \in \mathcal{N}.$$

6.3 Linearization and Spectrum of Jacobian

Assuming $\tau_i > 0$, the dynamical model (6.1) can be written in the following vector form:

$$\begin{bmatrix} \dot{\delta} \\ \dot{\omega} \\ \dot{v} \end{bmatrix} = \begin{bmatrix} \omega \\ -T^{-1}\omega + T^{-1}\Lambda^p(P^{\text{set}} - P(\delta, v)) \\ T^{-1}v^0 - T^{-1}v + T^{-1}\Lambda^q(Q^{\text{set}} - Q(\delta, v)) \end{bmatrix}, \quad (6.3)$$

where $T = \text{diag}(\tau_1, \dots, \tau_n)$, $\Lambda^p = \text{diag}(\lambda_1^p, \dots, \lambda_n^p)$, and $\Lambda^q = \text{diag}(\lambda_1^q, \dots, \lambda_n^q)$. The Jacobian of vector field of (6.3) is given by

$$J := \begin{bmatrix} 0 & I & 0 \\ -T^{-1}\Lambda^p\nabla_\delta P & -T^{-1} & -T^{-1}\Lambda^p\nabla_v P \\ -T^{-1}\Lambda^q\nabla_\delta Q & 0 & -T^{-1}(I + \Lambda^q\nabla_v Q) \end{bmatrix} \in \mathbb{R}^{3n \times 3n}, \quad (6.4)$$

where $I \in \mathbb{R}^{n \times n}$ is the identity matrix and $0 \in \mathbb{R}^{n \times n}$ is the zero matrix. Moreover, $[\nabla_\delta P, \nabla_v P] \in \mathbb{R}^{n \times 2n}$ is the Jacobian of the active flow function $P : \mathbb{R}^{2n} \rightarrow \mathbb{R}^n$ given by $(\delta, v) \mapsto P(\delta, v)$ in (6.2a). Likewise, $[\nabla_\delta Q, \nabla_v Q] \in \mathbb{R}^{n \times 2n}$ is the Jacobian of the reactive flow function $Q : \mathbb{R}^{2n} \rightarrow \mathbb{R}^n$ given by $(\delta, v) \mapsto Q(\delta, v)$ in (6.2b). Let us also define

$$L := \begin{bmatrix} \nabla_\delta P & \nabla_v P \\ \nabla_\delta Q & \nabla_v Q \end{bmatrix} \in \mathbb{R}^{2n \times 2n}. \quad (6.5)$$

Specifically, L is the Jacobian of the power flow vector field $(P, Q) : \mathbb{R}^{2n} \rightarrow \mathbb{R}^{2n}$ given by $(\delta, v) \mapsto (P(\delta, v), Q(\delta, v))$. We now look into the spectral properties of L . Let us use the notation $L^1 := \nabla_\delta P$, $L^2 := \nabla_v P$, $L^3 := \nabla_\delta Q$, and $L^4 := \nabla_v Q$. According to the power flow equations (6.2), the entries of matrix L are

$$L_{ii}^1 = \frac{\partial P_i}{\partial \delta_i} = \sum_{j=1, j \neq i}^n v_i v_j Y_{ij} \sin(\theta_{ij} - \delta_i + \delta_j), \quad \forall i \in \mathcal{N} \quad (6.6)$$

$$L_{ij}^1 = \frac{\partial P_i}{\partial \delta_j} = -v_i v_j Y_{ij} \sin(\theta_{ij} - \delta_i + \delta_j), \quad \forall i \in \mathcal{N}, j \neq i \quad (6.7)$$

$$L_{ii}^2 = \frac{\partial P_i}{\partial v_i} = 2v_i Y_{ii} \cos(\theta_{ii}) + \sum_{j=1, j \neq i}^n v_j Y_{ij} \cos(\theta_{ij} - \delta_i + \delta_j), \quad \forall i \in \mathcal{N} \quad (6.8)$$

$$L_{ij}^2 = \frac{\partial P_i}{\partial v_j} = v_i Y_{ij} \cos(\theta_{ij} - \delta_i + \delta_j), \quad \forall i \in \mathcal{N}, j \neq i \quad (6.9)$$

$$L_{ii}^3 = \frac{\partial Q_i}{\partial \delta_i} = \sum_{j=1, j \neq i}^n v_i v_j Y_{ij} \cos(\theta_{ij} - \delta_i + \delta_j), \quad \forall i \in \mathcal{N} \quad (6.10)$$

$$L_{ij}^3 = \frac{\partial Q_i}{\partial \delta_j} = -v_i v_j Y_{ij} \cos(\theta_{ij} - \delta_i + \delta_j), \quad \forall i \in \mathcal{N}, j \neq i \quad (6.11)$$

$$L_{ii}^4 = \frac{\partial Q_i}{\partial v_i} = -2v_i Y_{ii} \sin(\theta_{ii}) - \sum_{j=1, j \neq i}^n v_j Y_{ij} \sin(\theta_{ij} - \delta_i + \delta_j), \quad \forall i \in \mathcal{N} \quad (6.12)$$

$$L_{ij}^4 = \frac{\partial Q_i}{\partial v_j} = -v_i Y_{ij} \sin(\theta_{ij} - \delta_i + \delta_j), \quad \forall i \in \mathcal{N}, j \neq i. \quad (6.13)$$

Matrix L plays a prominent role in the spectrum of the Jacobian matrix J (and as a consequence, in the stability properties of the equilibrium points of the third-order model). We illustrate this role in the following subsection.

6.3.1 Spectral Relationship Between Matrices J and L

The next proposition shows that the eigenvalues of J and L are linked through a singularity constraint.

Proposition 7. $\lambda \in \sigma(J)$ if and only if the matrix $\mathcal{Q}(\lambda) := \Lambda L + \text{diag}(\lambda^2 T + \lambda I, \lambda T + I)$ is singular. Here $\Lambda := \text{diag}(\Lambda^p, \Lambda^q)$.

Proof. Let $\lambda \in \sigma(J)$ and (x, y, z) be the corresponding eigenvector. Then

$$\begin{bmatrix} 0 & I & 0 \\ -T^{-1}\Lambda^p\nabla_\delta P & -T^{-1} & -T^{-1}\Lambda^p\nabla_v P \\ -T^{-1}\Lambda^q\nabla_\delta Q & 0 & -T^{-1}(I + \Lambda^q\nabla_v Q) \end{bmatrix} \begin{bmatrix} x \\ y \\ z \end{bmatrix} = \lambda \begin{bmatrix} x \\ y \\ z \end{bmatrix} \quad (6.14)$$

which implies

$$\begin{cases} y = \lambda x, \\ -[T^{-1}\Lambda^p\nabla_\delta P]x - T^{-1}y - [T^{-1}\Lambda^p\nabla_v P]z = \lambda y, \\ -[T^{-1}\Lambda^q\nabla_\delta Q]x - T^{-1}(I + \Lambda^q\nabla_v Q)z = \lambda z. \end{cases} \quad (6.15)$$

Substituting $y = \lambda x$ in the second and third equations, we get

$$\begin{cases} [T^{-1}\Lambda^p\nabla_\delta P]x + \lambda T^{-1}x + \lambda^2 x + [T^{-1}\Lambda^p\nabla_v P]z = 0, \\ [T^{-1}\Lambda^q\nabla_\delta Q]x + T^{-1}(I + \Lambda^q\nabla_v Q)z + \lambda z = 0, \end{cases} \quad (6.16)$$

or equivalently

$$\begin{cases} [\Lambda^p\nabla_\delta P]x + [\Lambda^p\nabla_v P]z + \lambda x + \lambda^2 Tx = 0, \\ [\Lambda^q\nabla_\delta Q]x + [\Lambda^q\nabla_v Q]z + z + \lambda Tz = 0, \end{cases} \quad (6.17)$$

which can be written in the matrix form

$$\begin{bmatrix} \Lambda^p \\ \Lambda^q \end{bmatrix} \begin{bmatrix} \nabla_\delta P & \nabla_v P \\ \nabla_\delta Q & \nabla_v Q \end{bmatrix} \begin{bmatrix} x \\ z \end{bmatrix} + \begin{bmatrix} \lambda^2 T + \lambda I & \\ & \lambda T + I \end{bmatrix} \begin{bmatrix} x \\ z \end{bmatrix} = 0. \quad (6.18)$$

Thus, $\mathcal{Q}(\lambda) := \Lambda L + \text{diag}(\lambda^2 T + \lambda I, \lambda T + I)$ is singular. Conversely, suppose there exists $\lambda \in \mathbb{C}$ such that $\mathcal{Q}(\lambda)$ is singular. Choose a nonzero $(x, z) \in \ker(\mathcal{Q}(\lambda))$ and let $y := \lambda x$. Accordingly, the characteristic equation (6.14) holds, and consequently, λ is an eigenvalue of J . \square

The next proposition illustrates how the kernels of J and L are related.

Proposition 8. *The Jacobian matrix J is nonsingular if and only if the matrix $N := L + \text{diag}(0, \Lambda^{-q})$ is nonsingular. Moreover, $\ker(N) = \text{proj}(\ker(J))$, i.e., the kernel of N*

is the orthogonal projection of the kernel of J onto the linear subspace $\mathbb{R}^n \times \{0\} \times \mathbb{R}^n$. Finally, the geometric multiplicity of the zero eigenvalue in $\sigma(J)$ and $\sigma(N)$ are equal.

Proof. According to Proposition 7, we have $0 \in \sigma(J)$ if and only if $Q(0) := \Lambda L + \text{diag}(0, I)$ is singular, where $\Lambda := \text{diag}(\Lambda^p, \Lambda^q)$. This is equivalent to the singularity of $N := L + \text{diag}(0, \Lambda^{-q})$. Moreover, according to the proof of Proposition 7, we have $(x, 0, z) \in \ker(J)$ if and only if $(x, z) \in \ker(N)$. This shows the second part of the proposition.

Finally, we know $\{(x_1, 0, z_1), \dots, (x_m, 0, z_m)\}$ is a set of linearly independent eigenvectors in $\ker(J)$ if and only if $\{(x_1, z_1), \dots, (x_m, z_m)\}$ is a set of linearly independent eigenvectors in $\ker(N)$, i.e., $\dim(\ker(J)) = \dim(\ker(N))$. \square

As the role of L in the spectrum of J became more clear, observe that matrices L^1 and L^3 have zero row sum. According to the next proposition, this property results in the singularity of the Jacobian matrix J .

Proposition 9. *The Jacobian matrix J defined in (6.4) has a zero eigenvalue with the corresponding right eigenvector $(\mathbf{1}, \mathbf{0}, \mathbf{0}) \in \mathbb{R}^{3n}$.*

Proof. According to Proposition 8, $0 \in \sigma(J)$ if and only if the matrix $N := L + \text{diag}(0, \Lambda^{-q})$ is singular. Set $u := (\mathbf{1}, \mathbf{0}) \in \mathbb{R}^{2n}$

$$Nu = \begin{bmatrix} L^1 & L^2 \\ L^3 & L^4 + \Lambda^{-q} \end{bmatrix} \begin{bmatrix} \mathbf{1} \\ \mathbf{0} \end{bmatrix} = \begin{bmatrix} L^1 \mathbf{1} \\ L^3 \mathbf{1} \end{bmatrix} = 0,$$

where the last equality follows from the fact that matrices L^1 and L^3 have zero row sum. This implies that $0 \in \sigma(N)$, i.e., N is singular. The second part of Proposition 8 implies that $(\mathbf{1}, \mathbf{0}, \mathbf{0}) \in \mathbb{R}^{3n}$ is the corresponding eigenvector of the Jacobian matrix J . \square

6.4 Stability of Droop-Controlled Inverters

Now we are ready to present our main result on the stability of equilibrium points in the droop-controlled inverter model (6.1). We first make use of the loose physical interaction between active power P and reactive power Q in power systems.

Assumption 4 ($P - \delta/Q - v$ decoupling). *In matrix L defined in (6.5), at least one of the two matrices $\nabla_v P$ and $\nabla_\delta Q$ is negligible.*

The next lemma shows the role of $P - \delta/Q - v$ decoupling in the spectrum of the Jacobian matrix J :

Lemma 9. *Under Assumption 4, the spectrum of the Jacobian matrix J defined in (6.4) is the union of spectrum of two matrices J^1 and J^4 , i.e., $\sigma(J) = \sigma(J^1) \cup \sigma(J^4)$, where*

$$J^1 := \begin{bmatrix} 0 & I \\ -T^{-1}\Lambda^p\nabla_\delta P & -T^{-1} \end{bmatrix}, \quad J^4 := -T^{-1}(I + \Lambda^q\nabla_v Q) \quad (6.19)$$

Proof. The Jacobian matrix J presented in (6.4) can be written as

$$J = \begin{bmatrix} J^1 & J^2 \\ J^3 & J^4 \end{bmatrix},$$

where J^1 and J^4 are defined in (6.19), and J^2 and J^3 are

$$J^2 = \begin{bmatrix} 0 \\ -T^{-1}\Lambda^p\nabla_v P \end{bmatrix}, \quad J^3 = \begin{bmatrix} -T^{-1}\Lambda^q\nabla_\delta Q & 0 \end{bmatrix}. \quad (6.20)$$

If $\nabla_v P = 0$, then $J^2 = 0$. In this case, for any $\lambda \in \sigma(J)$, there exists a nonzero eigenvector

(x, y) such that

$$\begin{bmatrix} J^1 & 0 \\ J^3 & J^4 \end{bmatrix} \begin{bmatrix} x \\ y \end{bmatrix} = \lambda \begin{bmatrix} x \\ y \end{bmatrix}, \quad (6.21)$$

that is, $J^1x = \lambda x$ and $J^3x + J^4y = \lambda y$. If $x \neq 0$, from $J^1x = \lambda x$, we conclude that $\lambda \in \sigma(J^1)$. If $x = 0$, then $J^4y = \lambda y$, i.e., $\lambda \in \sigma(J^4)$. Hence, $\sigma(J) \subset \sigma(J^1) \cup \sigma(J^4)$.

Conversely, suppose $\lambda \in \sigma(J^1) \cup \sigma(J^4)$. There are two cases:

1. If $\lambda \in \sigma(J^4)$, then there exists a nonzero y such that $J^4y = \lambda y$. Set $x = 0$, and observe that (x, y) in this case satisfies (6.21). Hence, $\lambda \in \sigma(J)$.
2. If $\lambda \in \sigma(J^1)$, then there exists a nonzero x such that $J^1x = \lambda x$. Consider the following two cases: Case 1) If $\lambda \notin \sigma(J^4)$, then $J^4 - \lambda I$ is nonsingular, and we can define $y := -(J^4 - \lambda I)^{-1} J^3x$. Thus, (x, y) satisfies (6.21). Hence, $\lambda \in \sigma(J)$. Case 2) If $\lambda \in \sigma(J^4)$, then we have already proved that $\lambda \in \sigma(J)$.

This shows that $\sigma(J) \supset \sigma(J^1) \cup \sigma(J^4)$. Combining this with the result of the previous step, we conclude $\sigma(J) = \sigma(J^1) \cup \sigma(J^4)$. Similar argument can be proved under the condition that $\nabla_\delta Q = 0$, that is, $J^3 = 0$. \square

Let us define the following set:

$$\Omega = \{(\delta, \omega, v) \in \mathbb{R}^{3n} : 0 < \theta_{ij} + \delta_i - \delta_j < \pi, \forall (i, j) \in \mathcal{A}, v > 0\}, \quad (6.22)$$

where \mathcal{A} is the set of arcs associated with the underlying graph of the power grid. The next theorem provides a sufficient condition for the stability of voltage dynamics (6.1c).

Theorem 14. *Let $(\delta^*, 0, v^*) \in \Omega$, and suppose for all $i \in \mathcal{N}$, we have positive droop coefficients $\lambda_i^p > 0$, $\lambda_i^q > 0$ and positive time constant $\tau_i > 0$. If the condition*

$$-Q_i + \sum_{j=1}^n (v_i^*)^2 Y_{ij} \sin(\theta_{ij} - \delta_i^* + \delta_j^*) \leq \frac{v_i^*}{\lambda_i^q}, \quad \forall i \in \mathcal{N} \quad (6.23)$$

holds then the nonzero eigenvalues of the matrix $J^4 := -T^{-1}(I + \Lambda^q \nabla_v Q)$ are located in the open left-half plane.

Proof. According to the Gershgorin circle theorem, every eigenvalue of J^4 lies within at least one of the Gershgorin discs $\mathbb{D}(c_i, r_i)$. Note $\mathbb{D}(c_i, r_i)$ is a closed disc centered at c_i with radius r_i such that

$$c_i = -\frac{1}{\tau_i} - \frac{\lambda_i^q}{\tau_i} L_{ii}^4 = -\frac{1}{\tau_i} + \frac{\lambda_i^q}{\tau_i} (2v_i^* Y_{ii} \sin(\theta_{ii}) + \sum_{j=1, j \neq i}^n v_j^* Y_{ij} \sin(\theta_{ij} - \delta_i^* + \delta_j^*)), \quad (6.24)$$

$$r_i = \sum_{j=1, j \neq i}^n \frac{\lambda_i^q}{\tau_i} |L_{ij}^4| = \sum_{j=1, j \neq i}^n \frac{\lambda_i^q}{\tau_i} v_i^* Y_{ij} \sin(\theta_{ij} - \delta_i^* + \delta_j^*), \quad (6.25)$$

where $L^4 = \nabla_v Q$. In (6.25), we have used the assumption of $(\theta_{ij} - \delta_i^* + \delta_j^*) \in (0, \pi), \forall (i, j) \in \mathcal{A}$, which implies $\sin(\theta_{ij} - \delta_i^* + \delta_j^*) > 0, \forall (i, j) \in \mathcal{A}$. Hence, $r_i \geq 0$ for all $i \in \mathcal{N}$. A sufficient condition for the stability of J^4 is to have all discs $\mathbb{D}(c_i, r_i)$ on the left-half plane, i.e., $c_i \leq 0, |c_i| \geq r_i$. The condition $c_i \leq 0$ is equivalent to

$$c_i \leq 0 \iff -\frac{1}{\tau_i} + \frac{\lambda_i^q}{\tau_i} (2v_i^* Y_{ii} \sin(\theta_{ii}) + \sum_{j=1, j \neq i}^n v_j^* Y_{ij} \sin(\theta_{ij} - \delta_i^* + \delta_j^*)) \leq 0 \quad (6.26)$$

$$\iff -1 + \lambda_i^q \left(2v_i^* Y_{ii} \sin(\theta_{ii}) + \sum_{j=1, j \neq i}^n v_j^* Y_{ij} \sin(\theta_{ij} - \delta_i^* + \delta_j^*) \right) \leq 0 \quad (6.27)$$

$$\iff \lambda_i^q \left(2v_i^* Y_{ii} \sin(\theta_{ii}) + \sum_{j=1, j \neq i}^n v_j^* Y_{ij} \sin(\theta_{ij} - \delta_i^* + \delta_j^*) \right) \leq 1 \quad (6.28)$$

$$\iff \lambda_i^q \left(2(v_i^*)^2 Y_{ii} \sin(\theta_{ii}) + \sum_{j=1, j \neq i}^n v_i^* v_j^* Y_{ij} \sin(\theta_{ij} - \delta_i^* + \delta_j^*) \right) \leq v_i^* \quad (6.29)$$

$$\iff \lambda_i^q \left((v_i^*)^2 Y_{ii} \sin(\theta_{ii}) + \sum_{j=1}^n v_i^* v_j^* Y_{ij} \sin(\theta_{ij} - \delta_i^* + \delta_j^*) \right) \leq v_i^* \quad (6.30)$$

$$\iff \lambda_i^q ((v_i^*)^2 Y_{ii} \sin(\theta_{ii}) - Q_i) \leq v_i^* \quad (6.31)$$

$$\iff (v_i^*)^2 Y_{ii} \sin(\theta_{ii}) - Q_i \leq \frac{v_i^*}{\lambda_i^q}. \quad (6.32)$$

Next, the condition $|c_i| \geq r_i$ is equivalent to (note that since $c_i \leq 0$ from the above condition, we get $|c_i| = -c_i$):

$$\begin{aligned} |c_i| \geq r_i &\iff \frac{1}{\tau_i} - \frac{\lambda_i^q}{\tau_i} \left(2v_i^* Y_{ii} \sin(\theta_{ii}) + \sum_{j=1, j \neq i}^n v_j^* Y_{ij} \sin(\theta_{ij} - \delta_i^* + \delta_j^*) \right) \\ &\geq \frac{\lambda_i^q}{\tau_i} \sum_{j=1, j \neq i}^n v_i^* Y_{ij} \sin(\theta_{ij} - \delta_i^* + \delta_j^*). \end{aligned}$$

Equivalently,

$$|c_i| \geq r_i \iff \frac{1}{\lambda_i^q} - \left(2v_i^* Y_{ii} \sin(\theta_{ii}) + \sum_{j=1, j \neq i}^n v_j^* Y_{ij} s_{ij} \right) \geq \sum_{j=1, j \neq i}^n v_i^* Y_{ij} s_{ij} \quad (6.33)$$

$$\iff \frac{1}{\lambda_i^q} \geq 2v_i^* Y_{ii} \sin(\theta_{ii}) + \sum_{j=1, j \neq i}^n v_j^* Y_{ij} s_{ij} + \sum_{j=1, j \neq i}^n v_i^* Y_{ij} s_{ij} \quad (6.34)$$

$$\iff \frac{v_i^*}{\lambda_i^q} \geq 2(v_i^*)^2 Y_{ii} \sin(\theta_{ii}) + \sum_{j=1, j \neq i}^n v_i^* v_j^* Y_{ij} s_{ij} + \sum_{j=1, j \neq i}^n (v_i^*)^2 Y_{ij} s_{ij} \quad (6.35)$$

$$\iff \frac{v_i^*}{\lambda_i^q} \geq -Q_i + (v_i^*)^2 Y_{ii} \sin(\theta_{ii}) + \sum_{j=1, j \neq i}^n (v_i^*)^2 Y_{ij} s_{ij} \quad (6.36)$$

$$\iff \frac{v_i^*}{\lambda_i^q} \geq -Q_i + \sum_{j=1}^n (v_i^*)^2 Y_{ij} s_{ij}. \quad (6.37)$$

where $s_{ij} := \sin(\theta_{ij} - \delta_i^* + \delta_j^*)$. Since $(\theta_{ij} - \delta_i^* + \delta_j^*) \in (0, \pi), \forall (i, j) \in \mathcal{A}$, we have $\sin(\theta_{ij} - \delta_i^* + \delta_j^*) > 0$, and (6.37) implies (6.32), hence $c_i \leq 0$. Thus, (6.23) is a sufficient condition for the nonzero eigenvalues of J^4 to be in the left-half plane. This completes the proof. \square

Corollary 3. *Suppose the nominal voltage is uniform at all buses, i.e., $v_i^* = v, \forall i$. Then the sufficient condition (6.23) can be written as:*

$$2Q_i + \frac{v_i^*}{\lambda_i^q} \geq 0, \quad \forall i \in \mathcal{N}. \quad (6.38)$$

Proof. Under the uniform voltage, we have

$$(v_i^*)^2 Y_{ii} \sin(\theta_{ii}) + \sum_{j=1, j \neq i}^n (v_i^*)^2 Y_{ij} \sin(\theta_{ij} - \delta_i^* + \delta_j^*) = -Q_i, \quad \forall i \in \mathcal{N}.$$

Hence, condition (6.23) can be simplified as (6.38). \square

Theorem 15. *Let $(\delta^*, 0, v^*) \in \Omega$ be an equilibrium point of system (6.1), and suppose for all $i \in \mathcal{N}$, we have positive droop coefficients $\lambda_i^p > 0$, $\lambda_i^q > 0$ and positive time constant $\tau_i > 0$. Assume also that Assumption 4 holds at this equilibrium point. If the two conditions*

$$-Q_i + \sum_{j=1}^n (v_i^*)^2 Y_{ij} \sin(\theta_{ij} - \delta_i^* + \delta_j^*) < \frac{v_i^*}{\lambda_i^q}, \quad \forall i \in \mathcal{N} \quad (6.39)$$

$$-Q_i - (v_i^*)^2 Y_{ii} \sin(\theta_{ii}) \leq \frac{1}{2\tau_i \lambda_i^p}, \quad \forall i \in \mathcal{N} \quad (6.40)$$

hold, then all the nonzero eigenvalues of the Jacobian matrix J are located in the left half plane. Moreover, the equilibrium point $(\delta^, 0, v^*)$ is asymptotically stable.*

Proof. On the one hand, according to Theorem 14, under the assumptions of the theorem, if (6.39) holds, all eigenvalues of the matrix $J^4 = -T^{-1}(I + \Lambda^q \nabla_v Q)$ are located in the open left-half plane. Notice that condition (6.39) should hold strictly, hence J^4 has no zero eigenvalue. On the other hand, according to Theorem 10, under the assumptions of the theorem if (6.40) holds, all the nonzero eigenvalues of the matrix J^1 defined in (6.19) are located in the open left-half plane. Translating to the inertia and damping notation, note that $\frac{d_i^2}{2m_i} = \frac{1/(\lambda_i^p)^2}{2\tau_i/\lambda_i^p} = \frac{1}{2\tau_i \lambda_i^p}$. Finally, according to Lemma 9, under Assumption 4, we have $\sigma(J) = \sigma(J^1) \cup \sigma(J^4)$. Therefore, all the nonzero eigenvalues of the Jacobian matrix J are located in the left half plane. Based on the same argument as in the proof of Theorem 10, the zero eigenvalue of J is simple, and the equilibrium point is asymptotically stable. \square

Remark 10 (On the role of τ_i , λ_i^p and λ_i^q). *From (6.39) and (6.40), we observe that by decreasing τ_i , λ_i^p and λ_i^q , the upper bound of the conditions increases. In this way, it is*

always possible to make the conditions (6.39) and (6.40) satisfied by decreasing τ_i , λ_i^p and λ_i^q .

6.5 Perturbation Bounds for Eigenvalues: The Impact of Coupling Terms

The stability certificates developed in the previous section are based on the $P - \delta/Q - v$ decoupling assumption described in Assumption 4. This assumption stems from the loose physical interaction between active power P and reactive power Q , which holds typically in power systems. A natural question we can ask is: What is the impact of the coupling terms $\nabla_v P$ and $\nabla_\delta Q$ on the eigenvalues of the Jacobian matrix J . In this section, we aim to address this question and provide residual bounds for the eigenvalues of J . Recall the block partition of matrix J

$$J = \begin{bmatrix} J^1 & J^2 \\ J^3 & J^4 \end{bmatrix}, \quad (6.41)$$

with J^1 to J^4 presented in (6.19)-(6.20). The next lemma from [101, Theorem 5] demonstrates the effect of J^2 and J^3 as perturbations to matrix J .

Lemma 10. *Consider matrix J partition as in (6.41), and suppose J is diagonalizable. Let $\tilde{\lambda}$ be an eigenvalue of J^1 and $\tilde{\lambda} \notin \sigma(J^4)$. Let X be a matrix that diagonalizes J , i.e., X is invertible and $\Sigma := X^{-1}JX$ is a diagonal matrix. Then there is an eigenvalue λ of J such that*

$$|\lambda - \tilde{\lambda}| \leq \kappa(X) \|J^2\| \|J^3\| \|(J^4 - \tilde{\lambda}I)^{-1}\|. \quad (6.42)$$

Here $\|\cdot\|$ denotes the spectral norm (i.e., ℓ_2 -norm), and $\kappa(X) := \|X\| \|X^{-1}\|$ is the condition number of X .

Proof. See [101, Theorem 5] □

A major concern about the eigenvalue bound in Lemma 10 is the requirement that the perturbed matrix J (as opposed to the unperturbed matrix) must be diagonalizable. Moreover, matrix X in (6.42) is a matrix that diagonalizes J . This is not desirable because the diagonalizability of J and the value of $\kappa(X)$ depend on the perturbation terms J^2 and J^3 . Note that $\|J^2\| = \|T^{-1}\Lambda^p\nabla_v P\|$ and $\|J^3\| = \|T^{-1}\Lambda^q\nabla_\delta Q\|$. Decreasing droop coefficients Λ^p and Λ^q , and increasing time constants T will make $\|J^2\|$ and $\|J^3\|$ smaller. However, terms $\kappa(X)$ and $\|(J^4 - \tilde{\lambda}I)^{-1}\|$ in (6.42) also depend on Λ^p and Λ^q .

The next lemma alleviates a number of these concerns, and provides an eigenvalue perturbation bound which is a function of perturbation terms as well as the condition number of the unperturbed matrix:

Lemma 11. *Consider matrix J partition as in (6.41), and let us decompose J as*

$$J = \begin{bmatrix} J^1 & J^2 \\ J^3 & J^4 \end{bmatrix} = J^d + J^c, \text{ with } J^d = \begin{bmatrix} J^1 & 0 \\ 0 & J^4 \end{bmatrix}, J^c = \begin{bmatrix} 0 & J^2 \\ J^3 & 0 \end{bmatrix}.$$

Notice that J^d is the decoupled Jacobian and J^c is the coupling Jacobian. Suppose J^d is diagonalizable (i.e., J^1 and J^4 are diagonalizable), and let X be a matrix that diagonalizes J^d , i.e., $J^d = X\Sigma X^{-1}$ in which X is nonsingular and Σ is diagonal. If λ is an eigenvalue of J , there is an eigenvalue $\tilde{\lambda}$ of J^d such that

$$|\tilde{\lambda} - \lambda| \leq \kappa(X)\|J^c\|. \quad (6.43)$$

Here $\|\cdot\|$ is a matrix norm induced by an absolute norm on \mathbb{C}^n , and $\kappa(X) := \|X\|\|X^{-1}\|$ is the condition number of X .

Proof. see Bauer–Fike theorem [57, Theorem 6.3.2]. □

Note that $\kappa(X)$ plays an important role in the error bounds of eigenvalues. Fortunately, there are fast methods to find an upper bound on $\kappa(X)$. See [102], for example. The next

corollary provides a guideline for choosing the parameters of the third-order model in order to achieve the desired eigenvalue bound.

Corollary 4. *Consider the notation of Lemma 11 and suppose the decoupled Jacobian J^d is diagonalizable. For any $\varepsilon > 0$, there exist positive time constants τ_i and droop coefficients λ_i^p, λ_i^q such that $|\tilde{\lambda} - \lambda| \leq \varepsilon$, whenever*

$$\lambda_i^p / \tau_i \leq \varepsilon / (\kappa(X) \|L^c\|), \quad \forall i \in \mathcal{N} \quad (6.44)$$

$$\lambda_i^q / \tau_i \leq \varepsilon / (\kappa(X) \|L^c\|), \quad \forall i \in \mathcal{N} \quad (6.45)$$

where

$$L^c = \begin{bmatrix} 0 & 0 & 0 \\ 0 & 0 & \nabla_v P \\ \nabla_\delta Q & 0 & 0 \end{bmatrix}. \quad (6.46)$$

Proof. Recall

$$\begin{aligned} J^c &= \begin{bmatrix} 0 & J^2 \\ J^3 & 0 \end{bmatrix} = \begin{bmatrix} 0 & 0 & 0 \\ 0 & 0 & -T^{-1}\Lambda^p \nabla_v P \\ -T^{-1}\Lambda^q \nabla_\delta Q & 0 & 0 \end{bmatrix} \\ &= \begin{bmatrix} 0 & 0 & 0 \\ 0 & -T^{-1}\Lambda^p & 0 \\ 0 & 0 & -T^{-1}\Lambda^q \end{bmatrix} \begin{bmatrix} 0 & 0 & 0 \\ 0 & 0 & \nabla_v P \\ \nabla_\delta Q & 0 & 0 \end{bmatrix}. \end{aligned}$$

Since spectral norm is submultiplicative, we have,

$$\|J^c\| \leq \left(\max(\max_i |\lambda_i^p / \tau_i|, \max_i |\lambda_i^q / \tau_i|) \right) \|L^c\|$$

where L^c is the coupling part of the power flow Jacobian

$$L^c = \begin{bmatrix} 0 & 0 & 0 \\ 0 & 0 & \nabla_v P \\ \nabla_\delta Q & 0 & 0 \end{bmatrix}. \quad (6.47)$$

According to the bound (6.43) in Lemma 11, we have

$$|\tilde{\lambda} - \lambda| \leq \kappa(X) \|J^c\| \leq \kappa(X) \left(\max(\max_i |\lambda_i^p / \tau_i|, \max_i |\lambda_i^q / \tau_i|) \right) \|L^c\|. \quad (6.48)$$

Hence, we need $\kappa(X) \left(\max(\max_i |\lambda_i^p / \tau_i|, \max_i |\lambda_i^q / \tau_i|) \right) \|L^c\| \leq \varepsilon$, and this can be achieved by choosing λ_i^p, λ_i^q and τ_i such that

$$\max(\max_i |\lambda_i^p / \tau_i|, \max_i |\lambda_i^q / \tau_i|) \leq \varepsilon / (\kappa(X) \|L^c\|). \quad (6.49)$$

If λ_i^p, λ_i^q and τ_i are chosen such that (6.49) holds, then the desired eigenvalue error bound holds. This completes the proof. \square

6.6 Numerical Results

In this section, we test the loose physical interaction between active power P and reactive power Q , and the practicality of Assumption 4. We also illustrate the validity of spectrum decoupling in Lemma 9 as well as the stability certificates in Theorem 15.

Fig. 6.1 shows the ℓ_2 -norm, i.e., maximum singular value of the four blocks of matrix L defined in (6.5), namely, $\|\nabla_\delta P\|$, $\|\nabla_v P\|$, $\|\nabla_\delta Q\|$, and $\|\nabla_v Q\|$ in different IEEE standard test systems. For each test case, matrix L is evaluated at the equilibrium point, which is obtained from the converged load flow data in MATPOWER [69]. Accordingly, the values of $\|\nabla_v P\|$ and $\|\nabla_\delta Q\|$ are significantly smaller than the values of $\|\nabla_\delta P\|$ and $\|\nabla_v Q\|$ in all four test systems. This confirms the practicality of Assumption 4 and the loose physical

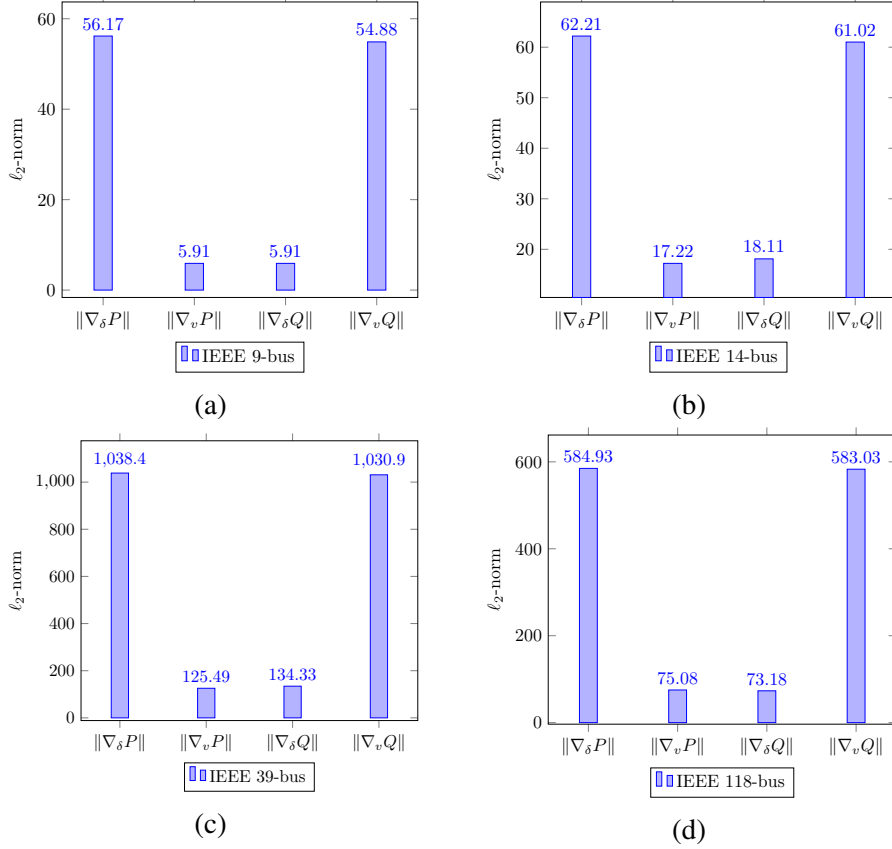


Figure 6.1: Verifying the loose physical interaction between active power P and reactive power Q .

interaction between active power P and reactive power Q .

Table 6.1 provides the dynamic parameters λ^p , λ^q , and τ as well as the variation of stability certificates in the aforementioned test systems. All these systems have a connected underlying graph and nonzero transfer conductances. Recall that in Chapter 3, we investigated the stability of these systems based on the second-order swing equation model. Recall also that we have verified the validity of the assumption $\varphi_{ij} \in (0, \pi), \forall (i, j) \in \mathcal{A}$ with $\varphi_{ij} := \theta_{ij} - \delta_i^* + \delta_j^*$ at an equilibrium point $(\delta^*, 0, v^*)$. The last column of Table 6.1 verifies the practicality of this assumption again. Note that voltage magnitudes are always positive, i.e., $v^* > 0$ holds in any power grid. Next, let us define

$$\mathcal{V}_i := -Q_i + \sum_{j=1}^n (v_i^*)^2 Y_{ij} \sin(\theta_{ij} - \delta_i^* + \delta_j^*) - \frac{v_i^*}{\lambda_i^q},$$

Table 6.1: Dynamic parameters, domain of stability certificates, and angle range.

Test case	λ^p	λ^q	τ	$\text{Dom}(\mathcal{V}_i)$	$\text{Dom}(\mathcal{S}_i)$	$\text{Dom}(\varphi_{ij}/\pi)$
IEEE 9-bus	0.1	0.5	0.1	$[-2.4, -1.7]$	$[-44.5, -43.8]$	$[0.46, 0.52]$
IEEE 14-bus	0.1	0.5	0.1	$[-2.7, -1.7]$	$[-46.62, -21.4]$	$[0.41, 0.67]$
IEEE 39-bus	0.1	0.5	0.1	$[-8.07, -1.61]$	$[-34.46, -15.42]$	$[0.30, 0.64]$
IEEE 118-bus	0.04	0.2	0.09	$[-6.9, -1.2]$	$[-135.6, 42.01]$	$[0.42, 0.63]$

$$\mathcal{S}_i := -Q_i - (v_i^*)^2 Y_{ii} \sin(\theta_{ii}) - \frac{1}{2\tau_i \lambda_i^p}.$$

According to Theorem 15, if for all $i \in \mathcal{N}$, we have $\mathcal{V}_i < 0$ and $\mathcal{S}_i \leq 0$, then the equilibrium point of the third-order model is asymptotically stable. The 5th and 6th columns of Table 6.1 provide the domain of variations of \mathcal{V}_i and \mathcal{S}_i , i.e., $\text{Dom}(\mathcal{V}_i) := [\min_i \mathcal{V}_i, \max_i \mathcal{V}_i]$ and $\text{Dom}(\mathcal{S}_i) := [\min_i \mathcal{S}_i, \max_i \mathcal{S}_i]$. Accordingly, $\mathcal{V}_i < 0$ holds for all test cases, certifying that matrix J^4 is a Hurwitz matrix. Moreover $\mathcal{S}_i \leq 0$ holds for all test cases, except the IEEE 118-bus system. Condition $\mathcal{S}_i \leq 0$ certifies that matrix J^1 is Hurwitz. We will see shortly that the equilibrium points of all the test systems in Table 6.1 are asymptotically stable. Therefore, the violation of $\mathcal{S}_i \leq 0$ in the 118-bus system is due to the fact that Theorem 15 provides sufficient conditions for asymptotic stability, and these conditions may not be necessary in some cases. In Chapter 3, we discussed that even in such cases, the above stability certificates can be used to quantitatively measure the degree of stability.

Next, Fig. 6.2 depicts the spectrum of J as well as J^1 and J^4 . Recall that J^1 corresponds to the Jacobian of the second-order swing equation model (6.1a)-(6.1b) while J^4 is the Jacobian of the voltage dynamics (6.1c). In this figure, black asterisks, red circles, and blue triangles respectively depict the eigenvalues of matrices J , J^1 and J^4 . As can be seen, the result of Lemma 9 holds with reasonable accuracy in all these test cases. In other words, due to the loose coupling between active and reactive powers (see Fig. 6.1), the spectrum of J is roughly equal to the union of spectrums of J^1 and J^4 . This figure also confirms the stability of equilibrium points in all test cases of Table 6.1, as all nonzero eigenvalues of the third-order model are located in the left half plane.

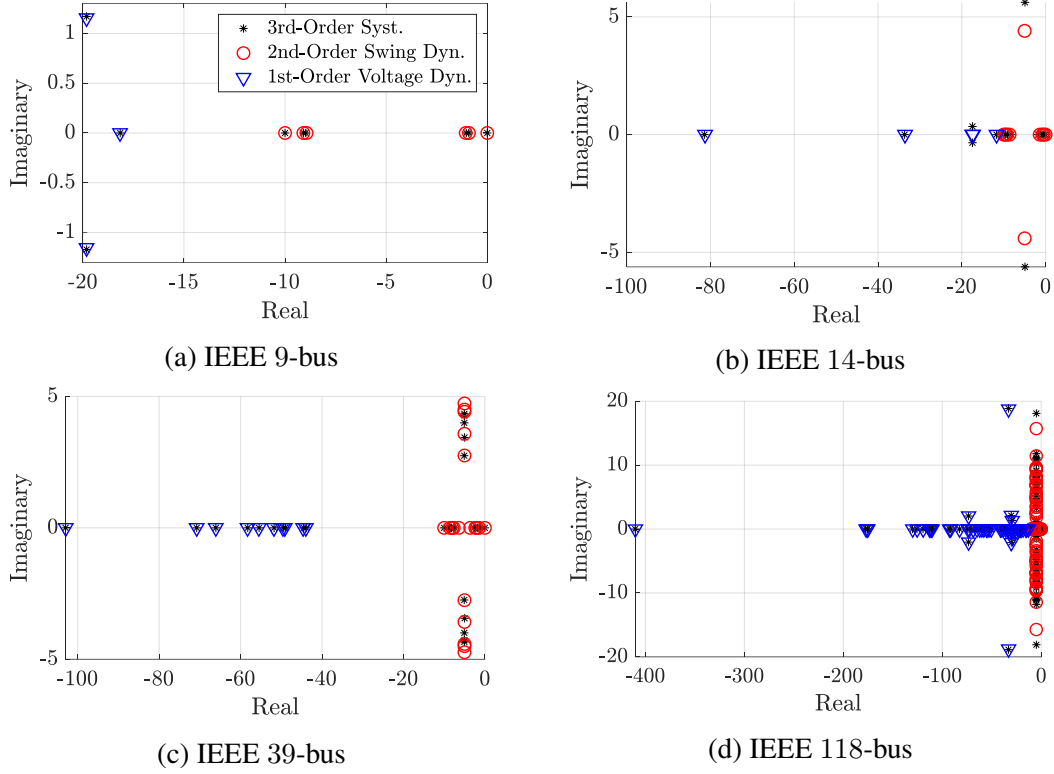


Figure 6.2: Spectrum of J , and its diagonal blocks J^1 and J^4 . Verifying Lemma 9 and Theorem 15

6.7 Final Remarks

This chapter is aimed at developing stability certificates for the third-order model of droop-controlled inverters. According to the derived certificates, two inequalities should hold at each node of the system. To check these inequalities at each node, we only require the local information about the reactive power consumption, voltage magnitude and the parameters of the inverter at the node. Therefore, the proposed certificates can be utilized for distributed and fast stability assessment and monitoring. In order to develop these certificates, we have made use of the loose physical linkage between active and reactive powers. We have also investigated the role of coupling terms and the robustness of the decoupled model under coupling perturbations. A worthwhile direction for future research would be generalizing the developed stability certificates to higher-order models.

Part II

Optimization with Stability Constraints

CHAPTER 7

OPTIMIZATION-BASED LOAD SHEDDING IN SINGLE MICROGRIDS

This chapter proposes an adaptive optimization-based approach for under frequency load shedding (UFLS) in microgrids (μ Gs) following an unintentional islanding. In the first step, the total amount of load curtailments is determined based on the system frequency response (SFR) model. Then, the proposed mixed-integer linear programming (MILP) model is executed to find the best location of load drops. The novel approach specifies the least cost load shedding scenario while satisfying network operational limitations. A look-up table is arranged according to the specified load shedding scenario to be implemented in the network if the islanding event occurs in the μ G. To be adapted with system real-time conditions, the look-up table is updated periodically. The efficiency of the proposed framework is thoroughly evaluated in a test μ G with a set of illustrative case studies.

7.1 Introduction

In recent years, the proliferation of distributed energy resources (DERs) has led to an increase in on-site electricity service procurement for customers. This new trend has a set of advantages and disadvantages over the conventional centralized power generation paradigm in terms of reliability, cost of maintenance, economies of scale, resiliency, and sustainability, to name a few [103]. Moreover, deploying DERs in a widespread and efficient manner requires practical mechanisms to identify and resolve the challenges of integration. In this context, microgrids (μ Gs) are emerging as a flexible way to aggregate DERs. The Department of Energy (DOE) defines a μ G as “a group of interconnected loads and DERs within clearly defined electrical boundaries that acts as a single controllable entity with respect to the grid. A μ G can connect and disconnect from the grid to enable it to operate in both grid-connected or island mode” [104].

A μ G may enter the island mode either intentionally or unintentionally. In the case of intentional islanding, the exact time of the islanding is known and the required adjustments in the μ G power exchange with the upstream grid can be made to ensure the security of the grid following the islanding. On the contrary, an unintentional islanding usually occurs in μ Gs in the event of unforeseen faults in the upstream grid. IEEE 929-1988 Std. [105] necessitates the disconnection of DERs once the unintentional islanding event happens in the μ G. Furthermore, IEEE 1547-2003 Std. [106] enforces DERs to detect the unintentional islanding and cease energizing the μ G within maximum 2 sec. following the islanding event. Therefore, in the case of unintentional islanding, blackouts seem inevitable.

It goes without saying that the current practice of disconnecting the DERs following an islanding event is not economical since it imposes immense costs on the μ G. When a μ G with DERs is islanded, usually the frequency will change. The frequency will either go up if there is excess generation or down if there is excess load. The former can be controlled by reducing the output power of the distributed generators (DGs) or other DERs [107]. However, coping with the latter is more challenging. It is worth mentioning that in the normal operating condition, photovoltaic (PV) systems usually use maximum power point tracking and variable speed wind turbines optimize power coefficient (C_p) to produce maximum power. Thus, if all of the DGs are operating at maximum power and the frequency still goes down, some loads have to be shed to bring the frequency back to the allowable range. Nonetheless, it is possible that PV generators and wind turbines withhold production (these resources are non-dispatchable, but curtailable), and this is a growing trend in power system operation which provides further flexibility.

Conventional under frequency load shedding (UFLS) scheme is currently used as the last resort in the bulk power system to stop declining frequency and to maintain the security of the whole network following under frequency events (e.g., large generation rejection or important tie-line disconnection) [108]. This method sheds a constant amount of load, based on experience, at predetermined frequency threshold with intentional time delay.

The main weakness of the conventional UFLS scheme is to drop a fixed amount of load at certain locations regardless of the severity of the contingency and network conditions. To address the weaknesses of conventional UFLS scheme, researchers have proposed adaptive load shedding schemes, which can be classified into two main categories: decentralized and centralized algorithms. Decentralized approaches use local voltage and frequency signals at each bus to make the decision about the load shedding process at that bus. Indeed, using these algorithms, the location, speed, and the amount of load curtailments are adjusted adaptively to preserve the system stability following severe incidents.

Centralized methods, on the other hand, use the data gathered from the grid in order to decide which load to be shed. The centralized schemes proposed in [109] drop loads at different buses based on their VQ margin and post-fault voltage magnitude. Reference [110] adopts both voltage and frequency information provided by phasor measurement units (PMUs) to implement the appropriate load shedding scenario in the network. Other centralized methods determine the amount and location of load drops according to the complete post-fault information about the network [111, 112, 113, 114].

7.1.1 Main Results

Owing to the differences between μ Gs and bulk power systems, the load shedding mechanism for a μ G should be treated differently. μ Gs usually have small generators and, hence, small inertia. As a consequence, the frequency declines more rapidly in μ Gs. This chapter presents a centralized adaptive optimization-based load shedding scheme to curtail the minimum amount of loads to preserve the μ G stability following an unintentional islanding event. The developed technique arranges a look-up table including the optimum amount and location of load curtailments. The main contributions of the new methodology can be summarized as follows:

1. Given a specific amount of power exchange between the μ G and the upstream grid, the optimal total amount of load shedding is determined. Specifically, this value

depends on the response of both the generators and the loads to the islanding event. These responses are reflected in the system frequency response (SFR) model as well as the μ G dynamic and static frequency limitations.

2. We developed a mixed-integer linear programming (MILP) model for obtaining the amount of load drops at different buses. In the optimization model, an approximation of the μ G AC operational limitations are considered to ensure the network security following the islanding event.
3. A hierarchical structure is proposed in this chapter so as to reduce both data and communication requirements of the new centralized algorithm. To give more explanation, the majority of the needed information are periodically updated and only a practically tractable share is gathered in real time.

7.1.2 Chapter Outline

The rest of this chapter is organized as follows. Section 7.2 presents the overview of the proposed load shedding algorithm. In Section 7.3, a method for estimating the total amount of load curtailments is developed. Section 7.4 is devoted to introducing the optimization-based load shedding scheme. Section 7.5 exhibits the efficiency of the novel approach using an illustrative case study. Eventually, conclusion is given in Section 7.6.

7.2 Overview of the Proposed Load Shedding Algorithm

The general framework of the proposed load shedding algorithm is depicted in Fig. 7.1. In the first step, the μ G master controller (μ GMC) gathers the network data periodically (e.g., $\Delta T = 5$ min.) and runs the state estimation (SE) in order to obtain the proposed scheme's input parameters (operating point of the μ G, load and generation data, and μ G topology). Then, the optimum total amount of load curtailments is determined based on the μ G SFR model and the power exchange between the μ G and the upstream grid. Note

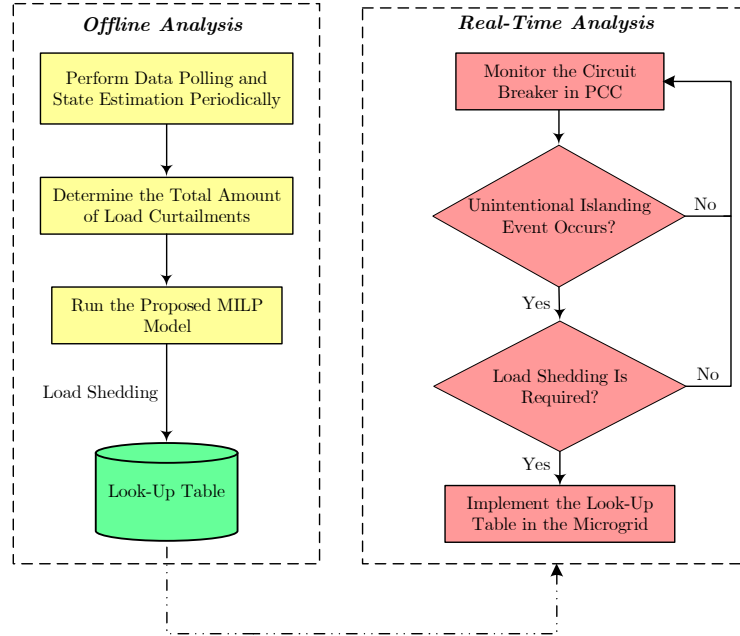


Figure 7.1: The general framework of the proposed load shedding algorithm.

that the obtained total amount of load drops satisfies the μ G dynamic and static frequency limitations. The total amount of load shedding along with the SE data are fed into the proposed optimization model in order to arrange a look-up table including the location of load drops as well as appropriate post load shedding strategies. On the other side, the status of point of common coupling (PCC) circuit breaker is monitored using indication (i.e., binary) data. If an unintentional islanding happens and the amount of power mismatch is greater than a specific value, the pre-specified load shedding scenarios will be implemented in the μ G. Detailed explanations about different parts of the proposed methodology are provided in the following sections.

7.3 Optimal Amount and Threshold for Activation of Load Shedding

The aim of this section is to determine the minimum amount of load curtailments as well as a threshold for activation of the load shedding process, while the μ G dynamic and steady-state frequency limitations are satisfied. The minimum dynamic and steady-state frequencies are indicated in a typical frequency response of a μ G following an unintentional is-

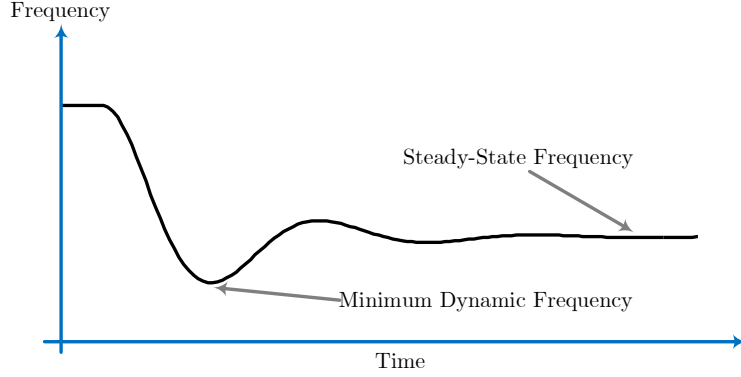


Figure 7.2: A typical frequency response of a μG following an unintentional islanding event.

landing event, Fig. 7.2.

7.3.1 Frequency Response of the μG to an Islanding Event

As the first step, the frequency response of the μG to an islanding event should be specified. To do so, we use the aggregated SFR model of the μG as shown in Fig. 7.3 [115], [32]. This model is an equivalent single machine model of all DGs in the μG , where the frequency of the center of inertia is considered by ignoring intermachine oscillations. In this model, τ^T is the turbine time constant, τ^V is the governor valve time constant, H is the inertia constant, D is the damping coefficient, and R is the governor droop control.

The transfer function $\frac{1}{2Hs+D}$ in the forward path represents the swing equation of the equivalent DG as well as the effects of the μG loads which are lumped into a single damping constant D . Moreover, the transfer functions in the feedback loop are associated with the governor droop, governor time constant, and turbine time constant of the equivalent DG [32].

The transfer function of the adopted SFR model can be written as (7.1).

$$\mathcal{H}(s) = \frac{\alpha_1 s^2 + \alpha_2 s + \alpha_3}{s^3 + \beta_1 s^2 + \beta_2 s + \beta_3}, \quad (7.1)$$

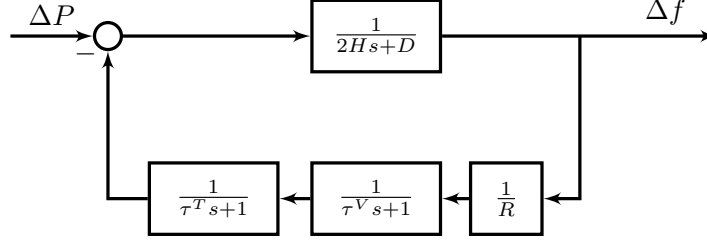


Figure 7.3: Block diagram of the adopted SFR model.

where

$$\alpha_1 = \frac{1}{2H}, \alpha_2 = \frac{1}{2H} \left(\frac{1}{\tau^T} + \frac{1}{\tau^V} \right), \alpha_3 = \frac{1}{2H\tau^T\tau^V}$$

$$\beta_1 = \frac{D}{2H} + \frac{1}{\tau^T} + \frac{1}{\tau^V}, \beta_2 = \frac{1}{\tau^T\tau^V} + \frac{D}{2H} \left(\frac{1}{\tau^T} + \frac{1}{\tau^V} \right)$$

$$\beta_3 = \frac{\frac{1}{R} + D}{2H\tau^T\tau^V}.$$

Note that $\alpha_1, \alpha_2, \alpha_3, \beta_1, \beta_2, \beta_3$ are auxiliary parameters.

7.3.2 Threshold for Activation of Load Shedding Scheme

Let P^M be the μG pre-fault energy exchange with the upstream grid. In the wake of an unintentional islanding, the governors and loads in the μG will respond to the incident, thereby compensating for a portion of power mismatch. Consequently, load shedding is not necessary in all cases. Specifically, the minimum amount of power mismatch which would activate the load shedding process is obtained by (7.2).

$$P_{thr}^M = \min \left\{ P_{thr,SSF}^M, P_{thr,DF}^M \right\}, \quad (7.2)$$

where $P_{thr,SSF}^M$ and $P_{thr,DF}^M$ are the steady-state and dynamic thresholds of P^M , respectively. Suppose that the μG is not equipped with any load shedding scheme. In this condition, if an unintentional islanding happens, the input power deviation of the SFR model in Fig. 7.3 is defined as (7.3).

$$\Delta P(t) = -P^M u(t), \quad \Delta P(s) = \frac{-P^M}{s}, \quad (7.3)$$

where $u(t)$ is the unit step function. Hence, the Laplace form of the frequency deviation function is obtained as (7.4).

$$\Delta f(s) = \mathcal{H}(s) \Delta P(s) = \frac{\overbrace{\alpha_1 s^2 + \alpha_2 s + \alpha_3}^{\mathcal{F}(s)}}{s(s^3 + \beta_1 s^2 + \beta_2 s + \beta_3)} \left(-P^M\right). \quad (7.4)$$

Accordingly, $\mathcal{F}(s)$ can be decomposed into three terms using partial-fraction decomposition as follows:

$$\mathcal{F}(s) = \frac{\alpha_1 s^2 + \alpha_2 s + \alpha_3}{s(s^3 + \beta_1 s^2 + \beta_2 s + \beta_3)} = \frac{\delta_1}{s} + \frac{\delta_2}{s - m_1} + \frac{\delta_3 s + \delta_4}{s^2 + m_2 s + m_3}, \quad (7.5)$$

where

$$m_1 = \frac{-1}{3} \left(\beta_1 + c_1 + \frac{c_2}{c_1} \right), \quad m_2 = \frac{2}{3} \left(\beta_1 - \frac{c_1}{2} - \frac{c_2}{2c_1} \right),$$

$$m_3 = \frac{1}{9} \left[\left(\beta_1 - \frac{c_1}{2} - \frac{c_2}{2c_1} \right)^2 + \frac{3}{4} \left(c_1 - \frac{c_2}{c_1} \right)^2 \right],$$

$$c_1 = \sqrt[3]{\frac{c_3 + \sqrt{c_3^2 - 4c_2^3}}{2}},$$

$$c_2 = \beta_1^2 - 3\beta_2, \quad c_3 = 2\beta_1^3 - 9\beta_1\beta_2 + 27\beta_3,$$

$$\delta_1 = \frac{\alpha_3}{\beta_3}, \quad \delta_2 = \frac{\alpha_1 m_1^2 + \alpha_2 m_1 + \alpha_3}{m_1^3 + m_2 m_1^2 + m_3 m_1},$$

$$\delta_3 = -(\delta_1 + \delta_2), \quad \delta_4 = (\delta_1 \beta_2 + \delta_2 m_3 - \alpha_2) / m_1.$$

Note that $m_1, m_2, m_3, c_1, c_2, c_3, \delta_1, \delta_2, \delta_3, \delta_4$ are all auxiliary parameters. Taking the inverse Laplace transform of $\mathcal{F}(s)$, $\mathcal{F}(t)$ is given by:

$$\mathcal{F}(t) = \left(\delta_1 + \delta_2 e^{m_1 t} + \frac{\delta_3 e^{-\frac{m_2}{2} t}}{\cos(\phi)} \cos(\varpi t + \phi) \right) u(t), \quad (7.6)$$

where

$$\varpi = \sqrt{m_3 - \frac{m_2^2}{4}}, \quad \cos \phi = \frac{\varpi}{\sqrt{\varpi^2 + \left(\frac{m_2}{2} - \frac{\delta_3}{\delta_4} \right)^2}}.$$

Therefore, $\Delta f(t)$ can be written as (7.7).

$$\Delta f(t) = -P^M \mathcal{F}(t). \quad (7.7)$$

Steady-State Threshold of P^M

Given $\Delta f(t)$ as (7.7), Δf_{SSF} (i.e., steady state frequency deviation) can be computed as (7.8).

$$\Delta f_{SSF} = \lim_{t \rightarrow \infty} \Delta f(t) = \left(-P^M\right) \delta_1. \quad (7.8)$$

The load shedding process will be triggered if the value of Δf_{SSF} exceeds a given threshold Δf_{SSF}^{\max} , that is:

$$\left| \left(-P^M\right) \delta_1 \right| \geq |\Delta f_{SSF}^{\max}|. \quad (7.9)$$

Therefore, the minimum amount of P^M which violates the steady-state frequency limitation, and thus, triggers the load shedding process is acquired as follows:

$$P^M \geq |\Delta f_{SSF}^{\max}| \left(D + \frac{1}{R} \right). \quad (7.10)$$

Accordingly, we define the right hand side of (7.10) as the steady state threshold of P^M .

Dynamic Threshold of P^M

The time when the frequency nadir happens (i.e., when the lowest frequency is reached before the frequency starts to recover) can be calculated by putting the first derivative of $\Delta f(t)$ equal to zero:

$$t_{\min} = \min \left\{ t : t > 0, \frac{d\Delta f(t)}{dt} = 0 \right\}. \quad (7.11)$$

Here t_{\min} is the time when the minimum dynamic frequency occurs. Let Δf_{DF} denote the nadir value of frequency deviation, and Δf_{DF}^{\max} denote the given threshold for Δf_{DF} . Ac-

Accordingly, the second trigger for the load shedding process is associated with the violation of nadir frequency limitation, that is:

$$|\Delta f(t_{\min})| \geq |\Delta f_{DF}^{\max}|. \quad (7.12)$$

The solution to this inequality in terms of P^M , will provide another criterion or lower bound (denoted by $P_{thr,DF}^M$ in (7.2)) for the activation of the load shedding process.

7.3.3 Optimal Amount of Load Shedding

The minimum total amount of load curtailments satisfying both steady-state and dynamic frequency limitations is calculated as (7.13).

$$p^{Shed} = \max \left\{ p_{SSF}^{Shed}, p_{DF}^{Shed} \right\}, \quad (7.13)$$

where p_{SSF}^{Shed} and p_{DF}^{Shed} are obtained as follows. Suppose that the load shedding scheme is implemented in the μG with a delay of t^{Shed} , subsequent to the unintentional islanding event. Indeed, t^{Shed} is the time instant when load shedding is implemented. Accordingly, the input power deviation of the SFR model will be defined as (7.14).

$$\Delta P(t) = -P^M u(t) + p^{Shed} u(t - t^{Shed}). \quad (7.14)$$

Taking the Laplace transform of $\Delta P(t)$ yields

$$\Delta P(s) = \frac{1}{s} \left(-P^M + p^{Shed} e^{-t^{Shed}s} \right). \quad (7.15)$$

Hence, the Laplace form of the frequency deviation function is obtained as (7.16).

$$\Delta f(s) = \mathcal{F}(s) \left(-P^M + p^{Shed} e^{-t^{Shed}s} \right), \quad (7.16)$$

where $\mathcal{F}(s)$ is obtained from (7.5). Taking the inverse Laplace transform of (7.16), $\Delta f(t)$ can be written as (7.17) below

$$\Delta f(t) = -P^M \mathcal{F}(t) + p^{Shed} \mathcal{F}(t - t^{Shed}), \quad (7.17)$$

where $\mathcal{F}(t)$ is calculated in (7.6).

Load Shedding Value Based on the Steady-State Frequency Limitation

Given $\Delta f(t)$ as (7.17), Δf_{SSF} can be computed as (7.18) [111].

$$\Delta f_{SSF} = \lim_{t \rightarrow \infty} \Delta f(t) = \left(-P^M + p_{SSF}^{Shed}\right) \delta_1. \quad (7.18)$$

Therefore, the minimum total amount of load shedding satisfying the steady-state frequency limitation (i.e., $|\Delta f_{SSF}| \leq |\Delta f_{SSF}^{\max}|$) is acquired as follows:

$$p_{SSF}^{Shed} = P^M - |\Delta f_{SSF}^{\max}| \left(D + \frac{1}{R}\right). \quad (7.19)$$

Load Shedding Value Based on the Dynamic Frequency Limitation

Similar to the previous section, the time when the frequency nadir happens is acquired by solving (7.11), where $\Delta f(t)$ is calculated according to (7.17). By applying the nadir frequency limitation (i.e., $|\Delta f_{DF}| \leq |\Delta f_{DF}^{\max}|$), the minimum amount of load shedding satisfying dynamic frequency limitation (i.e., p_{DF}^{Shed}) is obtained. It should be noted that the proposed method in this chapter is aimed at bringing the frequency to the permissible range (according to Δf_{SSF}^{\max} and Δf_{DF}^{\max}) with the minimum amount of load shedding. Obviously, the frequency should finally bring back to 60 Hz, but this transition can happen with a short delay (2-3 minutes) with the advantage of shedding fewer loads. Subsequent to load shedding, DERs will try to bring the frequency back to 60 Hz. If this cannot happen (e.g., due to some limitations in the output of DERs), further loads will be curtailed. This idea

is consistent with the load-frequency control mechanisms which are done in three different successive steps (i.e., primary control, secondary control, tertiary control).

7.4 Optimization-Based Load Shedding Scheme

7.4.1 Basic Model

In this section, the basic model of the μ G load shedding scheme is presented. Consider a μ G with the set of buses Ω_N , the set of lines Ω_L , set of DGs Ω_G , and set of renewable energy source (RES) Ω_{RES} . For each bus $i \in \Omega_N$, let Ω_{B_i} denote the set of load blocks at bus i . We also use \mathcal{M}_G and \mathcal{M}_{RES} to denote the mapping of the set of DGs and RESs into the set of buses. The optimization model of the proposed load shedding scheme is as follows:

$$\min \sum_{i \in \Omega_N} \sum_{b \in \Omega_{B_i}} \lambda_{ib}^{VOLL} (1 - x_{ib}) \bar{p}_{ib}^D \quad (7.20)$$

subject to

$$\sum_{g:(g,i) \in \mathcal{M}_G} p_g^G + \sum_{r:(r,i) \in \mathcal{M}_{RES}} p_r^{RES} - \sum_{b \in \Omega_{B_i}} x_{ib} p_{ib}^D = \sum_{(i,j) \in \Omega_L} f_{(i,j)}^P, \forall i \in \Omega_N \quad (7.21)$$

$$\sum_{g:(g,i) \in \mathcal{M}_G} q_g^G + \sum_{r:(r,i) \in \mathcal{M}_{RES}} q_r^{RES} - \sum_{b \in \Omega_{B_i}} x_{ib} q_{ib}^D = \sum_{(i,j) \in \Omega_L} f_{(i,j)}^Q, \forall i \in \Omega_N \quad (7.22)$$

$$f_{(i,j)}^P = G_{(i,j)} \left(V_i^2 - V_i V_j \cos(\theta_i - \theta_j) \right) - B_{(i,j)} V_i V_j \sin(\theta_i - \theta_j), \forall (i,j) \in \Omega_L \quad (7.23)$$

$$f_{(i,j)}^Q = -B_{(i,j)} \left(V_i^2 - V_i V_j \cos(\theta_i - \theta_j) \right) - G_{(i,j)} V_i V_j \sin(\theta_i - \theta_j), \forall (i,j) \in \Omega_L \quad (7.24)$$

$$-f_{(i,j)}^{P,\max} \leq f_{(i,j)}^P \leq f_{(i,j)}^{P,\max}, \forall (i, j) \in \Omega_L \quad (7.25)$$

$$-f_{(i,j)}^{Q,\max} \leq f_{(i,j)}^Q \leq f_{(i,j)}^{Q,\max}, \forall (i, j) \in \Omega_L \quad (7.26)$$

$$\begin{aligned} f_{(i,j)}^P + f_{(j,i)}^P &= \frac{G^{(i,j)}}{G_{(i,j)}^2 + B_{(i,j)}^2} |I_{(i,j)}|^2 \leq f_{(i,j)}^{P, Loss, \max} \\ &= \frac{G^{(i,j)}}{G_{(i,j)}^2 + B_{(i,j)}^2} |I_{(i,j)}^{\max}|^2, \forall (i, j) \in \Omega_L \end{aligned} \quad (7.27)$$

$$V_i^{\min} \leq V_i \leq V_i^{\max}, \forall i \in \Omega_N \quad (7.28)$$

$$p_{ib}^D = \bar{p}_{ib}^D \left(\kappa_{ib}^{PI} (V_i/V_i^*)^2 + \kappa_{ib}^{PC} (V_i/V_i^*) + \kappa_{ib}^{PP} \right), \forall i \in \Omega_N, b \in \Omega_{B_i} \quad (7.29)$$

$$q_{ib}^D = \bar{q}_{ib}^D \left(\kappa_{ib}^{QI} (V_i/V_i^*)^2 + \kappa_{ib}^{QC} (V_i/V_i^*) + \kappa_{ib}^{QP} \right), \forall i \in \Omega_N, b \in \Omega_{B_i} \quad (7.30)$$

$$-R_g^D \leq p_g^G - p_g^{G,0} \leq R_g^U, \forall g \in \Omega_G \quad (7.31)$$

$$p_g^{G,\min} \leq p_g^G \leq p_g^{G,\max}, \forall g \in \Omega_G \quad (7.32)$$

$$q_g^{G,\min} \leq q_g^G \leq q_g^{G,\max}, \forall g \in \Omega_G \quad (7.33)$$

$$\sum_{i \in \Omega_N} \sum_{b \in \Omega_{B_i}} (1 - x_{ib}) p_{ib}^D \geq p^{Shed} \quad (7.34)$$

$$x_{ib} \in \{0, 1\}, \forall i \in \Omega_N, b \in \Omega_{B_i}. \quad (7.35)$$

The objective function, (7.20), is the load shedding cost in the μ G, which should be minimized. λ_{ib}^{VOLL} is the value of lost load, which is a socioeconomic parameter and varies for different types of loads (e.g., industrial, commercial, agricultural, residential, and general loads). x_{ib} is a binary variable indicating the load shedding status of the load at bus $i \in \Omega_N$ and block $b \in \Omega_{B_i}$. We also assume \bar{p}_{ib}^D is the pre-fault active power consumption of the load. The group of equations (7.21)–(7.24) is related to the AC power flow equations. Here variables p_{ib}^D and q_{ib}^D are the active and reactive power consumption of the load at bus $i \in \Omega_N$ and block $b \in \Omega_{B_i}$ following the load shedding process. For each DG $g \in \Omega_G$, variables p_g^G and q_g^G are active and reactive power output of the DG following the load shedding process. For each RES $r \in \Omega_{RES}$, the parameters p_r^{RES} and q_r^{RES} are pre-fault active and reactive power production of the RES obtained from state estimation. Moreover, $G_{(i,j)}$ and $B_{(i,j)}$ are the conductance and susceptance of line $(i,j) \in \Omega_L$. V_i and θ_i are the voltage magnitude and angle at bus $i \in \Omega_N$, following the load shedding process. Finally, $f_{(i,j)}^P$ and $f_{(i,j)}^Q$ are the active and reactive power flow of line $(i,j) \in \Omega_L$.

Line flow limits and bus voltage constraints are modeled through (7.25)–(7.27) and (7.28), respectively. Note that variable $I_{(i,j)}$ is the current flow of line $(i,j) \in \Omega_L$. Incorporation of a suitable load model for μ G loads plays an important role in power system stability studies [112]. Therefore, the active and reactive power demands at different buses are modeled with voltage-dependent load model referred to as ZIP model, (7.29)–(7.30) [116]. In this model, the parameters κ_{ib}^{PI} , κ_{ib}^{PC} , and κ_{ib}^{PP} are coefficients of constant impedance, constant current, and constant power terms in the active power load at bus $i \in \Omega_N$ and block $b \in \Omega_{B_i}$. The parameters κ_{ib}^{QI} , κ_{ib}^{QC} , and κ_{ib}^{QP} denote similar coefficients for the corresponding reactive power load. Furthermore, parameter V_i^* denotes the pre-fault voltage magnitude at bus $i \in \Omega_N$.

Constraints (7.31)–(7.33) revolve around DG's ramp-up and ramp-down limits (7.31) and active and reactive power generation limits of DGs (7.32)–(7.33). The parameters R_g^U and R_g^D are ramp-up and ramp-down limits of DG $g \in \Omega_G$. Moreover, parameter $p_g^{G,0}$

Table 7.1: Constituent Terms in the Linearized Power Flow Equations [117]

Term	Approximation	Max. Abs. Error
V_i^2	$2V_i - 1$	0.0025
$V_i V_j \cos(\theta_i - \theta_j)$	$V_i + V_j + \cos(\theta_i - \theta_j) - 2$	0.0253
$V_i V_j \sin(\theta_i - \theta_j)$	$\sin(\theta_i - \theta_j)$	0.0659
$\sin(\theta_i - \theta_j)$	$\theta_i - \theta_j$	0.0553

denotes the active power generation of this DG before the load shedding process. The minimum total load shedding constraint is expressed as (7.34), and finally, the status of loads is characterized by a binary variable in (7.35).

7.4.2 Linearization of the Basic Model

The developed problem in Section 7.4.1 is a mixed-integer nonlinear programming (MINLP) model. In order to attain computational efficiency, the nonlinear equations ought to be linearized. The nonlinear terms $x_{ib}p_{ib}^D$ and $x_{ib}q_{ib}^D$ in (7.21)–(7.22) and (7.34) are the product of a binary and continuous variables. We can linearize these terms with the big-M method by introducing auxiliary semi-continuous variables (i.e., $\alpha_{ib}^P \triangleq x_{ib}p_{ib}^D$ and $\alpha_{ib}^Q \triangleq x_{ib}q_{ib}^D$) and the set of equations (7.36)–(7.39). In order to reduce the integrality gap in the linearized version of the aforementioned constraints, Big-Ms (i.e., M_{ib} and M'_{ib}) should be as small as possible, and it is usually challenging to determine correct values for them to use for each specific implementation. However, in this particular application, we can set $M_{ib} = \bar{p}_{ib}^D$ and $M'_{ib} = \bar{q}_{ib}^D$, $\forall i \in \Omega_N, b \in \Omega_{B_i}$. Note that these data (i.e., the upper bounds of active and reactive loads) are usually available in any system.

Moreover, considering reasonable assumptions given in Table 7.1 [117], AC power flow equations are replaced by their piecewise linear approximation form as (7.40)–(7.49). Finally, considering the permissible range for bus voltage magnitudes at different buses (i.e., $0.9 \leq V_i, V_i^* \leq 1.1$), (7.29)–(7.30) can be reasonably approximated by (7.50)–(7.51) [112]. With these changes, the proposed model is transformed into an MILP model.

$$-(1 - x_{ib}) M_{ib} \leq \alpha_{ib}^P - p_{ib}^D \leq M_{ib} (1 - x_{ib}), \forall i \in \Omega_N, b \in \Omega_{B_i} \quad (7.36)$$

$$-x_{ib} M_{ib} \leq \alpha_{ib}^P \leq M_{ib} x_{ib}, \forall i \in \Omega_N, b \in \Omega_{B_i} \quad (7.37)$$

$$-(1 - x_{ib}) M'_{ib} \leq \alpha_{ib}^Q - q_{ib}^D \leq M'_{ib} (1 - x_{ib}), \forall i \in \Omega_N, b \in \Omega_{B_i} \quad (7.38)$$

$$-x_{ib} M'_{ib} \leq \alpha_{ib}^Q \leq M'_{ib} x_{ib}, \forall i \in \Omega_N, b \in \Omega_{B_i} \quad (7.39)$$

$$f_{(i,j)}^P = G_{(i,j)} (V_i - V_j - \omega_{(i,j)} + 1) - B_{(i,j)} (\theta_i - \theta_j), \forall (i, j) \in \Omega_L \quad (7.40)$$

$$f_{(i,j)}^Q = -B_{(i,j)} (V_i - V_j - \omega_{(i,j)} + 1) - G_{(i,j)} (\theta_i - \theta_j), \forall (i, j) \in \Omega_L \quad (7.41)$$

$$\omega_{(i,j)} = \sum_{p \in \Omega_P} s_{(i,j)p} C_p^B, \forall (i, j) \in \Omega_L \quad (7.42)$$

$$\theta_i - \theta_j = \sum_{p \in \Omega_P} s_{(i,j)p} B_p^B, \forall (i, j) \in \Omega_L \quad (7.43)$$

$$\sum_{p \in \Omega_P} s_{(i,j)p} = 1, \forall (i, j) \in \Omega_L \quad (7.44)$$

$$\sum_{p \in \Omega_P} v_{(i,j)p} = 1, \forall (i, j) \in \Omega_L \quad (7.45)$$

$$s_{(i,j)p_1} \leq v_{(i,j)p_1}, \forall (i, j) \in \Omega_L \quad (7.46)$$

$$s_{(i,j)p} \leq v_{(i,j)p} - v_{(i,j)(p-1)}, \forall (i, j) \in \Omega_L, p \in \Omega_P, p \neq \{p_1, p_n\} \quad (7.47)$$

$$s_{(i,j)p_n} \leq v_{(i,j)(p_{n-1})}, \forall (i, j) \in \Omega_L \quad (7.48)$$

$$v_{(i,j)p_n} = 0, \forall (i, j) \in \Omega_L \quad (7.49)$$

$$p_{ib}^D = \bar{p}_{ib}^D \left(\kappa_{ib}^{PI} \left(1 + 2 (V_i - V_i^*) \right) + \kappa_{ib}^{PC} (V_i/V_i^*) + \kappa_{ib}^{PP} \right), \forall i \in \Omega_N, b \in \Omega_{B_i} \quad (7.50)$$

$$q_{ib}^D = \bar{q}_{ib}^D \left(\kappa_{ib}^{QI} \left(1 + 2 (V_i - V_i^*) \right) + \kappa_{ib}^{QC} (V_i/V_i^*) + \kappa_{ib}^{QP} \right), \forall i \in \Omega_N, b \in \Omega_{B_i}. \quad (7.51)$$

In (7.42), $\omega_{(i,j)}$ is a piecewise linear approximation of $\cos(\theta_i - \theta_j)$. Ω_P is the set of linearization segments in this approximation. For each break point $p \in \Omega_P$, B_p^B is value of the break point and C_p^B is the value of Cosine function at the point. Note for each line $(i, j) \in \Omega_L$ and break point $p \in \Omega_P$, $s_{(i,j)p}$ is an auxiliary positive variable and $v_{(i,j)p}$ is an auxiliary binary variable.

7.5 Numerical Results

In this section, the performance of the proposed scheme for the μ G load shedding problem is thoroughly evaluated using a large-scale μ G. All simulations were conducted on a PC with Intel Core™ i5 CPU @2.67 GHz and 4 GB RAM. The optimization model was implemented in the GAMS® IDE environment. The MILP and MINLP models were solved with IBM ILOG CPLEX® and BONMIN solvers, respectively. The modified IEEE 33-bus test system, which is a radial medium voltage (i.e., 12.66 kV) distribution system, is used as the test μ G in this chapter. The system topology and components are depicted in Fig. 7.4 and the feeders' and loads' data are obtained from [118] and [119]. The test μ G includes three DGs, whose technical data are given in Table 7.2. Meanwhile, three wind turbines as RESs

Table 7.2: Technical Data of DG Units

Parameter	DG ₁	DG ₂	DG ₃	DG ₄
$p^{DG,\min}$ (MW)	1	1	1	1
$p^{DG,\max}$ (MW)	4	3.38	3.38	4.72
$q^{DG,\min}$ (MW)	-0.5	-0.5	-0.5	-0.5
$q^{DG,\max}$ (MW)	2	2	2	2
R^U (MW/min.)	2.4	2.4	2.4	2.4
R^D (MW/min.)	2.4	2.4	2.4	2.4

Table 7.3: μ G Dynamic Data [107]

Parameter	Value	Parameter	Value
H (sec.)	2	τ^V (sec.)	0.1
D	1	τ^T (sec.)	0.5
R	0.05	t^{Shed} (msec.)	100
Δf_{SSF}^{\max} (Hz)	0.2	Δf_{DF}^{\max} (Hz)	0.5

with a total capacity of 3 MW are installed at buses 14, 16, and 31. To have a more realistic study, the load at each node of the μ G is divided into three load blocks. Furthermore, five different load types (i.e., general, residential, agricultural, commercial, and industrial) with different VOLLs are taken into account, Fig. 7.5 [112]. Finally, the test system's dynamic data can be found in Table 7.3.

In this section, three different contingencies are simulated in the test system, Table 7.4. To evaluate the performance of the proposed methodology, it is compared with the conventional UFLS scheme. The amount and setting of conventional UFLS relays have been designed according to [120]. The simulation results are summarized in the following figures and tables. According to Fig. 7.6, the amount of load shedding in the proposed method is less than that of the conventional UFLS approach. Considering the SFR model in the developed approach is the main reason of this observation. Similarly, the load shedding cost associated with the proposed method is much less than that of the conventional UFLS approach, Fig. 7.7. The reason is that in the conventional case, the locations of candidate loads to be shed are fixed, despite the fact that the VOLL of different feeders changes during the day. Therefore, in the conventional case, the interruption cost of dropped loads

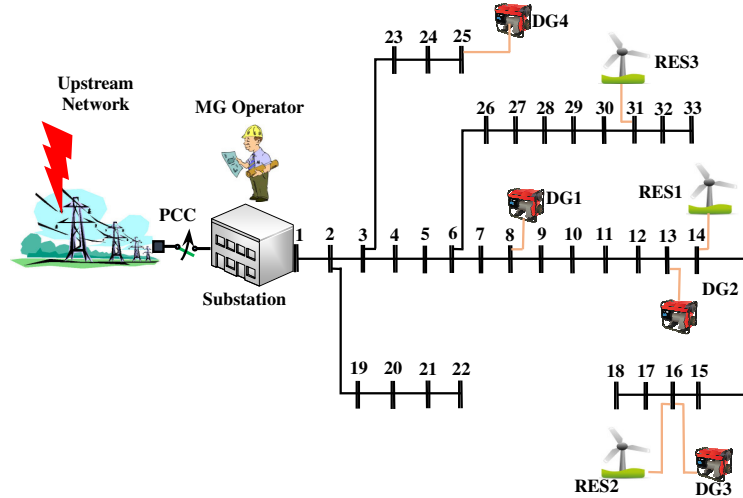


Figure 7.4: Single line diagram of the simulated μG [119].

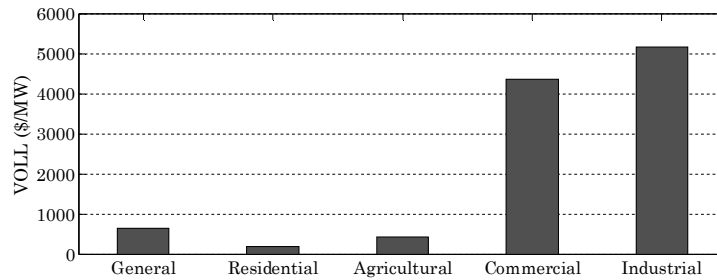


Figure 7.5: VOLL for different types of loads.

is not optimum around-the-clock. It is worth mentioning that in the proposed method, although the loads are shed according to their VOLL, operational limitations play a more important role. Indeed, the model is implemented in such a way that the load shedding cost is minimized, and at the same time, the network operational limitations are preserved.

As can be seen in Fig. 7.8, for all unintentional islanding events, minimum frequency of the μG is greater in the proposed approach due to its high speed in event indication and implementing the load shedding scenario. Taking a glance at Fig. 7.9 yields that the steady-state frequency of the μG following all contingencies is higher for the conventional UFLS method. On the other hand, the steady-state frequency associated with the proposed scheme is still in the safe range. Therefore, it can be inferred that the conventional method sheds non-optimal amount of loads encountering different events. These results prove that

Table 7.4: Simulated Contingencies

Contingency No.	P^M (MW)	p_{SSF}^{Shed}	p_{DF}^{Shed}
1	3	1.81	1.7
2	4	2.81	2.86
3	5	3.81	4.15

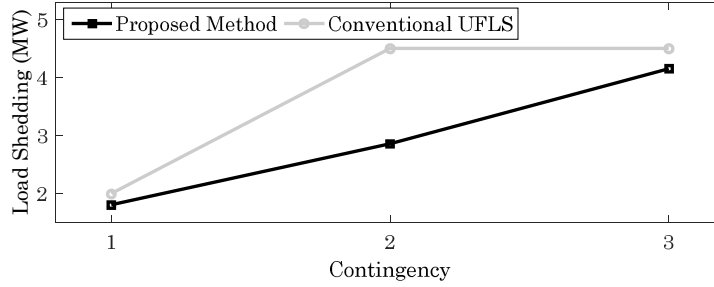


Figure 7.6: Comparison between the proposed and conventional UFLS methods in terms of load shedding.

the proposed method is capable of preserving the system from collapsing and moving it to a new steady state and stable condition.

It is worth mentioning that keeping the bus voltages and line flows within the permissible range would guarantee a secure μG operation following the load shedding process. Therefore, if these constraints are violated in the network, the proposed methodology seeks to return them to the permissible range by modifying the available control variables.

Table 7.5 provides the curtailed load blocks in contingency 2 for both the nonlinear and linear optimization models, where differences are highlighted in red bold. In this contingency, the optimal values of the objective function for the nonlinear and linear models are \$623.4 and \$625.6, respectively. Accordingly, the load shedding costs are roughly equal in these two models, and the curtailed loads are identical in most cases. Moreover, Table 7.6 shows a comparison between the computation time of the two models, which has been obtained using a relative optimality criterion (i.e., Optcr) of 10^{-2} . As can be seen, the computation time is considerably diminished in the linear model, and this is highly effective in precarious situations such as the load shedding process, since prompt measures can keep electromechanical dynamics away from becoming stability threatening.

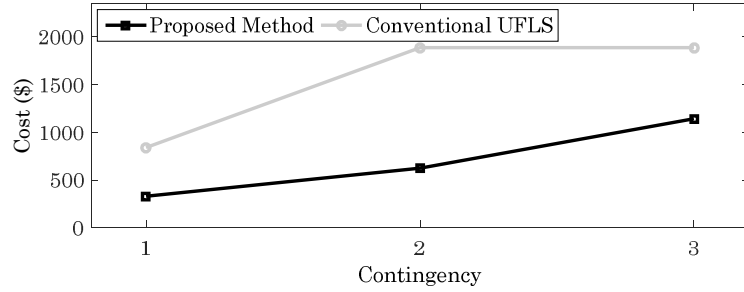


Figure 7.7: Comparison between the proposed and conventional UFLS methods in terms of load shedding cost.

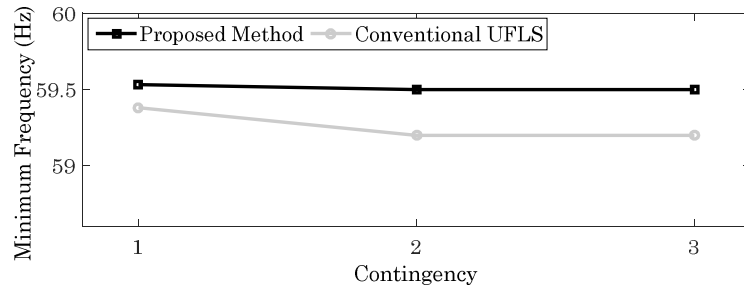


Figure 7.8: Comparison between the proposed and conventional UFLS methods in terms of minimum dynamic frequency.

7.6 Final Remarks

The proliferation of μ Gs all over the world has been remarkable in recent years, and their growth prospects in the future are astounding. μ Gs can improve the resilience of the grid based on their self-supply and island-mode capabilities. However, when a μ G unintentionally enters the island mode, a considerable number of customers (or even all of them) are disconnected from the grid in order to maintain the load-generation equilibrium. New methodologies are therefore required to optimize the load shedding process in μ Gs. In this chapter, an optimization-based load shedding model is presented as a promising tool to attain this goal. Mathematically, the load shedding model is formulated as a MILP problem. The structure of the proposed scheme reduces its communication requirements which is a major challenge in practice. The most relevant aspects of the proposed load shedding scheme are illustrated using a large-scale case study based on a 33-bus μ G. It was observed that the proposed method sheds less amount of load in comparison with

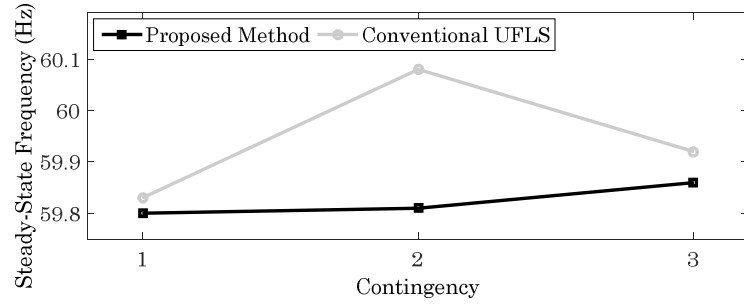


Figure 7.9: Comparison between the proposed and conventional UFLS methods in terms of steady-state frequency.

the conventional UFLS approach. Meanwhile, the developed structure outperformed the conventional scheme in terms of load shedding cost and minimum dynamic frequency following the load shedding process. Future studies could reformulate power flow equations for radial systems (since the complex power flow equations presented in this chapter are not necessary for radial networks). Moreover, an unbalanced power flow model can be adopted to make the proposed load shedding method more practical in real world applications.

Table 7.5: Comparison Between the Linear and Nonlinear Load Shedding Optimization Models

Bus #	Nonlinear Model			Linear Model		
	Load Block #			Load Block #		
	B1	B2	B3	B1	B2	B3
2	1.06			1.06		
3		0.96			0.96	
5		0.65			0.65	
6			0.63			
7						2.22
10		0.70	0.69		0.70	0.68
11					0.51	
12		0.67			0.67	
15		0.75	0.71		0.74	
16			0.68	0.74		0.67
17			0.69			0.68
18				1.03		
20	0.95		0.95	0.95		0.95
21			0.95			0.95
22	0.95			0.94		
24			4.62			4.61
25	4.72			4.72		
28		0.66			0.66	
30	2.16			2.16		
32			2.42			
33	0.67	0.66	0.70	0.67		0.69

Table 7.6: Computation Time of the Linear and Nonlinear Models

Contingency No.	Nonlinear model	Linear model
1	93 sec.	9 sec.
2	214 sec.	7 sec.
3	40 sec.	7 sec.

CHAPTER 8

STABILITY-CONSTRAINED OPTIMIZATION IN MULTI-MICROGRIDS

High penetration of distributed energy resources (DERs) is transforming the paradigm in power system operation. The ability to provide electricity to customers while the main grid is disrupted has introduced the concept of microgrids (μ Gs) with many challenges and opportunities. Emergency control of dangerous transients caused by the transition between the grid-connected and island modes in μ Gs is one of the main challenges in this context. To address this challenge, this chapter proposes a comprehensive optimization and real-time control framework for maintaining frequency stability of multi- μ G networks under an islanding event and for achieving optimal load shedding and network topology control with AC power flow constraints. We also develop a strong mixed-integer second-order cone programming (MISOCP)-based reformulation and a cutting plane algorithm for scalable computation. We believe this is the first time in the literature that such a framework for multi- μ G network control is proposed, and its effectiveness is demonstrated with extensive numerical experiments.

8.1 Introduction

Microgrids (μ Gs), as building blocks of smart distribution grids, provide a unique infrastructure for integrating a wide range of distributed energy resources (DERs) with different static and dynamic characteristics. They are able to operate in island mode and energize a portion of the grid while the main grid is down. This islanding capability of μ Gs is highly beneficial for both customers and electric utilities, especially in areas with frequent electrical outages. Although dynamic islanding is one of the basic objectives of building a μ G, IEEE Std. 929-2000 [14] and IEEE Std. 1547.7-2013 [15] mandate that DERs shall detect the unintentional island mode and cease to energize the grid within two seconds, mainly

due to safety concerns as well as complying with conventional control/protection schemes. Operation of DERs during intentional islanding has also been under consideration for future revisions of IEEE Std. 1547. Based on the current practices and standards, blackouts in μ Gs seem inevitable in the event of islanding (especially an unscheduled islanding which may occur subsequent to detection of abnormal conditions at the interconnection(s)).

Intuitively, the disconnection of DERs is not an ideal solution, particularly in a restructured environment where electric utilities compete to provide a more reliable service to customers. In this context, a recent draft standard for interoperability of DERs in 2017 has provided some guidance on scheduled and unscheduled islanding processes [121]. This draft standard defines an intentional local island as any portion of the grid that is totally within the bounds of a local power grid (e.g., a μ G), and further states that DERs may have to adjust several settings which shall be enabled only when the intentional island is isolated from the main grid. This standard calls for adaptive protection and control schemes to be used in such circumstances. This chapter is motivated by this need, and is aimed at providing a practical solution to the islanding process in modern distribution networks which are comprised of multiple μ Gs, referred to as multi-microgrid (multi- μ G) networks.

In a similar vein, [122, 123, 124] acknowledge that the current practice of disconnecting DERs following a disturbance is no longer a reliable solution. Specifically, reference [122] proposes an under frequency load shedding (UFLS) scheme to be used subsequent to islanding in a distribution system. This scheme sheds an optimal number of loads based on a set of criteria including frequency, rate of change of frequency, customers' willingness to pay, and load histories. The authors in [123] investigate autonomous operation of a distribution system as an individual μ G. The paper demonstrates the transient behavior of such a μ G due to preplanned and unplanned islanding processes. The authors also emphasize that future studies should develop control strategies/algorithms for multiple electronically interfaced DERs to achieve optimum response in terms of stability. In [124], a controller for distributed generation (DG) inverters is designed for both grid-connected and inten-

tional islanding modes. Moreover, an islanding-detection algorithm is developed in order to switch between the two modes.

On the other hand, the operation of multi- μ Gs has been studied in the literature from different perspectives, such as their on-line dynamic security assessment [125], interactive control for guaranteed small signal stability [126], transient stability assessment [127], electricity market operator design [128], hierarchical outage management [129], and self-healing [130] to name a few. Another set of literature that are conceptually related to our work are the recent studies on different relaxations of AC power flow equations [131].

8.1.1 Main Results

In this chapter, we propose a novel framework for the resilient operation of multi- μ G networks after a scheduled or unscheduled islanding in a distribution system. The framework is strategically designed in two parts. In the first part, we develop a near real-time decision support tool which is used to determine the optimal reconfiguration of the multi- μ G network, cooperation between μ Gs (sharing their resources), new operating point of dispatchable DERs, and emergency load curtailments (if necessary). The second part of the framework pertains to the real-time monitoring and control of multi- μ Gs based on the outcomes of the decision support tool. The main contributions of this chapter are summarized below.

- We formulate the real-time resilient operation, including optimal power flow, optimal load shedding, and optimal topology reconfiguration, of a multi- μ G network as a mixed-integer nonlinear programming (MINLP) problem. Then, we propose a mixed-integer second order cone programming (MISOCP) relaxation to this problem, which considerably improves the computational efficiency of our control framework and renders it scalable in practical systems.
- We derive necessary constraints for keeping the nadir and steady state frequency of the network within the permissible ranges, and introduce a new reformulation

for frequency limitation constraints. This reformulation implicitly guarantees the frequency stability of the network after dangerous transients such as islanding.

- We develop a set of valid inequalities and a separation scheme for incorporating the frequency constraints in the operation of a multi- μ G network, and based on that, we establish a cutting-plane approach to eliminate the frequency violations in a computationally effective way.

8.1.2 Chapter Outline

The rest of this chapter is organized as follows. Section 8.2 introduces a resilient multi- μ G network and gives an overview of the proposed scheme. The frequency response of multi- μ Gs to an islanding process is discussed in Section 8.3. In Section 8.4, a basic MINLP model for the real-time resilient operation of multi- μ Gs is presented. Section 8.5 is devoted to solution methodology, including the MISOCP relaxation and cutting plane algorithm. Section 8.6 exhibits the efficiency of the novel approach using an illustrative case study, and finally, the chapter concludes with Section 8.7.

8.2 Resilient Operation of Multi-Microgrids

8.2.1 Structure of a Multi-Microgrid Network

A distribution network may experience a scheduled islanding due to several reasons such as enhanced reliability, economic dispatch decisions for self-supply, pre-emptive action prior to inclement weather, etc. Moreover, unscheduled islanding happens subsequent to the detection of abnormal conditions at the interconnection(s) [121]. In either case, the distribution system can be further partitioned into multiple μ Gs, thereby improving the resilience of the system. Fig. 8.1 depicts a distribution network under such circumstances. As can be seen in this example, the distribution network is composed of four μ Gs, where each μ G is connected to the rest of the system through the point of common coupling

(PCC). Note that μ Gs in a multi- μ G network are commonly integrated via voltage-source-converter-(VSC)-based interfaces at the PCC, and the behavior of each μ G is characterized by the control scheme of its interface [132]. PCCs are commonly equipped with intelligent electronic devices (IEDs) with synchrophasor capability [125]. A communication network connects the IEDs to the distribution management system (DMS).

In Fig. 8.1(a), a set of buses (white fill in the figure), namely linking buses, are not categorized to any μ G. Additionally, the lines (dashed/dotted in Fig. 8.1(a), or equivalently l_1 to l_5 in Fig. 8.1(b)) between such buses, namely linking lines, are equipped with switching relays, enabling various configurations for the multi- μ G network. This portion of the distribution network that consists of the linking buses and linking lines is called the *linking grid*. Fig. 8.1(b) illustrates the linking grid associated with the multi- μ G network of Fig. 8.1(a). Finally, the buses by which each μ G is connected to the linking grid (gray fill in the figure) are called boundary buses.

8.2.2 Overview of the Proposed Resilient Operation Scheme

The general framework of the proposed resilience management scheme is illustrated in Fig. 8.2. This framework can be divided into two stages: i) near real-time decision support tool, and ii) real-time monitoring and control. In the first stage, the distribution system operator (DSO) leverages the state estimation (SE) module and obtains the input parameters of an optimization model. These data include the generation/consumption level of DERs/Loads, real and reactive power exchange at PCCs, and the status of the circuit breakers (i.e., network topology). Subsequently, the optimization model is solved and the following resilient operation strategies are determined: optimal configuration of the linking network, cooperation between μ Gs (sharing their DERs), new operating point of dispatchable DERs, and emergency load curtailments (if necessary). Note that the frequency limitations of the system are embedded in the optimization model to ensure the frequency stability of multi- μ Gs following the islanding event. In the next step, a look-up table is generated based on the

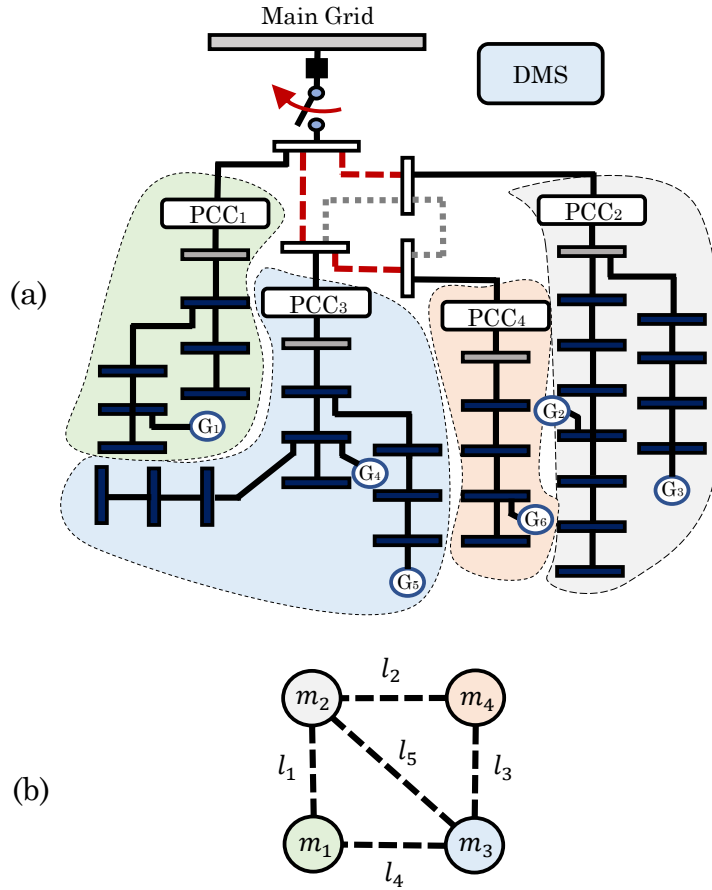


Figure 8.1: Schematic diagram of a distribution system under islanding. (a) Multi- μ G network. (b) Linking grid.

results of the optimization model. On the other side, in the second stage, the status of the main circuit breaker (i.e., the islanding status of the distribution network) is monitored using indication data. If an unscheduled/scheduled islanding happens, the pre-specified strategies will be implemented in the multi- μ G network.

The principal focus of this chapter is on the first stage (left-hand side of Fig. 8.2), i.e., developing a near real-time decision support tool that will be thoroughly discussed in the following sections. The second stage (right-hand side of Fig. 8.2) corresponds to the mechanisms for implementing such decisions. The details of these mechanisms, which are enabled by synchrophasor technology, go beyond the scope of this chapter.

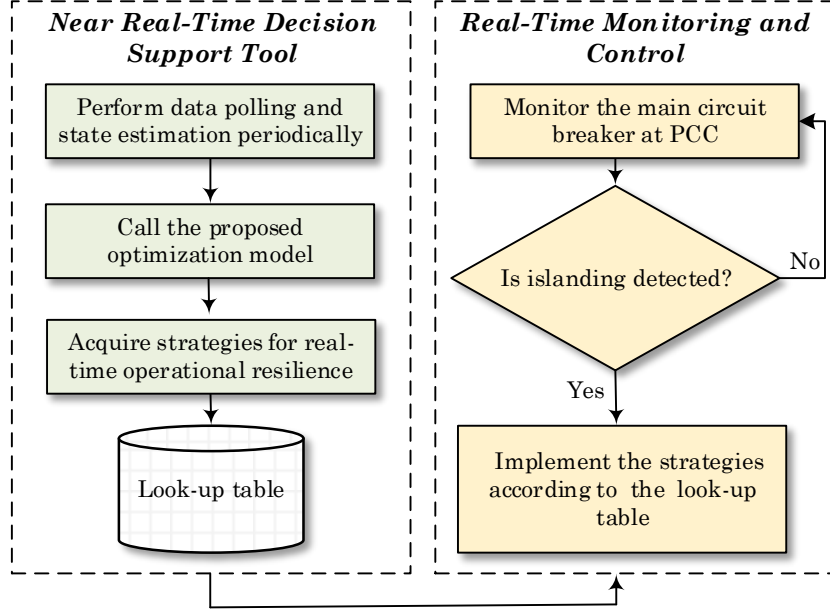


Figure 8.2: The general framework of the proposed resilient operation approach.

8.3 Frequency Response of Multi-Microgrids Subsequent to Islanding

In this section, we will derive the steady-state and nadir frequencies of a multi- μ G network subsequent to an imbalance between real power generation and consumption. Later in Section 8.4.5, we will use these two metrics to construct our proposed frequency constraints, ensuring that they will remain in the permissible range during the transition between the grid-connected and island modes.

8.3.1 Inertial Response

As mentioned earlier, μ Gs in a multi- μ G network are integrated via VSC-based interfaces at the PCC. Meanwhile, VSC-based interfaces are controlled in such a way that they emulate the behavior of conventional synchronous machines [127]. Inspired by this fact, let us first focus on inertial response of μ Gs. Suppose \mathcal{M} is the set of all μ Gs in the multi- μ G network. The artificial swing equation describes the inertial frequency dynamics of each $m \in \mathcal{M}$,

$$\frac{d\Delta\omega_m}{dt} = \frac{1}{2H_m} \left(\Delta P_m^M - \Delta P_m^E \right), \quad (8.1)$$

where $\Delta\omega_m$ is the frequency deviation in p.u.; H_m is the artificial inertia constant in seconds; ΔP_m^M and ΔP_m^E are the mechanical and electrical power deviations in p.u., respectively. Based on (8.1), modeling interconnected μ Gs can be realized by the so-called aggregation method [32]. Without loss of generality, we assume that for each $m \in \mathcal{M}$, equation (8.1) is per-unitized based on a common power, S_{Base} . We define the center of inertia (COI) frequency as

$$\omega_{COI} := \frac{\sum_{m \in \mathcal{M}} H_m \omega_m}{\sum_{m \in \mathcal{M}} H_m}. \quad (8.2)$$

Proposition 10. *The swing equation of a fictitious equivalent generator whose frequency is equal to ω_{COI} has the same form as*

$$\frac{d\Delta\omega_{COI}}{dt} = \frac{1}{2H_a} \left(\Delta P_a^M - \Delta P_a^E \right), \quad (8.3)$$

where H_a , ΔP_a^M , and ΔP_a^E are defined below

$$H_a := \sum_{m \in \mathcal{M}} H_m, \quad (8.4)$$

$$\Delta P_a^M := \sum_{m \in \mathcal{M}} \Delta P_m^M, \quad \Delta P_a^E := \sum_{m \in \mathcal{M}} \Delta P_m^E. \quad (8.5)$$

Proof. A complete proof of this basic result cannot be easily located in the literature. Therefore, we provide one here. Consider a small deviation from the initial value in (8.2), i.e., $\Delta\omega_{COI} := \omega_{COI} - \omega_{COI}^0$ and $\Delta\omega_m := \omega_m - \omega_m^0$, and take derivative of its both sides with respect to t :

$$\frac{d\Delta\omega_{COI}}{dt} = \frac{\sum_{m \in \mathcal{M}} H_m \frac{d\Delta\omega_m}{dt}}{\sum_{m \in \mathcal{M}} H_m}. \quad (8.6)$$

Then, re-arrange (8.1) as

$$H_m \frac{d\Delta\omega_m}{dt} = \frac{1}{2} \left(\Delta P_m^M - \Delta P_m^E \right). \quad (8.7)$$

Now substitute (8.7) in (8.6), as

$$\frac{d\Delta\omega_{COI}}{dt} = \frac{\sum_{m \in \mathcal{M}} \frac{1}{2} (\Delta P_m^M - \Delta P_m^E)}{\sum_{m \in \mathcal{M}} H_m}. \quad (8.8)$$

With the definition of (8.4)-(8.5), we get (8.3). \square

In the rest of the chapter, the COI frequency is simply denoted by ω instead of ω_{COI} .

8.3.2 Droop Response

Now we construct the aggregated system frequency response (SFR) model of a multi- μG network as depicted in Fig. 8.3. In this model, the transfer function $\frac{1}{2H_a s + D}$ in the forward path represents the swing equation (8.3) as well as the frequency-dependent behavior of the loads which is lumped into a single damping constant D . In this chapter, this damping constant D is assumed to remain unchanged while aggregating different μG s. Different feedback loops in Fig. 8.3 model the contribution of each μG to the droop control of the multi- μG network [32]. For each $m \in \mathcal{M}$, R_m is the droop constant of the VSC; T_m and T'_m are the corresponding time constants.

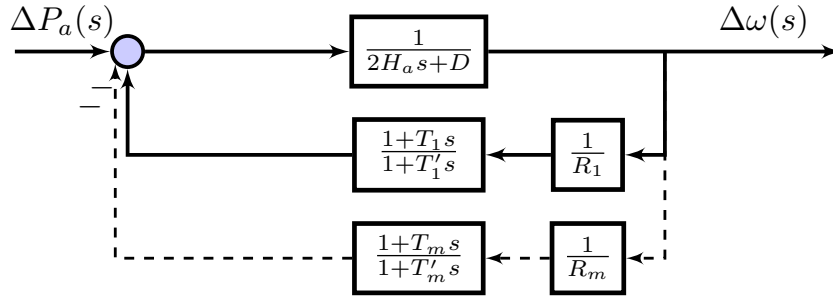


Figure 8.3: Block diagram of the aggregated SFR model.

In general, the order of this SFR model is $|\mathcal{M}| + 1$. In particular, however, we are interested in the steady state and nadir outputs of the SFR model. It can be shown that the steady state output of this general-order model is not a function of the time constant T'_m . Moreover, the results of a sensitivity analysis on the parameters of a similar SFR model

confirms that the nadir frequency is less sensitive to T'_m [133]. Accordingly, we assume identical values of T'_m for all μ Gs in the multi- μ G network, i.e., $T' := T'_m, \forall m \in \mathcal{M}$. Consequently, the transfer function of the aggregated SFR model can be written as (8.9), with the additional parameters defined in (8.10):

$$\mathcal{H}(s) = \frac{1 + T's}{2H_a T' (s^2 + 2\xi\omega_n s + \omega_n^2)}, \quad (8.9)$$

$$\omega_n := \sqrt{\frac{D + 1/R_a}{2H_a T'}}, \quad \xi := \frac{2H_a + T'D + K_a}{2\sqrt{2H_a T' (D + 1/R_a)}}, \quad (8.10a)$$

$$\frac{1}{R_a} := \sum_{m \in \mathcal{M}} \frac{1}{R_m}, \quad K_a := \sum_{m \in \mathcal{M}} \frac{T_m}{R_m}, \quad (8.10b)$$

where $\Delta P_a(s)$ is the disturbance power in the multi- μ G.

8.3.3 Steady State and Nadir Frequencies at COI

In general, the dynamic behavior of the aggregated SFR model can be described by two parameters ξ and ω_n . If $\xi = 0$, we will have an oscillatory system where the transient response will not die out. If $\xi \in (0, 1)$, the transient frequency response is oscillatory (under-damped). When $\xi = 1$, we are in the critically-damped condition, and finally, if $\xi \in (1, +\infty)$, the frequency response will be over-damped. We shall now analyze the frequency response of the system to the unit-step input, i.e., $\Delta P_a(s) = 1/s$ for three cases: the under-damped, critically-damped, and over-damped cases.

Proposition 11. *In the under-damped case, the steady state and nadir COI frequencies of a multi- μ G network after a unit-step disturbance can be obtained by (8.11) and (8.12), respectively, i.e.,*

$$\Delta\omega(t^{ss}) = \frac{1}{D + 1/R_a}, \quad (8.11)$$

$$\Delta\omega(t^N) = \frac{1}{D + 1/R_a} \left(1 + \sqrt{\frac{T' - R_a K_a}{2H_a R_a}} e^{-\xi\omega_n t^N} \right), \quad (8.12)$$

where t^N in (8.12) can be calculated as follows:

$$t^N = \begin{cases} \frac{1}{\omega_r} \left(\pi - \tan^{-1} \left(\frac{\omega_r T'}{1 - \xi\omega_n T'} \right) \right), & \text{if } \xi\omega_n T' < 1, \\ \frac{\pi}{2\omega_r}, & \text{if } \xi\omega_n T' = 1, \\ \frac{1}{\omega_r} \left(\tan^{-1} \left(\frac{\omega_r T'}{\xi\omega_n T' - 1} \right) \right), & \text{if } \xi\omega_n T' > 1. \end{cases} \quad (8.13)$$

Additionally, in the critically-damped and over-damped cases, the nadir COI frequency is equal to the steady state COI frequency, and both can be calculated according to (8.11).

Proof. In the under-damped case, the poles of the system are $s_{1,2} = -\xi\omega_n \pm j\omega_r$, where $\omega_r = \omega_n \sqrt{1 - \xi^2}$ is the damped natural frequency and $j = \sqrt{-1}$ is the imaginary unit. In this case, the unit-step response is

$$\Delta\omega(t) = \frac{1}{2H_a T'} \left(\frac{1}{\omega_n^2} + \frac{e^{-\xi\omega_n t}}{\omega_r} \left(T' \sin(\omega_r t) - \frac{1}{\omega_n} \sin(\omega_r t + \phi) \right) \right), \quad (8.14)$$

where $\phi := \tan^{-1}(\frac{\sqrt{1-\xi^2}}{\xi})$. By definition, the steady state frequency is equal to $\Delta\omega(t^{ss}) := \lim_{t \rightarrow +\infty} \Delta\omega(t)$, which leads to (8.11). The time when the frequency nadir happens (when the lowest frequency is reached before the frequency starts to recover) can be calculated by solving the optimization problem $t^N := \min\{t : \frac{d\Delta\omega(t)}{dt} = 0, t \in \mathbb{R}_{++}\}$. The closed-form solution to this problem is equal to (8.13). Additionally, substitution of t^N in (8.14) yields (8.12). Observe that when the two poles of the transfer function (8.9) are nearly equal, i.e., $s_{1,2} = -\omega_n$, the system is approximated by a critically-damped one. Moreover, in the over-damped case, the two poles of the transfer function are negative real and unequal, i.e., $s_{1,2} = -\xi\omega_n \pm \omega_n \sqrt{\xi^2 - 1}$. In the last two cases, no overshoot or undershoot is observed

in the transient response of the system, and consequently, the nadir frequency is equal to the steady state frequency which is identical to (8.11). \square

The interested reader is referred to Proposition 3 in [46] for similar results under different settings. Now we are ready to adopt the steady-state and nadir frequencies at COI in order to build our optimization model for the resilient operation of a multi- μ G network.

8.4 Resilient Operation Problem Formulation

Consider a linking grid $\tilde{\mathcal{N}} = (\tilde{\mathcal{B}}, \tilde{\mathcal{L}})$, where $\tilde{\mathcal{B}}$ and $\tilde{\mathcal{L}}$ denote the set of linking buses and linking lines, respectively. We assume that the distribution network under study is comprised of a set of μ Gs, i.e., $m \in \mathcal{M}$, where each μ G is modeled as a disjoint network $\mathcal{N}_m = (\mathcal{B}_m, \mathcal{L}_m)$. Without loss of generality, we assume only one PCC for each μ G, and the corresponding boundary bus is denoted by $\hat{\mathcal{B}}$. In this section, we aim to introduce an optimization model which is able to determine the optimal resilience improvement strategy, including optimal load shedding and network topology control with AC power flow, in the wake of a scheduled/unscheduled islanding in a multi- μ G network. Our model is formulated as follows.

8.4.1 Objective Function

The objective function (8.15) is to minimize the total load shedding cost in all μ Gs:

$$\min \sum_{m \in \mathcal{M}} \sum_{i \in \mathcal{B}_m} \lambda_{mi}^{VOLL} (1 - x_{mi}) \bar{p}_{mi}^D, \quad (8.15)$$

where λ_{mi}^{VOLL} is the value of lost load (VOLL) in μ G m and bus i ; \bar{p}_{mi}^D is the pre-islanding active power consumption obtained from state estimation (SE); and x_{mi} is a binary variable indicating the status of such a load after islanding happens.

8.4.2 Real-Time AC Power Flow Limitations in μ Gs

The set of constraints (8.16)-(8.25) which are defined for each $m \in \mathcal{M}$ guarantee the AC power flow security of each μ G after the islanding event. Let G_{mij} and B_{mij} be the conductance and susceptance of line (i, j) in μ G m ; and f_{mij}^P and f_{mij}^Q be the active and reactive flow of that line. Additionally, let p_{mg}^G and q_{mg}^G be the active and reactive power output of DER g in μ G m ; and similarly, p_{mi}^D and q_{mi}^D be the active and reactive power consumption of the load at bus i in μ G m . We define V_{mi} and θ_{mi} as the voltage magnitude and angle of bus i in μ G m . Finally, ΔP_m and ΔQ_m denote the active and reactive power exchange between the μ G m and the linking grid (through the VSC). Based on this notation, constraints (8.16) and (8.17) model the active and reactive power balance within each μ G. Similarly, constraints (8.18) and (8.19) are related to the active and reactive power balance at the boundary buses. Note that \mathcal{O} in these equations is the mapping of the set of DERs into the set of buses. The set of equations (8.20)-(8.23) constitute the AC power flow equations, line flow limits, and voltage bounds in each μ G. Finally, active and reactive power demands at different buses are modeled by the voltage-dependent ZIP model (8.24) and (8.25), where κ^{PI} , κ^{PC} , and κ^{PP} denote the coefficients of constant impedance, constant current, and constant power terms in active power loads, respectively. These coefficients are defined in the same way for reactive power loads.

$$\sum_{g:(g,i) \in \mathcal{O}_m} p_{mg}^G - x_{mi} p_{mi}^D = \sum_{(i,j) \in \mathcal{L}_m} f_{mij}^P, \forall i \in \mathcal{B}_m \quad (8.16)$$

$$\sum_{g:(g,i) \in \mathcal{O}_m} q_{mg}^G - x_{mi} q_{mi}^D = \sum_{(i,j) \in \mathcal{L}_m} f_{mij}^Q, \forall i \in \mathcal{B}_m \quad (8.17)$$

$$\sum_{g:(g,i) \in \mathcal{O}_m} p_{mg}^G - x_{mi} p_{mi}^D + \Delta P_m = \sum_{(i,j) \in \mathcal{L}_m} f_{mij}^P, \forall i \in \hat{\mathcal{B}}_m \quad (8.18)$$

$$\sum_{g:(g,i) \in \mathcal{O}_m} q_{mg}^G - x_{mi} q_{mi}^D + \Delta Q_m = \sum_{(i,j) \in \mathcal{L}_m} f_{mij}^Q, \forall i \in \hat{\mathcal{B}}_m \quad (8.19)$$

$$f_{mij}^P = G_{mij} \left(V_{mi}^2 - V_{mi} V_{mj} \cos(\theta_{mi} - \theta_{mj}) \right) - B_{mij} V_{mi} V_{mj} \sin(\theta_{mi} - \theta_{mj}), \forall (i, j) \in \mathcal{L}_m \quad (8.20)$$

$$f_{mij}^Q = -B_{mij} \left(V_{mi}^2 - V_{mi} V_{mj} \cos(\theta_{mi} - \theta_{mj}) \right) - G_{mij} V_{mi} V_{mj} \sin(\theta_{mi} - \theta_{mj}), \forall (i, j) \in \mathcal{L}_m \quad (8.21)$$

$$f_{mij}^P + f_{mji}^P \leq f_{mij}^{\max}, \forall (i, j) \in \mathcal{L}_m \quad (8.22)$$

$$V_{mi}^{\min} \leq V_{mi} \leq V_{mi}^{\max}, \forall i \in (\mathcal{B}_m \cup \hat{\mathcal{B}}_m) \quad (8.23)$$

$$p_{mi}^D = \bar{p}_{mi}^D \left(\kappa_{mi}^{PI} V_{mi}^2 + \kappa_{mi}^{PC} V_{mi} + \kappa_{mi}^{PP} \right), \forall i \in (\mathcal{B}_m \cup \hat{\mathcal{B}}_m) \quad (8.24)$$

$$q_{mi}^D = \bar{q}_{mi}^D \left(\kappa_{mi}^{QI} V_{mi}^2 + \kappa_{mi}^{QC} V_{mi} + \kappa_{mi}^{QP} \right), \forall i \in (\mathcal{B}_m \cup \hat{\mathcal{B}}_m). \quad (8.25)$$

8.4.3 Real-Time AC Power Flow Limitations in the Linking Grid

Similarly, this group of constraints are associated with the AC power flow limitations of the linking grid. Here, line switching is available, therefore, Z_{mk} is a binary variable indicating the status of the linking line (m, k) . It is worth mentioning that connection/disconnection of μ Gs to the linking grid is performed through the switchgear located at PCCs and line switching in the linking grid is commonly available through the distribution automation switches and isolators [125]. Let M_{mk} be a sufficiently large positive number. In these constraints, in terms of notation, we use tilde over the variables and parameters to make the difference between the linking grid and the rest of the distribution grid. In particular, equations (8.26) and (8.27) model the active and reactive power balance at external buses. The group of constraints (8.28)-(8.35) are associated with the AC power flow equations (where the lines are allowed to be switched on and off), line flow limits, and voltage bounds in the linking grid.

$$-\Delta P_m = \sum_{(m,k) \in \tilde{\mathcal{L}}} \tilde{f}_{mk}^P, \forall m \in \mathcal{M} \quad (8.26)$$

$$-\Delta Q_m = \sum_{(m,k) \in \tilde{\mathcal{L}}} \tilde{f}_{mk}^Q, \forall m \in \mathcal{M} \quad (8.27)$$

$$\begin{aligned} & -\tilde{f}_{mk}^P + \tilde{G}_{mk} \left(\tilde{V}_m^2 - \tilde{V}_m \tilde{V}_k \cos(\theta_m - \theta_k) \right) \\ & - \tilde{B}_{mk} \tilde{V}_m \tilde{V}_k \sin(\theta_m - \theta_k) \\ & + (1 - Z_{mk}) M_{mk} \geq 0, \forall (m, k) \in \tilde{\mathcal{L}} \end{aligned} \quad (8.28)$$

$$\begin{aligned} & -\tilde{f}_{mk}^P + \tilde{G}_{mk} \left(\tilde{V}_m^2 - \tilde{V}_m \tilde{V}_k \cos(\theta_m - \theta_k) \right) \\ & - \tilde{B}_{mk} \tilde{V}_m \tilde{V}_k \sin(\theta_m - \theta_k) \\ & - (1 - Z_{mk}) M_{mk} \leq 0, \forall (m, k) \in \tilde{\mathcal{L}} \end{aligned} \quad (8.29)$$

$$\begin{aligned} & -\tilde{f}_{mk}^Q - \tilde{B}_{mk} \left(V_m^2 - \tilde{V}_m \tilde{V}_k \cos(\theta_m - \theta_k) \right) \\ & - \tilde{G}_{mk} \tilde{V}_m \tilde{V}_k \sin(\theta_m - \theta_k) \\ & + (1 - Z_{mk}) M'_{mk} \geq 0, \forall (m, k) \in \tilde{\mathcal{L}} \end{aligned} \quad (8.30)$$

$$\begin{aligned} & -\tilde{f}_{mk}^Q - \tilde{B}_{mk} \left(V_m^2 - \tilde{V}_m \tilde{V}_k \cos(\theta_m - \theta_k) \right) \\ & - \tilde{G}_{mk} \tilde{V}_m \tilde{V}_k \sin(\theta_m - \theta_k) \\ & - (1 - Z_{mk}) M'_{mk} \leq 0, \forall (m, k) \in \tilde{\mathcal{L}} \end{aligned} \quad (8.31)$$

$$-\tilde{f}_{mk}^{P,\max} Z_{mk} \leq \tilde{f}_{mk}^P \leq \tilde{f}_{mk}^{P,\max} Z_{mk}, \forall (m, k) \in \tilde{\mathcal{L}} \quad (8.32)$$

$$-\tilde{f}_{mk}^{Q,\max} Z_{mk} \leq \tilde{f}_{mk}^Q \leq \tilde{f}_{mk}^{Q,\max} Z_{mk}, \forall (m, k) \in \tilde{\mathcal{L}} \quad (8.33)$$

$$\tilde{f}_{mk}^P + \tilde{f}_{km}^P \leq \tilde{f}_{mk}^{P,\text{Loss},\max}, \forall (m, k) \in \tilde{\mathcal{L}} \quad (8.34)$$

$$\tilde{V}_m^{\min} \leq \tilde{V}_m \leq \tilde{V}_m^{\max}, \forall i \in \tilde{\mathcal{B}}, m \in \mathcal{M}. \quad (8.35)$$

8.4.4 DER Output Limitations and Binary Variable Declaration

Finally, (8.36)-(8.39) pertain to the limitations on the output of the generators and the declaration of binary variables. In these constraints, R^D , R^U , and $p^{G,0}$ are the ramp-down, ramp-up, and pre-islanding active power generation of DERs, respectively.

$$-R_{mg}^D \leq p_{mg}^G - p_{mg}^{G,0} \leq R_{mg}^U, \quad \forall g \in \mathcal{G}_m, m \in \mathcal{M} \quad (8.36)$$

$$p_{mg}^{G,\min} \leq p_{mg}^G \leq p_{mg}^{G,\max}, \quad \forall g \in \mathcal{G}_m, m \in \mathcal{M} \quad (8.37)$$

$$q_{mg}^{G,\min} \leq q_{mg}^G \leq q_{mg}^{G,\max}, \quad \forall g \in \mathcal{G}_m, m \in \mathcal{M} \quad (8.38)$$

$$x \in \{0, 1\}^{|\mathcal{M}| \times |\mathcal{B} \cup \hat{\mathcal{B}}|}, \quad Z \in \{0, 1\}^{|\tilde{\mathcal{L}}|}. \quad (8.39)$$

8.4.5 Frequency Constraints and Reformulation

In Section 8.3, we developed the steady-state and nadir frequencies of a multi- μ G network subsequent to an imbalance between real power generation and consumption. Indeed, these are two important metrics which are employed to ensure the frequency security of the network. Therefore, we aim to keep these two metrics within the permissible range while the multi- μ G network moves from the grid-connected mode to the island mode. Note that subsequent to the islanding process, the distribution network might be partitioned into different components (each component might include one or more μ Gs), and the frequency security limitations must be met for each component separately. We propose the following constraints for ensuring the frequency security of the multi- μ G network for each $\mathcal{S} \subseteq \tilde{\mathcal{N}}, \mathcal{S} \neq \emptyset$:

$$\begin{aligned} \Delta\omega_N^{\min} &\leq \alpha_{\mathcal{S}} \sum_{m \in \tilde{\mathcal{B}}_{\mathcal{S}}} \left(-\Delta P_m^0 + \sum_{i \in \mathcal{B}_m} (1 - x_{mi}) p_{mi}^D \right) \\ &+ \mathcal{I}_M(\mathcal{S} \text{ is connected}) + \mathcal{I}_M(\mathcal{S} \text{ is isolated}), \quad (8.40a) \\ \Delta\omega_N^{\max} &\geq \alpha_{\mathcal{S}} \sum_{m \in \tilde{\mathcal{B}}_{\mathcal{S}}} \left(-\Delta P_m^0 + \sum_{i \in \mathcal{B}_m} (1 - x_{mi}) p_{mi}^D \right) \end{aligned}$$

$$- \mathcal{I}_M (\mathcal{S} \text{ is connected}) - \mathcal{I}_M (\mathcal{S} \text{ is isolated}), \quad (8.40b)$$

$$\Delta\omega_{ss}^{\min} \leq \beta_{\mathcal{S}} \sum_{m \in \tilde{\mathcal{B}}_{\mathcal{S}}} \left(-\Delta P_m^0 + \sum_{i \in \mathcal{B}_m} (1 - x_{mi}) p_{mi}^D \right) + \mathcal{I}_M (\mathcal{S} \text{ is connected}) + \mathcal{I}_M (\mathcal{S} \text{ is isolated}), \quad (8.40c)$$

$$\Delta\omega_{ss}^{\max} \geq \beta_{\mathcal{S}} \sum_{m \in \tilde{\mathcal{B}}_{\mathcal{S}}} \left(-\Delta P_m^0 + \sum_{i \in \mathcal{B}_m} (1 - x_{mi}) p_{mi}^D \right) - \mathcal{I}_M (\mathcal{S} \text{ is connected}) - \mathcal{I}_M (\mathcal{S} \text{ is isolated}), \quad (8.40d)$$

where \mathcal{I}_M is the indicator function whose value is equal to 0 if the condition is satisfied, and equal to a sufficiently large number, otherwise. Moreover, $\alpha_{\mathcal{S}}$ and $\beta_{\mathcal{S}}$ are the nadir and steady state values of the unit-step frequency response, which are calculated in (8.12) and (8.11), respectively. The use of subscript \mathcal{S} in these two parameters emphasizes that they should be calculated for each $\mathcal{S} \subseteq \tilde{\mathcal{N}}$, that is, the associated parameters H_a , R_a , and K_a are obtained by (8.4) and (8.10b), where $m \in \mathcal{M}$ is replaced by $m \in \tilde{\mathcal{B}}_{\mathcal{S}}$. Note that $\Delta\omega_N^{\min}/\Delta\omega_N^{\max}$ and $\Delta\omega_{ss}^{\min}/\Delta\omega_{ss}^{\max}$ denote the lower/upper bound on the nadir and steady state frequencies, respectively. Moreover, ΔP_m^0 denotes the pre-islanding power exchange between μG m and the linking grid. In (8.40), the first term on the right-hand side of the inequities is indeed the multiplication of the unit-step response by the post-islanding net power mismatch (i.e., pre-islanding power exchange minus the amount of post-islanding load shedding). Let us further investigate these frequency security constraints by defining

$$\tilde{\mathcal{L}}(\mathcal{S}) := \{(m, k) \in \tilde{\mathcal{L}} : m, k \in \tilde{\mathcal{B}}_{\mathcal{S}}, m > k\}, \quad (8.41a)$$

$$\delta(\mathcal{S}) := \{(m, k) \in \tilde{\mathcal{L}} : m \in \tilde{\mathcal{B}}_{\mathcal{S}}, k \notin \tilde{\mathcal{B}}_{\mathcal{S}}, m > k\}. \quad (8.41b)$$

Given a subgraph \mathcal{S} of $\tilde{\mathcal{N}}$, $\tilde{\mathcal{L}}(\mathcal{S})$ in (8.41a) denotes the set of edges in the subgraph \mathcal{S} , i.e., the set of edges in $\tilde{\mathcal{L}}$ whose both ends are in $\tilde{\mathcal{B}}_{\mathcal{S}}$. Additionally, (8.41b) describes the cutset $\delta(\mathcal{S})$, i.e., the set of edges that have exactly one end in $\tilde{\mathcal{B}}_{\mathcal{S}}$. Now, we will provide an equivalent reformulation for (8.40) using a spanning tree characterization. This reformulation

will help us verify the frequency constraints in each connected component of the grid. It also provides new insights into the way we interpret the frequency constraints. We will focus on the inequality (8.40a); (8.40b)-(8.40d) can be similarly analyzed.

Proposition 12. *Inequality (8.40a) is equivalent to (8.42a), that is,*

$$\begin{aligned} \Delta\omega_N^{\min} &\leq \alpha_{\mathcal{S}} \sum_{m \in \tilde{\mathcal{B}}_{\mathcal{S}}} \left(-\Delta P_m^0 + \sum_{i \in \mathcal{B}_m} (1 - x_{mi}) p_{mi}^D \right) \\ &+ \min \{0 : (8.43a) - (8.43d)\} + \sum_{(m,k) \in \delta(\mathcal{S})} (Z_{mk}) M_N, \\ &\quad \forall \mathcal{S} \subseteq \tilde{\mathcal{N}}, \mathcal{S} \neq \emptyset \end{aligned} \tag{8.42a}$$

where

$$u_{mk} \leq Z_{mk}, \quad \forall (m, k) \in \tilde{\mathcal{L}}(\mathcal{S}), \tag{8.43a}$$

$$\sum_{(m,k) \in \tilde{\mathcal{L}}(\mathcal{S})} u_{mk} = |\tilde{\mathcal{B}}_{\mathcal{S}}| - 1, \tag{8.43b}$$

$$\sum_{(m,k) \in \delta(\mathcal{S})} u_{mk} \geq 1, \quad \forall \mathcal{S} \subseteq \tilde{\mathcal{N}}, \mathcal{S} \neq \emptyset, \tilde{\mathcal{N}}, \tag{8.43c}$$

$$u_{mk} \in \{0, 1\}, \quad \forall (m, k) \in \tilde{\mathcal{L}}(\mathcal{S}). \tag{8.43d}$$

Proof. The minimization problem embedded in (8.42a) has an optimal value equal to 0 if there exists an spanning tree in \mathcal{S} . Otherwise, the problem is infeasible and the objective value will be equal to $+\infty$, making (8.42a) redundant. Here, we use the definition of a tree as a connected graph containing $n - 1$ edges (n is the number of nodes in the graph). Accordingly, (8.43a) ensures that the spanning tree is a subgraph of \mathcal{S} . Additionally, (8.43b) and (8.43c) guarantee that the spanning tree has $|\tilde{\mathcal{B}}_{\mathcal{S}}| - 1$ edges and satisfies the connectivity requirement, respectively. Finally, the last term in (8.42a) ensures that \mathcal{S} is a component. \square

Note that both (8.40) and their reformulation in the form of (8.42a) have an exponential

number of constraints. We will propose a cutting-plane approach to deal with this issue in Section 8.5.

8.4.6 Overall MINLP Formulation

Before passing to solution methodology of the problem, let us review the overall MINLP formulation of the multi- μ G resilient operation problem. The decision variables of this formulation are: i) the status of loads (x_{mi}); ii) the status of linking lines (Z_{mk}); iii) active and reactive flow of lines ($f_{mij}^P, f_{mij}^Q, \tilde{f}_{mk}^P, \tilde{f}_{mk}^Q$); iv) active and reactive power of DERs and loads ($p_{mg}^G, q_{mg}^G, p_{mi}^D, q_{mi}^D$); v) voltage magnitudes and angles (V_{mi}, θ_{mi}); vi) active and reactive power exchange between the μ Gs and the linking grid ($\Delta P_m, \Delta Q_m$); and vii) spanning tree variable (u_{mk}). For the sake of brevity, let \mathcal{X} be the set of constraints (8.16)-(8.39) and let \mathcal{F} represent the set of constraints in (8.40). Now, we introduce $\mathcal{MINLP}(\mathcal{X}, \mathcal{F})$ as follows:

$$\begin{aligned} \vartheta = \min & \sum_{m \in \mathcal{M}} \sum_{i \in \mathcal{B}_m} \lambda_{mi}^{VOLL} (1 - x_{mi}) \bar{p}_{mi}^D \\ \text{s.t.} & \quad (8.16)-(8.40). \end{aligned}$$

8.5 Solution Methodology

The formulation $\mathcal{MINLP}(\mathcal{X}, \mathcal{F})$ is a nonconvex nonlinear optimization problem. Moreover, the developed frequency limitations in (8.40) as well as their equivalent reformulations in (8.42a) induce exponentially many constraints. In this section, we will address these challenges.

8.5.1 MISOCP Reformulation and Convexification

Observe that all the nonlinearity and nonconvexity of $\mathcal{MINLP}(\mathcal{X}, \mathcal{F})$ stem from three sources: i) the nonlinear terms V_{mi}^2 , $V_{mi}V_{mj} \cos(\theta_{mi} - \theta_{mj})$, and $V_{mi}V_{mj} \sin(\theta_{mi} - \theta_{mj})$ in constraints (8.20)-(8.21) and also the similar terms in (8.28)-(8.31), ii) the quadratic term V_{mi}^2 in constraints (8.24)-(8.25), iii) the bilinear terms $x_{mi}p_{mi}^D$ and $x_{mi}q_{mi}^D$ in constraints

(8.16)-(8.19) and (8.40). In this section, we will convexify/linearize the aforementioned terms, leading to an MISOCP relaxation of the multi- μ G resilient operation problem.

MISOCP Relaxation of AC Power Flow Equations

Based on the recent development in SOCP relaxation of standard AC-OPF [134], we define the following auxiliary variables for each $(i, j) \in \mathcal{L}_m$ and $m \in \mathcal{M}$:

$$C_{mij} := V_{mi}V_{mj} \cos(\theta_{mi} - \theta_{mj}), \quad (8.44a)$$

$$S_{mij} := V_{mi}V_{mj} \sin(\theta_{mi} - \theta_{mj}). \quad (8.44b)$$

Observe that (8.44) implies (8.45), that is

$$C_{mij}^2 + S_{mij}^2 = C_{mii}C_{mjj}, \quad (8.45a)$$

$$S_{mij} = -S_{mji}, C_{mij} = C_{mji}. \quad (8.45b)$$

Similarly, we define $\tilde{C}_{mk} := \tilde{V}_m\tilde{V}_k \cos(\theta_m - \theta_k)$ and $\tilde{S}_{mk} = \tilde{V}_m\tilde{V}_k \sin(\theta_m - \theta_k)$ for each $(m, k) \in \tilde{\mathcal{L}}$, and the following constraints will be inferred:

$$\tilde{C}_{mk}^2 + \tilde{S}_{mk}^2 = \tilde{C}_{mm}\tilde{C}_{kk}, \quad (8.46a)$$

$$\tilde{S}_{mk} = -\tilde{S}_{km}, \tilde{C}_{mk} = \tilde{C}_{km}. \quad (8.46b)$$

Note that the convex relaxation of (8.45a) and (8.46a) are:

$$C_{mij}^2 + S_{mij}^2 \leq C_{mii}C_{mjj}, \quad (8.47a)$$

$$\tilde{C}_{mk}^2 + \tilde{S}_{mk}^2 \leq \tilde{C}_{mm}\tilde{C}_{kk}. \quad (8.47b)$$

With a change of variables for each $m \in \mathcal{M}$ and $(i, j) \in \mathcal{L}_m$, constraints (8.20) and (8.21) can be written as

$$f_{mij}^P = G_{mij} (C_{mii} - C_{mij}) - B_{mij} S_{mij}, \quad (8.48a)$$

$$f_{mij}^Q = -B_{mij} (C_{mii} - C_{mij}) - G_{mij} S_{mij}, \quad (8.48b)$$

and the voltage bound (8.23) for each $m \in \mathcal{M}$ and $i \in (\mathcal{B}_m \cup \hat{\mathcal{B}}_m)$ is transformed into

$$(V_{mi}^{\min})^2 \leq C_{mii} \leq (V_{mi}^{\max})^2. \quad (8.49)$$

Likewise, a change of variables for each $(m, k) \in \tilde{\mathcal{L}}$ leads to the constraints (8.50) as the counterparts of (8.28)-(8.31):

$$- \tilde{f}_{mk}^P + \tilde{G}_{mk} (\tilde{C}_{mm} - \tilde{C}_{mk}) - \tilde{B}_{mk} \tilde{S}_{mk} \quad (8.50a)$$

$$+ (1 - Z_{mk}) M_{mk} \geq 0,$$

$$- \tilde{f}_{mk}^P + \tilde{G}_{mk} (\tilde{C}_{mm} - \tilde{C}_{mk}) - \tilde{B}_{mk} \tilde{S}_{mk} \quad (8.50b)$$

$$- (1 - Z_{mk}) M_{mk} \leq 0,$$

$$- \tilde{f}_{mk}^Q - \tilde{B}_{mk} (\tilde{C}_{mm} - \tilde{C}_{mk}) - \tilde{G}_{mk} \tilde{S}_{mk} \quad (8.50c)$$

$$+ (1 - Z_{mk}) M'_{mk} \geq 0,$$

$$- \tilde{f}_{mk}^Q - \tilde{B}_{mk} (\tilde{C}_{mm} - \tilde{C}_{mk}) - \tilde{G}_{mk} \tilde{S}_{mk} \quad (8.50d)$$

$$- (1 - Z_{m,k}) M'_{mk} \leq 0,$$

and similarly the voltage bound (8.35) for each $m \in \mathcal{M}$ and $i \in \tilde{\mathcal{B}}$ can be written as:

$$(\tilde{V}_m^{\min})^2 \leq \tilde{C}_{mm} \leq (\tilde{V}_m^{\max})^2. \quad (8.51)$$

MISOCP Relaxation of ZIP Load Models

Using the SOCP auxiliary variables defined in Section 8.5.1, the ZIP load models (8.24) and (8.25) can be written as (8.52) for each $m \in \mathcal{M}$ and $i \in (\mathcal{B}_m \cup \hat{\mathcal{B}}_m)$, that is

$$p_{mi}^D = \bar{p}_{mi}^D \left(\kappa_{mi}^{PI} C_{mii} + \kappa_{mi}^{PC} \sqrt{C_{mii}} + \kappa_{mi}^{PP} \right), \quad (8.52a)$$

$$q_{mi}^D = \bar{q}_{mi}^D \left(\kappa_{mi}^{QI} C_{mii} + \kappa_{mi}^{QC} \sqrt{C_{mii}} + \kappa_{mi}^{QP} \right). \quad (8.52b)$$

The convex relaxation of these two constraints can be written as

$$\bar{p}_{mi}^D \left(\kappa_{mi}^{PI} C_{mii} + \kappa_{mi}^{PC} \sqrt{C_{mii}} + \kappa_{mi}^{PP} \right) - p_{mi}^D \geq 0, \quad (8.53a)$$

$$\bar{q}_{mi}^D \left(\kappa_{mi}^{QI} C_{mii} + \kappa_{mi}^{QC} \sqrt{C_{mii}} + \kappa_{mi}^{QP} \right) - q_{mi}^D \geq 0. \quad (8.53b)$$

Since the variable C_{mii} is bounded by the closed interval $[C_{mii}^{\min}, C_{mii}^{\max}]$, the convex relaxation (8.53) can be tightened by introducing the following two hyperplanes which pass through the end points for each $i \in (\mathcal{B}_m \cup \hat{\mathcal{B}}_m)$ and $m \in \mathcal{M}$:

$$p_{mi}^D - p_{mi}^{D,\min} \geq \frac{p_{mi}^{D,\max} - p_{mi}^{D,\min}}{C_{mii}^{\max} - C_{mii}^{\min}} \left(C_{mii} - C_{mii}^{\min} \right), \quad (8.54a)$$

$$q_{mi}^D - q_{mi}^{D,\min} \geq \frac{q_{mi}^{D,\max} - q_{mi}^{D,\min}}{C_{mii}^{\max} - C_{mii}^{\min}} \left(C_{mii} - C_{mii}^{\min} \right). \quad (8.54b)$$

Proposition 13. *Constraints (8.53a) and (8.53b) are SOCP representable in terms of C_{mii}^2 .*

Proof. We focus on constraint (8.53a); constraint (8.53b) is similarly analyzed. First, we rearrange and square both sides of the constraint for each $i \in (\mathcal{B}_m \cup \hat{\mathcal{B}}_m)$ and $m \in \mathcal{M}$ such that

$$\kappa_{mi}^{PC} \sqrt{C_{mii}} \geq \frac{p_{mi}^D}{\bar{p}_{mi}^D} - \kappa_{mi}^{PI} C_{mii} - \kappa_{mi}^{PP} \quad (8.55)$$

$$\left(\kappa_{mi}^{PC} \right)^2 C_{mii} \geq \left(\frac{p_{mi}^D}{\bar{p}_{mi}^D} - \kappa_{mi}^{PI} C_{mii} - \kappa_{mi}^{PP} \right)^2. \quad (8.56)$$

Note that $C_{mii} = (\frac{C_{mii+1}}{2})^2 - (\frac{C_{mii-1}}{2})^2$, therefore (8.56) can be written as the following SOCP constraint for each $i \in (\mathcal{B}_m \cup \hat{\mathcal{B}}_m)$ and $m \in \mathcal{M}$:

$$\left(\kappa_{mi}^{PC}\right)^2 \left(\frac{C_{mii} + 1}{2}\right)^2 \geq \left(\kappa_{mi}^{PC}\right)^2 \left(\frac{C_{mii} - 1}{2}\right)^2 + \left(\frac{p_{mi}^D}{\bar{p}_{mi}^D} - \kappa_{mi}^{PI} C_{mii} - \kappa_{mi}^{PP}\right)^2. \quad (8.57)$$

The proof is complete. □

Linearization of the Bilinear Terms

Finally, let us linearize the bilinear terms $x_{mi}p_{mi}^D$ and $x_{mi}q_{mi}^D$ in (8.16)-(8.19) and (8.40), where each bilinear term involves the product of a binary variable and a nonnegative continuous variable. We linearize these disjunctive terms via the big-M method by introducing auxiliary semi-continuous variables $\rho_{mi} := x_{mi}p_{mi}^D$ and $\sigma_{mi} := x_{mi}q_{mi}^D$ and defining additional constraints for each $i \in (\mathcal{B}_m \cup \hat{\mathcal{B}}_m)$ and $m \in \mathcal{M}$:

$$- (1 - x_{mi}) \check{M}_{mi}^p \leq \rho_{mi} - p_{mi}^D \leq \check{M}_{mi}^p (1 - x_{mi}), \quad (8.58a)$$

$$- x_{mi} \check{M}_{mi}^p \leq \rho_{mi} \leq \check{M}_{mi}^p x_{mi}, \quad (8.58b)$$

$$- (1 - x_{mi}) \check{M}_{mi}^q \leq \sigma_{mi} - q_{mi}^D \leq \check{M}_{mi}^q (1 - x_{mi}), \quad (8.58c)$$

$$- x_{mi} \check{M}_{mi}^q \leq \sigma_{mi} \leq \check{M}_{mi}^q x_{mi}. \quad (8.58d)$$

In order to reduce the integrality gap in (8.58), the big-Ms (i.e., \check{M}_{mi}^p and \check{M}_{mi}^q) should be as small as possible, and it is usually challenging to determine correct values for them to use for each specific implementation. However, in this particular application, we can set $\check{M}_{mi}^p = \bar{p}_{mi}^D$ and $\check{M}_{mi}^q = \bar{q}_{mi}^D$. Note that these data (i.e., the upper bounds of active and reactive loads) are usually available in any system. Now, substituting the auxiliary variables ρ_{mi} and σ_{mi} into the constraints (8.16)-(8.19), we get the linear constraints (8.59a)-(8.59b) for each $m \in \mathcal{M}$, $i \in \mathcal{B}_m$, and also the constraints (8.59c)-(8.59d) for each $m \in \mathcal{M}$,

$i \in \hat{\mathcal{B}}_m$:

$$\sum_{g:(g,i) \in \mathcal{O}_m} p_{mg}^G - \rho_{mi} = \sum_{(i,j) \in \mathcal{L}_m} f_{mij}^P, \quad (8.59a)$$

$$\sum_{g:(g,i) \in \mathcal{O}_m} q_{mg}^G - \sigma_{mi} = \sum_{(i,j) \in \mathcal{L}_m} f_{mij}^Q, \quad (8.59b)$$

$$\sum_{g:(g,i) \in \mathcal{O}_m} p_{mg}^G - \rho_{mi} + \Delta P_m = \sum_{(i,j) \in \mathcal{L}_m} f_{mij}^P, \quad (8.59c)$$

$$\sum_{g:(g,i) \in \mathcal{O}_m} q_{mg}^G - \sigma_{mi} + \Delta Q_m = \sum_{(i,j) \in \mathcal{L}_m} f_{mij}^Q. \quad (8.59d)$$

Complementarily, the frequency constraints (8.40) can be written as (8.60) for each $\mathcal{S} \subseteq \tilde{\mathcal{N}}, \mathcal{S} \neq \emptyset$, where the indicator function \mathcal{I}_M is modeled using the big-M method and the bilinear terms are replaced with their linear counterparts:

$$\begin{aligned} \Delta\omega_N^{\min} &\leq \alpha_{\mathcal{S}} \sum_{m \in \tilde{\mathcal{B}}_{\mathcal{S}}} \left(-\Delta P_m^0 + \sum_{i \in \mathcal{B}_m} (p_{mi}^D - \rho_{mi}) \right) \\ &+ \sum_{(m,k) \in \tilde{\mathcal{L}}(\mathcal{S})} (1 - Z_{mk}) M_N + \sum_{(m,k) \in \delta(\mathcal{S})} (Z_{mk}) M_N, \end{aligned} \quad (8.60a)$$

$$\begin{aligned} \Delta\omega_N^{\max} &\geq \alpha_{\mathcal{S}} \sum_{m \in \tilde{\mathcal{B}}_{\mathcal{S}}} \left(-\Delta P_m^0 + \sum_{i \in \mathcal{B}_m} (p_{mi}^D - \rho_{mi}) \right) \\ &- \sum_{(m,k) \in \tilde{\mathcal{L}}(\mathcal{S})} (1 - Z_{mk}) M_N - \sum_{(m,k) \in \delta(\mathcal{S})} (Z_{mk}) M_N, \end{aligned} \quad (8.60b)$$

$$\begin{aligned} \Delta\omega_{ss}^{\min} &\leq \beta_{\mathcal{S}} \sum_{m \in \tilde{\mathcal{B}}_{\mathcal{S}}} \left(-\Delta P_m^0 + \sum_{i \in \mathcal{B}_m} (p_{mi}^D - \rho_{mi}) \right) \\ &+ \sum_{(m,k) \in \tilde{\mathcal{L}}(\mathcal{S})} (1 - Z_{mk}) M_{ss} + \sum_{(m,k) \in \delta(\mathcal{S})} (Z_{mk}) M_{ss}, \end{aligned} \quad (8.60c)$$

$$\begin{aligned} \Delta\omega_{ss}^{\max} &\geq \beta_{\mathcal{S}} \sum_{m \in \tilde{\mathcal{B}}_{\mathcal{S}}} \left(-\Delta P_m^0 + \sum_{i \in \mathcal{B}_m} (p_{mi}^D - \rho_{mi}) \right) \\ &- \sum_{(m,k) \in \tilde{\mathcal{L}}(\mathcal{S})} (1 - Z_{mk}) M_{ss} - \sum_{(m,k) \in \delta(\mathcal{S})} (Z_{mk}) M_{ss}. \end{aligned} \quad (8.60d)$$

Overall MISOCP Formulation

Before proceeding further with the analysis, let us define the set \mathcal{R} as the set of constraints (8.22), (8.26), (8.27), (8.32)-(8.34), (8.36)-(8.39), (8.45b), (8.46b), (8.47)-(8.51), (8.53), (8.54), (8.58), and (8.59). Recall that \mathcal{F} is the set of frequency constraints. Now, we can formally define $MISOCP(\mathcal{R}, \mathcal{F})$, as the MISOCP relaxation of the multi- μ G resilient operation problem:

$$\begin{aligned} \psi = \min & \sum_{m \in \mathcal{M}} \sum_{i \in \mathcal{B}_m} \lambda_{mi}^{VOLL} (1 - x_{mi}) \bar{p}_{mi}^D \\ \text{s.t.} & \text{ (8.22), (8.26), (8.27), (8.32)-(8.34), (8.36)-(8.39), (8.45b),} \\ & \text{(8.46b), (8.47)-(8.51), (8.53), (8.54), (8.58)-(8.60).} \end{aligned}$$

It remains to deal with the exponential number of constraints in \mathcal{F} . This is the topic of the next section.

8.5.2 Cutting Plane Algorithm for Frequency Constraints

In this section, we propose a cutting plane approach to solve $MISOCP(\mathcal{R}, \mathcal{F})$. The idea is to construct $\{\mathcal{F}_k\}_{k \geq 0}$, that is a sequence of relaxations of the set \mathcal{F} , and dynamically update \mathcal{F}_k to obtain stronger relaxations in each iteration. Recall that the set \mathcal{F} contains exponentially many frequency constraints.

With this aim in mind, let $\mathcal{C}_S^1, \mathcal{C}_S^2, \mathcal{C}_S^3$, and \mathcal{C}_S^4 denote respectively the constraints (8.60a), (8.60b), (8.60c), and (8.60d), for a given connected component \mathcal{S} of the linking grid, where $\mathcal{S} \subseteq \tilde{\mathcal{N}}, \mathcal{S} \neq \emptyset$. Moreover, let the graph $\tilde{\mathcal{N}}^*$ represent the configuration of the linking grid for a given solution to $MISOCP(\mathcal{R}, \mathcal{F}_k)$, and let $\mathcal{Q} = \{\mathcal{S}_{v_1}, \mathcal{S}_{v_2}, \dots, \mathcal{S}_{v_N}\}$ denote the set of connected components of $\tilde{\mathcal{N}}^*$ where $\{v_1, v_2, \dots, v_N\} \subseteq \{1, 2, \dots, |\tilde{\mathcal{B}}|\}$. For each component in \mathcal{Q} , we check the inequalities $\{\mathcal{C}_S^\gamma\}_{\gamma=1}^4$; if any frequency violation is detected, the corresponding valid inequality will be added to the set \mathcal{F}_k . In other words, let \mathcal{A} be the set of feasible solutions to the problem $MISOCP(\mathcal{R}, \mathcal{F})$. In each iteration, if an optimal

Algorithm 1 Multi- μ G resilient operation algorithm

```

1: Initialize  $k \leftarrow 0$ ,  $\mathcal{F}_k \leftarrow \emptyset$ , Flag  $\leftarrow$  NO
2: while Flag = NO do
3:   Solve  $MISOCP(\mathcal{R}, \mathcal{F}_k)$  to obtain the graph  $\tilde{\mathcal{N}}^*$  representing the optimal configuration of the linking grid
4:   Compute  $\mathcal{Q} = \{\mathcal{S}_{v_1}, \mathcal{S}_{v_2}, \dots, \mathcal{S}_{v_N}\}$  as the set of connected components of  $\tilde{\mathcal{N}}^*$ 
5:   Flag  $\leftarrow$  YES
6:   for  $v = v_1$  to  $v_N$  do
7:     for  $\gamma = 1$  to 4 do
8:       if  $\mathcal{S}_v$  violates  $\mathcal{C}_{\mathcal{S}_v}^\gamma$  then
9:         Flag  $\leftarrow$  NO
10:         $\mathcal{F}_k \leftarrow \mathcal{F}_k \cup \{\mathcal{C}_{\mathcal{S}_v}^\gamma\}$ 
11:       end if
12:     end for
13:   end for
14:    $k \leftarrow k + 1$ 
15: end while

```

solution of $MISOCP(\mathcal{R}, \mathcal{F}_k)$ is in the set \mathcal{A} , we stop since we have already found an optimal solution to $MISOCP(\mathcal{R}, \mathcal{F})$. Otherwise, we generate a cut and add it to \mathcal{F}_k to separate the point from the set \mathcal{A} and obtain stronger relaxations in the next iteration. Algorithm 1 provides the details of the proposed cutting plane approach.

As can be seen, in Algorithm 1, we need a function to return the connected components of the undirected graph $\tilde{\mathcal{N}}^*$. Recall that a connected component of an undirected graph is a maximal connected subgraph of the graph. This function can be implemented via depth-first or breadth-first algorithm. See [135] for details.

Theorem 16. *Algorithm 1 converges to an optimal solution of the MISOCP-based multi- μ G resilient operation problem, i.e., $MISOCP(\mathcal{R}, \mathcal{F})$, in a finite number of iterations.*

Proof. Let x_{mi}^* and Z_{mk}^* be an optimal solution to the problem $MISOCP(\mathcal{R}, \mathcal{F}_0)$ where $i \in (\mathcal{B}_m \cup \hat{\mathcal{B}}_m)$, $m \in \mathcal{M}$, $(m, k) \in \tilde{\mathcal{L}}$, and $\mathcal{F}_0 = \emptyset$. If x_{mi}^* and Z_{mk}^* satisfy (8.60), then Algorithm 1 converges to the optimal solution in one iteration. Otherwise, in each iteration, at least one constraint will be added to the set \mathcal{F}_k . We observe that the total number of constraints in (8.60) is $4r$, where r is the number of possible connected components of $\tilde{\mathcal{N}}$.

Since each connected component is examined at most once in this algorithm, the number of iterations needed for the convergence of the algorithm is less than $4r$. \square

8.6 Numerical Results

In this section, the performance of the proposed framework for the multi- μ G resilient operation problem is thoroughly evaluated. All simulations are conducted on a 64-bit PC with Intel Core i7 CPU 2.8 GHz processor and 16 GB RAM. The algorithm is implemented in the GAMS IDE environment [136]. We use BONMIN V1.8 [137] to solve MINLPs and CPLEX V12.4 [138] to solve the MISOCPs. Moreover, we use the 39-bus multi- μ G network (depicted in Fig. 8.1) as our test system. This network is composed of six DERs, whose technical data are given in Table 8.1. Feeders' and loads' data are adopted from different portions of a standard IEEE distribution test system whose data can be found in [139]. To have a more realistic study, five different load types (i.e., general, residential, agricultural, commercial, and industrial) with different VOLLs are taken into account (see Fig. 5 in [120]). Finally, the μ Gs' dynamic data is given in Table 8.2.

Table 8.1: Technical Data of DERs

Parameters	DERs					
	G ₁	G ₂	G ₃	G ₄	G ₅	G ₆
$p^{G,\min} [\times 100 \text{ kW}]$	1	1	1	1	1	1
$p^{G,\max} [\times 100 \text{ kW}]$	5	2	5	2	2	5
$q^{G,\min} [\times 100 \text{ kVAr}]$	-5	-2	-5	-2	-2	-5
$q^{G,\max} [\times 100 \text{ kVAr}]$	5	2	5	2	2	5
$R^D \setminus R^D [\times 100 \text{ kW/min}]$	2	1	2	1	1	2

Table 8.2: Dynamic Parameters of the VSC Controller in each μ G

Parameter	Value	Parameter	Value	Parameter	Value
H [sec.]	0.9	D	1	T' [sec.]	0.1
R	0.08	$\Delta\omega_N$ [Hz]	0.5	V_{Base} [kV]	12.66
T [sec.]	0.008	$\Delta\omega_{ss}$ [Hz]	0.1	S_{Base} [MW]	5

We assume that all μ Gs in Fig. 8.1 were initially connected to the main grid through

the dashed lines (in red). Subsequent to islanding, these lines along with the main circuit breaker trip. The proposed MISOCP-based resilient operation approach determines the optimal strategy which may include re-closing the dashed lines and switching the dotted lines (in gray), leading to different configurations for the distribution network. In order to evaluate our framework, we compare it with the following two schemes:

- *MINLP-Based Scheme*: In this scheme, we follow our resilient operation scheme; however, we use $\text{MINLP}(\mathcal{X}, \mathcal{F})$ as the decision support tool in Algorithm 1.
- *Conventional UFLS Scheme*: In this scheme, subsequent to islanding of the distribution network, each μG individually enters the island mode where the conventional UFLS relays will curtail the necessary blocks of loads until reaching the equilibrium point. The settings of these relays are obtained from [120].

8.6.1 Comparison with the MINLP-Based Scheme

Solution and Computation Time

Table 8.3 provides a comparison between the MINLP-based and MISOCP-based schemes considering different severities for the islanding event (we define severity as the amount of power flow from the main grid to the distribution network before the islanding). The computation times in this table are obtained using a relative optimality criterion (i.e., Optcr) of zero.

As can be seen, although the computation time is considerably diminished in the MISOCP-based model, the solution quality (in terms of load curtailment) is the same, and this is highly effective in precarious situations such as the emergency management of distribution networks, since prompt measures can keep electromechanical dynamics away from becoming stability threatening.

Table 8.3: Comparison Between the MISOCP and MINLP Models

Islanding Severity [kW]	MISOCP-Based Scheme		MINLP-Based Scheme	
	Curtailement [kW]	Computation time [sec.]	Curtailement [kW]	Computation time [sec.]
2700	2248.4	57.21	2248.8	2978.8
3200	2725	52.74	2725	7185.7
3700	3208.4	73.58	3209.4	9593.5

Convergence

In order to see more details about the convergence of Algorithm 1, let us analyze the second islanding event (with the severity of 3200 kW). For this event, Table 8.4 provides the objective function value, the cardinality of the set \mathcal{F}_k , the amount of load shedding, the configuration of the multi- μ G network, and the elapsed time in each iteration of the algorithm while solving $MISOCP(\mathcal{R}, \mathcal{F})$. Accordingly, the algorithm converges in 15 iterations. In each iteration, a set of cuts are generated to separate a given solution of $MISOCP(\mathcal{R}, \mathcal{F}_k)$, that is a mixed integer solution, from the set \mathcal{A} . This separation in each iteration leads to an interplay between load shedding adjustments and network topology control, demonstrated in the 4th and 5th columns of Table 8.4. It must be emphasized that when a mixed integer solution is cut off, the corresponding integer solution (i.e., the projection onto the space of integer variables) may not be cut off. For instance, in the 7th iteration in in Table 8.4, the amount of load shedding is 2295 kW and the connected edges of the linking grid are l_1 , l_3 , and l_5 (see Fig. 8.1(b)). Although a valid inequality cuts off this mixed integer solution in the next iteration, the corresponding integer solution appears again in the 15th iteration with a different amount of load shedding.

As another interesting result, in the eighth iteration, the distribution network is partitioned into two sub-systems and the objective function is increased by 8.5%. Eventually, in the 15th iteration, the optimal resilience improvement strategy is achieved while the distribution system is reconfigured as one connected component.

For the sake of comparison, Table 8.5 provides the outputs of Algorithm 1 while solv-

ing $MINLP(\mathcal{X}, \mathcal{F})$. As can be seen, the algorithm converges in a more number of iterations and the computation time of each iteration is considerably more than that of the MISOCP-based model. The final solutions (the objective function, load curtailment, and configuration of the linking grid), nevertheless, are quite the same as the ones in Table 8.4.

Table 8.4: Convergence of the Proposed Algorithm While Solving $MISOCP(\mathcal{R}, \mathcal{F})$

k	ψ [$\times 100$ \$]	$ \mathcal{F}_k $	Curtailment [$\times 100$ kW]	Connected edges of $\tilde{\mathcal{N}}$	Elapsed time/iter [sec.]
0	1579.09	0	22.98	l_1, l_2, l_3	6.0
1	1579.09	1	22.93	l_2, l_4, l_5	3.8
2	1579.09	2	22.91	l_2, l_3, l_4	4.0
3	1579.09	3	23.07	l_1, l_3, l_4	4.6
4	1579.09	4	22.87	l_3, l_4, l_5	3.2
5	1579.09	5	22.93	l_1, l_2, l_5	2.9
6	1579.09	6	23.03	l_1, l_2, l_4	2.6
7	1579.09	7	22.95	l_1, l_3, l_5	2.7
8	1714.69	8	23.40	l_2, l_3, l_5	1.6
9	2069.38	10	24.29	l_1, l_4	5.9
10	2081.35	12	24.92	l_1, l_5	3.9
11	2081.35	13	24.92	l_4, l_5	2.0
12	2086.23	14	24.11	l_2, l_5	2.4
13	2086.23	15	24.15	l_3, l_5	2.2
14	2086.23	16	24.07	l_2, l_3	2.7
15	2235.96	17	27.25	l_1, l_3, l_5	2.4

8.6.2 Comparison with the Conventional UFLS Scheme

Fig. 8.4 provides a comparison between the MISOCP-based scheme and the conventional UFLS scheme while they are coping with the second islanding event (with severity of 3200 kW). To have a more realistic result, we assume the communication latency to be 100 ms in the proposed scheme. We also consider the intentional delay of the UFLS relays to be 100 ms. Since the distribution network is partitioned into four μ Gs in the conventional UFLS scheme, this figure compares the amount of load shedding, nadir frequency, and steady state frequency in each μ G (denoted by m_1 to m_4), on the one hand, and the same indices in the multi- μ G network which is obtained from the proposed MISOCP-based

Table 8.5: Convergence of the Proposed Algorithm While Solving $MINLP(\mathcal{X}, \mathcal{F})$

k	ϑ [$\times 100$ \$]	$ \mathcal{F}_k $	Curtailed [$\times 100$ kW]	Connected edges of $\tilde{\mathcal{N}}$	Elapsed time/iter [sec.]
0	1579.09	0	22.89	l_1, l_3, l_4	664.2
1	1579.09	1	22.88	l_1, l_2, l_4	478.1
2	1579.09	2	22.87	l_1, l_2, l_3, l_5	391.9
3	1579.09	3	22.86	l_1, l_2, l_5	329.8
4	1579.09	4	22.87	l_2, l_3, l_4, l_5	341.4
5	1579.09	5	22.84	l_2, l_4, l_5	246.3
6	1579.09	6	22.86	l_1, l_3, l_5	285.5
7	1579.09	7	22.83	l_3, l_4, l_5	185.0
8	1579.09	8	22.86	l_1, l_2, l_3	165.0
9	1579.09	9	22.86	l_2, l_3, l_4	124.1
10	1714.69	10	23.14	l_2, l_3, l_5	291.7
11	2069.38	12	24.06	l_1, l_4	516.6
12	2081.35	14	24.68	l_1, l_5	387.5
13	2081.35	15	24.71	l_4, l_5	353.4
14	2086.23	16	23.86	l_2, l_5	322.2
15	2086.23	17	23.88	l_3, l_5	530.0
16	2086.23	18	23.89	l_2, l_3	172.6
17	2235.96	19	27.25	l_1, l_3, l_4	1400.7

scheme, on the other hand.

Accordingly, the total amount of load shedding in our proposed scheme is 2725 kW, while the steady state and nadir frequencies are remained within the permissible range. In comparison, the total amount of load shedding in the conventional scheme is 3700 kW (even more than the initial power deficiency), and the frequency of the μ Gs violates the safe range. Specifically, in m_3 , the violation of frequency is more serious, and the conventional scheme fails to maintain the frequency stability of the network. The main reason for this observation is the rigidity of the conventional UFLS scheme in dealing with different contingencies. In this scheme, load shedding is implemented in several steps with fixed sizes, regardless of the intensity of the islanding. Therefore, it can be inferred that the conventional method sheds non-optimal amount of loads encountering islanding events. These results illustrate that the proposed method is capable of preserving the distribution network from collapsing and moving it to a new steady state and stable condition. Aside from the

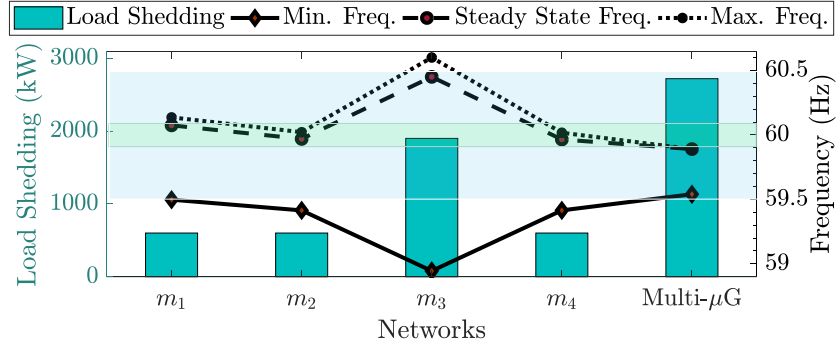


Figure 8.4: Comparison between the proposed MISOCP-based and conventional UFLS schemes for an islanding event with severity of 3200 kW. Permissible ranges of nadir and steady state frequencies are shown by horizontal bars.

COI frequency, keeping the bus voltages and line flows within the permissible range in our proposed scheme would guarantee a secure operation following the islanding process, and this is not considered in the conventional scheme.

8.7 Final Remarks

In this chapter, we propose a novel framework for the near real-time operation as well as the real-time control of multi- μ G networks. Our framework provides the optimal power flow, optimal load shedding, and optimal topology reconfiguration, while frequency dynamics and AC power flow limitations are taken into account. An exact reformulation of frequency constraints in a cutting plane algorithm with tight MISOCP relaxations is established, which significantly speeds up computation and achieves near optimal solution. To the best of our knowledge, this comprehensive optimization and control framework for the frequency stability of multi- μ Gs is proposed for the first time in the literature. Our numerical experiments further illustrate that the proposed emergency control scheme can successfully monitor, verify, and act to guarantee that the multi- μ G network remains within the operational limits during post-islanding frequency dynamics. It is practical for real-world applications and outperforms the conventional UFLS scheme in terms of load shedding amount, number of curtailed customers, and frequency stability.

CHAPTER 9

CONCLUSIONS AND FUTURE WORK

This dissertation is aimed at devising easy-to-check conditions to certify the stability of electric power systems and also developing control and optimization schemes for the stable operation of these systems. Our results are categorized into two parts, namely, Part I which is on the stability and control of nonlinear dynamical systems; and Part II which is devoted to optimization with stability constraints in power systems. In each of these parts, we make use of the underlying structure of the problems, such as the graph topology of power grids, to develop efficient and practical computational methods which are scalable to large-scale systems. In what follows, we briefly summarize our contributions and future directions.

9.1 Part I: Stability and Control of Nonlinear Dynamical Systems

In Chapter 2, we have presented a comprehensive study on the role of damping in a large class of dynamical systems, including electric power networks. Paying special attention to partially-damped systems, it is shown that damping plays a monotonic role in the hyperbolicity of the equilibrium points. We have proved that the hyperbolicity of the equilibrium points is intertwined with the observability of a pair of matrices, where the damping matrix is involved. We have also studied the aftermath of hyperbolicity collapse, and have shown both subcritical and supercritical Hopf bifurcations can occur as damping changes. It is shown that Hopf bifurcation cannot happen in small power systems with only one undamped generator. In the process, we have developed auxiliary results by proving some important spectral properties of the power system Jacobian matrix, establishing the relationship between a power system model and its referenced counterpart, and finally addressing a fundamental question from matrix perturbation theory. Among others, the numerical experiments have illustrated how damping can change the region of attraction of the equilibrium

points. **Future Directions:** *Although we have provided numerous results and discussions about the asymmetric case, most of the results in Chapter 2 are focused on symmetric setting, i.e., when inertia, damping, and the Jacobian matrices are symmetric. Moving forward, we need to extend these theories to asymmetric cases. Moreover, theoretical study of other types of bifurcation in power systems is left as a future work. Another open question is on the impact of inertia in the aforementioned class of second-order systems. Given the proliferation of renewable sources and the growing concerns over the loss of inertia in power systems, this open problem is of vital importance.*

Chapter 3 has been aimed at finding a computationally efficient way to certify the stability of power system equilibrium points. We have shown if the matrix norm of the Laplacian of the underlying graph is upper bounded by a specific value, then the equilibrium point is stable. The aforementioned upper bound is proportional to the square of damping and inverse of inertia at each node of the power grid. This fact also sheds light on the interplay of inertia, damping, and graph of the system, and provides profound insights into how power system should be designed and operated to be stable. **Future Directions:** *As a future work, the developed stability certificate can be incorporated as a constraint into various scheduling problems such as the optimal power flow problem in order to guarantee and improve the stability of solutions. Our results could also be extended towards tighter and nonlocal stability certificates.*

In Chapter 4, we have shown that under reasonable assumptions, the small-signal stability of the classical structure-preserving model is equivalent to its singular perturbation counterpart. Based on this equivalence, we developed a novel stability certificate for the structure-preserving model. Similar to the previous chapter, the certificate can be computed in a fully distributed fashion, using only local information, and can be used for real-time monitoring. The certificate suggests that the eigenvalues of the system will move towards the left half-plane by increasing generators' damping and decreasing generators' inertia. It also reveals a paradox that adding more transmission lines can lead to the violation of the

stability certificate and making the system unstable. **Future Directions:** *Moving forward, we need to further study the Braess's Paradox in the stability of networked systems. Finding more examples of this phenomenon, developing some conditions to detect and devising methods to mitigate it are potential future research directions.*

In Chapter 5, we have proposed new stability certificates for the small-signal stability of multi-microgrids. We proved that an equilibrium point of a multi-microgrid system is locally asymptotically stable if either i) the network is lossless; or ii) in a lossy network, a local condition is satisfied at each microgrid PCC/DER. This condition sheds new light on the interplay of system stability, network topology, and dynamic parameters. It also provides a fully distributed control scheme that is guaranteed to stabilize the multi-microgrid system. The proposed conditions in this chapter can improve the situational awareness of system operators by providing a fast stability certificate as well as showing how different corrective actions would make the equilibrium point stable. **Future Directions:** *In the literature, several stability criteria are developed based on various dynamical models, focusing on different aspects of stability. Finding a proper way to compare and merge these criteria and deriving a unified stability criterion will be an interesting direction for future work, and the framework proposed in [90, 91, 92] is a promising step towards this direction. Moreover, in this work, we have considered only devices whose dynamical model can be captured by swing equations (such as grid-forming inverters and diesel generators). Future studies could investigate the stability theory of multi-microgrids in the presence of various types distributed energy resources including both grid-forming and grid-feeding inverters.*

Chapter 6 is aimed at developing stability certificates for the third-order model of droop-controlled inverters. According to the derived certificates, two inequalities should hold at each node of the system. To check these inequalities at each node, we only require the local information about the reactive power consumption, voltage magnitude and the parameters of the inverter at the node. Therefore, the proposed certificates can be utilized for distributed and fast stability assessment and monitoring. In order to develop these certifi-

cates, we have made use of the loose physical linkage between active and reactive powers. We have also investigated the role of coupling terms and the robustness of the decoupled model under coupling perturbations. ***Future Directions:*** *A worthwhile direction for future research would be generalizing the developed stability certificates to higher-order models. Moreover, the proliferation of various DERs in recent years has increased the complexity and uncertainty of distribution systems and made it difficult to obtain accurate dynamical models for the system. This calls for novel model-free data-driven method to ensure the stability of power systems.*

9.2 Part II: Optimization with Stability Constraints

The proliferation of microgrids all over the world has been remarkable in recent years, and their growth prospects in the future are astounding. Microgrids can improve the resilience of the grid based on their self-supply and island-mode capabilities. However, when a microgrid unintentionally enters the island mode, a considerable number of customers (or even all of them) are disconnected from the grid in order to maintain the load-generation equilibrium. New methodologies are therefore required to optimize the load shedding process in microgrids. In Chapter 7, an optimization-based load shedding model is presented as a promising tool to attain this goal. Mathematically, the load shedding model is formulated as a MILP problem. The structure of the proposed scheme reduces its communication requirements which is a major challenge in practice. The most relevant aspects of the proposed load shedding scheme are illustrated using a large-scale case study based on a 33-bus microgrid. It was observed that the proposed method sheds less amount of load in comparison with the conventional UFLS approach. Meanwhile, the developed structure outperformed the conventional scheme in terms of load shedding cost and minimum dynamic frequency following the load shedding process. ***Future Directions:*** *Future studies could reformulate power flow equations for radial systems (since the complex power flow equations presented in this chapter are not necessary for radial networks). Moreover, an*

unbalanced power flow model can be adopted to make the proposed load shedding method more practical in real world applications.

Finally, in Chapter 8, we have proposed a novel framework for the near real-time operation as well as the real-time control of multi-microgrid networks. Our framework provides the optimal power flow, optimal load shedding, and optimal topology reconfiguration, while frequency dynamics and AC power flow limitations are taken into account. An exact reformulation of frequency constraints in a cutting plane algorithm with tight MISOCP relaxations is established, which significantly speeds up computation and achieves near optimal solution. To the best of our knowledge, this comprehensive optimization and control framework for the frequency stability of multi-microgrids is proposed for the first time in the literature. Our numerical experiments further illustrate that the proposed emergency control scheme can successfully monitor, verify, and act to guarantee that the multi-microgrid network remains within the operational limits during post-islanding frequency dynamics. It is practical for real-world applications and outperforms the conventional UFLS scheme in terms of load shedding amount, number of curtailed customers, and frequency stability.

Future Directions: *The approach in this chapter is mainly developed to target microgrids/DERs whose dynamics can be captured by swing equation dynamics. Recent years have seen major developments in new types of resources including DERs, intermittent resources (wind and solar), and storage. A question therefore remains unanswered: Whether there exists a unifying framework to systematically study the stability of these different dynamical models and also to incorporate the associated stability constraints into an optimization problem. We leave this question as an interesting challenge for future research, as the existing techniques can only tackle a narrow class of problems with specific structures.*

Appendices

APPENDIX A
DETAILED PROOFS OF CHAPTER 2

A.1 Proof of Lemma 5

Proof. Assume that all r -by- r principal submatrices of S are singular, and let us lead this assumption to a contradiction. Since $\text{rank}(S) = r$, all principal submatrices of size larger than r are also singular. Therefore, zero is an eigenvalue of every m -by- m principal submatrix of S for each $m \geq r$. Consequently, all principal minors of S of size m are zero for each $m \geq r$. Let $E_\ell(S)$ denote the sum of principal minors of S of size ℓ (there are $\binom{n}{\ell}$ of them), and observe that we have $E_m(S) = 0, \forall m \geq r$. Moreover, thought of as a formal polynomial in t , let $p_S(t) = \sum_{\ell=0}^n a_\ell t^\ell$ with $a_n = 1$ be the characteristic polynomial of S , and recall that the k -th derivative of $p_S(t)$ at $t = 0$ is $p_S^{(k)}(0) = k!(-1)^{n-k} E_{n-k}(S), \forall k \in \{0, 1, \dots, n-1\}$, and the coefficients of the characteristic polynomial are $a_k = \frac{1}{k!} p_S^{(k)}(0)$. In this case, our assumption leads to $a_k = p_S^{(k)}(0) = 0, \forall k \in \{0, 1, \dots, n-r\}$, i.e., zero is an eigenvalue of S with algebraic multiplicity at least $n-r+1$. But from the assumption of the lemma we know S is similar to $B \oplus 0_{n-r}$, that is, zero is an eigenvalue of S with algebraic multiplicity exactly $n-r$, and we arrive at the desired contradiction. \square

A.2 Stability of Symmetric Second-Order Systems with Nonsingular Damping

Theorem 3 provides a necessary and sufficient condition for the hyperbolicity of an equilibrium point $(x_0, 0)$ of the second-order system (2.1), when the inertia, damping, and Jacobian of f satisfy $M \in \mathbb{S}_{++}^n, D \in \mathbb{S}_+^n, \nabla f(x_0) \in \mathbb{S}_{++}^n$. In this section, we prove that if we replace the assumption $D \in \mathbb{S}_+^n$ with $D \in \mathbb{S}_{++}^n$, then the equilibrium point $(x_0, 0)$ is not only hyperbolic but also asymptotically stable. This asymptotic stability is proved for lossless swing equations in [63, Theorem 1, Part d]. The next theorem generalizes [63,

Theorem 1, Part d] to the second-order system (2.1) where the damping and inertia matrices are not necessarily diagonal.

Theorem 17 (stability in second-order systems: symmetric case). *Consider the second-order ODE system (2.1) with inertia matrix $M \in \mathbb{S}_{++}^n$ and damping matrix $D \in \mathbb{S}_{++}^n$. Suppose $(x_0, 0) \in \mathbb{R}^{n+n}$ is an equilibrium point of the corresponding first-order system (2.5) with the Jacobian matrix $J \in \mathbb{R}^{2n \times 2n}$ defined in (2.6) such that $L = \nabla f(x_0) \in \mathbb{S}_{++}^n$. Then, the equilibrium point $(x_0, 0)$ is locally asymptotically stable.*

Proof. We complete the proof in three steps:

Step 1: First, we show all real eigenvalues of J are negative. Assume $\lambda \in \mathbb{R}, \lambda \geq 0$ is a nonnegative eigenvalue of $J(x_0)$, and let us lead this assumption to a contradiction. According to Lemma 1,

$$\det(\lambda^2 M + \lambda D + L) = 0. \quad (\text{A.1})$$

Since all three matrices L, D , and M are positive definite, the matrix pencil $P(\lambda) = \lambda^2 M + \lambda D + L$ is also a positive definite matrix for any nonnegative λ . Hence $P(\lambda)$ is nonsingular, contradicting (A.1).

Step 2: Next, we prove that the eigenvalues of J cannot be purely imaginary. We provide two different proofs for this step. According to our assumption, the damping matrix D is nonsingular, and the pair $(M^{-1} \nabla f(x_0), M^{-1} D)$ is always observable because the nullspace of $M^{-1} D$ is trivial. Hence, according to Theorem 3, the equilibrium point $(x_0, 0)$ is hyperbolic, and $J(x_0)$ does not have any purely imaginary eigenvalue, so the first proof of this step is complete. For the second proof, let $\lambda \in \sigma(J(x_0))$, then according to Lemma 1, $\exists v \in \mathbb{C}^n, v \neq 0$ such that $(\lambda^2 M + \lambda D + L)v = 0$. Suppose, for the sake of contradiction, that $\lambda = i\beta \in \sigma(J(x_0))$ for some nonzero real β . Let $v = x + iy$, then

$((L - \beta^2 M) + i\beta D)(x + iy) = 0$, which can be equivalently written as

$$\begin{bmatrix} L - \beta^2 M & -\beta D \\ \beta D & L - \beta^2 M \end{bmatrix} \begin{bmatrix} x \\ y \end{bmatrix} = \begin{bmatrix} 0 \\ 0 \end{bmatrix}. \quad (\text{A.2})$$

Define the matrix

$$H(\beta) := \begin{bmatrix} \beta D & L - \beta^2 M \\ L - \beta^2 M & -\beta D \end{bmatrix}. \quad (\text{A.3})$$

Since $L \in \mathbb{S}_{++}^n$, $H(\beta)$ is a symmetric matrix. Notice also that $H(\beta)$ cannot be positive semidefinite due to the diagonal blocks $\pm\beta D$. Since $D \in \mathbb{S}_{++}^n$, the determinant of $H(\beta)$ can be expressed using Schur complement as

$$\det(H(\beta)) = \det(-\beta D) \det(\beta D + \beta^{-1}(L - \beta^2 M)D^{-1}(L - \beta^2 M)).$$

So we only need to consider the nonsingularity of the Schur complement. Define the following matrices for the convenience of analysis:

$$\begin{aligned} A(\beta) &:= L - \beta^2 M, \\ B(\beta) &:= D^{-\frac{1}{2}} A(\beta) D^{-\frac{1}{2}}, \\ E(\beta) &:= I + \beta^{-2} B(\beta)^2. \end{aligned}$$

The inner matrix of the Schur complement can be written as

$$\begin{aligned} &\beta D + \beta^{-1}(L - \beta^2 M)D^{-1}(L - \beta^2 M) \\ &= \beta D^{\frac{1}{2}}(I + \beta^{-2} D^{-\frac{1}{2}} A(\beta) D^{-1} A(\beta) D^{-\frac{1}{2}}) D^{\frac{1}{2}} \\ &= \beta D^{\frac{1}{2}}(I + \beta^{-2} B(\beta)^2) D^{\frac{1}{2}} = \beta D^{\frac{1}{2}} E(\beta) D^{\frac{1}{2}}. \end{aligned}$$

Notice that $E(\beta)$ and $B(\beta)$ have the same eigenvectors and the eigenvalues of $E(\beta)$ and $B(\beta)$ have a one-to-one correspondence: μ is an eigenvalue of $B(\beta)$ if and only if $1 + \beta^{-2}\mu^2$ is an eigenvalue of $E(\beta)$. Indeed, we have $E(\beta)v = v + \beta^{-2}B(\beta)^2v = v + \beta^{-2}\mu^2v = (1 + \beta^{-2}\mu^2)v$ for any eigenvector v of $B(\beta)$ with eigenvalue μ . Since $B(\beta)$ is symmetric, μ is a real number. Hence, $E(\beta)$ is positive definite (because $1 + \beta^{-2}\mu^2 > 0$), therefore $H(\beta)$ is nonsingular for any real nonzero β . Then, the eigenvector $v = x + iy$ is zero which is a contradiction. This proves that $J(x_0)$ has no eigenvalue on the punctured imaginary axis.

Step 3: Finally, we prove that any complex nonzero eigenvalue of $J(x_0)$ has a negative real part. For a complex eigenvalue $\alpha + i\beta$ of $J(x_0)$ with $\alpha \neq 0, \beta \neq 0$, by setting $v = x + iy$, the pencil singularity equation becomes

$$(L + (\alpha + i\beta)D + (\alpha^2 - \beta^2 + 2\alpha\beta i)M)(x + iy) = 0.$$

Similar to Step 2 of the proof, define the matrix $H(\alpha, \beta)$ as

$$H(\alpha, \beta) := \begin{bmatrix} L + \alpha D + (\alpha^2 - \beta^2)M & -\beta(D + 2\alpha M) \\ \beta(D + 2\alpha M) & L + \alpha D + (\alpha^2 - \beta^2)M \end{bmatrix}.$$

We only need to consider two cases, namely 1) $\alpha > 0, \beta > 0$ or 2) $\alpha < 0, \beta > 0$. For the first case, $\beta(D + 2\alpha M)$ is invertible and positive definite, therefore, we only need to look at the invertibility of the Schur complement

$$S(\alpha, \beta) + T(\alpha, \beta)S^{-1}(\alpha, \beta)T(\alpha, \beta),$$

where $S(\alpha, \beta) := \beta(D + 2\alpha M)$ and $T(\alpha, \beta) := L + \alpha D + (\alpha^2 - \beta^2)M$. Using the same manipulation as in Step 1 of the proof, we can see that the Schur complement is always invertible for any $\alpha > 0, \beta > 0$. This implies the eigenvector v is 0, which is a contradiction. Therefore, the first case is not possible. So any complex nonzero eigenvalue

of $J(x_0)$ has a negative real part. □

A.3 Proof of Theorem 4

Proof. There exist $\lambda \in \mathbb{R}_+, \lambda \neq 0$ and $x \in \mathbb{C}^n, x \neq 0$ such that

$$M^{-1}Lx = \lambda x \text{ and } M^{-1}Dx = 0. \quad (\text{A.4})$$

Define $\xi = \sqrt{-\lambda}$, which is a purely imaginary number. The quadratic matrix pencil $M^{-1}P(\xi) = \xi^2 I + \xi M^{-1}D + M^{-1}L$ is singular because $M^{-1}P(\xi)x = \xi^2 x + \xi M^{-1}Dx + M^{-1}Lx = -\lambda x + 0 + \lambda x = 0$. By Lemma 1, ξ is an eigenvalue of J . Similarly, we can show $-\xi$ is an eigenvalue of J . Therefore, $\sigma(J)$ contains a pair of purely imaginary eigenvalues. □

A.4 Proof of Proposition 2

Let us first prove the following useful lemma.

Lemma 12. *Let (δ^0, ω^0) be an equilibrium point of the swing equation (2.21) and $\Psi(\delta^0, \omega^0)$ be the corresponding equilibrium point of the referenced model (2.24). Let J^r denote the Jacobian of the referenced model at this equilibrium point. For any $\lambda \neq 0$, λ is an eigenvalue of J^r if and only if the quadratic matrix pencil $P(\lambda) := \lambda^2 M + \lambda D + \nabla P_e(\delta^0)$ is singular.*

Proof. The referenced model (2.24) can be written as

$$\begin{bmatrix} \dot{\psi} \\ \dot{\omega} \end{bmatrix} = \begin{bmatrix} T_1 \omega \\ -DM^{-1}\omega + M^{-1}(P_m - P_e^r(\psi)) \end{bmatrix}. \quad (\text{A.5})$$

Note that the Jacobian of the referenced flow function $\nabla P_e^r(\psi)$ is an $n \times (n - 1)$ matrix

and we have $\nabla P_e^r(\psi^0) = \nabla P_e(\delta^0)T_2$, where

$$T_2 := \begin{bmatrix} I_{n-1} \\ 0_{1 \times (n-1)} \end{bmatrix} \in \mathbb{R}^{n \times (n-1)}. \quad (\text{A.6})$$

Accordingly, the Jacobin of the referenced model (2.24) is

$$J^r = \begin{bmatrix} 0_{(n-1) \times (n-1)} & T_1 \\ -M^{-1}\nabla P_e(\delta^0)T_2 & -DM^{-1} \end{bmatrix}. \quad (\text{A.7})$$

Necessity: Let λ be a nonzero eigenvalue of J^r and (v_1, v_2) be the corresponding eigenvector with $v_1 \in \mathbb{C}^{n-1}$ and $v_2 \in \mathbb{C}^n$. Then

$$\begin{bmatrix} 0_{(n-1) \times (n-1)} & T_1 \\ -M^{-1}\nabla P_e(\delta^0)T_2 & -DM^{-1} \end{bmatrix} \begin{bmatrix} v_1 \\ v_2 \end{bmatrix} = \lambda \begin{bmatrix} v_1 \\ v_2 \end{bmatrix}, \quad (\text{A.8})$$

which implies that $T_1 v_2 = \lambda v_1$. Since $\lambda \neq 0$, we can substitute $\lambda^{-1}T_1 v_2 = v_1$ in the second equation to obtain

$$(\lambda^2 M + \lambda D + \nabla P_e(\delta^0)T_2 T_1) v_2 = 0. \quad (\text{A.9})$$

Since the eigenvector (v_1, v_2) is nonzero, we have $v_2 \neq 0$ (otherwise $v_1 = \lambda^{-1}T_1 0 = 0 \implies (v_1, v_2) = 0$), Eq. (A.9) implies that the matrix pencil $P(\lambda) = \lambda^2 M + \lambda D + \nabla P_e(\delta^0)T_2 T_1$ is singular. Next, we show that $\nabla P_e(\delta^0)T_2 T_1 = \nabla P_e(\delta)$. Since $\nabla P_e(\delta^0)$ has zero row sum, it can be written as

$$\nabla P_e(\delta^0) = \begin{bmatrix} A & b \\ c^\top & d \end{bmatrix}, \text{ where } A\mathbf{1} = -b, c^\top \mathbf{1} = -d.$$

Therefore, we have

$$\nabla P_e(\delta^0)T_2T_1 = \begin{bmatrix} A & b \\ c^\top & d \end{bmatrix} \begin{bmatrix} I_{n-1} \\ 0 \end{bmatrix} \begin{bmatrix} I_{n-1} & -\mathbf{1} \end{bmatrix} = \begin{bmatrix} A & -A\mathbf{1} \\ c^\top & -c^\top\mathbf{1} \end{bmatrix} = \begin{bmatrix} A & b \\ c^\top & d \end{bmatrix}.$$

Sufficiency: Suppose there exists $\lambda \in \mathbb{C}, \lambda \neq 0$ such that $P(\lambda) = \lambda^2 M + \lambda D + \nabla P_e(\delta^0)$ is singular. Choose a nonzero $v_2 \in \ker(P(\lambda))$ and let $v_1 := \lambda^{-1}T_1v_2$. Accordingly, the characteristic equation (A.8) holds, and consequently, λ is a nonzero eigenvalue of J^r . \square

Now, we are ready to prove Proposition 2.

Proof. Any equilibrium point (δ^0, ω^0) of the swing equation model (2.21) is contained in the set

$$\mathcal{E} := \{(\delta, \omega) \in \mathbb{R}^{2n} : \omega = 0, P_{m_j} = P_{e_j}(\delta), \quad \forall j \in \{1, \dots, n\}\}.$$

Let $(\psi^0, \omega^0) = \Psi(\delta^0, \omega^0)$, and note that $\omega^0 = 0$. From (2.22) and (2.25), we observe that $P_{e_j}(\delta^0) = P_{e_j}^r(\psi^0), \forall j \in \{1, \dots, n\}$ where $\psi_n^0 := 0$. Therefore, (ψ^0, ω^0) is an equilibrium point of the the referenced model (2.24).

To prove the second part, recall that λ is an eigenvalue of the Jacobian of (2.21) at (δ^0, ω^0) if and only if $\det(\nabla P_e(\delta^0) + \lambda D + \lambda^2 M) = 0$. According to Lemma 12, the nonzero eigenvalues J and J^r are the same. Moreover, the referenced model (2.24) has one dimension less than the swing equation model (2.21). This completes the proof. \square

A.5 Proof of Theorem 8

We prove the following lemmas first:

Lemma 13. *Let $A, B \in \mathbb{R}^{n \times n}$ and define*

$$C := \begin{bmatrix} A & -B \\ B & A \end{bmatrix}.$$

Then $\mathbf{rank}(C) = 2 \mathbf{rank}(A + \mathbf{i}B)$ which is an even number.

Proof. Let $V := \frac{1}{\sqrt{2}} \begin{bmatrix} I_n & \mathbf{i}I_n \\ \mathbf{i}I_n & I_n \end{bmatrix}$ and observe that $V^{-1} = \bar{V} = V^*$, where \bar{V} stands for the entrywise conjugate and V^* denotes the conjugate transpose of V . We have

$$V^{-1}CV = \begin{bmatrix} A - \mathbf{i}B & 0 \\ 0 & A + \mathbf{i}B \end{bmatrix} = (A - \mathbf{i}B) \oplus (A + \mathbf{i}B).$$

Since rank is a similarity invariant, we have $\mathbf{rank}(C) = \mathbf{rank}((A - \mathbf{i}B) \oplus (A + \mathbf{i}B)) = 2 \mathbf{rank}(A + \mathbf{i}B)$. \square

Lemma 14. $\lambda = \mathbf{i}\beta$ is an eigenvalue of J if and only if the matrix

$$\mathcal{M}(\beta) := \begin{bmatrix} L - \beta^2 M & -\beta D \\ \beta D & L - \beta^2 M \end{bmatrix}$$

is singular. Here $L = \nabla P_e(\delta^0)$.

Proof. According to Lemma 1, $\mathbf{i}\beta \in \sigma(J)$ if and only if $\exists x \in \mathbb{C}^n, x \neq 0$ such that

$$(L - \beta^2 M + \mathbf{i}\beta D)x = 0. \tag{A.10}$$

Define $A := L - \beta^2 M, B := \beta D$, and let $x = u + \mathbf{i}v$. Rewrite (A.10) as $(A + \mathbf{i}B)(u + \mathbf{i}v) = (Au - Bv) + \mathbf{i}(Av + Bu) = 0$, which is equivalent to

$$\begin{bmatrix} A & -B \\ B & A \end{bmatrix} \begin{bmatrix} u \\ v \end{bmatrix} = 0.$$

\square

Now, we are ready to prove Theorem 8: According to Lemma 14, $\mathbf{i}\beta \in \sigma(J)$ for some

nonzero real β if and only if the matrix

$$\mathcal{M}(\beta) := \begin{bmatrix} L - \beta^2 M & -\beta D \\ \beta D & L - \beta^2 M \end{bmatrix}$$

is singular. Recall that $L := \nabla P_e(\delta^0)$. In the sequel, we will show under the assumptions of Theorem 8, $\mathcal{M}(\beta)$ is always nonsingular. First, we prove the theorem for $n = 2$. In this case,

$$L = \begin{bmatrix} a_{12} & -a_{12} \\ -a_{21} & a_{21} \end{bmatrix}, a_{12} > 0, a_{21} > 0.$$

According to Lemma 13, we have $\mathbf{rank}(\mathcal{M}(\beta)) = 2 \mathbf{rank}(L - \beta^2 M - \mathbf{i}\beta D)$, and $L - \beta^2 M - \mathbf{i}\beta D$ is full rank because

$$L - \beta^2 M - \mathbf{i}\beta D = \begin{bmatrix} a_{12} - \beta^2 m_1 & -a_{12} \\ -a_{21} & a_{21} - \beta^2 m_2 - \mathbf{i}\beta d_2 \end{bmatrix},$$

and $\det(L - \beta^2 M - \mathbf{i}\beta D) = (a_{12} - \beta^2 m_1)(a_{21} - \beta^2 m_2 - \mathbf{i}\beta d_2) - a_{12} a_{21}$. It is easy to see that the real part and imaginary parts of the determinant cannot be zero at the same time. Therefore, $\mathcal{M}(\beta)$ is also nonsingular and a partially damped 2-generator system cannot have any pure imaginary eigenvalues.

Now, we prove the theorem for $n = 3$. Let $A \in \mathbb{R}^{2n \times 2n}$. For index sets $\mathcal{I}_1 \subseteq \{1, \dots, 2n\}$ and $\mathcal{I}_2 \subseteq \{1, \dots, 2n\}$, we denote by $A[\mathcal{I}_1, \mathcal{I}_2]$ the (sub)matrix of entries that lie in the rows of A indexed by \mathcal{I}_1 and the columns indexed by \mathcal{I}_2 . For a 3-generator system, the matrix L can be written as

$$L = \begin{bmatrix} a_{12} + a_{13} & -a_{12} & -a_{13} \\ -a_{21} & a_{21} + a_{23} & -a_{23} \\ -a_{31} & -a_{32} & a_{31} + a_{32} \end{bmatrix}$$

where $a_{jk} \geq 0, \forall j, k \in \{1, 2, 3\}, j \neq k$ and $a_{jk} = 0 \iff a_{kj} = 0$. Moreover, $M = \text{diag}(m_1, m_2, m_3)$ and $D = \text{diag}(0, d_2, d_3)$. We complete the proof in three steps:

- Step 1: We show that the first four columns of $\mathcal{M}(\beta)$ are linearly independent, i.e., $\text{rank}(\mathcal{M}(\beta)) \geq 4$.

To do so, we show that the equation

$$\mathcal{M}(\beta) [\{1, \dots, 6\}, \{1, 2, 3, 4\}] \begin{bmatrix} x_1 \\ x_2 \\ x_3 \\ x_4 \end{bmatrix} = 0$$

has only the trivial solution.

- (i) If $a_{12} + a_{13} - \beta^2 m_1 \neq 0$, then $x_4 = 0$. Moreover, we have $\beta d_2 x_2 = 0$ and $\beta d_3 x_3 = 0$ which imply $x_2 = x_3 = 0$ because β, d_2 , and d_3 are nonzero scalars. Finally, the connectivity assumption requires that at least one of the two entries a_{21} and a_{31} are nonzero, implying that $x_1 = 0$.

- (ii) If $a_{12} + a_{13} - \beta^2 m_1 = 0$, then by expanding the fifth and sixth rows we get

$$\begin{aligned} \beta d_2 x_2 - a_{21} x_4 &= 0 \implies x_2 = \frac{a_{21}}{\beta d_2} x_4, \\ \beta d_3 x_3 - a_{31} x_4 &= 0, \implies x_3 = \frac{a_{31}}{\beta d_3} x_4. \end{aligned}$$

Expanding the first row and substituting x_2 and x_3 from above gives

$$-a_{12} x_2 - a_{13} x_3 = 0 \implies -\frac{a_{12} a_{21}}{\beta d_2} x_4 - \frac{a_{13} a_{31}}{\beta d_3} x_4 = 0.$$

The connectivity assumption (and the fact that $a_{kj} \geq 0, \forall k \neq j$ and $a_{kj} = 0 \iff a_{jk} = 0$) leads to $x_4 = 0$. This implies $x_2 = x_3 = 0$ and further $x_1 = 0$

due to the connectivity assumption.

- Step 2: We prove that the first five columns of $\mathcal{M}(\beta)$ are linearly independent, i.e., $\text{rank}(\mathcal{M}(\beta)) \geq 5$.

To do so, we show that the equation

$$\mathcal{M}(\beta) [\{1, \dots, 6\}, \{1, 2, 3, 4\}] \begin{bmatrix} x_1 \\ x_2 \\ x_3 \\ x_4 \end{bmatrix} = \begin{bmatrix} 0 \\ -\beta d_2 \\ 0 \\ -a_{12} \\ a_{21} + a_{23} - \beta^2 m_2 \\ -a_{32} \end{bmatrix}$$

has no solution, i.e., the fifth column is not in the span of the first four columns.

Based on the equation in the fourth row we consider the following situations:

- (i) If $a_{12} + a_{13} - \beta^2 m_1 = 0$ and $a_{12} \neq 0$, then there exists no solution.
- (ii) If $a_{12} + a_{13} - \beta^2 m_1 = 0$ and $a_{12} = 0$, then $a_{13} = \beta^2 m_1$. Expanding the first row yields $-a_{13}x_3 = 0 \implies x_3 = 0$. Expanding the second row provides $(a_{23} - \beta^2 m_2)x_2 = -\beta d_2 \implies x_2 = -\frac{\beta d_2}{(a_{23} - \beta^2 m_2)}$. Note that we assume $(a_{23} - \beta^2 m_2) \neq 0$, since otherwise the system has no solution. Finally, we expand the fifth row and substitute x_2 into it:

$$\begin{aligned} \beta d_2 x_2 = a_{23} - \beta^2 m_2 &\implies -\frac{(\beta d_2)^2}{(a_{23} - \beta^2 m_2)} = a_{23} - \beta^2 m_2 \\ &\implies -(\beta d_2)^2 = (a_{23} - \beta^2 m_2)^2 \end{aligned}$$

which is a contradiction.

- (iii) If $a_{12} + a_{13} - \beta^2 m_1 \neq 0$ and $a_{12} = 0$, then $x_4 = 0$. By expanding the fifth and

sixth rows we get

$$\beta d_2 x_2 = a_{23} - \beta^2 m_2 \implies x_2 = \frac{a_{23} - \beta^2 m_2}{\beta d_2},$$

$$\beta d_3 x_3 = -a_{32}, \implies x_3 = -\frac{a_{32}}{\beta d_3}.$$

Expanding the second row and substituting x_2 and x_3 from above gives

$$(a_{23} - \beta^2 m_2)x_2 - a_{23}x_3 = -\beta d_2 \implies \frac{(a_{23} - \beta^2 m_2)^2}{\beta d_2} + \frac{a_{23}a_{32}}{\beta d_3} = -\beta d_2$$

which is a contradiction.

(iv) If $a_{12} + a_{13} - \beta^2 m_1 \neq 0$ and $a_{12} \neq 0$, then $x_4 = \frac{-a_{12}}{a_{12} + a_{13} - \beta^2 m_1}$. By expanding the fifth and sixth rows and substituting x_4 we get

$$\beta d_2 x_2 + \frac{a_{12}a_{21}}{a_{12} + a_{13} - \beta^2 m_1} = a_{21} + a_{23} - \beta^2 m_2,$$

$$\beta d_3 x_3 + \frac{a_{12}a_{31}}{a_{12} + a_{13} - \beta^2 m_1} = -a_{32}.$$

Now we expand the first row to get $x_1 = \frac{a_{12}x_2 + a_{13}x_3}{a_{12} + a_{13} - \beta^2 m_1}$. Finally, we expand the second row and substitute for $x_1, x_2,$ and x_3 :

$$-a_{21} \frac{a_{12}x_2 + a_{13}x_3}{a_{12} + a_{13} - \beta^2 m_1} + (a_{21} + a_{23} - \beta^2 m_2)x_2 - a_{23}x_3 = -\beta d_2,$$

which implies

$$\left((a_{21} + a_{23} - \beta^2 m_2) - \frac{a_{12}a_{21}}{a_{12} + a_{13} - \beta^2 m_1} \right) x_2$$

$$- \left(a_{23} + \frac{a_{13}a_{21}}{a_{12} + a_{13} - \beta^2 m_1} \right) x_3 = -\beta d_2,$$

or equivalently

$$\frac{1}{\beta d_2} \left((a_{21} + a_{23} - \beta^2 m_2) - \frac{a_{12} a_{21}}{a_{12} + a_{13} - \beta^2 m_1} \right)^2 + \frac{1}{\beta d_3} \left(a_{23} + \frac{a_{13} a_{21}}{a_{12} + a_{13} - \beta^2 m_1} \right)^2 = -\beta d_2.$$

which is a contradiction.

- Step 3: $\text{rank}(\mathcal{M}(\beta))$ is an even number.

Finally, Lemma 13 precludes the rank of $\mathcal{M}(\beta)$ from being equal to 5. Therefore, $\text{rank}(\mathcal{M}(\beta)) = 6$, i.e., $\mathcal{M}(\beta)$ is always nonsingular. This completes the proof.

APPENDIX B
DETAILED PROOFS OF CHAPTER 3

B.1 Proof of Theorem 10

We complete the proof in three steps:

Step 1: First, we show that the zero eigenvalue of J is simple. According to Proposition 4, if $(\delta^*, \omega^*) \in \Omega$, the Jacobian matrix L is a singular M-matrix, and consequently, it has at least one zero eigenvalue. Consider the weighted directed graph $\mathcal{G} = (\mathcal{N}, \mathcal{A}, \mathcal{W})$ constructed in the beginning of Section 3.3.2. If $(\delta^*, \omega^*) \in \Omega$, the arc weights w_{ij} are positive for all arcs $(i, j) \in \mathcal{A}$. Moreover, there are two arcs (i, j) and (j, i) between nodes i and j if and only if the two nodes are connected in the underlying undirected graph of the power grid. Therefore, if the underlying undirected graph of the power grid is connected, then the directed graph \mathcal{G} is strongly connected. Now, we need the following lemma from graph theory to complete the proof: consider a weighted directed graph \mathcal{G} with positive weights. If \mathcal{G} is strongly connected, then the zero eigenvalue of its Laplacian is simple (see [87] and references therein). Note that the geometric multiplicity of the zero eigenvalue in $\sigma(J)$ and $\sigma(L)$ are equal. See also Proposition 6.

Step 2: Next, we show all the nonzero real eigenvalues of J are negative. Let $\lambda \in \mathbb{R}$ be an eigenvalue of J , then according to Lemma 1,

$$\det(L + \lambda D + \lambda^2 M) = 0. \tag{B.1}$$

Consider the Gershgorin disk \mathbb{D}_i centered at $c_i := L_{ii} + \lambda D_i + \lambda^2 M_i$ with radius $r_i := L_{ii} = \sum_{j \neq i} |L_{ij}|$. According to the Gershgorin circle theorem, every eigenvalue of the matrix $L + \lambda D + \lambda^2 M$ lies within at least one of the discs $\mathbb{D}_i, \forall i \in \mathcal{N}$. Now assume for the sake of contradiction that $\lambda > 0$, but this implies that $c_i > r_i, \forall i \in \mathcal{N}$, and consequently none

of the Gershgorin disks contains the origin (i.e., 0 cannot be an eigenvalue), contradicting (B.1).

Step 3: Finally, we show if condition (3.8) holds, then the nonzero eigenvalues of J are located in the left half plane. This result holds for real nonzero eigenvalues of J , as shown in the previous step. Now let $\lambda \in \mathbb{C}$, $\lambda \in \sigma(J)$, then according to Lemma 1, $\exists v \in \mathbb{C}^n$, $v \neq 0$ such that

$$(L + \lambda D + \lambda^2 M) v = 0. \quad (\text{B.2})$$

It is always possible to normalize v such that $\max_{i \in \mathcal{N}} |v_i| = 1$. Here and in the rest of this proof, if $x \in \mathbb{C}$, then $|x|$ denotes the modulus of x . Let $k := \operatorname{argmax}_{i \in \mathcal{N}} |v_i|$, and spell out the k -th row of (B.2):

$$\sum_{i \in \mathcal{N}} L_{ki} v_i + \lambda D_k v_k + \lambda^2 M_k v_k = 0, \quad (\text{B.3})$$

which can be rewritten as

$$L_{kk} v_k + \lambda D_k v_k + \lambda^2 M_k v_k = - \sum_{i \in \mathcal{N}, i \neq k} L_{ki} v_i. \quad (\text{B.4})$$

Using the triangle inequality, we have

$$\left| - \sum_{i \in \mathcal{N}, i \neq k} L_{ki} v_i \right| \leq \sum_{i \in \mathcal{N}, i \neq k} |L_{ki}| |v_i| \leq \sum_{i \in \mathcal{N}, i \neq k} |L_{ki}|.$$

Let us also define $\mathcal{R} := \sum_{i \in \mathcal{N}, i \neq k} |L_{ki}|$. Now assume that $\lambda = \alpha + \mathbf{i}\beta$ with $\alpha \geq 0$, $\beta \neq 0$ is a nonzero eigenvalue of J , and let us lead this assumption to a contradiction. Equation (B.4) implies that

$$\mathcal{R}^2 \geq |L_{kk} v_k + \lambda D_k v_k + \lambda^2 M_k v_k|^2$$

$$\begin{aligned}
&= |L_{kk} + \lambda D_k + \lambda^2 M_k|^2 |v_k|^2 \\
&= |L_{kk} + \alpha D_k + (\alpha^2 - \beta^2)M_k + \mathbf{i}(2\alpha\beta M_k + \beta D_k)|^2 \\
&= L_{kk}^2 + (\alpha D_k + (\alpha^2 - \beta^2)M_k)^2 + 2L_{kk}(\alpha D_k + \alpha^2 M_k) \\
&\quad - 2L_{kk}\beta^2 M_k + 4\alpha^2\beta^2 M_k^2 + \beta^2 D_k^2 + 4\alpha\beta^2 M_k D_k.
\end{aligned}$$

Recall that if $(\delta^*, \omega^*) \in \Omega$, matrix L has zero row sum, i.e., $\mathcal{R} = L_{kk}$. By cancelling \mathcal{R}^2 and L_{kk}^2 terms and moving $2L_{kk}\beta^2 M_k$ and $\beta^2 D_k^2$ to the left-hand side, we arrive at

$$\begin{aligned}
\beta^2(2L_{kk}M_k - D_k^2) &\geq (\alpha D_k + (\alpha^2 - \beta^2)M_k)^2 \\
&\quad + 2L_{kk}(\alpha D_k + \alpha^2 M_k) \\
&\quad + 4\alpha^2\beta^2 M_k^2 + 4\alpha\beta^2 M_k D_k. \tag{B.5}
\end{aligned}$$

According to our assumption in condition (3.8), we have $(2L_{kk}M_k - D_k^2) \leq 0$, thus the left-hand side of the inequality (B.5) is nonpositive. If $\alpha \geq 0$ and $\beta \neq 0$, the right-hand side of (B.5) would be positive, which is the desired contradiction. The idea used in this part of the proof was inspired by Skar [58]. Note that the simple zero eigenvalue of the Jacobian matrix J stems from the translational invariance of the flow function (3.4). As mentioned earlier (see Section 2.5.3), we can eliminate this eigenvalue by choosing a reference bus and refer all other bus angles to it. Therefore, the set of equilibrium points $\{\delta^* + \alpha \mathbf{1} : \alpha \in \mathbb{R}\}$ will collapse into one equilibrium point. Such an equilibrium point will be asymptotically stable.

APPENDIX C
DETAILED PROOFS OF CHAPTER 4

C.1 Proofs of Corollary 1 and Theorem 11

The structure-preserving model (4.1) can be written as the following system of first-order differential equations:

$$\dot{\delta}_i = \omega_i \quad \forall i \in \mathcal{G}, \quad (\text{C.1a})$$

$$d_i \dot{\delta}_i = -P_{d_i} - P_{e_i} \quad \forall i \in \mathcal{L}, \quad (\text{C.1b})$$

$$m_i \dot{\omega}_i = -d_i \omega_i + P_{m_i} - P_{e_i} \quad \forall i \in \mathcal{G}, \quad (\text{C.1c})$$

where ω_i is the deviation of angular frequency from its nominal value. Similarly, the singular perturbation model (4.4) can be written as

$$\dot{\delta}_i = \omega_i \quad \forall i \in \mathcal{G}, \quad (\text{C.2a})$$

$$\dot{\delta}_i = \omega_i \quad \forall i \in \mathcal{L}, \quad (\text{C.2b})$$

$$m_i \dot{\omega}_i = -d_i \omega_i + P_{m_i} - P_{e_i} \quad \forall i \in \mathcal{G}, \quad (\text{C.2c})$$

$$\varepsilon \dot{\omega}_i = -d_i \omega_i - P_{d_i} - P_{e_i} \quad \forall i \in \mathcal{L}. \quad (\text{C.2d})$$

In the sequel, we use m_i as an alias for $\varepsilon, \forall i \in \mathcal{L}$ in order to represent its physical interpretation. In other words, $m_i = \varepsilon, \forall i \in \mathcal{L}$. Let us define $D = \mathbf{diag}(d_1, \dots, d_{n_0}, d_{n_0+1}, \dots, d_n)$, and $M = \mathbf{diag}(m_1, \dots, m_{n_0}, m_{n_0+1}, \dots, m_n)$. The Jacobian of (C.2) is

$$J = \begin{bmatrix} 0 & I \\ -M^{-1}L & -M^{-1}D \end{bmatrix}, \quad (\text{C.3})$$

where L is the Jacobian of the flow function (4.3). Now, we are ready to present an outline of the proof of Corollary 1 and Theorem 11.

C.1.1 Outline of the Proof of Corollary 1

Proof. According to Theorem 10, if condition

$$\sum_{j \neq i} V_i V_j Y_{ij} \sin(\theta_{ij} - \delta_i^* + \delta_j^*) \leq \frac{d_i^2}{2m_i}, \quad \forall i \in \mathcal{L} \cup \mathcal{G} \quad (\text{C.4})$$

holds, then the equilibrium point is asymptotically stable. Note that

$$\begin{aligned} Q_i &= - \sum_{j=1}^n V_i V_j Y_{ij} \sin(\theta_{ij} - \delta_i^* + \delta_j^*) \\ &= -V_i^2 B_{ii} - \sum_{j=1, j \neq i}^n V_i V_j Y_{ij} \sin(\theta_{ij} - \delta_i^* + \delta_j^*) \end{aligned}$$

where $B_{ii} = Y_{ii} \sin(\theta_{ii})$. Hence, condition (C.4) can be re-written as

$$-Q_i - V_i^2 B_{ii} \leq \frac{d_i^2}{2m_i}, \quad \forall i \in \mathcal{L} \cup \mathcal{G}. \quad (\text{C.5})$$

For load buses, (C.5) becomes

$$-Q_i - V_i^2 B_{ii} \leq \frac{d_i^2}{2\varepsilon}, \quad \forall i \in \mathcal{L}. \quad (\text{C.6})$$

It is reasonable to assume that $\varepsilon \ll d_i, \forall i \in \mathcal{L}$. Thus, the right-hand side of (C.6) tends to infinity, and consequently, (C.6) holds trivially for load buses. Therefore, if condition

$$-Q_i - V_i^2 B_{ii} \leq \frac{d_i^2}{2m_i}, \quad \forall i \in \mathcal{G}. \quad (\text{C.7})$$

is satisfied, then the equilibrium point is locally asymptotically stable. \square

C.1.2 Outline of the Proof of Theorem 11

Proof. We follow the Tikhonov's theorem [29]. The proof is outlined in the following 4 steps:

1. Define a reference bus, and write the referenced swing equation model according to Section 2.5.3. This will put us in a convenient position to apply Tikhonov's theorem.
2. The boundary layer model associated with the singular perturbation model (C.2) can be simplified to the linear differential equation

$$\frac{dy_i}{d\tau} = -d_i y_i \quad \forall i \in \mathcal{L}, \quad (\text{C.8})$$

where τ is the the new time variable defined as

$$\tau = \frac{t - t_0}{\varepsilon}, \quad (\text{C.9})$$

and y_i is defined as

$$y_i = \omega_i + \frac{P_{d_i}}{d_i} + \frac{1}{d_i} P_{e_i}, \quad \forall i \in \mathcal{L}. \quad (\text{C.10})$$

Therefore, the origin is a globally exponentially stable equilibrium point of this boundary layer model as $d_i > 0, \forall i \in \mathcal{L}$. Now, Statement (i) of Theorem 11 follows from [29, Section 7, Corollary 2.3].

3. Let K be the Jacobian of the first order system (C.1). Show that K is a Schur complement of J . Then, show if K has r eigenvalues with negative real part, then there exists a sufficiently small ε such that J also has r eigenvalues with negative real part.
4. To prove Statement (ii) of Theorem 11, assume for the sake of contradiction that x^* is not an asymptotically stable equilibrium point of (C.1). Since x^* is hyperbolic,

there must exist an eigenvalue in the right half-plane. Using step 3 of this proof, we reach the contradiction that system (C.2) is not asymptotically stable.

□

APPENDIX D
DETAILED PROOFS OF CHAPTER 5

D.1 Proof of Proposition 5

proof of (i). Let $(v_1, v_2) \in \ker(J)$ where $v_1, v_2 \in \mathbb{R}^n$. Then

$$\begin{bmatrix} 0 & I \\ -M^{-1}L & -M^{-1}D \end{bmatrix} \begin{bmatrix} v_1 \\ v_2 \end{bmatrix} = 0, \quad (\text{D.1})$$

which implies that $v_2 = 0$ and $M^{-1}Lv_1 = 0$. Since M is non-singular, $Lv_1 = 0$, i.e. $v_1 \in \ker(L)$. Therefore, $\text{proj}(\ker(J)) \subseteq \ker(L)$. Conversely, let $v_1 \in \ker(L)$. Set $v_2 = 0$. Then $(v_1, v_2) \in \ker(J)$ as it satisfies (D.1). □

proof of (ii) and (iii). From part (i) of this proposition, we know that $(v, 0) \in \ker(J) \iff v \in \ker(L)$. Therefore, $\{(v_1, 0), \dots, (v_m, 0)\}$ is a set of linearly independent eigenvectors in $\ker(J)$ if and only if $\{v_1, \dots, v_m\}$ is a set of linearly independent eigenvectors in $\ker(L)$, i.e., $\dim(\ker(J)) = \dim(\ker(L))$. Finally, part (iii) is an immediate consequence of either of the first two parts. □

D.2 Proof of Theorem 12

proof of (a). This is an immediate consequence of Propositions 5 and 6. □

proof of (b). See [17, Proof of Theorem 1]. □

proof of (c). The result holds for real nonzero eigenvalues of J , as shown in the previous part. Now let $\lambda \in \mathbb{C}$, $\lambda \in \sigma(J)$, then according to Lemma 1, $\exists v \in \mathbb{C}^n$, $v \neq 0$ such that

$$(L + \lambda D + \lambda^2 M)v = 0. \quad (\text{D.2})$$

It is always possible to normalize v such that $\max_{i \in \mathcal{N}} |v_i| = 1$. Here and in the rest of this proof, if $x \in \mathbb{C}$, then $|x|$ denotes the modulus of x . Let $k := \operatorname{argmax}_{i \in \mathcal{N}} |v_i|$, and spell out the k -th row of (D.2):

$$L_{kk}v_k + \lambda d_k v_k + \lambda^2 m_k v_k = - \sum_{i=1, i \neq k}^n L_{ki} v_i. \quad (\text{D.3})$$

Using the triangle inequality, we have

$$\left| - \sum_{i=1, i \neq k}^n L_{ki} v_i \right| \leq \sum_{i=1, i \neq k}^n |L_{ki}| |v_i| \leq \sum_{i=1, i \neq k}^n |L_{ki}|.$$

Define $\mathcal{R} := \sum_{i=1, i \neq k}^n |L_{ki}|$. Now assume that $\lambda = \alpha + i\beta$ with $\alpha \geq 0, \beta \neq 0$ is a nonzero eigenvalue of J , and let us lead this assumption to a contradiction. Recall $|v_k| = \|v\|_\infty = 1$. Equation (D.3) implies that

$$\begin{aligned} \mathcal{R}^2 &\geq |L_{kk}v_k + \lambda d_k v_k + \lambda^2 m_k v_k|^2 = |L_{kk} + \lambda d_k + \lambda^2 m_k|^2 \\ &= L_{kk}^2 + (\alpha d_k + (\alpha^2 - \beta^2)m_k)^2 + 2L_{kk}(\alpha d_k + \alpha^2 m_k) \\ &\quad - 2L_{kk}\beta^2 m_k + 4\alpha^2 \beta^2 m_k^2 + \beta^2 d_k^2 + 4\alpha\beta^2 m_k d_k. \end{aligned}$$

Recall that if $(\delta^*, \omega^*) \in \Omega$, matrix L has zero row sum, i.e., $\mathcal{R} = L_{kk}$. By cancelling \mathcal{R}^2 and L_{kk}^2 terms and moving $2L_{kk}\beta^2 m_k$ and $\beta^2 d_k^2$ to the left-hand side, we arrive at

$$\begin{aligned} \beta^2(2L_{kk}m_k - d_k^2) &\geq (\alpha d_k + (\alpha^2 - \beta^2)m_k)^2 \\ &\quad + 2L_{kk}(\alpha d_k + \alpha^2 m_k) \\ &\quad + 4\alpha^2 \beta^2 m_k^2 + 4\alpha\beta^2 m_k d_k. \end{aligned} \quad (\text{D.4})$$

Now, note that the outgoing reactive power flow at PCC k is

$$Q_k = - \sum_{i=1}^n V_k V_i Y_{ki} \sin(\theta_{ki} - \delta_k^* + \delta_i^*)$$

$$\begin{aligned}
&= -V_k^2 B_{kk} - \sum_{i=1, i \neq k}^n V_k V_i Y_{ki} \sin(\theta_{ki} - \delta_k^* + \delta_i^*) \\
&= -V_k^2 B_{kk} - L_{kk},
\end{aligned} \tag{D.5}$$

where $B_{kk} = Y_{kk} \sin(\theta_{kk})$. Therefore condition (5.8) implies that $(2L_{kk}m_k - d_k^2) \leq 0$, thus the left-hand side of the inequality (D.4) is nonpositive. If $\alpha \geq 0$ and $\beta \neq 0$, the right-hand side of (D.4) will be positive, which is the desired contradiction. According to Proposition 5, the simple zero eigenvalue of the Jacobian matrix J stems from the translational invariance of the flow function (5.2). As mentioned earlier, we can eliminate this eigenvalue by choosing a reference bus and refer all other bus angles to it. Therefore, the set of equilibrium points $\{\delta^* + \alpha \mathbf{1} : \alpha \in \mathbb{R}\}$ will collapse into one equilibrium point. Such an equilibrium point will be asymptotically stable. \square

proof of (d). See the proof of Theorem 17. \square

D.3 Proof of Lemma 8

Proof. Consider the nodal admittance matrix $Y \in \mathbb{C}^{n \times n}$ which satisfies Assumptions 2 and 3. Let Y induce a network $\mathcal{G} = (\mathcal{N}, \mathcal{E})$ with the set of active nodes $\alpha \subset \mathcal{N}$ and passive nodes $\beta = \mathcal{N} \setminus \alpha$. According to Definition 6, the Kron reduced matrix after removing node $k_0 \in \beta$ is $Y^r \in \mathbb{C}^{(n-1) \times (n-1)}$ defined as

$$Y_{ik}^r = Y_{ik} - Y_{ik_0} Y_{k_0 k} / Y_{k_0 k_0}, \quad \forall i, k \neq k_0 \tag{D.6}$$

First, we prove that Y^r satisfies Assumption 2. Recall that the following two classes of matrices are invariant under Kron reduction [27]: i) matrices with zero row sum; ii) symmetric matrices. In other words, Y^r is a symmetric matrix with zero row sum. Hence, we can restrict our analysis to off-diagonal entries, and aim to prove that $Y^r = G^r + \mathbf{i}B^r$ satisfies $G_{ik}^r \leq 0, B_{ik}^r \geq 0$, for all $i \neq k$. Consider $Y_{ik} = G_{ik} + \mathbf{i}B_{ik}$ with $G_{ik} \leq 0$ and

$B_{ik} \geq 0$ and note that for off-diagonal entries $Y_{ik}^r, i \neq k$, we have

$$\begin{aligned}
Y_{ik} - Y_{ik}^r &= Y_{ik_0} Y_{k_0k} / Y_{k_0k_0} \\
&= (G_{ik_0} + \mathbf{i}B_{ik_0})(G_{k_0k} + \mathbf{i}B_{k_0k}) / (G_{k_0k_0} + \mathbf{i}B_{k_0k_0}) \\
&= ((G_{ik_0}G_{k_0k} - B_{ik_0}B_{k_0k}) \\
&\quad + \mathbf{i}(G_{ik_0}B_{k_0k} + B_{ik_0}G_{k_0k}))(G_{k_0k_0} - \mathbf{i}B_{k_0k_0}) / \eta,
\end{aligned}$$

where $\eta = G_{k_0k_0}^2 + B_{k_0k_0}^2$. Observe that

$$\begin{aligned}
\text{Im}(Y_{ik_0} Y_{k_0k} / Y_{k_0k_0}) \eta &= G_{k_0k_0} G_{ik_0} B_{k_0k} + G_{k_0k_0} B_{ik_0} G_{k_0k} \\
&\quad - B_{k_0k_0} (G_{ik_0} G_{k_0k} - B_{ik_0} B_{k_0k}) \leq 0,
\end{aligned}$$

where the inequality holds because under Assumptions 2 and 3, we have

$$\begin{aligned}
G_{k_0k_0} G_{ik_0} B_{k_0k} &\leq 0, G_{k_0k_0} B_{ik_0} G_{k_0k} \leq 0, \\
G_{ik_0} G_{k_0k} - B_{ik_0} B_{k_0k} &\leq 0, -B_{k_0k_0} \geq 0.
\end{aligned}$$

This proves that $B_{ik}^r \geq 0$, for all $i \neq k$. Also observe that

$$\begin{aligned}
\text{Re}(Y_{ik_0} Y_{k_0k} / Y_{k_0k_0}) \eta &= G_{k_0k_0} G_{ik_0} G_{k_0k} - G_{k_0k_0} B_{ik_0} B_{k_0k} \\
&\quad + B_{k_0k_0} G_{ik_0} B_{k_0k} + B_{k_0k_0} B_{ik_0} G_{k_0k} \\
&\geq G_{k_0k_0} G_{ik_0} G_{k_0k} - \nu_{\max}^2 G_{k_0k_0} G_{ik_0} G_{k_0k} \\
&\quad + \nu_{\min}^2 G_{k_0k_0} G_{ik_0} G_{k_0k} + \nu_{\min}^2 G_{k_0k_0} G_{ik_0} G_{k_0k} \\
&= (1 + 2\nu_{\min}^2 - \nu_{\max}^2) G_{k_0k_0} G_{ik_0} G_{k_0k} \geq 0,
\end{aligned}$$

where the inequality holds because under Assumptions 2 and 3, we have $1 + 2\nu_{\min}^2 - \nu_{\max}^2 \geq 0$ and $G_{k_0k_0}G_{ik_0}G_{k_0k} \geq 0$. This shows that $G_{ik}^r \leq 0$ for all $i \neq k$, and completes the first part of proof. Next, we prove that $B_{kk}^r \geq B_{kk}$ for all $k \neq k_0$. Observe that

$$\text{Im}(Y_{kk}^r - Y_{kk})\eta = (G_{k_0k_0}^2 - B_{k_0k_0}^2)B_{k_0k_0} - 2G_{k_0k_0}G_{kk_0}B_{kk_0}.$$

According to Assumption 2, we have $G_{k_0k_0} \geq 0, B_{k_0k_0} \leq 0, G_{kk_0} \leq 0, B_{kk_0} \geq 0, \forall k \neq k_0$. Assumption 3 says $|G_{kk_0}| \leq |B_{kk_0}|$. Hence $(G_{k_0k_0}^2 - B_{k_0k_0}^2)B_{k_0k_0} \geq 0$ and $-2G_{k_0k_0}G_{kk_0}B_{kk_0} \geq 0$. This implies that $B_{kk}^r \geq B_{kk}$, and completes the proof. \square

D.4 Proof of Theorem 13

Proof. Let the nodal admittance matrix of \mathcal{G}^d be $Y \in \mathbb{C}^{n \times n}$ which satisfies Assumptions 2 and 3. Suppose \mathcal{G}^d has the set of active nodes $\alpha \subset \mathcal{N}^d$ and passive nodes $\beta = \mathcal{N}^d \setminus \alpha$. After properly labeling the nodes, we can have $\beta = \{n - |\beta| + 1, \dots, n\}$. In order to get the admittance matrix Y^r of the Kron reduced network \mathcal{G}^r , we need to remove the set of passive nodes β according to Definition 6, and this can be accomplished by constructing a sequence of matrices $\{Y^{(\ell)}\}_{\ell=1}^{|\beta|}$, where $Y^{(\ell)} \in \mathbb{C}^{(n-\ell) \times (n-\ell)}$ is defined as

$$Y_{ik}^{(\ell)} = Y_{ik}^{(\ell-1)} - Y_{im_\ell}^{(\ell-1)}Y_{m_\ell k}^{(\ell-1)} / Y_{m_\ell m_\ell}^{(\ell-1)}, \quad (\text{D.7})$$

where $i, k \in \{1, \dots, n - \ell\}$, $Y^{(0)} = Y$, $Y^{(|\beta|)} = Y^r$, and $m_\ell = n - \ell + 1$. Observe that the matrix sequence $\{Y^{(\ell)}\}_{\ell=1}^{|\beta|}$ is well-defined. Now, according to Lemma 8, for each $\ell \in \{1, \dots, |\beta|\}$ matrix $Y^{(\ell)}$ satisfies Assumptions 2. Hence, Y^r satisfies both Assumptions 2 and 3.

Next, Let $V \in \mathbb{C}^n$ and $S \in \mathbb{C}^n$ be the vector of nodal voltages and power injections of network \mathcal{G}^d , respectively. It can be shown that if the vector of nodal voltages of the reduced network \mathcal{G}^r is $V[\alpha]$, then the vector of power injections in the reduced network is $S[\alpha]$. Hence, if the voltage magnitudes in the original and Kron-reduced networks are

equal, then the reactive power Q_i at active nodes in the two networks are equal.

Moreover, Lemma 8 asserts that $B_{ii}^{(\ell)} \geq B_{ii}^{(\ell-1)}$, for all $i \in \{1, \dots, n - \ell\}$. Since this inequality holds for all $\ell \in \{1, \dots, |\beta|\}$, by induction, we conclude that $B_{ii}^r \geq B_{ii}, \forall i \in \{1, \dots, n - |\beta|\}$ where B_{ii}^r and B_{ii} are the i th diagonal entries of the Kron-reduced and original admittance matrices, respectively. Note that $-Q_i - B_{ii}^r V_i^2 \leq -Q_i - B_{ii} V_i^2$. Therefore, if $-Q_i - B_{ii} V_i^2 \leq d_i^2/2m_i$ holds for active nodes in the original network, then $-Q_i - B_{ii}^r V_i^2 \leq \frac{d_i^2}{2m_i}$ also holds and according to Theorem 12, the stability of the system is guaranteed. □

REFERENCES

- [1] P. M. Anderson and A. A. Fouad, *Power System Control and Stability*. John Wiley & Sons, 2008.
- [2] H.-D. Chiang, M. W. Hirsch, and F. F. Wu, “Stability regions of nonlinear autonomous dynamical systems”, *IEEE Trans. Automat. Control*, vol. 33, no. 1, pp. 16–27, 1988.
- [3] J. Zaborszky, G. Huang, B. Zheng, and T.-C. Leung, “On the phase portrait of a class of large nonlinear dynamic systems such as the power system”, *IEEE Trans. Automat. Control*, vol. 33, no. 1, pp. 4–15, 1988.
- [4] H.-D. Chiang, *Direct Methods for Stability Analysis of Electric Power Systems: Theoretical Foundation, BCU Methodologies, and Applications*. John Wiley & Sons, 2011.
- [5] P. Varaiya, F. F. Wu, and R.-L. Chen, “Direct methods for transient stability analysis of power systems: Recent results”, *Proc. IEEE*, vol. 73, no. 12, pp. 1703–1715, 1985.
- [6] T. L. Vu and K. Turitsyn, “Lyapunov functions family approach to transient stability assessment”, *IEEE Trans. Power Syst.*, vol. 31, no. 2, pp. 1269–1277, 2015.
- [7] H.-D. Chiang, “Study of the existence of energy functions for power systems with losses”, *IEEE Trans. Circuits Syst.*, vol. 36, no. 11, pp. 1423–1429, 1989.
- [8] T. Athay, R. Podmore, and S. Virmani, “A practical method for the direct analysis of transient stability”, *IEEE Trans. Power App. Syst.*, no. 2, pp. 573–584, 1979.
- [9] Y. Zhang and L. Xie, “A transient stability assessment framework in power electronic-interfaced distribution systems”, *IEEE Trans. Power Syst.*, vol. 31, no. 6, pp. 5106–5114, 2016.
- [10] A. Gholami and X. A. Sun, “Towards resilient operation of multimicrogrids: An MISOCP-based frequency-constrained approach”, *IEEE Trans. Control Netw. Syst.*, vol. 6, no. 3, pp. 925–936, 2019.
- [11] J. Schiffer, D. Goldin, J. Raisch, and T. Sezi, “Synchronization of droop-controlled microgrids with distributed rotational and electronic generation”, in *52nd IEEE Conf. Decision Control*, 2013, pp. 2334–2339.

- [12] Q.-C. Zhong and G. Weiss, “Synchronverters: Inverters that mimic synchronous generators”, *IEEE Trans. Industrial Electronics*, vol. 58, no. 4, pp. 1259–1267, 2010.
- [13] T. L. Vu, H. D. Nguyen, J. Slotine, and K. Turitsyn, “Reconfigurable microgrid architecture for blackout prevention”, 2019.
- [14] *IEEE Recommended Practice for Utility Interconnected Photovoltaic (PV) Systems*, 2000.
- [15] *IEEE Guide for Conducting Distribution Impact Studies for Distributed Resource Interconnection*, 2013.
- [16] S. J. Skar, “Stability of multi-machine power systems with nontrivial transfer conductances”, *SIAM J. Appl. Math.*, vol. 39, no. 3, pp. 475–491, 1980.
- [17] A. Gholami and X. A. Sun, “A fast certificate for power system small-signal stability”, in *59th IEEE Conf. Decision Control*, arXiv:2008.02263, 2020, pp. 3383–3388.
- [18] H.-D. Chiang and F. F. Wu, “Stability of nonlinear systems described by a second-order vector differential equation”, *IEEE Trans. Circuits Syst.*, vol. 35, no. 6, pp. 703–711, 1988.
- [19] A. Laub and W. Arnold, “Controllability and observability criteria for multivariable linear second-order models”, *IEEE Trans. Automat. Control*, vol. 29, no. 2, pp. 163–165, 1984.
- [20] F. Ma, M. Morzfeld, and A. Imam, “The decoupling of damped linear systems in free or forced vibration”, *J. Sound Vib.*, vol. 329, no. 15, pp. 3182–3202, 2010.
- [21] S. Adhikari, *Structural Dynamic Analysis with Generalized Damping Models: Analysis*. John Wiley & Sons, 2013.
- [22] F. Dorfler and F. Bullo, “Synchronization and transient stability in power networks and nonuniform kuramoto oscillators”, *SIAM J. Control Optim.*, vol. 50, no. 3, pp. 1616–1642, 2012.
- [23] ———, “On the critical coupling for kuramoto oscillators”, *SIAM J. Appl. Dyn. Syst.*, vol. 10, no. 3, pp. 1070–1099, 2011.
- [24] J. A. Acebron, L. L. Bonilla, C. J. P. Vicente, F. Ritort, and R. Spigler, “The kuramoto model: A simple paradigm for synchronization phenomena”, *Rev. Modern Phys.*, vol. 77, no. 1, pp. 137–185, 2005.

- [25] I. V. Belykh, B. N. Brister, and V. N. Belykh, “Bistability of patterns of synchrony in kuramoto oscillators with inertia”, *Chaos*, vol. 26, no. 9, p. 094 822, 2016.
- [26] B. N. Brister, V. N. Belykh, and I. V. Belykh, “When three is a crowd: Chaos from clusters of kuramoto oscillators with inertia”, *Phys. Rev. E*, vol. 101, p. 062 206, 6 2020.
- [27] F. Dorfler and F. Bullo, “Kron reduction of graphs with applications to electrical networks”, *IEEE Trans. Circuits Syst. I: Reg. Papers*, vol. 60, no. 1, pp. 150–163, 2012.
- [28] A. R. Bergen and D. J. Hill, “A structure preserving model for power system stability analysis”, *IEEE Trans. Power Appar. Syst.*, no. 1, pp. 25–35, 1981.
- [29] P. Kokotovic, H. K. Khali, and J. O’reilly, *Singular Perturbation Methods in Control: Analysis and Design*. Siam, 1999, vol. 25.
- [30] D. Braess, A. Nagurney, and T. Wakolbinger, “On a paradox of traffic planning”, *Transportation Science*, vol. 39, no. 4, pp. 446–450, 2005.
- [31] B. Stott and O. Alsac, “Fast decoupled load flow”, *IEEE Trans. Power Appar. Syst.*, vol. PAS-93, no. 3, pp. 859–869, 1974.
- [32] P. Kundur, *Power System Stability and Control*. New York, NY, USA: McGraw-Hill, 1994.
- [33] R. Miller and A. Michel, “Asymptotic stability of systems: Results involving the system topology”, *SIAM J. Control Optim.*, vol. 18, no. 2, pp. 181–190, 1980.
- [34] F. J. Koerts, M. Burger, A. J. van der Schaft, and C. D. Persis, “Topological and graph-coloring conditions on the parameter-independent stability of second-order networked systems”, *SIAM J. Control Optim.*, vol. 55, no. 6, pp. 3750–3778, 2017.
- [35] D. N. Kosterev, C. W. Taylor, and W. A. Mittelstadt, “Model validation for the august 10, 1996 wscs system outage”, *IEEE Trans. Power Syst.*, vol. 14, no. 3, pp. 967–979, 1999.
- [36] (). “Eastern interconnection forced oscillation event report on january 11, 2019”. North American Electric Reliability Corporation, (visited on 2019).
- [37] K. Koorehdavoudi, S. Roy, T. Prevost, F. Xavier, P. Panciatici, and V. M. Venkatasubramanian, “Input-output properties of the power grid’s swing dynamics: Dependence on network parameters”, in *2019 IEEE Conf. Control Technology Applications (CCTA)*, IEEE, 2019, pp. 92–97.

- [38] M. Mokhtari, F. Aminifar, D. Nazarpour, and S. Golshannavaz, “Wide-area power oscillation damping with a fuzzy controller compensating the continuous communication delays”, *IEEE Trans. Power Syst.*, vol. 28, no. 2, pp. 1997–2005, 2012.
- [39] A. Arapostathis, S. Sastry, and P. Varaiya, “Global analysis of swing dynamics”, *IEEE Trans. Circuits Syst.*, vol. 29, no. 10, pp. 673–679, 1982.
- [40] E. Abed and P. Varaiya, “Oscillations in power systems via hopf bifurcation”, in *20th IEEE Conference on Decision and Control*, IEEE, 1981, pp. 926–929.
- [41] J. Alexander, “Oscillatory solutions of a model system of nonlinear swing equations”, *Int. J. Elec. Power Ener. Syst.*, vol. 8, no. 3, pp. 130–136, 1986.
- [42] H. G. Kwatny and X.-M. Yu, “Energy analysis of load-induced flutter instability in classical models of electric power networks”, *IEEE Trans. Circuits Syst.*, vol. 36, no. 12, pp. 1544–1557, 1989.
- [43] H. Kwatny and G. Piper, “Frequency domain analysis of hopf bifurcations in electric power networks”, *IEEE Trans. Circuits Syst.*, vol. 37, no. 10, pp. 1317–1321, 1990.
- [44] I. A. Hiskens and P. B. Reddy, “Switching-induced stable limit cycles”, *Nonlinear Dyn.*, vol. 50, no. 3, pp. 575–585, 2007.
- [45] P. B. Reddy and I. A. Hiskens, *Limit-induced stable limit cycles in power systems*. IEEE Russia Power Tech, 2005.
- [46] F. Paganini and E. Mallada, “Global performance metrics for synchronization of heterogeneously rated power systems: The role of machine models and inertia”, in *55th Annu. Allert. Conf. Commun. Control Comput.*, 2017, pp. 324–331.
- [47] T. W. Mak, P. Van Hentenryck, and I. A. Hiskens, “A nonlinear optimization model for transient stable line switching”, in *2017 American Control Conf. (ACC)*, 2017, pp. 2085–2092.
- [48] H. Hijazi, T. W. Mak, and P. Van Hentenryck, “Power system restoration with transient stability”, in *Proc. AAAI Conf. Artificial Intelligence*, vol. 29, 2015.
- [49] D. K. Molzahn, B. C. Lesieutre, and C. L. DeMarco, “A sufficient condition for power flow insolvability with applications to voltage stability margins”, *IEEE Trans. Power Syst.*, vol. 28, no. 3, pp. 2592–2601, 2013.
- [50] C. Jozs, D. K. Molzahn, M. Tacchi, and S. Sojoudi, “Transient stability analysis of power systems via occupation measures”, in *IEEE Conf. Innov. Smart Grid Technol.*, Washington, DC, USA, 2019.

- [51] S. V. Dhople, Y. C. Chen, L. DeVille, and A. D. Dominguez-Garcia, “Analysis of power system dynamics subject to stochastic power injections”, *IEEE Trans. Circuits Syst. I: Regul. Pap.*, vol. 60, no. 12, pp. 3341–3353, 2013.
- [52] C. Zhao, U. Topcu, N. Li, and S. Low, “Design and stability of load-side primary frequency control in power systems”, *IEEE Trans. Automat. Control*, vol. 59, no. 5, pp. 1177–1189, 2014.
- [53] T. L. Vu and K. Turitsyn, “A framework for robust assessment of power grid stability and resiliency”, *IEEE Trans. Automat. Control*, vol. 62, no. 3, pp. 1165–1177, 2016.
- [54] R. Ortega, M. Galaz, A. Astolfi, Y. Sun, and T. Shen, “Transient stabilization of multimachine power systems with nontrivial transfer conductances”, *IEEE Trans. Automat. Control*, vol. 50, no. 1, pp. 60–75, 2005.
- [55] E. Weitenberg, Y. Jiang, C. Zhao, E. Mallada, C. De Persis, and F. Dorfler, “Robust decentralized secondary frequency control in power systems: Merits and tradeoffs”, *IEEE Trans. Automat. Control*, vol. 64, no. 10, pp. 3967–3982, 2018.
- [56] F. Tisseur and K. Meerbergen, “The quadratic eigenvalue problem”, *SIAM Rev.*, vol. 43, no. 2, pp. 235–286, 2001.
- [57] R. A. Horn and C. R. Johnson, *Matrix Analysis*, 2nd ed. New York: Cambridge University Press, 2013.
- [58] S. J. Skar, “Stability of power systems and other systems of second order differential equations”, Ph.D. dissertation, Dept. Math., Iowa State Univ., Iowa, USA, 1980.
- [59] Y. A. Kuznetsov, *Elements of Applied Bifurcation Theory*. Springer Science & Business Media, 2004, vol. 112.
- [60] A. Greenbaum, R.-c. Li, and M. L. Overton, “First-order perturbation theory for eigenvalues and eigenvectors”, *SIAM Rev.*, vol. 62, no. 2, pp. 463–482, 2020.
- [61] D. S. Schmidt, “Hopf’s bifurcation theorem and the center theorem of liapunov with resonance cases”, *J. Math. Anal. Appl.*, vol. 63, no. 2, pp. 354–370, 1978.
- [62] G. Poole and T. Boullion, “A survey on M-matrices”, *SIAM Rev.*, vol. 16, no. 4, pp. 419–427, 1974.
- [63] A. Gholami and X. A. Sun, “Stability of multi-microgrids: New certificates, distributed control, and braess’s paradox”, *IEEE Trans. Control Netw. Syst.*, 2021.

- [64] A. J. Conejo, M. Carrion, and J. M. Morales, *Decision Making under Uncertainty in Electricity Markets*. Springer, 2010.
- [65] P. Kundur, J. Paserba, V. Ajjarapu, G. Andersson, A. Bose, C. Canizares, N. Hatziargyriou, D. Hill, A. Stankovic, C. Taylor, *et al.*, “Definition and classification of power system stability”, *IEEE Trans. Power Syst.*, vol. 19, no. 2, pp. 1387–1401, 2004.
- [66] F. Dorfler and F. Bullo, “Synchronization and transient stability in power networks and nonuniform kuramoto oscillators”, *SIAM J. Control Optimiz.*, vol. 50, no. 3, pp. 1616–1642, 2012.
- [67] F. Ebrahimzadeh, M. Adeen, and F. Milano, *On the impact of topology on power system transient and frequency stability*. IEEEIC-ICPS Europe, 2019.
- [68] C. Chicone, *Ordinary Differential Equations with Applications*. Springer Science & Business Media, 2006, vol. 34.
- [69] R. D. Zimmerman and C. E. Murillo-Sanchez. (2019). “MATPOWER”. version 7.0.
- [70] T. Ishizaki, A. Chakraborty, and J.-I. Imura, “Graph-theoretic analysis of power systems”, *Proc. IEEE*, vol. 106, no. 5, pp. 931–952, 2018.
- [71] J. Ma, S. Feuerborn, C. Black, and V. M. Venkatasubramanian, “A comprehensive software suite for power grid stability monitoring based on synchrophasor measurements”, in *2017 IEEE Power & Energy Society Innovative Smart Grid Technologies Conf. (ISGT)*, IEEE, 2017, pp. 1–5.
- [72] J. Follum, N. Zhou, and J. W. Pierre, “Evaluation of mode estimation accuracy for small-signal stability analysis”, in *2011 North American Power Symp.*, IEEE, 2011, pp. 1–7.
- [73] A. Gholami and X. A. Sun, “The impact of damping in second-order dynamical systems with applications to power grid stability”, *SIAM J. Appl. Dyn. Syst.*, 2021, arXiv:2010.06662 [math.DS].
- [74] A. Michel, A. Fouad, and V. Vittal, “Power system transient stability using individual machine energy functions”, *IEEE Trans. Circuits Syst.*, vol. 30, no. 5, pp. 266–276, 1983.
- [75] F. Dorfler and F. Bullo, “Topological equivalence of a structure-preserving power network model and a non-uniform kuramoto model of coupled oscillators”, in *2011 50th IEEE Conf. Decision and Control and European Control Conf.*, IEEE, 2011, pp. 7099–7104.

- [76] T. L. Vu and K. Turitsyn, “A framework for robust assessment of power grid stability and resiliency”, *IEEE Trans. Automat. Control*, vol. 62, no. 3, pp. 1165–1177, 2016.
- [77] F. Wilches-Bernal, R. H. Byrne, and J. Lian, “Damping of inter-area oscillations via modulation of aggregated loads”, *IEEE Trans. Power Syst.*, vol. 35, no. 3, pp. 2024–2036, 2019.
- [78] F. Wilches-Bernal, C. Lackner, J. H. Chow, and J. J. Sanchez-Gasca, “Effects of wind turbine generators on inter-area oscillations and damping control design”, in *Proc. 52nd Hawaii Int. Conf. Syst. Sci.*, 2019.
- [79] J. H. Chow and J. J. Sanchez-Gasca, “Linear analysis and small-signal stability”, in *Power System Modeling, Computation, and Control*. 2020, pp. 149–173.
- [80] F. Milano and I. Dassios, “Primal and dual generalized eigenvalue problems for power systems small-signal stability analysis”, *IEEE Trans. Power Syst.*, vol. 32, no. 6, pp. 4626–4635, 2017.
- [81] X. Wang, Y. Koç, R. E. Kooij, and P. Van Mieghem, “A network approach for power grid robustness against cascading failures”, in *7th int. workshop on reliable networks design and modeling (RNDM)*, 2015, pp. 208–214.
- [82] C. Balestra, F. Kaiser, D. Manik, and D. Witthaut, “Multistability in lossy power grids and oscillator networks”, *Chaos*, vol. 29, no. 12, p. 123 119, 2019.
- [83] E. B. T. Tchuisseu, D. Gomila, P. Colet, D. Witthaut, M. Timme, and B. Schäfer, “Curing Braess’ paradox by secondary control in power grids”, *New J. Phys.*, vol. 20, no. 8, p. 083 005, 2018.
- [84] J. A. Torres and S. Roy, “Graph-theoretic analysis of network input–output processes: Zero structure and its implications on remote feedback control”, *Automatica*, vol. 61, pp. 73–79, 2015.
- [85] K. Koorehdavoudi, M. Hatami, S. Roy, V. Venkatasubramanian, P. Panciatici, F. Xavier, and J. A. Torres, “Input-output characteristics of the power transmission network’s swing dynamics”, in *55th IEEE Conf. Decision Control*, 2016, pp. 1846–1852.
- [86] F. Ebrahimzadeh, M. Adeen, and F. Milano, “On the impact of topology on power system transient and frequency stability”, in *EEEICI-ICPS Europe*, IEEE, 2019.
- [87] F. Dorfler, J. W. Simpson-Porco, and F. Bullo, “Electrical networks and algebraic graph theory: Models, properties, and applications”, *Proc. IEEE*, vol. 106, no. 5, pp. 977–1005, 2018.

- [88] J. W. Simpson-Porco, F. Dorfler, and F. Bullo, “Synchronization and power sharing for droop-controlled inverters in islanded microgrids”, *Automatica*, vol. 49, no. 9, pp. 2603–2611, 2013.
- [89] J. Schiffer, R. Ortega, A. Astolfi, J. Raisch, and T. Sezi, “Conditions for stability of droop-controlled inverter-based microgrids”, *Automatica*, vol. 50, no. 10, pp. 2457–2469, 2014.
- [90] P. Vorobev, P.-H. Huang, M. Al Hosani, J. L. Kirtley, and K. Turitsyn, “A framework for development of universal rules for microgrids stability and control”, in *56th IEEE Conf. Decision Control*, IEEE, 2017, pp. 5125–5130.
- [91] ———, “Towards plug-and-play microgrids”, in *44th Annu. Conf. IEEE Ind. Electron. Soc.*, 2018, pp. 4063–4068.
- [92] P.-H. Huang, P. Vorobev, M. Al Hosani, J. L. Kirtley, and K. Turitsyn, “Plug-and-play compliant control for inverter-based microgrids”, *IEEE Trans. Power Syst.*, vol. 34, no. 4, pp. 2901–2913, 2019.
- [93] F. Paganini and E. Mallada, “Global analysis of synchronization performance for power systems: Bridging the theory-practice gap”, *IEEE Trans. Automat. Control*, vol. 65, no. 7, pp. 3007–3022, 2020.
- [94] A. S. Matveev, J. E. M. Martinez, R. Ortega, J. Schiffer, and A. Pyrkin, “A tool for analysis of existence of equilibria and voltage stability in power systems with constant power loads”, *IEEE Trans. Automat. Control*, 2020.
- [95] V. Purba, B. B. Johnson, M. Rodriguez, S. Jafarpour, F. Bullo, and S. V. Dhople, “Reduced-order aggregate model for parallel-connected single-phase inverters”, *IEEE Trans. Energy Convers.*, vol. 34, no. 2, pp. 824–837, 2019.
- [96] M. Khan, Y. Lin, B. Johnson, V. Purba, M. Sinha, and S. Dhople, “A reduced-order aggregated model for parallel inverter systems with virtual oscillator control”, in *IEEE 19th Workshop Control Modeling for Power Electron. (COMPEL)*, 2018, pp. 1–6.
- [97] X. Hou, Y. Sun, X. Zhang, J. Lu, P. Wang, and J. M. Guerrero, “Improvement of frequency regulation in vsg-based ac microgrid via adaptive virtual inertia”, *IEEE Trans. Power Electron.*, vol. 35, no. 2, pp. 1589–1602, 2019.
- [98] A. Gholami, T. Shekari, and S. Grijalva, “Proactive management of microgrids for resiliency enhancement: An adaptive robust approach”, *IEEE Trans. Sustain. Energy*, vol. 10, no. 1, pp. 470–480, 2017.

- [99] M. E. Baran and F. F. Wu, “Network reconfiguration in distribution systems for loss reduction and load balancing”, *IEEE Trans. Power Del.*, vol. 4, no. 2, pp. 1401–1407, 1989.
- [100] S. Kundu, S. Geng, S. P. Nandanoori, I. A. Hiskens, and K. Kalsi, “Distributed barrier certificates for safe operation of inverter-based microgrids”, in *2019 American Control Conference (ACC)*, IEEE, 2019, pp. 1042–1047.
- [101] R. Mathias, “Quadratic residual bounds for the hermitian eigenvalue problem”, *SIAM journal on matrix analysis and applications*, vol. 19, no. 2, pp. 541–550, 1998.
- [102] E. Jiang and P. C. Lam, “An upper bound for the spectral condition number of a diagonalizable matrix”, *Linear algebra and its applications*, vol. 262, pp. 165–178, 1997.
- [103] J. A. Momoh, S. Meliopoulos, and R. Saint, “Centralized and distributed generated power systems-a comparison approach”, *Future grid initiative white paper, PSERC*, pp. 1–33, 2012.
- [104] D. T. Ton and M. A. Smith, “The U.S. Department of Energy’s microgrid initiative”, *The Electricity Journal*, vol. 25, no. 8, pp. 84–94, 2012.
- [105] *Recommended Practice for Utility Interconnected Photovoltaic (PV) Systems*, 2000.
- [106] *IEEE Standard for Interconnecting Distributed Resources Into Electric Power Systems*, 2003.
- [107] P. Mahat, Z. Chen, and B. Bak-Jensen, “Under frequency load shedding for an islanded distribution system with distributed generators”, *IEEE Trans. Power Del.*, vol. 25, no. 2, pp. 911–918, 2010.
- [108] B. Delfino, S. Massucco, A. Morini, P. Scalera, and F. Silvestro, “Implementation and comparison of different under frequency load-shedding schemes”, in *Proc. IEEE Power Eng. Soc. Summer Meeting*, vol. 1, 2001, pp. 307–312.
- [109] H. Seyedi and M. Sanaye-Pasand, “New centralized adaptive load shedding algorithms to mitigate power system blackouts”, *IET Gener. Transm. Distrib.*, vol. 3, no. 1, pp. 99–114, 2009.
- [110] J. Tang, J. Liu, F. Ponci, and A. Monti, “Adaptive load shedding based on combined frequency and voltage stability assessment using synchrophasor measurements”, *IEEE Trans. Power Syst.*, vol. 28, no. 2, pp. 2035–2047, 2013.

- [111] T. Shekari, F. Aminifar, and M. Sanaye-Pasand, “An analytical adaptive load shedding scheme against severe combinational disturbances”, *IEEE Trans. Power Syst.*, vol. 31, no. 5, pp. 4135–4143, 2016.
- [112] T. Shekari, A. Gholami, F. Aminifar, and M. Sanaye-Pasand, “An adaptive wide-area load shedding scheme incorporating power system real-time limitations”, *IEEE Syst. J.*, vol. 12, no. 1, pp. 759–767, 2018.
- [113] U. Rudez and R. Mihalic, “WAMS-based under frequency load shedding with short-term frequency prediction”, *IEEE Trans. Power Del.*, vol. 31, no. 4, pp. 1912–1920, 2016.
- [114] V. V. Terzija, “Adaptive underfrequency load shedding based on the magnitude of the disturbance estimation”, *IEEE Trans. Power Syst.*, vol. 21, no. 3, pp. 1260–1266, 2006.
- [115] Y. Lu, W. Kao, and Y. Chen, “Study of applying load shedding scheme with dynamic d-factor values of various dynamic load models to taiwan power system”, *IEEE Trans. Power Syst.*, vol. 20, no. 4, pp. 1976–1984, 2005.
- [116] IEEE Task Force on Load Representation for Dynamic Performance, “Bibliography on load models for power flow and dynamic performance simulation”, *IEEE Trans. Power Syst.*, vol. 10, no. 1, pp. 523–538, 1995.
- [117] P. A. Trodden, W. A. Bukhsh, A. Grothey, and K. I. McKinnon, “Optimization-based islanding of power networks using piecewise linear ac power flow”, *IEEE Trans. Power Syst.*, vol. 29, no. 3, pp. 1212–1220, 2014.
- [118] M. E. Baran and F. Wu, “Network reconfiguration in distribution system for loss reduction and load balancing”, *IEEE Trans. Power Del.*, vol. 4, no. 2, pp. 1401–1407, 1989.
- [119] A. Gholami, T. Shekari, F. Aminifar, and M. Shahidehpour, “Microgrid scheduling with uncertainty: The quest for resilience”, *IEEE Trans. Smart Grid*, vol. 7, no. 6, pp. 2849–2858, 2016.
- [120] A. Gholami, T. Shekari, and A. Sun, “An adaptive optimization-based load shedding scheme in microgrids”, in *Proceedings of the 51st Hawaii International Conference on System Sciences*, 2018.
- [121] *IEEE Draft Standard for Interconnection and Interoperability of Distributed Energy Resources with Associated Electric Power Systems Interfaces*, 2017.

- [122] P. Mahat, Z. Chen, and B. Bak-Jensen, "Under frequency load shedding for an islanded distribution system with distributed generators", *IEEE Trans. Power Del.*, vol. 25, no. 2, pp. 911–918, 2010.
- [123] F. Katiraei, M. R. Iravani, and P. W. Lehn, "Micro-grid autonomous operation during and subsequent to islanding process", *IEEE Trans. Power Del.*, vol. 20, no. 1, pp. 248–257, 2005.
- [124] I. J. Balaguer, Q. Lei, S. Yang, U. Supatti, and F. Z. Peng, "Control for grid-connected and intentional islanding operations of distributed power generation", *IEEE Trans. Ind. Electron.*, vol. 58, no. 1, pp. 147–157, 2011.
- [125] Y. Zhang and L. Xie, "Online dynamic security assessment of microgrid interconnections in smart distribution systems", *IEEE Trans. Power Syst.*, vol. 30, no. 6, pp. 3246–3254, 2015.
- [126] Y. Zhang, L. Xie, and Q. Ding, "Interactive control of coupled microgrids for guaranteed system-wide small signal stability", *IEEE Trans. Smart Grid*, vol. 7, no. 2, pp. 1088–1096, 2016.
- [127] Y. Zhang and L. Xie, "A transient stability assessment framework in power electronic-interfaced distribution systems", *IEEE Trans. Power Syst.*, vol. 31, no. 6, pp. 5106–5114, 2016.
- [128] W.-Y. Chiu, H. Sun, and H. V. Poor, "A multiobjective approach to multimicrogrid system design", *IEEE Trans. Smart Grid*, vol. 6, no. 5, pp. 2263–2272, 2015.
- [129] H. Farzin, M. Fotuhi-Firuzabad, and M. Moeini-Aghaie, "Enhancing power system resilience through hierarchical outage management in multi-microgrids", *IEEE Trans. Smart Grid*, vol. 7, no. 6, pp. 2869–2879, 2016.
- [130] Z. Wang, B. Chen, J. Wang, and C. Chen, "Networked microgrids for self-healing power systems", *IEEE Trans. Smart Grid*, vol. 7, no. 1, pp. 310–319, 2016.
- [131] C. Coffrin, H. L. Hijazi, and P. Van Hentenryck, "Strengthening the sdp relaxation of ac power flows with convex envelopes, bound tightening, and valid inequalities", *IEEE Trans. Power Syst.*, vol. 32, no. 5, pp. 3549–3558, 2016.
- [132] R. Majumder, A. Ghosh, G. Ledwich, and F. Zare, "Power management and power flow control with back-to-back converters in a utility connected microgrid", *IEEE Trans. Power Syst.*, vol. 25, no. 2, pp. 821–834, 2010.
- [133] H. Ahmadi and H. Ghasemi, "Security-constrained unit commitment with linearized system frequency limit constraints", *IEEE Trans. Power Syst.*, vol. 29, no. 4, pp. 1536–1545, 2014.

- [134] B. Kocuk, S. S. Dey, and X. A. Sun, “Strong SOCP relaxations for the optimal power flow problem”, *Oper. Res.*, vol. 64, no. 6, pp. 1177–1196, 2016.
- [135] D. B. West *et al.*, *Introduction to Graph Theory*. Prentice hall Upper Saddle River, 2001, vol. 2.
- [136] (2016). “GAMS User Manual”, (visited on 08/2017).
- [137] (2007). “BONMIN User Manual”, (visited on 08/2017).
- [138] (2016). “CPLEX User Manual”, (visited on 08/2017).
- [139] M. E. Baran and F. Wu, “Network reconfiguration in distribution system for loss reduction and load balancing”, *IEEE Trans. Power Del.*, vol. 4, no. 2, pp. 1401–1407, 1989.